



Sharif University of Technology
Mechanical Engineering Department

**Thermo-mechanical behavior of shape
memory alloys under multiaxial loadings:
constitutive modeling and numerical implementation
at small and finite strains**

A Dissertation
by
JAMAL ARGHAVANI

Submitted to the Office of Graduate Studies of
Sharif University of Technology, Tehran, Iran
in partial fulfillment of the requirements for the degree of

Doctor of Philosophy
in
Mechanical Engineering

Supervisors: Prof. Reza Naghdabadi
Prof. Saeed Sohrabpour
Advisor: Prof. Ferdinando Auricchio

September 2010

Thermo-mechanical behavior of shape memory alloys
under multiaxial loadings:
constitutive modeling and numerical implementation
at small and finite strains

A Dissertation
by
JAMAL ARGHAVANI

Submitted to the Office of Graduate Studies of
Sharif University of Technology, Tehran, Iran
in partial fulfillment of the requirements for the degree of
Doctor of Philosophy in Mechanical Engineering

Approved as to style and content by:

Reza Naghdabadi (Supervisor) Date

Saeed Sohrabpour (Supervisor) Date

Ferdinando Auricchio (Advisor) Date

Mohammad H. Kargarnovin (Committee member) Date

Mohammad R. Movahhedy (Committee member) Date

Mohammad T. Kazemi (Committee member) Date

Mohammad R. Eslami (Committee member) Date

September 2010

Abstract

Shape memory alloys (SMAs) are a type of smart materials which have unique features known as pseudo-elasticity, one-way and two-way shape memory effects. The interest in the mechanical behavior of SMAs is rapidly growing with the increasing number of potential industrial applications. The origin of SMA material features is a reversible thermo-elastic martensitic phase transformation between a high symmetry, austenitic phase and a low symmetry, martensitic phase. In most applications, SMAs experience general non-proportional thermo-mechanical loads. Thus, according to experimental observations, the so-called variant reorientation should be considered in the constitutive model development. Moreover, SMA structures typically undergo very large rotations and moderate strains (in the range of 10-15%) and the use of a finite deformation scheme is preferred.

In this thesis, we have studied the SMA behavior under multiaxial loadings at small and finite deformations. Considering variant reorientation accompanied by finite deformations, we have derived several SMA constitutive models and have proposed a robust and efficient numerical formulation. With the aim of properly modeling of the variant reorientation, based on continuum thermodynamics with internal variables, we have presented a class of SMA models in the small strain regime. We have shown that several available models can be identified as members of the proposed class of models. With emphasis on non-proportional loading and reorientation, we specifically have introduced a model which has the property of decoupling pure reorientation from pure phase transformation. In addition, we have shown that most available SMA models are basically the same under proportional loadings while they yield different results under non-proportional loading conditions.

We have also proposed finite deformation SMA constitutive models, which are extensions of available small strain models. The approach is based on the multiplicative decomposition of the deformation gradient into elastic and inelastic parts. The derived constitutive models are well-defined, singularity-free and fully-symmetric. In addition, we have proposed a model which utilizes interesting properties of the logarithmic strain. A main part of this thesis has been devoted to numerical implementation of the proposed constitutive models. To this end, we have proposed a logarithmic mapping, and defining a nucleation-completion condition, we have also proposed a robust and efficient integration algorithm. We have compared different models as well as integration algorithms in terms of robustness and computational efficiency. Implementing into a user defined subroutine (UMAT) in the commercial software ABAQUS, we have simulated several

SMA-based applications, i.e., an SMA spring, a nitinol stent and a smart micro-gripper. It has been shown that, comparing with the algorithms available in the literature, the proposed integration algorithm reduces the computational cost about 35%.

Keywords: shape memory alloys, pseudo-elasticity, constitutive modeling, numerical integration, large deformations, multiplicative decomposition, UMAT.

Acknowledgments

First of all, I would like to thank my Supervisors Prof. Reza Naghdabadi and Prof. Saeed Sohrabpour for their guidance and support during the course of my PhD studies. I am especially grateful to Prof. Reza Naghdabadi who taught me the art of being a researcher and for the opportunity to learn Continuum Mechanics, both through discussions and courses. Of the many courses I have taken, throughout undergraduate and graduate school, I will certainly remember those on Continuum Mechanics and Nonlinear Elasticity, taught by Prof. Naghdabadi.

I am also especially grateful to Prof. Ferdinando Auricchio who taught me the beauty of Computational Mechanics. I learned a lot through meetings and discussions we had during my sixteen months stay in Pavia, Italy. I also wish to acknowledge his financial support.

I owe special thanks to Dr. Alessandro Reali for his help during my visit in Pavia, Italy. I would also like to thank Dr. Alessandro Reali and Dr. Jaafar Ghanbari for useful discussions on coding during this research.

I would like to acknowledge the financial support of Iranian Ministry of Science, Research and Technology, National Elite Foundation, Sharif University of Technology and also the support of Department of Structural Mechanics, University of Pavia, Italy.

I would like to thank Mohammad Arghavani, Abdollah Bayati, Jaafar Ghanbari, Kam-biz Behfar, Abolhasan Shamsi, Mohsen Asghari, Shoja Ramezani, Kamyar Ghavam, Ahmad Khayer Dastjerdi, Mostafa Baghani, Javad Ashrafi, Elisa Reali, Michele Conti, Simone Morganti, Giuseppe Balduzzi, Chandan Sharma as well as many other friends whose advice and support greatly contributed to this work. The support and understanding of my family is deeply appreciated. Their love has been for me a powerful source of inspiration and energy. My mother, my father, my brothers, my sister and my wife always encouraged and supported me in these years. Last, but not least, I am enormously grateful to my wife Neda, for believing in me and providing me with the support and encouragement that have made all of this possible.

Table of Contents

Abstract	i
Acknowledgments	i
List of Tables	viii
List of Figures	xiii
1 Introduction to shape memory alloys	1
1.1 Smart materials	1
1.2 Shape memory Alloys	3
1.2.1 Shape memory effect	9
1.2.2 Pseudo-elasticity	10
1.2.3 SMA behavior under multiaxial loading	12
1.2.4 Classification of SMA behaviors	14
1.3 Applications	17
1.3.1 Couplings and Fasteners	18
1.3.2 Actuators	19
1.3.3 Adaptive materials and hybrid composites	21
1.3.4 Biomedical applications	22
1.3.5 Other applications	26
2 Literature review and research outline	27
2.1 Constitutive modeling approaches	27
2.2 Phenomenological SMA models	29
2.2.1 Models without internal variables	29
2.2.2 Models with internal variables	30

2.3	Literature review: models based on the continuum thermodynamics with internal variables	33
2.3.1	SMA modeling activities between 1980–1995	33
2.3.2	SMA modeling activities after 1995	35
2.3.3	Experimental studies on mechanical behavior of SMAs	38
2.4	Outline of the research	39
3	Preliminaries from nonlinear solid mechanics	42
3.1	Introduction	42
3.2	Kinematics	42
3.3	Balance equations	48
3.4	Constitutive equations	52
3.5	Weak form of equilibrium.	54
3.5.1	Weak form of linear momentum in the initial configuration	54
3.5.2	Weak form of linear momentum in the current configuration	56
3.6	Linearizations	56
3.6.1	Linearization of kinematical quantities	57
3.6.2	Linearization of constitutive equations	59
3.6.3	Linearization of weak form	61
3.7	Finite element formulation	63
4	Constitutive modeling: small deformation regime	65
4.1	Introduction	65
4.2	Some models available in the literature	66
4.2.1	Model proposed by Souza et al. (1998)	66
4.2.2	Model proposed by Panico and Brinson (2007)	69
4.2.3	A basic model extracted from Panico-Brinson model	71
4.2.4	A modified Panico-Brinson model	71
4.2.5	Model proposed by Lagoudas (2008)	72
4.3	Proposing a class of SMA constitutive models	73
4.3.1	Constitutive model development	75

4.3.2	Identification and comparison of some models in terms of formulation	81
4.4	Comparison of models in terms of numerical results	84
4.4.1	Uniaxial tests	85
4.4.2	Multiaxial proportional tests	86
4.4.3	Multiaxial non-proportional tests	87
4.5	Summary	94
5	Constitutive modeling: finite deformation regime	96
5.1	Introduction	96
5.2	Literature review: finite strain SMA constitutive models	97
5.3	Kinematics description	98
5.4	Finite strain extension of Panico and Brinson model	99
5.4.1	Representation with respect to the reference configuration	103
5.4.2	Linearization of the finite deformation SMA model	106
5.5	Finite strain extension of Souza model	107
5.5.1	Representation with respect to the reference configuration.	110
5.5.2	A singularity-free, continuous definition of the model	110
5.6	An approach to fully symmetrize constitutive models	112
5.7	A kinematic hardening model based on Hencky strain	113
5.7.1	Motivation	113
5.7.2	Constitutive model development	115
5.7.3	Representation with respect to the reference configuration	121
5.7.4	Proposing a Hencky-based SMA constitutive model	124
5.8	Extension into large rotation, small strain regime	128
5.8.1	Introduction	128
5.8.2	Kinematics description	128
5.8.3	Extension of Souza model to large rotation regime: Lagrangian formulation	129
5.8.4	Extension of Souza model to large rotation regime: Eulerian formulation	130

5.9	Summary	131
6	Numerical implementation: time-discretization and solution algorithms	140
6.1	Introduction	140
6.2	Numerical implementation of GLUS model	141
6.2.1	Time integration.	142
6.2.2	Solution algorithm.	143
6.2.3	Considerations on nucleation-completion condition.	144
6.2.4	Consistent tangent matrix.	147
6.3	Numerical implementation of GLSY model	149
6.4	Numerical implementation of HSGF model	151
6.4.1	Time integration.	151
6.5	Numerical implementation of HSSY model	152
6.5.1	Solution algorithm.	152
6.5.2	Considerations on nucleation-completion condition.	153
6.5.3	Consistent tangent matrix.	154
6.6	Numerical implementation of SSSR model	155
6.6.1	Consistent tangent matrix.	156
6.7	Numerical implementation of SSLR model	157
6.7.1	Method 1: Time-discretization based on Lagrangian formulation	157
6.7.2	Method 2: Time-discretization based on Eulerian formulation	158
6.8	Summary	160
7	Numerical examples and simulation of SMA-based applications	162
7.1	Introduction	162
7.2	Robustness study of different integration algorithms for GLUS model	162
7.2.1	Numerical examples: Gauss point level investigations	162
7.2.2	Numerical examples: Boundary value problems	169
7.2.3	Investigation of computational efficiency	172
7.3	Comparison of GLUS and GLSY models in terms of computational efficiency	173

7.4	Simulation of some BVPs using HSSY formulation	174
7.4.1	Uniaxial test	175
7.4.2	Pseudo-elastic stent	176
7.4.3	Spring actuator	176
7.5	Comparison of SSSR, SSLR and GLUS models	178
7.5.1	Simple tension test	178
7.5.2	Bending of a straight beam	178
7.5.3	Out-of-plane bending of a curved beam	178
7.6	Simulation of SMA-based devices: an SMA micro-gripper	180
7.7	Summary	184
8	Summary and conclusions	185
8.1	Summary	185
8.2	Conclusions	186
8.3	Future research directions	189
	References	190
	Appendices	206
A	Model derivation considering C as control variable	207
B	Details of derivations for Hencky-based model	209
C	Linearization of the asymmetric finite strain Souza model	211
D	Publications	213

List of Tables

2.1	SMA macro-modeling up to 1995	34
2.2	Experimental studies on mechanical behavior of SMAs	40
4.1	Basic Souza model	68
4.2	Basic model obtained from Panico-Brinson model	72
4.3	Modified basic Panico-Brinson model	73
4.4	Basic Lagoudas model	74
4.5	Material parameters used in the numerical tests (Panico and Brinson, 2007).	85
4.6	Material parameters adopted for Sittner et al. (1995) experiment.	89
4.7	Material parameters adopted for (Bouvet et al., 2002, 2004) experiment.	92
5.1	Finite strain extension of Panico and Brinson (2007) constitutive model	133
5.2	Finite-strain extension of Souza model.	134
5.3	Finite-strain extension of Souza model: proposed fully symmetric form.	135
5.4	Finite-strain Hencky-based kinematic hardening constitutive model	136
5.5	Finite-strain Hencky-based extension of Souza model	137
5.6	Simplified relations under the assumption of large rotations and small strains	137
5.7	Extension of Souza model to large rotation regime: Lagrangian formulation	138
5.8	Extension of Souza model to large rotation regime: Eulerian formulation	139
6.1	Different formulations and their abbreviations	141
6.2	Exponential and logarithmic mappings.	143
6.3	Solution algorithm for GLUS model based on <i>NC2</i> scheme	149

6.4	Solution algorithm for GLUS model based on <i>Reg</i> scheme	150
6.5	Solution algorithm for HSSY model based on <i>NC2</i> scheme.	154
6.6	Solution algorithm for SSLR model based on Lagrangian formulation. . .	158
6.7	Solution algorithm for SSLR model based on Eulerian formulation. . . .	161
7.1	Material properties	164
7.2	Convergence results for tension-compression tests.	165
7.3	Convergence results for the butterfly-shaped path: up to 10% strain. . .	168
7.4	Convergence results for the squared-shaped path: up to 10% strain. . . .	169
7.5	CPU times comparison.	173
7.6	Normalized CPU time comparison (exp+Reg).	174
7.7	Material properties	174
7.8	Material properties	178
7.9	Material properties	184

List of Figures

1.1	Actuation energy density diagram of different active materials (Lagoudas, 2008).	2
1.2	Actuation frequency diagram of different active materials (Lagoudas, 2008).	3
1.3	Temperature-induced phase transformation of an SMA without mechanical loading (Lagoudas, 2008).	5
1.4	Schematic of the shape memory effect of an SMA showing the detwinning of the material with an applied stress (Lagoudas, 2008).	6
1.5	Schematic of the shape memory effect of an SMA showing the unloading and subsequent heating to austenite under no load condition (Lagoudas, 2008).	6
1.6	Temperature-induced phase transformation in the presence of applied load (Lagoudas, 2008).	7
1.7	A pseudo-elastic loading path (Lagoudas, 2008).	8
1.8	Schematic of a pseudo-elastic stress-strain diagram (Lagoudas, 2008).	8
1.9	Schematic of a stress-temperature phase diagram for an SMA (Lagoudas, 2008).	9
1.10	Stress-strain-temperature data exhibiting the shape memory effect for a typical NiTi SMA (Lagoudas, 2008).	10
1.11	Phase diagram and two possible pseudo-elastic loading paths (Lagoudas, 2008).	11
1.12	A typical SMA pseudo-elastic loading cycle (Lagoudas, 2008).	11
1.13	Biaxial path with a square-shaped stress history; a) Stress path; (b) comparison of response of pure elastic, elasto-plastic and SMA materials (Panico and Brinson, 2007).	13
1.14	Asymmetric behavior under tension, compression and torsion (Orgeas and Favier, 1998).	14

1.15	Pseudo-elastic response of an as-received NiTi wire and stabilized hysteresis loop after 20 cycles (Lagoudas, 2008).	15
1.16	Pseudo-elastic behavior of a NiTi wire - development of internal loops (Dolce and Cardone, 2001).	16
1.17	Shape memory devices. Clockwise from top left: memory card ejector mechanism for laptop computers; Cryofit [®] hydraulic pipe couplings; Cryocon [®] electrical connector; fire safety lid release for public garbage receptacles (Schwartz, 2002).	19
1.18	Orthodontic applications of SMAs: (a) Nitinol braces used for alignment purposes in dental applications. (b) A schematic showing a NiTi drill used for root canal surgery (Lagoudas, 2008).	23
1.19	Cardiovascular devices: (a) Top view (above) and side view (below) of the Simon filter in the deployed configuration (Duerig et al., 1997). (b) A self-expanding Nitinol stent shown in the deployed configuration (above) and constrained state (below) (Lagoudas, 2008).	24
1.20	Orthopedic applications of SMAs. (a) Spinal vertebrae spacers showing the device in the martensitic and the deployed austenitic state (Duerig et al., 1997). (b) A schematic showing the prospective use of porous SMAs as artificial bone implants (Machado and Savi, 2003).	25
3.1	Linearized kinematics.	58
4.1	Model response for tension-compression uniaxial loading at constant temperature.	86
4.2	Model reproduction of the shape memory effect.	87
4.3	Stress path in proportional loading ($\tau_{eq} = \sqrt{3}\tau$, $\tan(\alpha) = \frac{\sqrt{3}\tau}{\sigma}$, $\alpha = \frac{\pi}{9}, \frac{\pi}{3}$).	87
4.4	Model prediction for proportional path 1: a) stress-strain curves, b) axial-shear strain response.	88
4.5	Model prediction for proportional path 2: a) stress-strain curves, b) axial-shear strain response.	88
4.6	Biaxial non-proportional loading: a) axial-shear stress path, b) comparison of model predictions for axial-shear strain response.	89
4.7	Model prediction compared to the experimental data by Sittner et al. (1995): a) uniaxial tension, b) torsion.	89

4.8	Comparison between model predictions and experimental data (Sittner et al., 1995): a) non-proportional biaxial tension-shear path, b) axial-shear strain response, c) axial stress-axial strain response, d) shear stress-shear strain response.	90
4.9	Proposed model prediction and comparison with AP (2002) and experimental results (Sittner et al., 1995): a) axial-shear triangle-shaped stress path, b) axial-shear strain response.	91
4.10	Proposed model prediction and comparison with AP (2002) and experimental results (Sittner et al., 1995): a) axial-shear L-shaped stress path, b) axial-shear strain response.	91
4.11	Uniaxial tension behavior predicted by the model and comparison with experimental results from Bouvet et al. (2004)	92
4.12	Comparison between simulation and experimental results (Bouvet et al., 2002): a) non-proportional biaxial loading path, b) corresponding strain path, c) axial stress-strain curve, d) hoop stress-strain curve.	93
4.13	Comparison between simulation and experimental results (Bouvet et al., 2004): a) non-proportional biaxial loading path, b) corresponding strain path, c) axial stress-strain curve, d) hoop stress-strain curve.	94
7.1	Simple shear test: shear deformation (left) and S_{12} component as a function of the shear amount κ (right). Lines denote $dt = 0.02s$ and the circles $dt = 0.2s$	164
7.2	Uniaxial tests: tension-compression tests (left) and torsion tests (right) under stress control: $T = 37^{\circ}C$ (upper); $T = -5^{\circ}C$ (center); $T = -25^{\circ}C$ (lower). For $T < A_f$ strain recovery induced by heating is indicated with a dashed-dot line. Stress increment per step during tension-compression tests: 15 MPa (line) and 150 MPa (circles). Stress increment per step during torsion tests: 10 MPa (line) and 100 MPa (circles).	166
7.3	Biaxial butterfly-shaped input under strain control up to 6% (upper-left) and 10% (upper-right); stress output at $T = 37^{\circ}C$ (center) and $T = -25^{\circ}C$ (lower) for two time step sizes: 0.02s (line) and 0.2s (circles).	167
7.4	Biaxial squared-shaped input under strain control up to 6% (upper-left) and 10% (upper-right); stress output at $T = 37^{\circ}C$ (center) and $T = -25^{\circ}C$ (lower) for two time step sizes: 0.02s (line) and 0.2s (circles).	168

7.5	Biaxial butterfly-shaped input (upper-left) and squared-shaped input (upper-right) under stress control; strain output at $T = 37^{\circ}C$ (centre) and $T = -25^{\circ}C$ (lower); strain output (lower) with strain recovery (dotted line) under temperature increment.	170
7.6	Pseudo-elastic spring: comparison of initial geometry and deformed configuration.	170
7.7	Force-displacement diagram for the SMA spring: pseudo-elasticity (left) and shape memory effect (right).	171
7.8	Shape memory effect in the simulated spring: deformed shape under maximum load (top) and after unloading (bottom).	171
7.9	Stent crimping: initial geometry (upper-left), crimped shape in PE case (upper-right), crimped shape in SME case (centre) and deformed shape in SME case after uncrimping (lower).	172
7.10	Illustration of the material behavior under uni-axial force-controlled test: a) pseudo-elasticity at $T = 37^{\circ}C$; b) shape memory effect at $T = -25^{\circ}C$	175
7.11	Pseudo-elastic stent crimping: a) initial geometry; b) crimped shape . . .	176
7.12	von-Mises stress versus percentage of catheter diameter reduction (at point A shown in Figure 7.9b).	176
7.13	Spring actuator: A) initial geometry and mesh; B) deformed shape due to the weight application at $T = -25^{\circ}C$; C) spring shape recovery and weight lifting due to heating to $T = 75^{\circ}C$; D) spring stretching due to cooling to $T = -25^{\circ}C$	177
7.14	a) Loading history during simulation; b) vertical displacement of the lower loaded end of spring versus temperature variation.	177
7.15	Geometry and mesh of the beam(top); force-displacement diagram and comparison of different formulations under tension test (down).	179
7.16	The cantilever beam under tip force, deformed shape when GLUS formulation is used (top); comparison of force-tip displacement diagram for different formulations (down).	180
7.17	Geometry and mesh description of the arc-shaped beam under an out of plane force (top); force-displacement diagram comparison for different formulations (down)	181

- 7.18 An SMA micro-gripper: a) starting configuration; b) memorization step of linear actuator; c) heating of linear actuator and consequent actuation of the gear one; d) heating of gear actuator with consequent re-opening. Contour plot of maximum principal logarithmic strain is reported. . . . 182
- 7.19 Simulation of micro-gripper with a sample: a) starting configuration; b) memorization step; c) heating of linear actuator and sample gripping; d) heating of rotary actuator with consequent re-opening. von Mises stress [MPa] distribution in the micro-gripper are depicted in the contour plot. 183

Chapter 1

Introduction to shape memory alloys

1.1 Smart materials

Material technology has had such a profound impact on the evolution of human civilization that historians have characterized periods in that evolution by such terms as the Stone Age, the Bronze Age, and the Iron Age. Each new era was brought about by the continuing quest for even better products, a quest that is very much in evidence today. The dawn of the 21st century will witness the emergence of the "Smart Materials Age" (Gandhi and Thompson, 1992).

Smart materials respond to environmental stimuli with particular changes in some variables e.g., temperature, moisture, electric or magnetic fields, pH, and stress. For that reason they are often also called responsive materials. Depending on changes in some external conditions, smart materials change either their properties (mechanical, electrical, appearance), their structure or composition, or their functions. Intelligent, smart, adaptive, active, sensory, metamorphic structures and/or materials and/or systems have all been used (many times interchangeably) to describe the research in this field (Spillman Jr. et al., 1996). In the following we address some smart materials.

Piezoelectric materials are materials that produce a voltage when stress is applied. Since this effect also applies in the reverse manner, a voltage across the sample will produce stress within the sample. *Shape memory alloys* and *shape memory polymers* are materials in which large deformation can be induced and recovered through temperature changes (shape memory effect) or stress changes (pseudo-elasticity). *Magnetostrictive* materials exhibit change in shape under the influence of magnetic field and also exhibit change in their magnetization under the influence of mechanical stress. *Magnetic shape memory alloys* are materials that change their shape in response to a significant change

in the magnetic field. *pH-sensitive polymers* are materials which swell/collapse when the pH of the surrounding media changes. *Temperature-responsive polymers* are materials which undergo changes upon temperature. *Halochromic materials* are commonly used materials that change their color as a result of changing acidity. *Chromogenic systems* change color in response to electrical, optical or thermal changes. *Photomechanical materials* change shape under exposure to light. *Electrorheological fluid (ERF)* is a smart suspension, whose structure and rheological properties can be quickly tuned by an external electric field. We refer to the encyclopedia of smart materials (Schwartz, 2002) to see a full list of smart materials and their applications.

Figures 1.1 and 1.2 compare the actuation energy densities and the actuation frequencies, respectively, of some common active materials. The actuation energy density (work output per unit mass) is denoted in Figure 1.1 by the dotted lines and is defined as the product of the actuation strain (related to the stroke of an actuator) with the actuation stress, assuming here that the active material is operating under constant stress. The specific actuation energy density for a specific active material can be calculated from Figure 1.1 by dividing the actuation energy density by the mass density. An increase

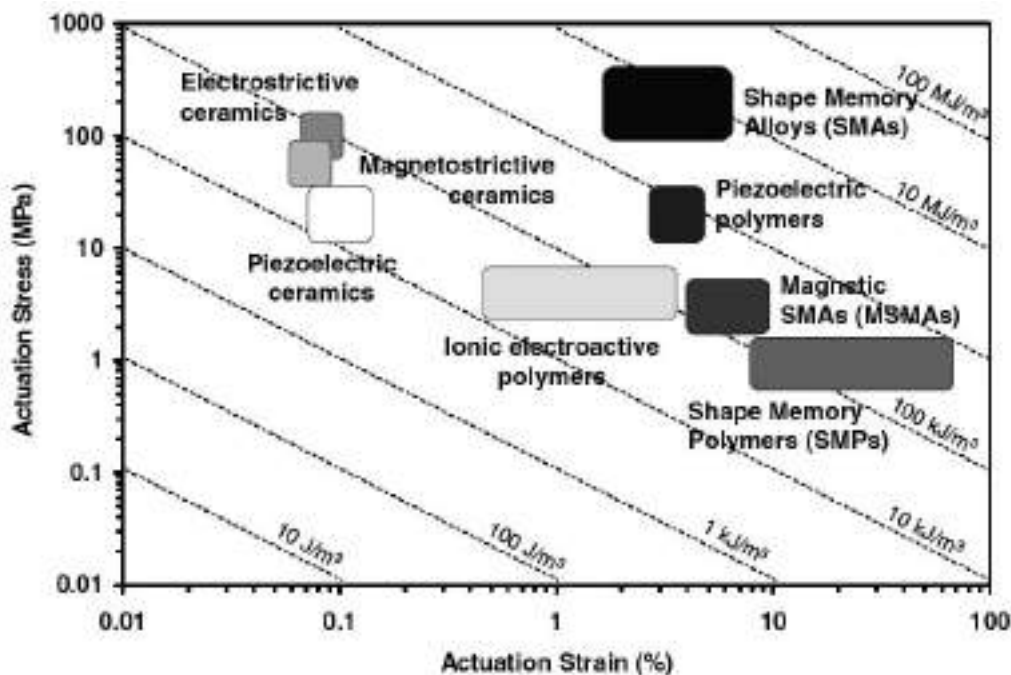


Figure 1.1: Actuation energy density diagram of different active materials (Lagoudas, 2008).

in temperature of an SMA can result in shape recovery even under high applied loads therefore resulting in high actuation energy densities as shown in Figure 1.1. SMAs do, however, exhibit low frequency response, as shown in Figure 1.2. Higher actuation frequencies are achievable for a class of SMAs called magnetic shape memory alloys.

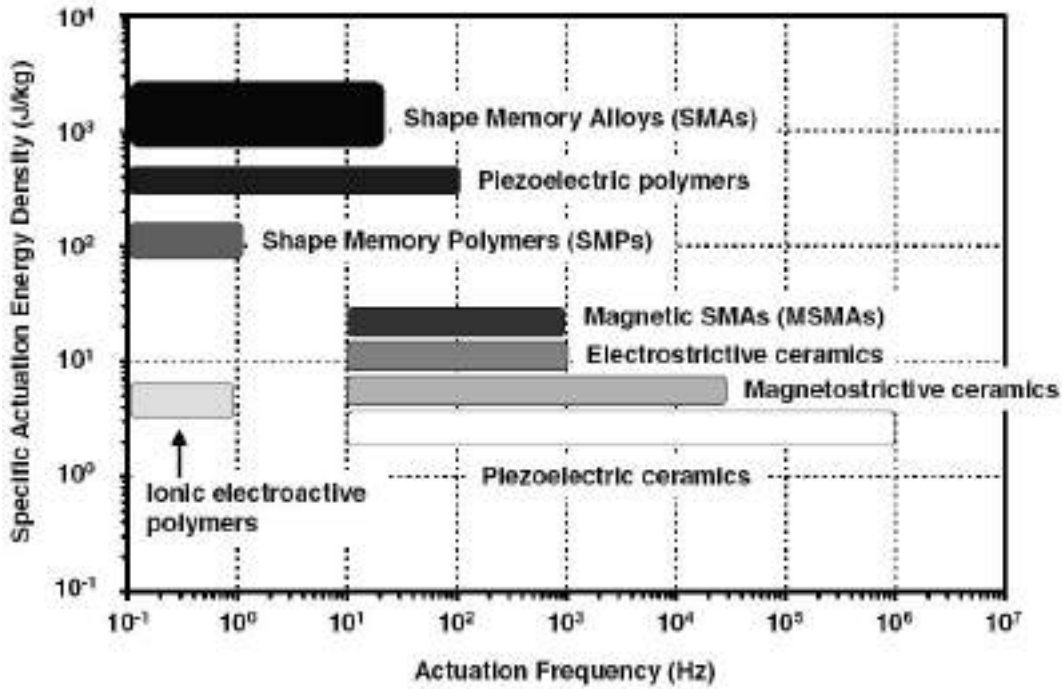


Figure 1.2: Actuation frequency diagram of different active materials (Lagoudas, 2008).

1.2 Shape memory Alloys

The martensitic transformation was perhaps the most widely studied metallurgical phenomenon during the early 1900s. The martensitic transformation, as observed in the Fe-C system, was established as an irreversible process. The concept of thermoelastic transformation explained the reversibility of martensitic transformation. The reversible martensitic transformation and the alloys that exhibited them remained unutilized until 1963. The breakthrough for engineering applications occurred with the discovery of NiTi by Buehler and coworkers while investigating materials useful for heat shielding (Buehler et al., 1963). It was noticed that in addition to its good mechanical properties, comparable to some common engineering metals, the material also possessed a shape recovery capability. The term NiTiNOL was coined for this NiTi material in honor of its discovery at the Naval Ordnance Laboratory (NOL). The term Shape Memory Effect (SME) was given to the associated shape recovery behavior. The discovery of Nitinol spearheaded active research interest into SMAs.

The first commercial SMA application, known as Cryofit[®], was pipe couplings in F-14 fighter aircraft¹ (Wayman and Harrison, 1989). Since the initial discovery of Nitinol in

¹The registered trademark symbol, designated by [®] (the circled "R") is a symbol used to provide notice that the preceding mark is a trademark or service mark that has been registered with a national trademark office. In some countries it is against the law to use the registered trademark symbol for a mark that is not officially registered in any country. Trademarks not so registered are instead marked with the trademark symbol [™], while unregistered service marks are marked with the service

1963, many commercial applications have been developed. During the 1970s, several uses of NiTi in biomedical applications appeared, but it was not until the 1990s that NiTi stents made their commercial breakthrough. By this time, SMAs had found additional applications in air conditioning vents, electronic cable connectors, valves and a variety of other products (Duerig et al., 1990; Lagoudas, 2008).

Within the typical operating temperature range, SMAs have two phases, each with a different crystal structure and therefore different properties. One is the high temperature phase called austenite (A) and the other is the low temperature phase called martensite (M). Austenite (generally cubic) has a different crystal structure from martensite (tetragonal, orthorhombic or monoclinic). The transformation from one structure to the other does not occur by diffusion of atoms, but rather by shear lattice distortion. Such a transformation is known as martensitic transformation. Each martensitic crystal formed can have a different orientation direction, called a *variant*. The assembly of martensitic variants can exist in two forms: *twinned* martensite (M^t), which is formed by a combination of self-accommodated martensitic variants, and *detwinned* (M^d) or reoriented martensite in which a specific variant is dominant. The reversible phase transformation from austenite (parent phase) to martensite (product phase) and vice versa forms the basis for the unique behavior of SMAs. Upon cooling in the absence of an applied load, the crystal structure changes from austenite to martensite. The phase transition from austenite to martensite (is termed the forward transformation) results in the formation of several martensitic variants, up to 24 for NiTi. The arrangement of variants occurs such that the average macroscopic shape change is negligible, resulting in twinned martensite. When the material is heated from the martensitic phase, the crystal structure transforms back to austenite, and this transition is called reverse transformation, during which there is no associated shape change. We remark that the martensitic transformation in SMAs consists mainly in a shear, without volume change (Lagoudas, 2008; Otsuka and Wayman, 1998).

The crystal structures of twinned martensite and austenite for an SMA and the transformation between them is shown in Figure 1.3. There are four characteristic temperatures associated with the phase transformation. During the forward transformation, austenite, under zero load, begins to transform to twinned martensite at the martensitic start temperature (M_s) and completes transformation to martensite at the martensitic finish temperature (M_f). At this stage, the transformation is complete and the material is fully in the twinned martensitic phase. Similarly, during heating, the reverse transformation initiates at the austenitic start temperature (A_s) and the transformation is completed at the austenitic finish temperature (A_f).

mark symbol SM. The proper manner to display these symbols is immediately following the mark in superscript style (source: wikipedia).

If a mechanical load is applied to the material in the twinned martensitic phase (at low

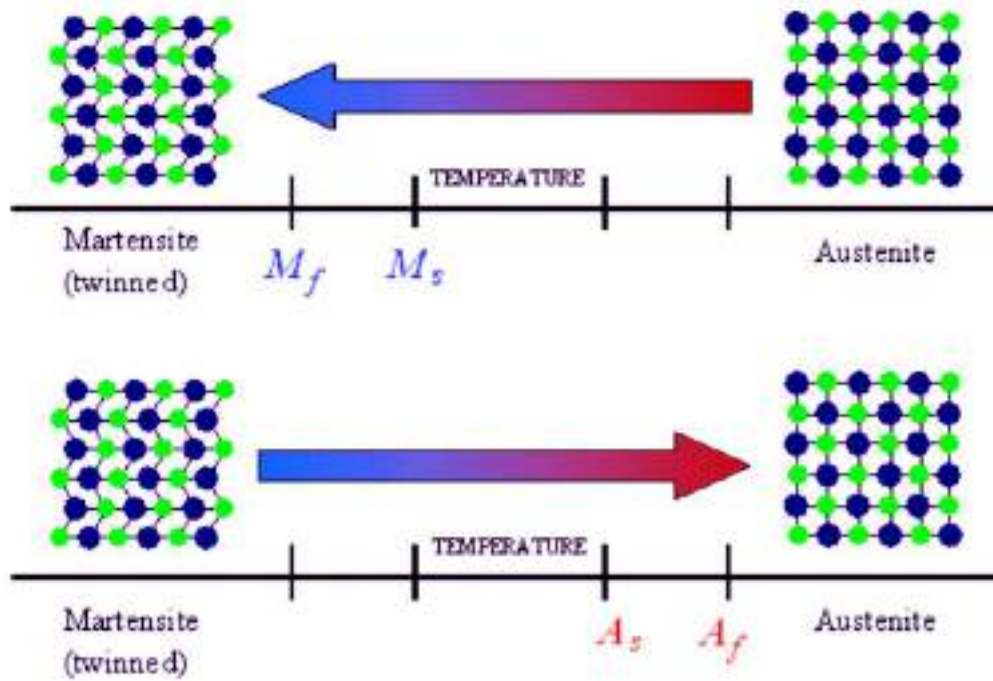


Figure 1.3: Temperature-induced phase transformation of an SMA without mechanical loading (Lagoudas, 2008).

temperature), it is possible to detwin the martensite by reorienting a certain number of variants (see Figure 1.4). The detwinning process results in a macroscopic shape change, where the deformed configuration is retained when the load is released. A subsequent heating of the SMA to a temperature above A_f will result in a reverse phase transformation (from detwinned martensite to austenite) and will lead to complete shape recovery (see Figure 1.5). Cooling back to a temperature below M_f (forward transformation) leads to the formation of twinned martensite again with no associated shape change observed. The process described above is referred to as the Shape Memory Effect (SME). The load applied must be sufficiently large to start the detwinning process. The minimum stress required for detwinning initiation is termed the detwinning start stress (σ_s). Sufficiently high load levels will result in complete detwinning of martensite where the corresponding stress level is called the detwinning finish stress (σ_f).

When the material is cooled with a mechanical load greater than σ_s applied in the austenitic phase, the phase transformation will result in the direct formation of detwinned martensite, producing a shape change. Reheating the material will result in shape recovery while the load is still applied. A schematic of the above-described loading path is shown in Figure 1.6. Recognizing that the forward and reverse transformations occur over a range of temperatures (M_s to M_f , A_s to A_f) for a given SMA composition, we can construct transformation regions in the stress-temperature space. The transfor-

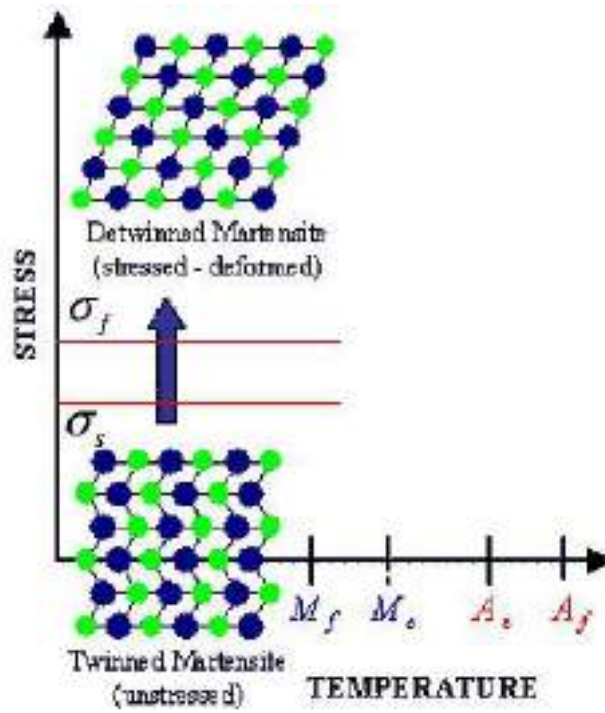


Figure 1.4: Schematic of the shape memory effect of an SMA showing the detwinning of the material with an applied stress (Lagoudas, 2008).

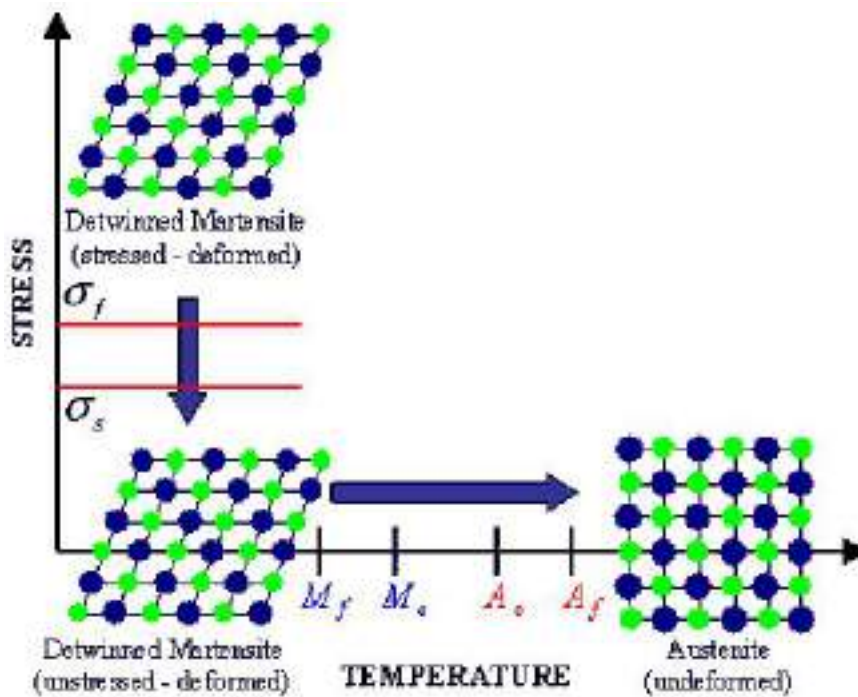


Figure 1.5: Schematic of the shape memory effect of an SMA showing the unloading and subsequent heating to austenite under no load condition (Lagoudas, 2008).

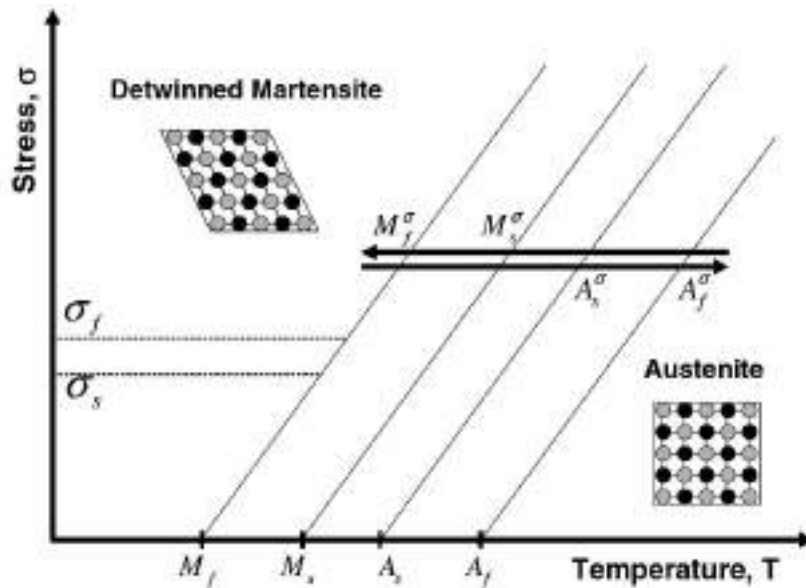


Figure 1.6: Temperature-induced phase transformation in the presence of applied load (Lagoudas, 2008).

mation temperatures strongly depend on the magnitude of the applied load, with higher values of applied load leading to higher transformation temperatures. Irrespective of the nature of applied load (tension or compression), the transformation temperatures increase with an increase in the magnitude of the load. Under an applied uniaxial tensile load with a corresponding stress, σ , the new transformation temperatures are represented as M_f^σ , M_s^σ , A_s^σ and A_f^σ for martensitic finish, martensitic start, austenitic start and the austenitic finish temperatures, respectively (Lagoudas, 2008).

In addition to thermally induced phase transformation, transformation can also be induced by applying a sufficiently high mechanical load to the material in the austenitic phase. The result of this load is fully detwinned martensite created from austenite. If the temperature of the material is above A_f , a complete shape recovery is observed upon unloading to austenite. This material behavior is called the pseudo-elastic effect. A loading path demonstrating the pseudo-elastic effect is shown schematically in Figure 1.7, while the associated macroscopic shape change due to the applied load is captured in the resulting stress-strain diagram, as shown schematically in Figure 1.8. The stress levels at which the martensite transformation initiates and completes are denoted by σ^{M_s} and σ^{M_f} , respectively. Similarly, as the SMA is unloaded, the stress levels at which the material initiates and completes its reverse transformation to austenite are denoted by σ^{A_s} and σ^{A_f} , respectively. If the material in the austenitic phase is tested above the M_s temperature, but below the A_f temperature, only partial shape recovery is observed (Lagoudas, 2008).

Figure 1.9 shows a schematic representation of the different phases of the SMA, which

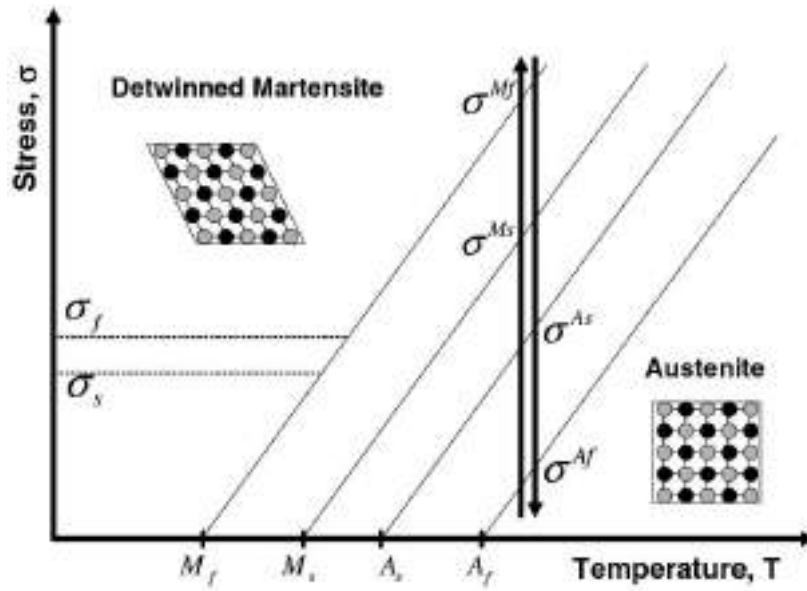


Figure 1.7: A pseudo-elastic loading path (Lagoudas, 2008).

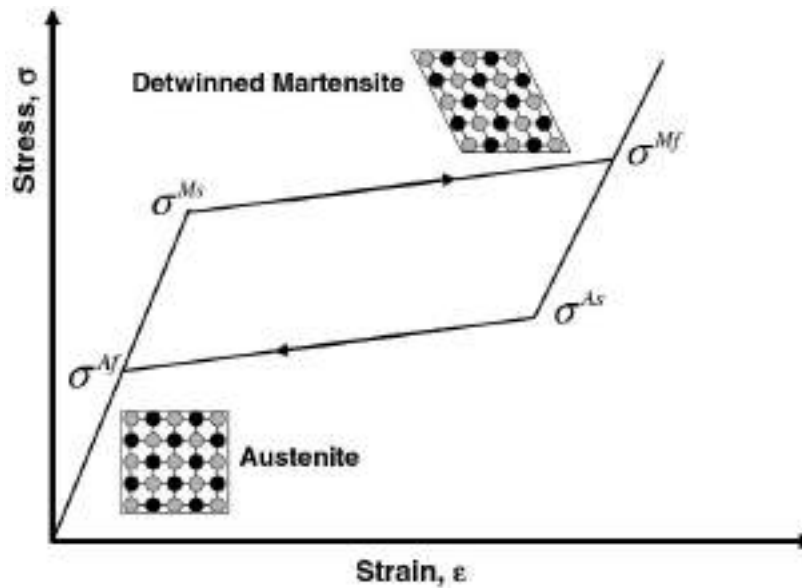


Figure 1.8: Schematic of a pseudo-elastic stress-strain diagram (Lagoudas, 2008).

include the austenitic phase and both the twinned (M^t) and detwinned (M^d) martensite, along with the transition zones, in a stress-temperature diagram. Such a diagram, illustrating the different phases in a stress-temperature space for a given SMA with fixed composition, is called the phase diagram. Construction of the phase diagram involves the interpretation of the SMA material response subjected to various thermo-mechanical loading paths resulting in shape memory thermal actuation under load and pseudo-elastic behavior. In the following, the two important characteristics of SMAs, namely the shape memory effect and pseudo-elasticity, will be discussed in more detail.

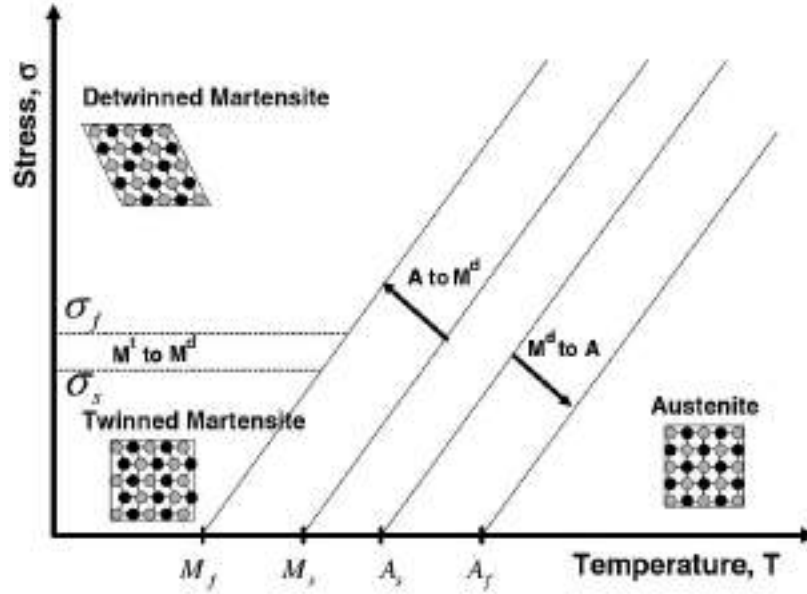


Figure 1.9: Schematic of a stress-temperature phase diagram for an SMA (Lagoudas, 2008).

1.2.1 Shape memory effect

An SMA exhibits the shape memory effect (SME) when it is deformed while in the twinned martensitic phase and then unloaded while at a temperature below A_s . When it is subsequently heated above A_f , the SMA will regain its original shape by transforming back into the parent austenitic phase. The nature of the SME can be better understood by following the thermo-mechanical loading path in a combined stress-strain-temperature space as shown in Figure 1.10. Starting from the parent phase (point A in Figure 1.10), the stress-free cooling of austenite below the forward transformation temperatures (M_s and M_f) results in the formation of twinned martensite (point B). When the twinned martensite is subjected to an applied stress that exceeds the start stress level (σ_s), the reorientation process is initiated, resulting in the growth of certain favorably oriented martensitic variants that grow at the expense of other less favorable variants. The stress level for reorientation of the variants is far lower than the permanent plastic yield stress of martensite. The detwinning process is completed at a stress level, σ_f , that is characterized by the end of the plateau in the $\sigma - \varepsilon$ diagram in Figure 1.10. The material is then elastically unloaded from C to D and the detwinned martensitic state is retained. Upon heating in the absence of stress, the reverse transformation initiates as the temperature reaches A_s (at E) and is completed at temperature

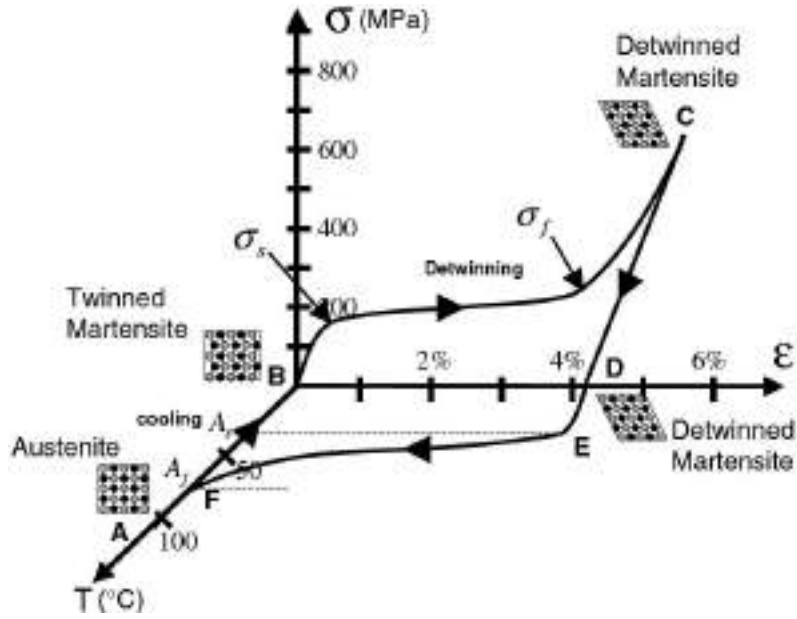


Figure 1.10: Stress-strain-temperature data exhibiting the shape memory effect for a typical NiTi SMA (Lagoudas, 2008).

A_f (point F), above which only the parent austenitic phase exists. In the absence of permanent plastic strain generated during detwinning, the original shape of the SMA is regained (indicated by A). The strain recovered due to the phase transformation from detwinned martensite to austenite is termed as the transformation strain. Subsequent cooling to martensite will again result in the formation of self-accommodated twinned martensitic variants with no associated shape change, and the whole cycle of the SME can be repeated. The above described phenomenon is called one-way shape memory effect, or simply SME, because the shape recovery is achieved only during heating after the material has been detwinned by an applied mechanical load.

1.2.2 Pseudo-elasticity

The pseudo-elastic (PE) behavior of SMAs is associated with stress-induced transformation, which leads to strain generation during loading and subsequent strain recovery upon unloading at temperatures above A_f . A pseudo-elastic thermo-mechanical loading path generally starts at a sufficiently high temperature where stable austenite exists, then develops under an applied load to a state at which detwinned martensite is stable, and finally returns to the austenitic phase when returned to zero stress state. An example of this path ($a \rightarrow b \rightarrow c \rightarrow d \rightarrow e \rightarrow a$) is shown in Figure 1.11 as path 1. Most commonly, a pseudo-elastic test is performed at a nominally constant temperature above A_f . The loading path for such a test is shown as path 2 in Figure 1.11 (Lagoudas,

2008).

To illustrate the pseudo-elastic behavior in greater detail, let us consider the thermo-

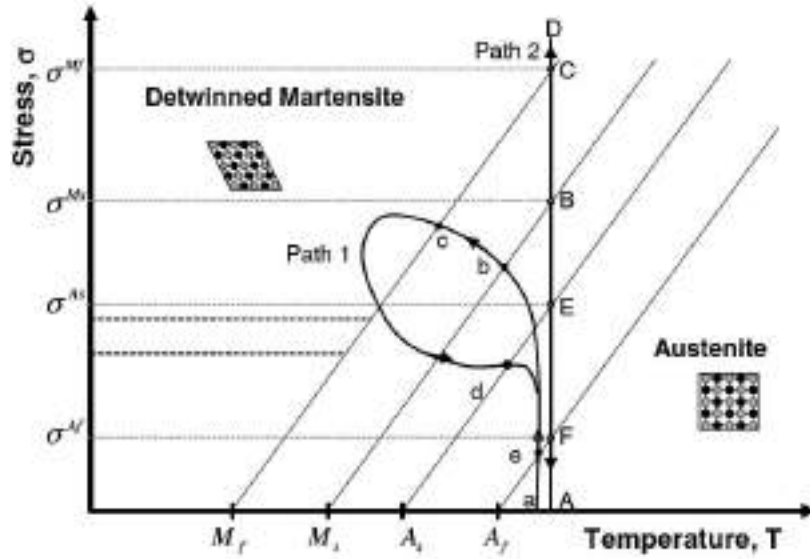


Figure 1.11: Phase diagram and two possible pseudo-elastic loading paths (Lagoudas, 2008).

mechanical loading path ($A \rightarrow B \rightarrow C \rightarrow D \rightarrow E \rightarrow F \rightarrow A$) in Figure 1.11, which starts at zero stress at a temperature above A_f . The corresponding $\sigma - \varepsilon$ experimental data for the loading path is shown in Figure 1.12. When a mechanical load is applied,

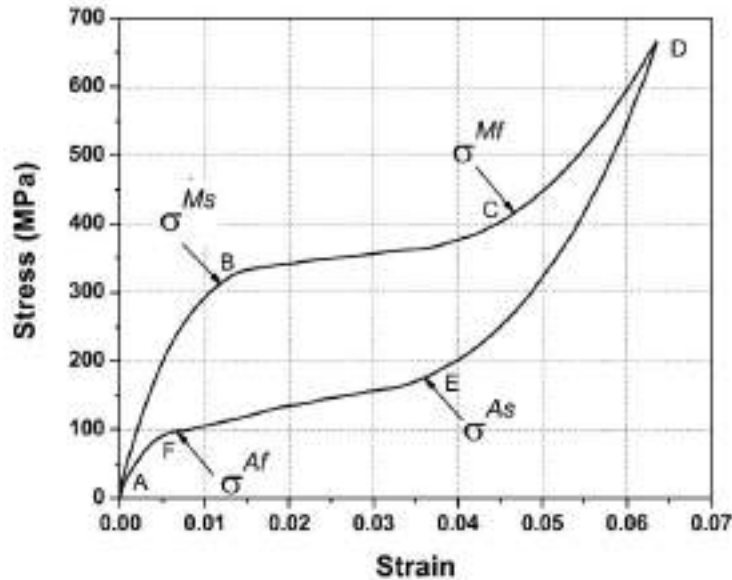


Figure 1.12: A typical SMA pseudo-elastic loading cycle (Lagoudas, 2008).

the parent phase (austenite) undergoes elastic loading ($A \rightarrow B$). At a specific load level, the loading path intersects the surface for initiation of martensitic transformation on the

phase diagram. This marks the stress level (σ^{M_s}) for the onset of transformation into martensite. Note that the stress-induced transformation from austenite to martensite is accompanied by the generation of large inelastic strains as shown in the stress-strain diagram of Figure 1.12. The transformation proceeds ($B \rightarrow C$), to the stress level (σ^{M_f}) where the loading path intersects the M_f transformation surface, indicating the end of the transformation.

The completion of martensitic transformation is indicated by a distinct change in slope on the $\sigma - \varepsilon$ curve, which is associated with the elastic loading of the martensitic phase. A subsequent increase in the stress causes no further transformation and only the elastic deformation of detwinned martensite occurs ($C \rightarrow D$). When the stress is released gradually by unloading, the martensite elastically unloads along the path ($D \rightarrow E$). At point E , the unloading path intersects the austenitic start surface (at σ^{A_s}), which causes the martensite to revert to austenite. The process is accompanied by the recovery of the strain due to phase transformation at the end of unloading. The end of the transformation back into austenite is denoted by the point at which the $\sigma - \varepsilon$ unloading curve rejoins the elastic region of austenite (point F corresponding to stress σ^{A_f}). The material then elastically unloads to A . The forward and reverse phase transformation during a complete pseudo-elastic cycle results in a hysteresis, which in the $\sigma - \varepsilon$ space, represents the energy dissipated in the transformation cycle. The transformation stress levels and the size of the hysteresis vary depending on the SMA material and testing conditions (Lagoudas, 2008).

The detwinned martensite that forms from austenite as a result of the applied stress during Path 1 or 2 in Figure 1.11 is one form of stress-induced martensite (SIM). SIM, in general, is martensite that forms from austenite in the presence of stress. There are many thermo-mechanical loading paths that can result in the formation of SIM.

1.2.3 SMA behavior under multiaxial loading

Even though significant interest in modeling the pseudo-elastic and pseudo-plastic behavior of shape memory alloys and NiTi in particular exists, the experimental data, which are used to fit the material models, are in most cases associated to simple uniaxial tests or even simple tension experiments. In order to develop reliable models, which may be used to simulate complex structures, it is of paramount importance to use multi-axial experiments so that material models can be cross-checked utilizing a high degree of complexity. Furthermore, temperature controlled multiaxial experiments, which cover the whole transformation temperature regime are requisite in order to characterize the path dependence of the one-way shape memory effect.

Basically, most experimental research in the field of shape memory alloys is conducted on Cu-based and NiTi shape memory alloys. on a relatively thick-walled (Radius-to-wall thickness ratio of $r/t = 2.2$) Cu-based specimen. Multiaxial experiments covering a wide range of temperatures have been performed by Grabe and Bruhns (2009). The experimental multiaxial data are interesting resources in order to allow for a broad cross-checking of material models as well as to give some explanations and hints how to model the non-linearity of the material with reference to pseudo-elasticity and the one-way effect. SMA constitutive models have been proposed at the mesoscale based on J_2 type transformation theory as a generalization to the multiaxial case. However, the experimental works show that the direction of transformation strain rate is not collinear with the deviatoric stress, in general. Accordingly, generalizations must reflect the role of the orientation distribution of transformed martensite variants, variant coalescence, and related phenomena. Figure 1.13 compares the response of an elastic, a plastic and an SMA material under a square-shaped axial-torsional stress-control path (Figure 1.13a). According to Figure 1.13b, the three material behaviors are completely

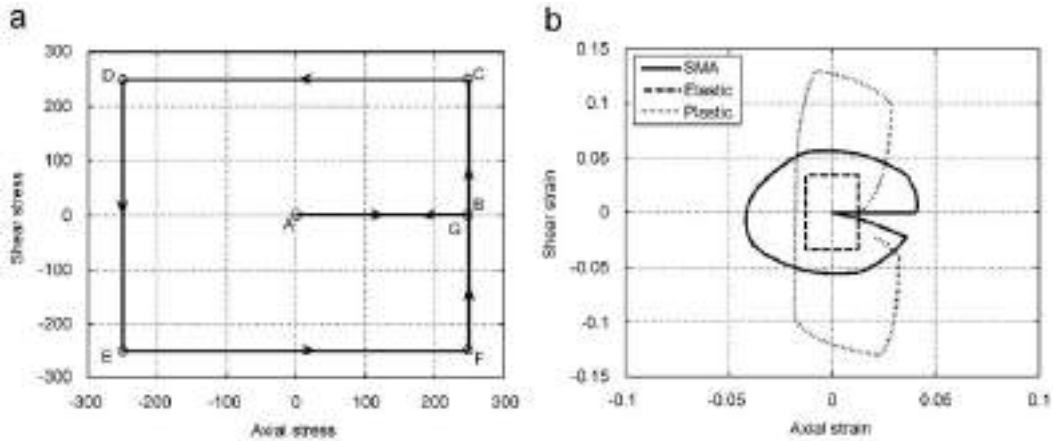


Figure 1.13: Biaxial path with a square-shaped stress history; a) Stress path; (b) comparison of response of pure elastic, elasto-plastic and SMA materials (Panico and Brinson, 2007).

different; in particular, the elastic response is purely affine to the stress loading path while the elasto-plastic response presents a large residual strain upon unloading and substantially less axial-shear coupling compared with the SMA behavior. This highlights the importance of using a proper modeling tool for SMA materials specifically under non-proportional loadings.

1.2.4 Classification of SMA behaviors

Two main characteristic behavior of SMAs is pseudo-elasticity and shape memory effect under a general three-dimensional multiaxial loading (i.e., the variant reorientation is also important) while other behaviors are of secondary importance. We may then categorize the SMA behaviors into two groups as follows:

Primary effects: include pseudo-elasticity, shape memory effect as well as variant reorientation. It is expected that an SMA constitutive model, at least, can capture these effects.

Secondary effects: cover other effects which may turn out to be relevant in some practical cases. We can include the following items in this category:

Tension-compression asymmetry

Experimental observations show that loading conditions have significant influences on the deformation behavior of SMAs. In particular, deformation behavior is observed to be asymmetric in tension and in compression (Figure 1.14). The physical origins of such an asymmetry is attributed to the low crystallographic symmetry of the martensite structure. This implies that conclusions derived from tensile deformation tests cannot be directly translated to other deformation modes and that independent experimental investigations of deformation modes other than tension are needed for a full characterization of the thermo-mechanical behavior of NiTi (Orgeas and Favier, 1998).

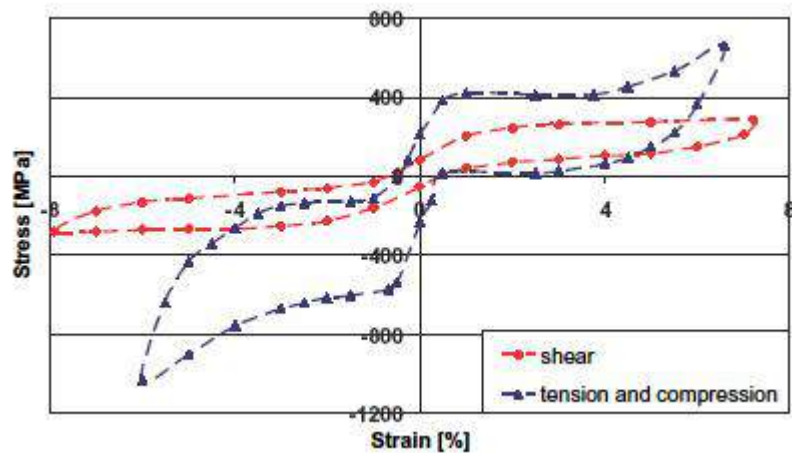


Figure 1.14: Asymmetric behavior under tension, compression and torsion (Orgeas and Favier, 1998).

Different elastic properties for austenite and martensite

Usually the elastic modulus of an SMA depends on the phase transformation level. In other words, the elastic properties of martensite and austenite phases are different (Auricchio et al., 2009b; Cernoch et al., 2004).

Progressive strain under cyclic loadings

Sometimes, as shown by many experimental observations, the stress-strain pseudo-elastic loop is not closed and a permanent inelastic strain remains after unloading (Figure 1.15). Moreover, if the SMA is subjected to cyclic loading, the permanent inelastic strain increases up to it reaches a stable value after a certain number of cycles (e.g., Sittner et al. (1995); Tanaka et al. (1995)). This particular behavior of pseudo-elastic SMAs under cyclic loading is sometimes called *ratcheting effect* (Feng and Sun, 2007) as observed in the mechanical behavior of classic metallic alloys under cyclic loading.

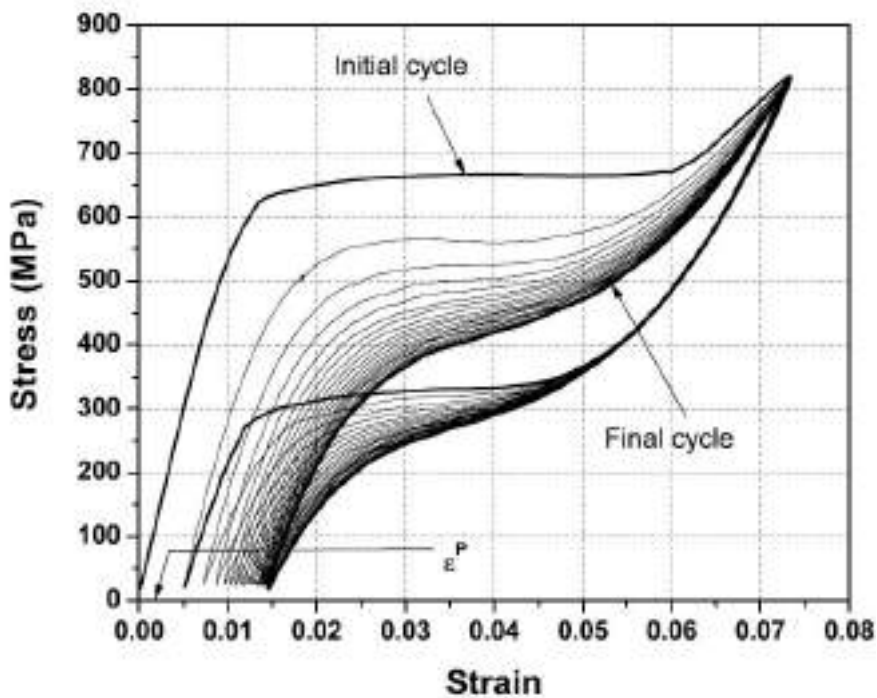


Figure 1.15: Pseudo-elastic response of an as-received NiTi wire and stabilized hysteresis loop after 20 cycles (Lagoudas, 2008).

Internal loops (subloops)

If the range of the cyclic thermo-mechanical loading does not fully cover the transformation zones, the martensitic and/or reverse transformations are not complete in each

cycle, resulting in subloops. Figure 1.16 shows an experimentally-observed behavior under incomplete phase transformation.

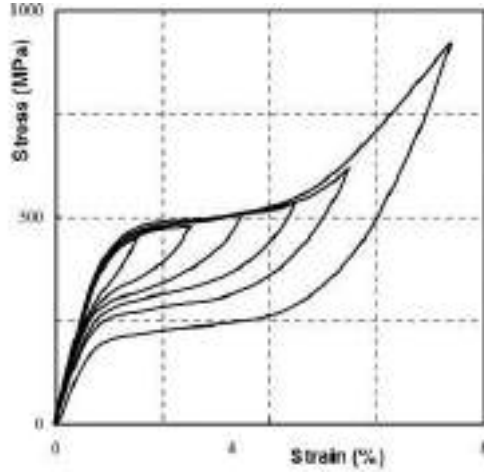


Figure 1.16: Pseudo-elastic behavior of a NiTi wire - development of internal loops (Dolce and Cardone, 2001).

Thermo-mechanical coupling

In problems involving SMA materials, thermo-mechanical coupling has to be taken into account due mainly to the latent heat associated to the martensitic transformation and heat production/absorption resulting from SMA material by internal dissipation process. It is known that the forward transformation ($A \rightarrow M$) is exothermal and the reverse transformation ($M \rightarrow A$) endothermal. It means that during forward phase change, the temperature of the SMA increases due to heat generation. Austenite thus becomes more stable and higher stress becomes required to drive the formation of martensite forward. During reverse phase change, because latent heat is predominant, the temperature of the SMA decreases making martensite more stable. Stress must then be decreased further for the reverse transformation to continue. Therefore, thermo-mechanical coupling explains the observed dependence of SMA behavior on strain rate. This was discussed, for example, by Shaw and Kyriakides (1995), Grabe and Bruhns (2008a) and Tobushi et al. (1998) who found that strain rate dependence can be neglected for rates lower than 2 %/min.

1.3 Applications

Many alloy systems show shape memory behavior but only a few of them have been developed on a commercial scale (NiTi, NiTi-X, Cu-Zn-Al). At present more than 90% of new SMA-applications are based on NiTi or ternary NiTi-Cu and NiTi-Nb alloys (Van Humbeeck, 2010). Other shape memory alloys are close to market introduction (Fe-Mn-Si) while still others have interesting potentials but are difficult to produce or suffer from brittleness such as alloys envisaged for applications at higher temperatures (Firstov et al., 2006).

Although NiTi SMAs are more expensive and more difficult to machine than Cu-based SMAs, there are several reasons why almost only NiTi SMAs are used in new developments. NiTi SMAs are much stronger and more ductile. NiTi SMAs show in general a higher stability in cyclic applications, NiTi SMAs are available in the shape of thin wires and thin films, and NiTi SMAs have a higher electrical resistivity making electrical activation much simpler. The requirements for medical applications (biocompatibility) also eliminate the Cu-based alloys. For some reasons, mainly Ni but also Ti can be partially (a few percent) replaced by Cu, Co, Fe, Nb or Mo. These elements can improve the hysteresis (stress and/or temperature hysteresis), corrosion, resistance, transformation temperatures, fatigue behavior and so on.

SMA applications can be divided into the following categories (Van Humbeeck, 2010):

1. The one and two way shape memory effects can be used for free recovery applications. This refers to applications in which the single function of the SMA-element is to cause motion or shape changes without any biasing stress.
2. The generation of recovery stresses can be used for diverse clamping devices, such as SMA-couplings and SMA-connectors, ranging from very small diameters (< 1 mm) to very large diameters (> 1 m).
3. Diverse actuation applications have been developed based on the work production capacity of SMAs.
4. Pseudo-elasticity is used in many biomedical and other super-elastic applications where higher reversible strains have to be combined with high stress plateaus.
5. Damping applications can be developed based on the high damping capacity of SMAs. The high damping capacity of the martensite phase is interesting for passive damping. The super-elastic hysteresis might be interesting for earthquake damping and isolation purposes.

Since a few years ago, shape memory alloys have found their specific position in many domains of industrial activities. A steadily growing amount of different SMA applications are now produced at large volumes, *but the large majority of applications is still in the biomedical field*. In the following we mention some applications.

1.3.1 Couplings and Fasteners

Heat-recoverable couplings as well as heat-to-shrink fasteners make use of the force created by a deformed SMA-element during constrained recovery. In fact, a coupling to connect titanium hydraulic tubing in the Grumman F-14 aircraft, developed by Raychem, was the first large scale application of SMA in 1971 (Otsuka and Wayman, 1998). The original alloy was a NiTiFe; Fe was alloyed to obtain a low transformation temperature down to -55°C . This should prevent that the coupling would transform into martensite at lower temperatures and thus would soften and start leaking. The mounting procedure was quite complicated: expansion of the ring in liquid nitrogen, storing (also during transport) in liquid nitrogen until mounting by just bringing it to room temperature.

The problem of liquid nitrogen storage has been later solved by stabilisation of martensite either thermal (in Cu-based alloys) or mechanical (in NiTiNb alloys). The development of NiTiNb alloy was a real breakthrough for the coupling business (Duerig et al., 1990). But also FeMnSi alloys received quite a lot of attention, in spite of their lower recoverable strain.

Dedicated applications were specifically named such as Crocon and Crofit[®] (hydraulic couplings), Crolive[®] (a more complicated tool to couple), Betaflex[™] and Crotact[™] electrical connectors for Zero Insertion Force (ZIF) connectors, and Tinel[®]-lock and Unilock[®] rings (Van Humbeeck, 2010).

The main advantages of all those systems are the followings (Otsuka and Wayman, 1998):

- Lightweight
- Easy installation even in difficult to access areas
- Proven reliability
- Good shock, vibration and thermal cycling properties can provide a hermetic seal

Disadvantages are:

- High cost relative to classic alternatives

- Remain operational in a limited temperature range (-20°C to 200°C)
- Limited memory amount of motion available

A specific class of couplings or fasteners based on SMA are heat sensitive elements that should lock or unlock two different parts within a short time and at a critical temperature. Those types of applications can be found especially in the area of fire (or excessive heat) protection and release mechanisms in space technology. In fact, the SMA-element is retained here in a non-constrained but deformed martensitic condition. During heating the one-way effect allows to release the part formerly hold by the SMA-device. As such, it can be classified also as a one-way SMA-actuator. Figure 1.17 shows some commercially available SMA-devices.



Figure 1.17: Shape memory devices. Clockwise from top left: memory card ejector mechanism for laptop computers; Cryofit[®] hydraulic pipe couplings; Cryocon[®] electrical connector; fire safety lid release for public garbage receptacles (Schwartz, 2002).

1.3.2 Actuators

Since the recovery force, e.g. generated by a constrained shape memory element, acts in the direction of the recoverable shape change, this force can be used to perform work. The shape memory element can thus be classified as a thermal actuator. Indeed thermal energy is directly converted into mechanical energy. Before selecting SMA for actuating

elements it is worth to overview the most important advantages and drawbacks of SMA actuation (Van Humbeeck, 2010).

Important reasons to select SMA as an actuation mechanism are:

- Simplicity of mechanism.
- Creation of clean, silent, spark-free and zero gravity working conditions.
- High power/weight (or power/volume) ratios.

In spite of those significant advantages, some drawbacks on the use of SMA-actuators have to be considered as:

- Low energy efficiency (It is advantageous to use tension loaded wires to get more efficiency)
- Limited bandwidth due to heating and cooling restrictions.
- Degradation and fatigue

Apart from some specific on/off applications such as an air damper for a multifunction electric oven or an SMA generated fog lamp protective louver, designers have shown a special interest in this type of applications, namely in robotic applications.

For robotic applications there are three important items that distinguishes several types:

- the type of deformation used for the active memory element: bending, torsion or pure tension.
- the position feedback that enables free positioning of the actuator.
- the way of heating (cooling) the active element (mainly resistive heating, induction heating, immersion heating, RF energy)

Space applications offer a few more arguments in favor of shape memory actuators. The main arguments are:

- almost zero-gravity action in contrast to most electrical engines.
- high power/volume (mass) density and simple mechanism. this can compensate for the low efficiency since the launch cost for every piece of material equals half the item's weight in gold.
- no dust particles created, no leakage of fluids

For space applications, most interest has been given to single action devices such as a release mechanism, truss mounting or solar panel deployment. But the applications of repeated action actuator in space stations, satellites or planet robots such as the Mars Pathfinder is gaining an increased interest (Van Humbeeck, 2010).

SMA-based actuators are also considered for repeated actions such as grippers, positioners, etc. The low thermal energy is here compensated by the ease of mechanism which includes a high gain on weight, high work/volume density and almost zero gravity accelerations.

1.3.3 Adaptive materials and hybrid composites

Smart materials involve three functions: sensor, actuator and control. Those three functions are generally combined by using different materials in combination with a control unit. Combination of several materials leads to structural elements that can be called hybrid composites. Hybrid composites connected with a control unit can then be used eventually as a smart structure.

More important for future new technologies are hybrid composites in which shape memory alloys can perform their specific role. The most envisaged applications can be summarized as follows:

Active strain energy tuning: Restrained wires are embedded in the matrix. If such composite plate vibrates at resonance, the wires can be heated which will develop a recovery stress at the composite matrix wire interface. This produces a change in energy balance.

Active modal modification: Unstrained wires are embedded. To change the modal response, the wires are heated resulting in a large increase of the elastic modulus of wires during the martensitic transformation.

Active shape control: The shape memory effect is used to change the shape of the composite matrix.

Active fatigue life and impact resistance improvement (self-repairing or self-healing): Super-elastic embedded deformed wires create compressive stresses inhibiting crack growth and even promoting crack closure. Embedded strained martensitic wires can also be activated by heating.

Active stress-relaxation: Stress- or strain-induced martensite can relax imposed stresses due to specific loading, differences in thermal expansion coefficients or thermal shocks. Depending on the type of application, the shape memory alloys can be embedded as thin wires, fibers, particles, thin films, while the matrix can be a metallic material, a ceramic, a polymer or a composite.

1.3.4 Biomedical applications

In recent years it became clear that the largest commercial successes of SMAs are linked to biomedical applications (Duerig et al., 1999). The combination of good biocompatibility, good strength and ductility with the specific functional properties such as shape memory effect and super-elasticity creates a unique material for medical applications. Especially the super-elastic effect of SMAs results in a unique combination of high strength, high stiffness and high pliability; no other material or technology can offer this unique combination. The temperature dependent character of the super-elastic effect, which is disadvantageous in other application areas, is of less importance in the biomedical field because of the stable temperature of the human body. NiTi with a proper surface treatment shows an excellent biocompatibility. Also the concept of a metallic material with an extreme elasticity and with nearly constant stress levels over a large strain area is something that can be tackled easier by designers.

As a consequence, regarding the specific functional properties, *the largest commercial successes of SMAs are linked with the use of pseudo-elasticity* (Van Humbeeck, 2010). In the following, we study some medical applications.

Orthodontic applications

The properties of SMAs have been successfully implemented in a variety of dental applications. Nitinol orthodontic arch wires have been used since the 1970s, and are more effective than other alternative materials. In a linear elastic material, like stainless steel, there is a large increment in stress, for a small increment in strain which results in a large amount of force on the tooth for a small amount of corrective motion. The advantage of pseudo-elastic arch wires is the ability to operate in the pseudo-elastic plateau, during which the material has a near-zero stress change over a large strain increment. As a result, they provide a nearly constant, moderate force to actively move the teeth over a longer period of time compared with stainless steel. Further, the material composition and processing can be engineered to produce different levels of optimal force. An example of Nitinol orthodontic braces is shown in Figure 1.18a. Another key dental application for SMAs involves the use of Nitinol drills in root canal surgery, which involves careful drilling within the tooth (Figure 1.18b). The advantage of these Nitinol drills is that they can bend to rather large angles, which induce large strains, yet still withstand the high cyclic rotations (Lagoudas, 2008).

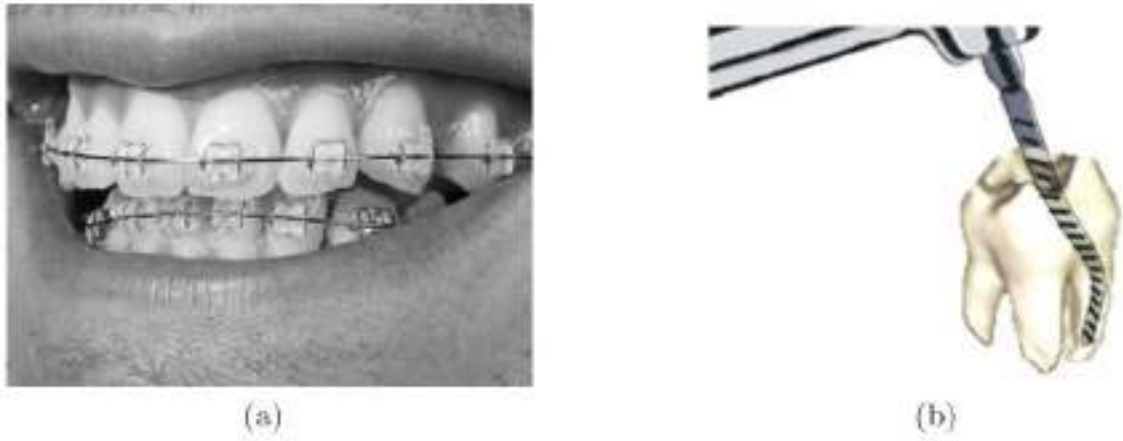


Figure 1.18: Orthodontic applications of SMAs: (a) Nitinol braces used for alignment purposes in dental applications. (b) A schematic showing a NiTi drill used for root canal surgery (Lagoudas, 2008).

Cardiovascular applications:

An early cardiovascular SMA device was the Simon Filter. The device acts as a filter that traps clots traveling in the blood stream. The trapped clots are then eventually dissolved. From the original expanded state, the device is deformed and constrained within a catheter. At the time of implantation, the filter is deployed in the blood vessel where the ambient temperature exceeds A_s of the filter material. The release from the constraint and the active properties of the SMA filter cause the filter to expand and it assumes its original shape as shown in Figure 1.19a (Duerig et al., 1997). Another application of SMAs in the cardiovascular field is the atrial septal occlusion device. This device is used to seal an atrial hole that is located on the surface dividing the upper heart chambers. The traditional surgical technique used to address this problem is highly invasive and dangerous. The atrial septal occlusion device provides a suitable alternative to such a surgery. This device also exploits the shape memory characteristics exhibited by SMAs, and consists of two umbrella shape halves that can be screwed together in the center. Initially, these halves are folded, constrained and introduced into the heart. The two halves are deployed on either side of the hole and are connected using a screw. The resulting sandwich configuration forms a patch that seals the hole.

A more common cardiovascular application is the self-expanding NiTi stent. Like other conventional stents, this device is used to support the inner circumference of tubular passages in the body such as blood vessels. Traditionally, stents are made using stainless steel. These stents are expanded from the size of the introduced catheter to the size of the artery walls by an inflatable balloon. As the balloon is deflated, the steel stent undergoes elastic unloading, often resulting in a loose fit. Furthermore, to reach

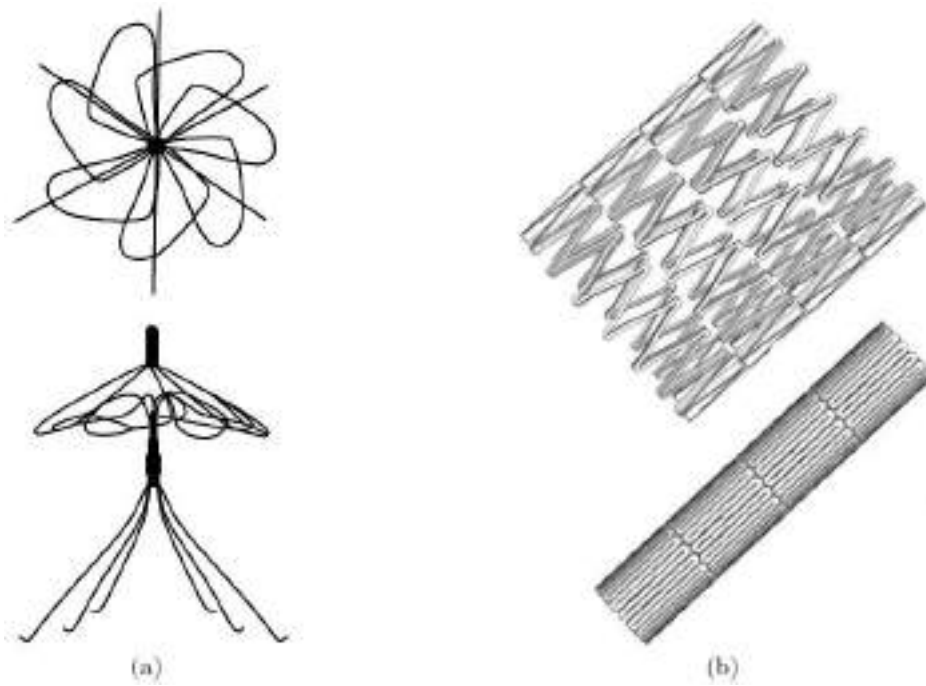


Figure 1.19: Cardiovascular devices: (a) Top view (above) and side view (below) of the Simon filter in the deployed configuration (Duerig et al., 1997). (b) A self-expanding Nitinol stent shown in the deployed configuration (above) and constrained state (below) (Lagoudas, 2008).

a particular nominal diameter, it is necessary to over-expand the stent to account for this unloading. This process of over-inflation can damage the vessels and can cause a condition where the blood vessel collapses after the procedure due to weakening of the walls. The self-expanding NiTi stents provide an attractive alternative to the traditional method. The device is generally laser cut from sheets or tubing and is then shape set to the appropriate diameter. After being constrained, the NiTi stent is introduced into the body where the temperature exceeds A_s of the stent material. It is then released in the artery where it expands to its original larger diameter and gently pushes outward on the walls. Furthermore, the device can adapt to any oblong passage as compared to the balloon inflated steel stents that are biased toward a circular shape. Figure 1.19b shows an illustration of a Nitinol stent in the constrained and deployed configuration.

Orthopedic applications:

The devices developed for orthopedic applications are used to support injured, weakened or fractured bones. One such device is the spinal vertebra spacer (Figure 1.20a), used to provide local reinforcement to the vertebrae and prevent motion during the healing

process. The device applies a constant force on the joint while providing flexibility (Machado and Savi, 2003). Porous SMAs represent a different kind of material form and can be used as artificial bone implants (Figure 1.20b). The porous nature of the material enables the existing bone tissue to migrate inward, increasing bonding strength. Furthermore, the implant properties (stiffness and porosity) can be engineered to match those of the bone. In a separate application, SMAs fasten to broken or fractured bones to facilitate healing. These devices include orthopedic staples and shape memory plates. The staple, for example, is installed in an open configuration at the fractured joint. An external heating source is used to heat the staple causing it to return to its original form via SME, which consequently provides a compressive force at the interface of the separated bones (Machado and Savi, 2003). The shape memory plate is a device used when a cast cannot be applied over the fracture surface (i.e. facial areas, jaw, nose). The plate is also shape set, deformed, installed and then actuated via (external) heating, providing a force which holds the fractured joints together (Machado and Savi, 2003).

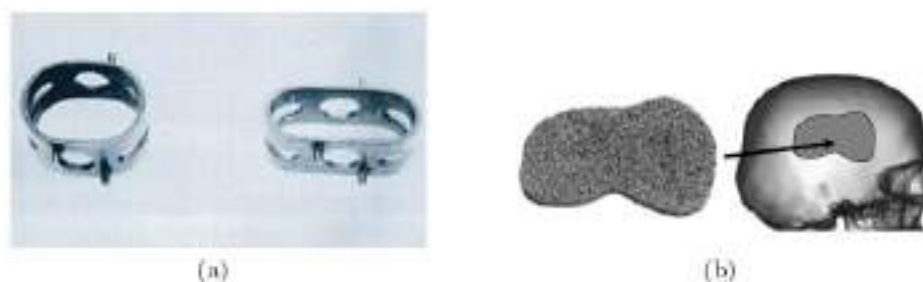


Figure 1.20: Orthopedic applications of SMAs. (a) Spinal vertebrae spacers showing the device in the martensitic and the deployed austenitic state (Duerig et al., 1997). (b) A schematic showing the prospective use of porous SMAs as artificial bone implants (Machado and Savi, 2003).

Surgical instrument applications:

Advances in medicine continue to enhance the use of minimally invasive surgery (MIS). Some of the enabling technologies advancing MIS includes instruments that can be inserted through these small openings followed by expansion to a desired size for the particular function. The pseudo-elastic and shape memory effect properties of SMAs allow for more creative design options compared to conventional materials. One such device is the SMA basket used to remove stones in the bile duct. Other instruments using the shape memory effect behavior include surgical tools with grippers, scissors and tongs used in laparoscopy procedures. Pseudo-elastic guide wires are widely used

in surgery due to their kink resistance and superior flexibility (Duerig et al., 1997).

1.3.5 Other applications

There are many other fields and applications that incorporate SMAs. The oil industry has shown extensive interest to use the SMA actuation capabilities in release devices and protection systems for downhole drilling equipment. The high-temperature operating conditions have also opened the avenue for the use of high-temperature SMAs (HTSMAs) in these devices (Lagoudas, 2008).

Flexible metallic eyeglasses and headphones, that can be bent without breaking are other applications that employ the pseudo-elastic behavior. SMAs have also been used in sporting goods like golf clubs where the SMA embedded in the club absorbs the impact of the strike.

Chapter 2

Literature review and research outline

2.1 Constitutive modeling approaches

From 1980 up to now, constitutive modeling of shape memory alloys has been an active research subject. The resulting models can be in general classified into three major categories:

Macroscopic phenomenological models (macro-models): Macroscopic phenomenological models are built on phenomenological thermodynamics and/or directly curve fitting experimental data. Many are based on the common phase diagram of SMA transformation where the transition regions of martensite to parent phase or parent phase to martensite transformation are determined experimentally and plotted in stress-temperature space. Researchers typically use the martensite volume fraction as an internal variable and different mathematical functions to describe a smooth transition.

These kinds of models are generally more suitable for engineering applications due to their simplicity and fast computations, but they can only describe the global mechanical response while all the microscopic details are ignored; because the phase diagram is built on experimental data, the models are also quite accurate. Based on continuum thermodynamics with internal variables, several three-dimensional macroscopic phenomenological models have been proposed, in the literature, with success.

In this research, we will use the macroscopic or phenomenological approach and will present more details in the next sections.

Microscopic thermodynamics models (micro models): Micro-models focus on the description of micro-scale features, such as nucleation, interface motion, twin growth, etc. (Abeyaratne and Knowles, 1990; Ball and James, 1987). They are extremely helpful to

understand the fundamental phenomena, but are often difficult to apply for engineering applications. They do not take into account phase volume fractions as a-priori internal variables, but as a consequence of interface movements. More details can be found, e.g., in Falk (1980), Falk (1983) and Ball and James (1987).

Micro-mechanics based macroscopic models (micro-macro models): The essence of the micro-mechanics-based models is in the modeling of a single grain and further averaging the results over a representative volume element (RVE) to obtain a polycrystalline response of the SMA. Such models have been presented in the literature by different researchers. As an example, Patoor et al. (1996) have modeled the behavior of a polycrystalline SMA by utilizing the model for single crystals and using the self-consistent averaging method to account for the interactions between the grains. A micro-mechanical model for SMAs which is able to capture different effects of SMA behavior such as super-elasticity and shape memory effect has been presented by Sun and Hwang (1993a,b). In other words, this group of models uses thermodynamics laws to describe the transformation and utilizes micro-mechanics to estimate the interaction energy due to the transformation in the material, which is a key factor in the transformation mechanism. Appropriate formulation of this interaction energy is very important and requires knowledge of the micro-structural evolution. Several assumptions at the micro-structure level is made to approximate the interaction energy (Fischer and Tanaka, 1992; Gao et al., 2000; Huang and Brinson, 1998; Huang et al., 2000; LExcellent et al., 1996; Patoor et al., 1994; Sun and Hwang, 1993a). These models appear to have good predictive capabilities and moreover, in some cases they are also able to successfully reproduce reorientation and detwinning of martensite variants (Gao and Brinson, 2002; Huang and Brinson, 1998; Marketz and Fischer, 1996; Thamburaja, 2005). However, they employ a large number of internal variables which makes computations time intensive, resulting in a difficult application for engineering purposes.

One can summarize the advantages and disadvantages of the different approaches by the following general remarks. First, the models developed with the macroscopic approach are generally easy to use and allow quick computations but they are less predictive. Concerning the micro-macro approach, it is much more predictive, but a large number of internal variables is introduced. That is the reason why micro-mechanical models still remain difficult to be used in structural engineering applications. The micro-level approach is more suitable for the development of fundamental studies than for the quantitative description of macroscopic behaviors.

2.2 Phenomenological SMA models

As we stated, we will use the phenomenological approach in the present study; consequently, in the following, we review phenomenological SMA constitutive models. The available phenomenological constitutive modeling approaches can be categorized in two groups:

2.2.1 Models without internal variables

In such models the material behavior is described by strain, stress, temperature, and entropy without the introduction of quantities representing phase mixture.

Polynomial potential models

In this approach, constitutive information are provided by a polynomial free energy function whose partial derivatives provide constitutive equations for strain (or stress) and entropy. In 1980, Falk proposed a Landau-Devonshire like free energy function based on the analogy between SMA uniaxial stress-strain curves and the electric field-magnetization curves of ferromagnetic materials. In his work, Non-monotone stress-strain curves were obtained, and the unstable negative slope part was interpreted as the occurrence of the phase transition. The actual pattern followed during the transformation was assumed to proceed at constant stress. The particular form of the Landau-Devonshire free energy accounts for the temperature dependence of the isothermal stress-strain behavior. We can address Falk (1980, 1983); Falk and Konopka (1990) as models in this group. The main advantage of these models is their simple form, but they are not able to model complicated behavior of the material as well as they do not describe accurately the evolutive nature of the processes.

Hysteresis models

Hysteresis models seek to reproduce experimentally observed curves that involve high nonlinearity and complex looping. They have been widely used in several fields, in particular for magnetic materials. In this approach, constitutive equations are proposed directly on the basis of their mathematical properties, often without explicit focus on their link with the underlying physical phenomena of interest.

Two main algorithm classes have received special attention in the context of SMA phase transformation. The first one is based on tracking sub-domain conversion/reversion and

lead to integral based algorithms. The most common of these is known as the Preisach algorithm and it has been used to describe uniaxial isothermal pseudo-elastic stress-strain SMA response (Huo, 1989; Ortin, 1992). The second algorithm class involves differential equations with separate forms for driving input increase and driving input decrease. Differential equations of Duhem-Madelung form have been used to model SMA phase fraction evolution during the thermally induced transformation (Ivshin and Pence, 1994; Likhacev and Koval, 1992).

2.2.2 Models with internal variables

The key feature of this approach is to introduce appropriate internal variables describing the material internal structure. Internal variables, along with a set of mechanical and thermal control variables, define a collection of state variables. A general thermodynamical consistent approach then allows to derive evolution equations for the internal variables. Mechanical control variables can be either strain or stress, while thermal control variables can be either temperature or entropy. The internal variables typically include one or more phase fractions and/or macroscopic transformation strains. The first application of such an approach to SMAs seems to be due to Tanaka and Nagaki (1982), where internal variables are employed to describe the development of the underlying phase mixture.

The models based on internal variables can furthermore be categorized into two groups:

Models with assumed phase transformation kinetics

Models with assumed phase transformation kinetics consider the involved martensitic volumetric fraction as internal variable, which is expressed as function of current values of stress and temperature. Several authors propose different functions to describe the volumetric fraction evolution. The model firstly developed by Tanaka and coworkers (Lin et al., 1994; Tanaka, 1986, 1990; Tanaka and Iwasaki, 1985; Tanaka and Nagaki, 1982; Tanaka et al., 1995) was originally conceived to describe three-dimensional problems involving SMAs. Nevertheless, its implementation was naturally restricted to the one-dimensional context. The authors considered exponential functions to describe phase transformations. Since an exponential function was adopted, there should be an extra consideration for the phase transformation final bounds.

Boyd and Lagoudas (1994) rewrote Tanaka's original model, for a three-dimensional theory, while the relations used to describe phase transformation evolution remained the same as in Tanaka's model. Liang and Rogers (1990) presented an alternative evolution law for the volumetric fraction based on cosine functions. The authors also developed a

three-dimensional model, in which they suggest that phase transformations are driven by the associated distortion energy. Brinson (1993) offered an alternative approach to the phase transformation kinetics, in which, besides considering cosine functions, the martensite fraction was split into two distinct quantities, the temperature-induced martensite and the stress-induced martensite. The author also considered different elastic moduli for austenite and martensite.

Models with internal variable(s) evolution equation(s)

These models are developed within a more rigorous thermodynamical continuum approach. The theory is then composed of physical laws, i.e. the constitutive equations that characterize the features typical of each material, and material behavior requirements that ensure thermo-dynamical process restrictions. Constitutive information are specified by two kinds of relations: *1. state equations* for the entities conjugate to control variables. These can be formulated directly or obtained as partial derivatives of a suitable free energy function after enforcing the Clausius-Duhem inequality for every process. If heat conduction is to be included, then a constitutive equation relating temperature gradient and heat flux (usually the Fourier equation) is also required; *2. kinetic equations* for the internal variables. In view of phase transformation hysteresis, these equations generally depend on the material past history. Standard practice in most internal variable models is to specify this dependence through equations relating the rates of the internal variables to the current state and its time derivatives. The internal state then follows from the solution of differential equations in time.

Although, sometimes employing formalisms are quite different, several models fitting into this basic framework have been proposed to describe SMA behavior. While most of the efforts are limited to modeling one-dimensional behavior of the material, in the last decade, motivated by extensive engineering applications as well as available multi-axial experimental data, considerable attention has been devoted into developing three-dimensional constitutive models. Nowadays, there are varieties of 3D phenomenological models trying to properly capture different aspects of SMA behaviors.

Compared with the extensive efforts in constitutive modeling, there are not considerable publications in the corresponding numerical implementation. This fact is partially due to unavailability of proper constitutive models suitable for the corresponding numerical implementation. High nonlinear behavior of material and complicated structure of models - compared to plasticity - are other obstacles in numerical implementation. It is generally accepted in the literature that in order to reach a computational tool for design and analysis of SMA devices and structures, 3D phenomenological constitutive models in the framework of continuum thermodynamics with internal variables should

be developed.

Micro-plane method

Another approach in constitutive modeling is based on micro-plane theory. This approach is interesting for its capability of extending a 1D constitutive model to a 3D one. The micro-plane modeling approach originated from the work of Taylor (1938), who studied the constitutive behavior of polycrystalline metals by developing relations between stress and strain vectors on generic planes of arbitrary orientations in the material and determining the macroscopic stress or strain tensors as a resultant of all these vectors. This concept was later modified by others and is commonly known as slip theory of plasticity. As slip is not the source of inelastic response for all types of materials, Bazant (1984) introduced a neutral term called the micro-plane theory, which can be used for general inelastic behavior. In this approach, a 1D constitutive law for one stress component and the associated strain component on each micro-plane is sufficient to generate a macroscopic 3D model by considering either of two main formulations in micro-plane theory named static constraint and kinematic constraint. In static constraint formulation, it is assumed that the stress vector acting on each micro-plane is the projection of the macroscopic stress tensor. In kinematic constraint formulation, the strain vector on any micro-plane is considered as the projection of the macroscopic strain tensor. Moreover, there are some particular material laws where both static and kinematic constraints coexist. Such a case is called double constraint formulation. Brocca et al. (2002) present a model based on micro-plane theory, which can model both shape memory and pseudo-elasticity. A micro-plane constitutive model for polycrystalline SMA is proposed in Kadkhodaei et al. (2007) by first deriving a 1D model and then generalizing it to a 3D case.

Fremond's model

Fremond (1987, 1996) developed a model for a three dimensional media, being able to reproduce both pseudo-elasticity and shape memory effect, with the aid of three internal variables that should obey internal constraints related to the coexistence of the different phases. The modified model takes into account some changes in the original formulation that allows new phenomena description such as linear hardening plasticity, plastic-phase transformation coupling, phase transformation due to temperature variation, internal subloops due to incomplete phase transformation, tension-compression asymmetry and transformation induced plasticity (TRIP). Based on the Fremond's model, several works have been published by a group around Paiva and Savi (Baêta-Neves et al., 2002, 2004;

Paiva et al., 2005, 2007; Savi and Paiva, 2005).

2.3 Literature review: models based on the continuum thermodynamics with internal variables

In this thesis we use continuum thermodynamics with internal variables which is, in our opinion, the most suited approach for the development of reliable 3D SMA constitutive equations, able to describe material response under complex multiaxial thermo-mechanical loadings. In the following we present a detailed literature review based on the continuum thermodynamics with internal variables.

2.3.1 SMA modeling activities between 1980–1995

After the discovery of Nitinol in 1963 and first commercial application as F-14 coupling in 1971, it seems that the first book on shape memory alloys appeared in 1975 by Perkins which presented some metallurgical aspects of SMAs. As we mentioned in previous sections, most of the works in the beginning of 1980 is devoted to micro-modeling or simple phenomenological ones. In a series of papers, Müller and his colleagues developed a systematic thermodynamic theory of pseudo-elasticity and presented a plausible one-dimensional theory which is very useful in understanding the physics of most phenomena in the material (Hu and Müller, 1993; Müller, 1986, 1989; Müller and Wilmanski, 1980; Müller and Xu, 1991).

Tanaka and Nagaki (1982) were evidently the first researchers who discussed martensitic transformations within the context of continuum thermodynamics with internal variables. The phase transformation is basically governed by the minimization of the free energy. The energy equation and Clausius-Duhem inequality were used to describe the hysteresis associated with the phase transformation (Lin et al., 1994; Tanaka, 1986, 1990; Tanaka and Iwasaki, 1985; Tanaka et al., 1995).

In 1987, another book on shape memory alloys appeared (Funakubo, 1987). In the setting of 3-D media, Bondaryev and Wayman (1988) proposed a phenomenological model inspired by the classical plasticity theory. Motivated by the work of Tanaka (1986), Liang and Rogers (1990) proposed a model with cosine kinetics for martensite volume fraction.

In 1990, there were several motivations toward SMA applications, e.g. various medical applications were introduced. Moreover, the first comprehensive book on engineering applications of SMAs appeared in 1990 (Duerig et al., 1990). Inspired from several SMA medical and industrial applications, it seems that, after 1990, there was more motivation

Table 2.1: SMA macro-modeling up to 1995

year	description
1963	NiTiNOL Discovery
1971	F-14 hydraulic coupling (first commercial application)
1975	Book: Perkins (1975)
≈ 1980	phenomenological thermodynamics approach
1982-1986	Tanka model (Tanaka and Nagaki (1982), Tanaka (1986))
1987	Book: Funakubo (1987)
1988	The paper by Bondaryev and Wayman (1988)
1990	Liang and Rogers (1990) model
1990	Book: Duerig et al. (1990)
≈ 1990	Various biomedical applications
1992	Raniecki et al. (1992) model
1993	Brinson (1993) decomposition
1994	Grasser and Cozzarelli (1994) model
1994	Boyd and Lagoudas (1994) model
1994	Ivshin and Pence (1994) model
1994	Raniecki and Lexcellent (1994) model
1995	Experiment by Shaw and Kyriakides (1995)
1995	Multiaxial experiment by Sittner et al. (1995)

toward SMA three-dimensional macro-modeling (e.g., Raniecki et al. (1992), Grasser and Cozzarelli (1994), Boyd and Lagoudas (1994), Ivshin and Pence (1994) and Raniecki and Lexcellent (1994)). However, one-dimensional modeling yet remained interesting due to the use of SMA wires in smart composites and similar applications e.g., for actuators; we can refer to the work by Brinson in 1993 where she introduced the decomposition of the martensite volume fraction into stress-induced and temperature-induced parts.

In 1995, two comprehensive experimental studies published which affected considerably the SMA modeling after on; the work by Shaw and Kyriakides (1995) presented several aspects of thermo-mechanical behavior of NiTi wires and addressed questions concerning local versus average measures of strains, spurious measurements of residual strains and dependence of the heat transfer conditions on the stress-strain curves. The work by Sittner et al. (1995), for the first time, presented a comprehensive multiaxial study on Cu-Al-Zn-Mn SMAs. Table 2.1 summarizes the main activities from NiTi discovery in 1963 up to 1995.

2.3.2 SMA modeling activities after 1995

Starting 1996, there was more motivation toward SMA three-dimensional modeling due to: it was generally accepted that continuum thermodynamics with internal variable is a proper tool for effective SMA 3-D macro-modeling, there was extensive multidimensional experimental data under proportional and non-proportional loadings and there was much interest in medical and industrial applications. However, due to simplicity in one-dimensional models and applications to smart composites (in a wire form), the one-dimensional modeling yet remained active, with focus on secondary effects, e.g., progressive accumulated strain in (wire) actuator applications, different material properties for austenite and martensite and so on. Therefore, it was expected that the future research to be directed toward proposing accurate 3D macro models and studying material behavior under multidimensional loading (e.g., phase transformation surface) and reporting more experimental data.

From a different aspect, engineering applications yet needed a proper computational tool in design and simulation of SMA devices, specifically for biomedical applications. Accordingly, developing a 3D SMA model to consider many SMA complicated behaviors does not mean that it is an effective SMA model in engineering applications. To this end, besides research activities in SMA modeling, it was necessary to decide on which behaviors should be included in modeling according to engineering requirements as well as corresponding computational tool development.

In the following, we focus on 3D macro-modeling, experimental studies and numerical implementations of SMA models. We remark that we only focus on the works which present a new modeling approach or a new model, skipping the works focused just on secondary effects modeling.

Following the work by Raniecki and Lexcellent (1994), Leclercq and Lexcellent (1996) presented a macroscopic description for the simulation of the global thermo-mechanical behavior of SMAs; two internal variables were taken into account, i.e., the volume fraction of self-accommodating (pure thermal effect) and oriented (stress-induced) product phases. Lubliner and Auricchio (1996) applied the generalized plasticity theory (Lubliner, 1984) to SMAs and proposed a three-dimensional model. In 1997, based on a plasticity-like return mapping method, Masud et al. presented a finite deformation finite element model for the pseudo-elastic response of shape memory alloys under stress loading-unloading conditions at constant temperature. Similarly, a plasticity-like finite element model for super-elastic SMA structures was proposed by Trochu and Qian (1997). Sittner et al. (1997) presented several experimental data on thin wall tubes made of CuAlZnMn subjected to combined axial and torsional loads in low temperature martensite state (SME). With the aid of developing a computational tool to be used

during the design of SMA-based devices, Auricchio et al. (1997) and Auricchio and Taylor (1997) proposed constitutive models in small and finite strain regimes, respectively, and implementing in the FEM, they solved several boundary value problems (BVP). Souza et al. (1998) proposed a model which can describes the main features of polycrystalline shape memory materials in the setting of 3D media. It had been conceived within the framework of generalized standard materials (Maugin, 1992), that internal variables were defined to describe the phase transformation processes. Raniecki and Lexcellent (1998) generalized the thermodynamic theory of pseudo-elastic behavior of SMAs to account for the large differences between hysteresis loops in tension and compression. In 1998, Otsuka and Wayman published a book on shape memory materials, with focus on metallurgical aspects.

Qidwai and Lagoudas (2000) investigated various transformation functions and proposed a generalized type transformation function. Auricchio (2001) presented a robust integration algorithm for a 3D finite-strain SMA model. Also, Liew et al. (2002) simulated multidimensional super-elastic behavior of shape memory alloys via nonlinear finite element method. Thamburaja and Anand (2002) presented a model for super-elastic behavior in tension-torsion of an initially textured NiTi shape memory alloy. Lexcellent et al. (2002) determined the initial surface of phase transformation under biaxial loading in some polycrystalline shape memory alloys both experimentally and numerically.

Auricchio and Petrini (2002) improved the model proposed by Souza et al. (1998) and obtained a robust integration algorithm. In another work, Auricchio and Petrini (2004a) included the asymmetric behavior and simulated several SMA-devices. Moreover, the same model was extended to capture thermo-mechanical coupling effects in Auricchio and Petrini (2004b).

Helm and Haupt (2003) have proposed a model to represent the multiaxial material behavior of shape memory alloys which is able to represent the main effects of shape memory alloys; i.e., the one-way shape memory effect, the two-way shape memory effect due to external loads, the pseudo-elastic and pseudo-plastic behavior as well as the transition range between pseudo-elasticity and pseudo-plasticity. Bouvet et al. (2004) have proposed a phenomenological model, taking into account the tension-compression asymmetry effect, the temperature effect, the return point memory effect and the influence of the loading path non-proportionality on the SMA mechanical behavior. Terriault et al. (2006) have proposed a non-isothermal finite element modeling of SMA actuators using the commercial software ANSYS[®]. Müller and Bruhns (2006) have proposed a thermodynamic finite strain model to describe the pseudo-elastic response of shape memory alloys. The model is based on a self-consistent Eulerian theory of finite deformations using the logarithmic rate. Based on a modified phase transformation diagram, Popov and Lagoudas (2007) proposed a 3D constitutive model for polycrystalline shape mem-

ory alloys (SMAs).

Thiebaud et al. (2007) have presented an implementation of a phenomenological model based on the so-called RL model (Raniecki and LExcellent, 1998) in a finite element code called COMSOL. Panico and Brinson (2007) have proposed a model that accounts for the effect of multiaxial stress states and non-proportional loading histories. The model is able to account for the evolution of both twinned and detwinned martensite. Moreover, this model accounts for the reorientation of the product phase according to loading direction. Within the framework of generalized standard materials with internal constraints, Zaki and Moumni (2007) have used the martensite volume fraction and the martensite orientation strain tensor as internal variables to account for self-accommodation, orientation and reorientation of martensite, as well as super-elasticity and one-way shape memory. In another work, Moumni et al. (2008) have simulated the pseudo-elastic response of SMAs as well as the one-way shape memory effect. In addition, they have compared the results with the experimental data reported in Sittner et al. (1995) and Tokuda et al. (1999).

Extending the small-strain model by Helm and Haupt (2003), Reese and Christ (2008) have recently suggested a finite strain phenomenological model and implemented into finite element formulation to simulate NiTi stents. After around 15 years of research in SMA modeling, Lagoudas published, to the our knowledge, the first book on constitutive modeling of shape memory alloys (Lagoudas, 2008). In an attempt to model variant reorientation, as an important phenomenon under non-proportional loading conditions, Arghavani et al. (2010c) have introduced a new set of internal variables, a scalar and a tensor to describe phase transformation and reorientation. In addition, Based on the new set of internal variables, they have proposed a new SMA constitutive model within small strain regime and have compared with several experimental data. In another work Arghavani et al. (2010e) have utilized the introduced internal variables and proposed a class of small strain SMA constitutive models. They have showed that several SMA models, available in the literature, appear to be the members of the proposed class. Thamburaja and Nikabdullah (2009) have developed a non-local and thermo-mechanically-coupled constitutive model for polycrystalline shape-memory alloys (SMAs) capable of undergoing austenite into martensite phase transformations. The theory is developed in the isotropic metal-plasticity setting using fundamental thermodynamic laws and the principle of micro-force balance. Moreover, Thamburaja (2010) has extended the model developed in Thamburaja and Nikabdullah (2009) to the finite strain regime.

More recently, Arghavani et al. (2010d) have extended the small strain model proposed by Panico and Brinson (2007) to finite deformation regime. They have used a multiplicative decomposition of the deformation gradient into elastic and inelastic parts together with an additive decomposition of the inelastic strain rate tensor into transformation

and reorientation parts. With the aim of obtaining a robust and efficient integration algorithm for a 3D finite strain SMA model, Arghavani et al. (2010b) have proposed a logarithmic mapping as well as a nucleation-completion condition to construct the integration algorithm. Moreover, they have compared the robustness and efficiency of different algorithms.

2.3.3 Experimental studies on mechanical behavior of SMAs

Even though significant interest exists in the modeling of pseudo-elastic and pseudo-plastic behavior of shape memory alloys, and NiTi in particular, however the experimental data, which are used to fit the material models, are in most cases associated with uniaxial tests or even simple tension experiments. In order to allow for the development of reliable models, which may be used to simulate complex structures, it is of paramount importance to use multiaxial experiments so that material models can be cross-checked utilizing a high degree of complexity.

Basically, most experimental research in the field of shape memory alloys is conducted on Cu-based and NiTi shape memory alloys. One of the early experimental analysis of the 3D behavior of SMAs was performed by Sittner et al. (1995, 1996). They investigated the stabilization of the transformation behavior in stress-induced martensite in NiTi hollow bar cylinders. A number of loading cycles were performed in combined tension-torsion and the specimen was then loaded in either tension or torsion revealed strain anisotropy, i.e. the appearance of other strain components. Similar studies concerning the examination of the path dependence, for NiTi, have been conducted by Rogueda et al. (1996). Jacobus et al. (1996) and Gall et al. (1997, 1998) have concentrated on the influence of the triaxial compression state on the material behavior of NiTi, analyzing zero hydrostatic pressure, triaxial compression, and hydrostatic compression states. Proportional and non-proportional loading experiments on SMA torque tubes have been conducted by Lim and McDowell (1999). They investigated the stress-temperature coupling in tension, compression and torsion. As to examine the initial surface of transformation onset, elaborate tests concerning internal pressure and bi-compression experiments on Cu-based SMA cylinders have been published, for instance, by the research group around Bouvet (see Bouvet et al. (2002, 2004)). In addition, McNaney et al. (2003) have addressed the combined tension/ torsion behavior for different box tests in the first axial/torsional quadrant varying the aspect ratios of the respective box shape. Extensive biaxial tests have also been performed by Helm (2001) and Helm and Haupt (2003) who presented their findings on box and butterfly shaped strain controlled experiments.

Moreover, when the interrelation of complex stress states and temperature variations ,

effect Sittner et al. (1997) and Tokuda et al. (2002, 1999) have conducted some multi-axial tension/ torsion experiments on a relatively thick-walled (radius-to-wall-thickness ratio of $r/t = 2.2$) Cu-based specimen at low temperature. Recently, Grabe and Bruhns (2008b) have used a new method of temperature control to study the tension/torsion tests of pseudo-elastic, polycrystalline NiTi shape memory alloys under controlled-temperature conditions. In another work, Grabe and Bruhns (2008a) have focused on the decoupling of thermal and viscous effects on the transformation stress level as the specimen material is subjected to heating and cooling due to latent heat generation and absorption during phase transition. They have conducted uniaxial and two-dimensional tension/torsion experiments to generalize the uniaxial findings.

More recently, Grabe and Bruhns (2009) have conducted several multi-axial experiments on polycrystalline NiTi within a wide temperature range to investigate the pseudo-elastic as well as the pseudo-plastic behavior within the distinct temperature regimes. Isothermal and temperature varying thermo-mechanical loading paths have been applied by means of an active temperature control to characterize the path dependence of pseudo-elasticity and the multi-axial one-way effect of the alloy. In the experiments, they focused on the determination of the dependence of the loading sequence, the related non-linearity of the material and the combined material interaction, e.g., referring to reorientation processes for complex loading paths with respect to pseudo-elasticity and the one-way effect.

We summarize the experimental studies on mechanical behavior of SMAs in Table 2.2.

2.4 Outline of the research

In this thesis, we develop several SMA constitutive models at small and finite deformations. To this end we use the following assumptions:

- we neglect the secondary effects, i.e.:
 - we assume that material exhibits symmetric behavior under tension and compression.
 - we neglect thermo-mechanical coupling effects.
 - we assume that the austenite and martensite phases have the same elastic properties.
 - we neglect the progressive strain under cyclic loadings.
- the material is assumed to be isotropic.

Table 2.2: Experimental studies on mechanical behavior of SMAs

year	material	description	Ref.
1995	CuAlZnMn	tension-torsion	Sittner et al. (1995, 1996)
1996	CuZnAl	tension-torsion	Rogueda et al. (1996)
1996	NiTi	3-D compression	Jacobus et al. (1996)
1997	NiTi	3-D compression	Gall et al. (1997)
1997	CuAlZnMn	tension-torsion	Sittner et al. (1997)
1998	CuZnAl	3-D compression	Gall et al. (1998)
1999	CuAlZnMn	tension-torsion	Tokuda et al. (1999)
1999	NiTi	axial-torsion	Lim and McDowell (1999)
2001	NiTi	axial-torsion	Helm (2001); Helm and Haupt (2003)
2002	CuAlBe	axial-axial	Bouvet et al. (2002)
2002	CuAlZnMn	tension-torsion	Tokuda et al. (2002)
2003	NiTi	tension-torsion	McNaney et al. (2003)
2004	CuAlBe	axial-axial	Bouvet et al. (2004)
2008	NiTi	axial-torsion	Grabe and Bruhns (2008a,b)
2009	NiTi	axial-torsion	Grabe and Bruhns (2009)

Employing the above mentioned assumptions and based on the continuum thermodynamics with internal variables, we develop a class of constitutive models within small deformation regime. We then extend the models proposed by Panico and Brinson (2007) and Souza et al. (1998) into finite deformation regime. Utilizing the multiplicative decomposition of the deformation gradient, we develop constitutive models in which both strains and rotations are assumed to be large. We propose a constitutive model in which only large rotations are considered (strain is assumed to be small). In addition, we discuss numerical implementation of the developed constitutive models. In this regard, we propose an integration algorithm and discuss in detail the corresponding solution algorithm. We also address the construction of the consistent tangent matrix. Implementing the developed integration algorithm into a user defined subroutine (UMAT) in the nonlinear finite element software ABAQUS, we finally simulate several boundary value problems and compare different algorithms in terms of robustness as well as efficiency. The results show that the developed computational tool is an effective tool which can be used in the design, analysis and optimization of SMA structures. The structure of the thesis is as follows.

After an introduction to shape memory alloys in Chapter 1 and a comprehensive review on different approaches in constitutive modeling of SMAs, specifically on SMA modeling within continuum thermodynamics with internal variables, in this Chapter (Chapter 2),

we present some basic preliminaries from nonlinear solid mechanics in chapter 3.

The rest of the thesis is then devoted to constitutive modeling in small and finite strain regimes and numerical implementation in FEM. To this end, in Chapter 4, after reviewing some small strain formulations available in the literature, we present a class of small-strain SMA models. We show that, several models, available in the literature, can be identified as members of the proposed class of models. With emphasis on non-proportional loading and reorientation, we specifically introduce a model with the property of decoupling pure reorientation from pure phase transformation.

In Chapter 5, we extend the small strain constitutive models proposed by Panico and Brinson (2007) and Souza et al. (1998) into finite strain regime. The approach is based on the use of a multiplicative decomposition of the deformation gradient into elastic and inelastic parts. We then use the finite strain extension of Souza model and improve it in several aspects, e.g.: well-defining the variables, presenting a fully-symmetric formulation. We also develop a finite strain constitutive model based on the Hencky strain measure.

Chapter 6 is totally devoted to numerical implementation of the developed constitutive models. We give details on time-discretization, integration algorithm and solution schemes.

In chapter 7, we propose an effective formulation for SMA simulation and compare the robustness and efficiency of different algorithms. To this end, we compare the finite strain, small strain and finite rotation formulations. Finally we present a summary and draw conclusions in Chapter 8. Moreover, we use several appendices to present the details of some derivations we have used in different chapters.

Chapter 3

Preliminaries from nonlinear solid mechanics

3.1 Introduction

This chapter contains a summary of the continuum mechanics background. The kinematical relations, the balance laws with their weak forms, the constitutive equations and the linearization, which is used in the finite element formulation, are described.

3.2 Kinematics

The kinematical relations concern the description of the deformation and motion of a body, the derivation of strain measures and the time derivatives of kinematical quantities. All kinematical relations are needed within the constitutive equations and the weak formulation of balance laws.

Motion and deformation gradient

The configuration of a body B is a one-to-one mapping $\varphi: B \rightarrow \mathbb{E}^3$ where the location of a particle \mathbf{X} is given as $\mathbf{x} = \varphi(\mathbf{X})$. The motion of body B is then given as a one-parametric series of configurations $\varphi_t: B \rightarrow \mathbb{E}^3$. The location of a particle \mathbf{X} at time $t \in \mathbb{R}^+$ yields

$$\mathbf{x} = \varphi_t(\mathbf{X}) = \varphi(\mathbf{X}, t) \quad (3.1)$$

If the motion is characterized with respect to the material coordinates \mathbf{X} , this is called material, referential or Lagrangian description. Another possibility is the use of the

spatial coordinates \mathbf{x} when the motion of body B has to be described and is called spatial or Eulerian description.

The equations of continuum mechanics can be formulated with respect to the deformed or undeformed configurations of a body. From the theoretical point of view, there is no difference or preference whether the equations are related to the initial or current configuration and the configuration can be chosen freely (Wriggers, 2008).

To describe the deformation process locally, the deformation gradient tensor \mathbf{F} with $J = \det(\mathbf{F}) > 0$ is introduced such that

$$\mathbf{dx} = \mathbf{F}d\mathbf{X} \quad \text{or} \quad \mathbf{F} = \text{Grad}\mathbf{x} = \frac{\partial \mathbf{x}}{\partial \mathbf{X}} \quad (3.2)$$

Knowing the deformation gradient allows to express further transformations of differential quantities between B and $\varphi(B)$. For example, the transformation of surface area elements between B and $\varphi(B)$ is given by the formula of Nanson as (Bonet and Wood, 2008)

$$\mathbf{da} = \mathbf{n}da = J\mathbf{F}^{-T}\mathbf{N}dA = J\mathbf{F}^{-T}\mathbf{dA} \quad (3.3)$$

where \mathbf{n} is the normal vector of the surface of the deformed body $\varphi(B)$ and \mathbf{N} is the normal vector in B . The transformation between volume elements of initial and current configuration is provided by the relation

$$dv = JdV \quad (3.4)$$

The polar decomposition of the deformation gradient splits the deformation gradient in a multiplicative way in a proper orthogonal rotation tensor \mathbf{R} (with $\mathbf{R}^{-1} = \mathbf{R}^T$) and the symmetrical right and left stretch tensors \mathbf{U} and \mathbf{V} as

$$\mathbf{F} = \mathbf{R}\mathbf{U} = \mathbf{V}\mathbf{R} \quad (3.5)$$

The right and left Cauchy-Green tensors \mathbf{C} and \mathbf{b} are then defined, respectively, as

$$\mathbf{C} = \mathbf{F}^T\mathbf{F} = \mathbf{U}^2, \quad \mathbf{b} = \mathbf{F}\mathbf{F}^T = \mathbf{V}^2 \quad (3.6)$$

Finally, by introducing a displacement vector $\mathbf{u}(\mathbf{X}, t)$ as

$$\mathbf{u}(\mathbf{X}, t) = \varphi(\mathbf{X}, t) - \mathbf{X} \quad (3.7)$$

the deformation gradient can be written as

$$\mathbf{F} = \text{Grad}[\mathbf{X} + \mathbf{u}(\mathbf{X}, t)] = \mathbf{1} + \text{Grad}\mathbf{u} = \mathbf{1} + \mathbf{H} \quad (3.8)$$

where the tensor $\mathbf{H} = \text{Grad}\mathbf{u}$ is called displacement gradient and $\mathbf{1}$ represents the second order identity tensor.

Strain measures

In this section, different strain measures are discussed. The first strain tensor referred to the initial configuration B and called Green-Lagrange strain tensor is defined by

$$\mathbf{E} = \frac{1}{2}(\mathbf{C} - \mathbf{1}) = \frac{1}{2}(\mathbf{U}^2 - \mathbf{1}) \quad (3.9)$$

The Green-Lagrange strain measure is often used in nonlinear structural engineering applications. Since this strain measure can describe arbitrary rigid body motions correctly, it is mostly applied for problems with large displacements but small strains, e.g. within beam or shell theory (Crisfield, 1997; Wriggers, 2008).

A generalization of (3.9) yields Seth-Hill class of strain measures defined by

$$\mathbf{E}^\alpha = \frac{1}{\alpha}(\mathbf{U}^\alpha - \mathbf{1}), \quad \alpha \in \mathbb{R} \quad (3.10)$$

This strain tensor is referred to the initial configuration B . It is constructed such that its linearization yields the classical linear strain measure. For $\alpha = 0$, the strain tensor

$$\mathbf{E}^0 = \log(\mathbf{U}) \quad (3.11)$$

follows which is known under the name of Hencky and also called logarithmic or natural strain measure.

The equivalent to the generalized strain measure (3.10) which is formulated with respect to the current configuration $\varphi(B)$ is given by

$$\mathbf{e}^\alpha = \frac{1}{\alpha}(\mathbf{V}^\alpha - \mathbf{1}), \quad \alpha \in \mathbb{R} \quad (3.12)$$

We observe that the Green-Lagrange strain is included in (3.10) for the special case of $\alpha = 2$. Moreover, the so-called Almansi strain tensor is obtained with $\alpha = -2$ from (3.12) as

$$\mathbf{e} := \mathbf{e}^{-2} = \frac{1}{2}(\mathbf{1} - \mathbf{V}^{-2}) = \frac{1}{2}(\mathbf{1} - \mathbf{b}^{-1}) \quad (3.13)$$

Finally, spectral decomposition of \mathbf{U} and \mathbf{V} is provided by

$$\mathbf{U} = \sum_{i=1}^3 \lambda_i \mathbf{N}_i \otimes \mathbf{N}_i, \quad \mathbf{V} = \sum_{i=1}^3 \lambda_i \mathbf{n}_i \otimes \mathbf{n}_i \quad (3.14)$$

where λ_i are the principal values of the stretch tensors, also called principal stretches. They are equal for \mathbf{U} and \mathbf{V} . The eigenvectors \mathbf{N}_i of \mathbf{U} are related to the reference configuration. The eigenvectors \mathbf{n}_i of \mathbf{V} are referred to the spatial configuration. The eigenvectors \mathbf{n}_i can be obtain from \mathbf{N}_i via the relation $\mathbf{n}_i = \mathbf{R}\mathbf{N}_i$.

The spectral decomposition of the Seth-Hill strain tensors are then given by

$$\mathbf{E}^\alpha = \sum_{i=1}^3 f_\alpha(\lambda_i) \mathbf{N}_i \otimes \mathbf{N}_i, \quad \mathbf{e}^\alpha = \sum_{i=1}^3 f_\alpha(\lambda_i) \mathbf{n}_i \otimes \mathbf{n}_i \quad (3.15)$$

where the scale function $f(\lambda_i, \alpha)$ is defined as:

$$f_\alpha(\lambda_i) = \begin{cases} \frac{1}{\alpha}(\lambda_i^\alpha - 1) & \text{if } \alpha \neq 0 \\ \ln(\lambda_i) & \text{if } \alpha = 0 \end{cases} \quad (3.16)$$

Transformation of vectors and tensors

Knowledge regarding the transformation between differential quantities in the current and reference configuration is essential for many theoretical derivations and their applications in finite element methods. Tangent fields which are related to the current configuration can be expressed in terms of quantities in the reference configuration. With the notation introduced in Marsden and Hughes (1983) this is called *pull back*. Conversely a push forward relates tangent fields referred to the reference configuration to the current configuration $\varphi(B)$.

For a covariant gradient of a scalar field $G(\mathbf{X}) = g(\mathbf{x}) = g[\varphi(\mathbf{X})]$ relation

$$\text{Grad}G = \mathbf{F}^T \text{grad}g \iff \frac{\partial G}{\partial X_I} = \frac{\partial g}{\partial x_i} \frac{\partial x_i}{\partial X_I} \quad (3.17)$$

$$\text{grad}g = \mathbf{F}^{-T} \text{Grad}G \quad (3.18)$$

can be derived. In an analogous way, the transformation for the covariant gradient of the vector field $\mathbf{W}(\mathbf{X}) = \mathbf{w}(\mathbf{x}) = \mathbf{w}[\varphi(\mathbf{X})]$ is obtained

$$\text{Grad}\mathbf{W} = \text{grad}\mathbf{w}\mathbf{F} \iff \text{grad}\mathbf{w} = \text{Grad}\mathbf{W}\mathbf{F}^{-1} \quad (3.19)$$

As an application, the deformation gradient is computed from a displacement field $\mathbf{u}[\varphi(\mathbf{X})]$ which is referred to the current configuration. With (3.8) and (3.19) it follows

$$\begin{aligned} \mathbf{F} &= \mathbf{1} + \text{Grad}\mathbf{u} \\ &= \mathbf{1} + \text{grad}\mathbf{u}\mathbf{F} \quad | \quad \mathbf{F}^{-1} \\ \implies \mathbf{F}^{-1} &= \mathbf{1} - \text{grad}\mathbf{u} \end{aligned} \quad (3.20)$$

Hence the inverse of the deformation gradient can be obtained directly with displacements which are referred to the current configuration. This result is applied in formulations of the finite element method.

Time derivatives

The dependence of the deformation $\varphi(\mathbf{X}, t)$ on time t has to be considered in nonlinear problems in case that the constitutive behavior is history dependent (e.g. in plasticity or visco-elasticity) or in case that the complete process is of dynamical nature. The

velocity of a material point with respect to the reference configuration is defined by the material time derivative

$$\mathbf{v}(\mathbf{X}, t) = \frac{D\varphi}{Dt} = \frac{\partial\varphi(\mathbf{X}, t)}{\partial t} = \dot{\varphi}(\mathbf{X}, t) \quad (3.21)$$

In the current configuration, the velocity $\hat{\mathbf{v}}$ of a particle which assumes point \mathbf{x} at time t in $\varphi(B)$ is given by

$$\hat{\mathbf{v}}(\mathbf{x}, t) = \hat{\mathbf{v}}(\varphi(\mathbf{X}, t), t) = \mathbf{v}(\mathbf{X}, t) \quad (3.22)$$

The acceleration is given in an analogous way by the second derivative with respect to time

$$\mathbf{a} = \ddot{\varphi}(\mathbf{X}, t) = \dot{\mathbf{v}}(\mathbf{X}, t) \quad (3.23)$$

Based on this definition, the acceleration can be determined with reference to the current configuration. With (3.22) and the chain rule, it yields

$$\hat{\mathbf{a}} = \dot{\hat{\mathbf{v}}} = \frac{\partial}{\partial t}[\hat{\mathbf{v}}(\varphi(\mathbf{X}, t), t)] = \frac{\partial\hat{\mathbf{v}}}{\partial t} + (\text{grad}\hat{\mathbf{v}})\hat{\mathbf{v}} \quad (3.24)$$

Time derivative of the deformation gradient \mathbf{F} yields with (3.21) and (3.19)

$$\dot{\mathbf{F}} = \text{Grad}\dot{\varphi}(\mathbf{X}, t) = \text{Grad}\mathbf{v} = (\text{grad}\hat{\mathbf{v}})\mathbf{F} \quad (3.25)$$

In this equation, the spatial velocity gradient $\text{grad}\hat{\mathbf{v}}$ occurs which is often denoted by \mathbf{l} . It can be written with (3.25) as

$$\mathbf{l} = \dot{\mathbf{F}}\mathbf{F}^{-1} \quad (3.26)$$

The symmetric and skew-symmetric parts of \mathbf{l} supply the strain rate tensor \mathbf{d} and the vorticity tensor \mathbf{w} , i.e.:

$$\mathbf{d} = \frac{1}{2}(\mathbf{l} + \mathbf{l}^T), \quad \mathbf{w} = \frac{1}{2}(\mathbf{l} - \mathbf{l}^T) \quad (3.27)$$

Equation (3.25) can now be used to compute the time derivative of the Green-Lagrange strain tensor (3.9)

$$\dot{\mathbf{E}} = \frac{1}{2} \left(\dot{\mathbf{F}}^T \mathbf{F} + \mathbf{F}^T \dot{\mathbf{F}} \right) \quad (3.28)$$

Using (3.26) in (3.28) with (3.27) yields the time derivative of \mathbf{E} as

$$\dot{\mathbf{E}} = \mathbf{F}^T \frac{1}{2} (\mathbf{l} + \mathbf{l}^T) \mathbf{F} = \mathbf{F}^T \mathbf{d} \mathbf{F} \quad (3.29)$$

This equation denotes a pull back of the strain rate tensor \mathbf{d} to the reference configuration.

Finally, the convective time derivative of a spatial tensor is considered which is also called Lie derivative. The Lie derivative is defined for a spatial tensor $\mathbf{g}(\mathbf{x}, t)$ with covariant basis by

$$\mathcal{L}_v \mathbf{g} = \mathbf{F} \left\{ \frac{\partial}{\partial t} [\mathbf{F}^{-1} \mathbf{g} \mathbf{F}^{-T}] \right\} \mathbf{F}^T \quad (3.30)$$

This means that tensor \mathbf{g} must be transformed first to the reference configuration by a pull back operation. Here the material time derivative can be computed and afterward the resulting quantity is related to the current configuration by a push forward operation. The analogous rule for the Lie derivative of a spatial tensor $\hat{\mathbf{g}}$ with contravariant basis is given by

$$\mathcal{L}_v \hat{\mathbf{g}} = \mathbf{F}^{-T} \left\{ \frac{\partial}{\partial t} [\mathbf{F}^T \hat{\mathbf{g}} \mathbf{F}] \right\} \mathbf{F}^{-1} \quad (3.31)$$

Corotational rate

An Eulerian symmetric second order tensor \mathcal{A} defined in a deforming material body is said to be objective if it obeys the transformation rule under the change of frame (Xiao et al., 1998)

$$\mathbf{x}^*(\mathbf{X}, t) = \mathbf{x}_0^* + \hat{\mathbf{Q}}(t)\mathbf{x}(\mathbf{X}, t) \implies \mathcal{A}^* = \hat{\mathbf{Q}}(t)\mathcal{A}\hat{\mathbf{Q}}(t)^T \quad (3.32)$$

where \mathbf{x} and \mathbf{x}^* are, respectively, the current position vectors of the material particle \mathbf{X} in two frames in question and $\hat{\mathbf{Q}}(t)$ is the proper orthogonal tensor characterizing the relative rotation between the two frames in question. Let $\boldsymbol{\Omega}^*$ be a given spin tensor, i.e. a skew-symmetric tensor varying with time. Then there is a rotation tensor $\hat{\mathbf{Q}} = \hat{\mathbf{Q}}(t)$ such that

$$\boldsymbol{\Omega}^* = \dot{\hat{\mathbf{Q}}}(t)^T \hat{\mathbf{Q}}(t) = -\hat{\mathbf{Q}}(t)^T \dot{\hat{\mathbf{Q}}}(t) \quad (3.33)$$

In a rotating frame with the spin $\boldsymbol{\Omega}^*$, an Eulerian tensor \mathcal{A} becomes $\hat{\mathbf{Q}}(t)\mathcal{A}\hat{\mathbf{Q}}(t)^T$ and therefore the material time rate of the latter is given by

$$\overline{(\hat{\mathbf{Q}}(t)\mathcal{A}\hat{\mathbf{Q}}(t)^T)} = \hat{\mathbf{Q}}(t)\dot{\mathcal{A}}\hat{\mathbf{Q}}(t)^T + \dot{\hat{\mathbf{Q}}}(t)\mathcal{A}\hat{\mathbf{Q}}(t)^T + \hat{\mathbf{Q}}(t)\mathcal{A}\dot{\hat{\mathbf{Q}}}(t)^T \quad (3.34)$$

which yields

$$\overline{(\hat{\mathbf{Q}}(t)\mathcal{A}\hat{\mathbf{Q}}(t)^T)} = \hat{\mathbf{Q}}(t)\overset{\circ}{\mathcal{A}}\hat{\mathbf{Q}}(t)^T \quad (3.35)$$

In deriving (3.35), we have used (3.33) and have defined the *corotational rate* of the Eulerian tensor $\overset{\circ}{\mathcal{A}}$ associated with the spin $\boldsymbol{\Omega}^*$ as:

$$\overset{\circ}{\mathcal{A}} = \dot{\mathcal{A}} + \mathcal{A}\boldsymbol{\Omega}^* - \boldsymbol{\Omega}^*\mathcal{A} \quad (3.36)$$

If the spin tensor $\boldsymbol{\Omega}^*$ is given in an arbitrary way, the corotational rate $\overset{\circ}{\mathcal{A}}$ need not be objective, i.e. whether or not a corotational rate is objective depends on its defining spin tensor. For instance, let $\boldsymbol{\Omega}^* = c\boldsymbol{\omega}$ with c a real constant. Then it defines an infinitely many corotational rates of \mathcal{A} when c runs over the reals. Of them, only the one with $c = 1$, i.e. the well-known Zaremba-Jaumann rate, is objective. The well known Green-Naghdi rate is also obtained from (3.36) when the spin tensor $\boldsymbol{\Omega}^* = \dot{\mathbf{R}}\mathbf{R}^T$ (with $\hat{\mathbf{Q}}(t) = \mathbf{R}^T$) is used. However different objective rates yields approximately the same result under small shear strain condition (ABAQUS/Standard, 2008; Naghdabadi et al.,

2005).

3.3 Balance equations

This section contains the differential equations which describe the local balance equations such as balance of mass, balance of linear and angular momentum as well as the first law of thermodynamics. These equations represent the fundamental relations of continuum mechanics.

Balance of mass

We consider only processes in which the mass of a system is conserved. This means that the change of mass has to be zero ($\dot{m} = 0$). Hence an infinitesimal mass element in initial and current configuration has to be equal which leads with $dm(\mathbf{X}) = \rho_0 dV$ and $dm(\mathbf{x}) = \rho dv$ to

$$\rho dv = \rho_0 dV \quad (3.37)$$

Here ρ_0 and ρ are the densities in initial and current configuration, respectively. With (3.4), the volume elements dV and dv can be transformed leading to the Lagrangian description of the mass balance

$$\rho_0 = J\rho \quad (3.38)$$

Balance of linear and angular momentum

The linear momentum or the translational momentum, for the continuous case, is given in the current and initial configuration with (3.37) by

$$\mathbf{L} = \int_{\varphi(B)} \rho \mathbf{v} dv = \int_B \rho_0 \mathbf{v} dV \quad (3.39)$$

The balance of linear momentum can be then expressed by

$$\dot{\mathbf{L}} = \int_{\varphi(B)} \rho \bar{\mathbf{b}} dv + \int_{\varphi(\partial B)} \mathbf{t} da \quad (3.40)$$

where $\rho \bar{\mathbf{b}}$ defines the volume force (e.g. gravitational force) and \mathbf{t} is the stress vector acting on the surface of the body. With Cauchy's theorem which relates the stress vector \mathbf{t} to the surface normal \mathbf{n} via the linear mapping

$$\mathbf{t} = \boldsymbol{\sigma} \mathbf{n} \quad (3.41)$$

the stress vector can be expressed in terms of Cauchy stress tensor $\boldsymbol{\sigma}$. Using now the divergence theorem, the local balance equation of linear momentum is derived from (3.40). With reference to the current configuration $\varphi(B)$ relation

$$\operatorname{div}\boldsymbol{\sigma} + \rho\bar{\mathbf{b}} = \rho\dot{\mathbf{v}} \quad (3.42)$$

is obtained. Following a similar approach, The balance of angular momentum demands the symmetry of the Cauchy stress tensor

$$\boldsymbol{\sigma} = \boldsymbol{\sigma}^T \quad (3.43)$$

First law of thermodynamics

Another balance law which postulates the conservation of energy in a thermodynamical process is the first law of thermodynamics. It reads: The change in time (material time derivative) of the total energy E is equal to the sum of the mechanical power P of all external loads plus the heat supply Q

$$\dot{E} = P + Q \quad (3.44)$$

The mechanical power due to volume and surface loads is given by

$$P = \int_{\varphi(B)} \rho\bar{\mathbf{b}} \cdot \mathbf{v} dv + \int_{\varphi(\partial B)} \mathbf{t} \cdot \mathbf{v} da \quad (3.45)$$

The heat supply

$$Q = - \int_{\varphi(\partial B)} \mathbf{q} \cdot \mathbf{n} da + \int_{\varphi(B)} \rho r dv \quad (3.46)$$

consists of a conduction through the surface of the body which is described by the heat flux vector \mathbf{q} and the surface normal \mathbf{n} and a distributed inner heat source r (specific heat supply).

The total energy is composed of the kinetic energy

$$K = \int_{\varphi(B)} \frac{1}{2} \rho \mathbf{v} \cdot \mathbf{v} dv \quad (3.47)$$

and the internal energy

$$U = \int_{\varphi(B)} \rho u dv \quad (3.48)$$

where u is the specific internal energy. Inserting relations (3.45)-(3.48) into equation (3.44) yields, after several manipulations, the local form of the first law of thermodynamics

$$\rho \dot{u} = \boldsymbol{\sigma} : \mathbf{d} + \rho r - \operatorname{div}\mathbf{q} \quad (3.49)$$

where the term $\boldsymbol{\sigma} : \mathbf{d}$ is called specific stress power.

In the framework of constitutive theory, the free Helmholtz energy ψ is often introduced by the relation

$$\psi = u - \eta T \quad (3.50)$$

Here η denotes the entropy of the system and T is the absolute temperature. With this definition, the first law of thermodynamics can be recast as

$$\rho \dot{\psi} = \boldsymbol{\sigma} : \mathbf{d} + \rho r - \operatorname{div} \mathbf{q} - \dot{\eta} T - \eta \dot{T} \quad (3.51)$$

Introduction of different stress tensors

Equations (3.42) and (3.43) are referred to the current configuration. Often it is desirable to relate all quantities to the initial configuration B . For this purpose, further stress tensors have to be introduced. Since a given stress vector does not change when referred to the current or initial configuration, the following transformation can be performed using Nansons formula (3.3) for surface elements

$$\int_{\partial\varphi(B)} \boldsymbol{\sigma} \mathbf{n} da = \int_{\partial B} \boldsymbol{\sigma} J \mathbf{F}^{-T} \mathbf{N} dA = \int_{\partial B} \mathbf{P} \mathbf{N} dA \quad (3.52)$$

which defines the first Piola-Kirchhoff stress tensor \mathbf{P} as

$$\mathbf{P} = J \boldsymbol{\sigma} \mathbf{F}^{-T} \quad (3.53)$$

The spatial stress tensor $\boldsymbol{\sigma}$ in (3.53) is multiplied only from one side by \mathbf{F} , hence the tensor \mathbf{P} is a two field tensor with one basis referred to the current and the other to the initial configuration.

Naturally, it is simpler to work in the initial configuration with symmetrical stress tensors. The second Piola-Kirchhoff stress was introduced through a complete transformation of the Cauchy stress to the initial configuration

$$\mathbf{S} = \mathbf{F}^{-1} \mathbf{P} = J \mathbf{F}^{-1} \boldsymbol{\sigma} \mathbf{F}^{-T} \quad (3.54)$$

\mathbf{S} does not represent a stress which can be interpreted physically. Hence it is a pure mathematical quantity which however plays a prominent role in constitutive theory (Wriggers, 2008), since \mathbf{S} is work conjugated to the Green-Lagrange strain tensor (3.9). Besides the Cauchy stress tensor $\boldsymbol{\sigma}$, often the so-called Kirchhoff stress tensor $\boldsymbol{\tau}$ is introduced which results from a push forward of the second Piola-Kirchhoff stress tensor \mathbf{S} to the current configuration

$$\boldsymbol{\tau} = \mathbf{F} \mathbf{S} \mathbf{F}^T, \quad \boldsymbol{\tau} = J \boldsymbol{\sigma} \quad (3.55)$$

Balance equations with respect to initial configuration

With the first Piola-Kirchhoff stress, the local balance of linear momentum (3.42) can be recast with respect to the initial configuration as

$$\text{Div} \mathbf{P} + \rho_0 \bar{\mathbf{b}} = \rho_0 \dot{\mathbf{v}} \quad (3.56)$$

where Div denotes the divergence operation with respect to the initial configuration. Furthermore, the use of (3.53) in the balance of angular momentum (3.43) yields

$$\mathbf{P} \mathbf{F}^T = \mathbf{F} \mathbf{P}^T \quad (3.57)$$

From this it is clear that the first Piola-Kirchhoff stress tensor is nonsymmetric. Using (3.54), the balance of angular momentum yields the symmetry of the second Piola-Kirchhoff stress tensor: $\mathbf{S} = \mathbf{S}^T$.

Transformation of the first law of thermodynamics (3.49) to the initial configuration is obtained with the transformation of the stress power using (3.29)

$$J \boldsymbol{\sigma} : \mathbf{d} = \boldsymbol{\tau} : \mathbf{d} = (\mathbf{F} \mathbf{S} \mathbf{F}^T) : (\mathbf{F}^{-T} \dot{\mathbf{E}} \mathbf{F}^{-1}) = \mathbf{S} : \dot{\mathbf{E}} \quad (3.58)$$

and (3.37) as

$$\rho_0 \dot{u} = \mathbf{S} : \dot{\mathbf{E}} - \text{Div} \mathbf{Q} + \rho_0 r_0 \quad (3.59)$$

Here the heat source r_0 and the heat flux vector \mathbf{Q} are referred to the initial configuration.

Time derivatives of stress tensors

The time derivative of stress tensors is of significance for the statement of incremental forms of constitutive equations. For stresses which are referred to the initial configuration (e.g. the second Piola-Kirchhoff stress tensor \mathbf{S}), the derivative with respect to time is given by the material time derivative

$$\dot{\mathbf{S}} = \frac{\partial \mathbf{S}}{\partial t} \quad (3.60)$$

Time derivatives for stress tensors like the Cauchy stress tensor $\boldsymbol{\sigma}$ which are related to the current configuration are computed according to (3.24)

$$\dot{\boldsymbol{\sigma}} = \frac{\partial \boldsymbol{\sigma}}{\partial t} + \text{grad} \boldsymbol{\sigma} \mathbf{v} \quad (3.61)$$

It can easily be shown that the material time derivative of the Cauchy stress tensor is not objective, but objectivity is an inevitable prerequisite for the formulation of constitutive equations. Hence numerous time derivatives were formulated - so-called objective time derivatives - which can be applied to compute stress rates. The Lie derivative of a stress

tensor provides an objective stress rate and is given for the Kirchhoff stress tensor using (3.30) as

$$\mathcal{L}_v \boldsymbol{\tau} = \mathbf{F} \left\{ \frac{\partial}{\partial t} [\mathbf{F}^{-1} \boldsymbol{\tau} \mathbf{F}^{-T}] \right\} \mathbf{F}^T \quad (3.62)$$

With $\dot{\mathbf{F}}^{-1} = -\mathbf{F}^{-1} \dot{\mathbf{F}} \mathbf{F}^{-1}$ and some algebraic manipulations,

$$\mathcal{L}_v \boldsymbol{\tau} = \dot{\boldsymbol{\tau}} - \mathbf{l} \boldsymbol{\tau} - \boldsymbol{\tau} \mathbf{l}^T \quad (3.63)$$

can be derived using (3.26). The term $\mathcal{L}_v \boldsymbol{\tau}$ is also called Oldroyd stress rate. It is equivalent to the Lie derivative of the Kirchhoff stress tensor. We observe that the Lie derivative of $\boldsymbol{\tau}$ is obtained as push forward of the material time derivative of the second Piola- Kirchhoff stress if (3.55) is employed in (3.62)

$$\mathcal{L}_v \boldsymbol{\tau} = \mathbf{F} \dot{\mathbf{S}} \mathbf{F}^T \quad (3.64)$$

Another objective stress rate called the Jaumann stress rate is applied in many formulations of elasto-plastic material behavior at finite strains. This rate is defined by

$$\overset{\Delta}{\boldsymbol{\tau}} = \dot{\boldsymbol{\tau}} - \boldsymbol{w} \boldsymbol{\tau} + \boldsymbol{\tau} \boldsymbol{w} \quad (3.65)$$

Since $\mathbf{l} = \mathbf{d} + \boldsymbol{w}$ is valid, the Lie derivative of $\boldsymbol{\tau}$ can be written with (3.63) as

$$\mathcal{L}_v \boldsymbol{\tau} = \overset{\Delta}{\boldsymbol{\tau}} - \mathbf{d} \boldsymbol{\tau} - \boldsymbol{\tau} \mathbf{d} \quad (3.66)$$

This relates the Jaumann stress rate to the Lie derivative (3.62).

By the exchange of the deformation gradient \mathbf{F} by the rotation tensor for the polar decomposition \mathbf{R} in the Lie derivatives above, further objective stress rates can be defined. An example is given by

$$\mathcal{L}_v^R(\boldsymbol{\tau}) = \dot{\boldsymbol{\tau}} - \boldsymbol{\Omega} \boldsymbol{\tau} + \boldsymbol{\tau} \boldsymbol{\Omega}, \quad \boldsymbol{\Omega} = \dot{\mathbf{R}} \mathbf{R}^T \quad (3.67)$$

This stress rate is called Green-Naghdi stress rate.

3.4 Constitutive equations

The kinematical relations and balance laws derived so far are not sufficient to solve a boundary or initial value problem in continuum mechanics. For a complete set of equations, a constitutive equation has to be formulated which characterizes the material response of a solid body.

The constitutive theory describes either the microscopic or the macroscopic behavior of a material. For most materials like steel or concrete which are used in technical applications, a macroscopic description is sufficient. In that case the functional dependence

of stresses or heat flux with respect to the motion or temperature has to be considered. Since real materials can exhibit very complex behavior, approximations have to be applied within the derivation process of constitutive equations. These, however, have to be extensive enough to cover all effects observed in experimental investigations. Furthermore, basic principles from mechanics have to be obeyed to obtain theoretically sound constitutive equations. These principles, which are listed in the following, can contribute on their part to a simplification of the constitutive equations (Wriggers, 2008).

Using the *principle of determinism*, a decision will be made with regard to independent and dependent variables which occur in the constitutive equations. Classically motion and temperature are chosen as unknowns. The *principle of equipresence* demands the same set of variables for all constitutive equations. By the *principle of local action*, the material functions are restricted to a pointwise dependence on the deformation gradient, the temperature and its gradient. Finally, the invariance or *objectivity* of constitutive equations with respect to rigid body motions is postulated.

Another essential restriction for constitutive equations is provided by the *second law of thermodynamics*. The second law of thermodynamics postulates that heat cannot flow itself from a system with low temperature to a system with a higher temperature. Another physical observation is that a substance with equally distributed temperature which is free of heat sources can only receive mechanical energy but not release it. These observations lead to two inequalities which contain mathematical statements regarding the local entropy production and the entropy production as a result of heat conduction. An essential postulate states that for closed systems the entropy always increases ($d\eta > 0$) within an irreversible process. With this the direction of process has to be considered. Since only the weaker form of the second law of thermodynamics is needed, one inequality is sufficient. By introducing the absolute temperature T ($T > 0$), the entropy production is given by

$$\Gamma = \frac{d}{dt} \int_{\varphi(B)} \rho \eta dv - \int_{\varphi(B)} \frac{\rho r}{T} dv + \int_{\varphi(\partial B)} \frac{1}{T} \mathbf{q} \cdot \mathbf{n} da \quad (3.68)$$

The postulate that $\Gamma \geq 0$, leads by addition of the energy balance (3.49) to the second law of thermodynamics

$$\rho \dot{\eta} \geq \frac{\rho r}{T} - \operatorname{div} \left(\frac{\mathbf{q}}{T} \right) \quad (3.69)$$

With the introduction of the free Helmholtz energy (3.50), $\psi = u - T\eta$, the so-called reduced form of the second law of thermodynamics can be defined by using (3.49)

$$\rho(\eta \dot{T} + \dot{\psi}) - \boldsymbol{\sigma} : \mathbf{d} - \frac{1}{T} \mathbf{q} \cdot \operatorname{grad} T \leq 0 \quad (3.70)$$

The free Helmholtz energy ψ denotes the part of inner energy which performs work at constant temperature (Wriggers, 2008).

With inequalities (3.69) and (3.70), the irreversibility of processes can be described

in which mechanical energy is transformed to heat energy (e.g. in case of friction or inelastic deformations). The material form of (3.69) is derived in the same way as the first law of thermodynamics, leading to

$$\rho_0 \dot{\eta} \geq \frac{\rho_0 r_0}{T} - \operatorname{div}\left(\frac{\mathbf{Q}}{T}\right) \quad (3.71)$$

Some special cases of thermodynamical processes can now be stated: (1) supply of heat energy is excluded as well in the interior as over the surface of the body ($r_0 = 0, \mathbf{Q} = \mathbf{0}$); such process is called *adiabatic*. (2) A process in which the temperature in the body is kept constant ($T = \text{const.}$) is known as *isothermal* process.

Constitutive model development – for shape memory alloys – is the subject of the next two chapters where we present the details of model derivation.

3.5 Weak form of equilibrium.

For the analysis of nonlinear initial boundary value problems in continuum mechanics, a coupled system of partial differential equations has to be solved which consist of kinematical relations, local balance of momentum and the constitutive equations. An analytical solution of systems of nonlinear partial differential equations is only possible for a selected number of simple initial boundary value problems. Hence approximate methods like the method of finite differences or finite elements have to be applied to solve this set of equations. The use of the finite element method, which is based on a variational formulation of the equations expands the solution range to a broad spectrum of applications. The necessary variational formulation will be described in the following sections based on a referential and spatial description (Wriggers, 2008).

Several approaches can be applied to derive the variational formulation. In the engineering literature, the principle of virtual work is often basis for the derivation of the finite element approximations. It can, however, easily be shown that this formulation is equivalent to using the weak form. In the following section, several variational formulations are derived which can be applied in the context of finite elements.

3.5.1 Weak form of linear momentum in the initial configuration

When an approximation \mathbf{u}_h of the exact solution \mathbf{u} is inserted in the equations, then an error will occur since the approximate solution is usually not equal to the exact solution. Hence the insertion of the approximate solution into the momentum balance equation

$\text{Div}\mathbf{P} + \rho_0\bar{\mathbf{b}} - \rho_0\dot{\mathbf{v}}$ will lead to

$$\text{Div}\mathbf{P}(\mathbf{u}_h) + \rho_0\bar{\mathbf{b}} - \rho_0\dot{\mathbf{v}}_h = \mathbf{R} \quad (3.72)$$

The residual \mathbf{R} , which denotes the error not fulfilling the momentum balance equation by \mathbf{u}_h , will now be reduced to zero in a weak sense by multiplying the residual by a weighting function $\boldsymbol{\eta}$ and by integrating the residual over the whole domain. The vector-valued function $\boldsymbol{\eta} = \{\boldsymbol{\eta} | \boldsymbol{\eta} = \mathbf{0} \text{ on } \partial B_u\}$ is often called virtual displacement or test function. This procedure leads to

$$\int_B \text{Div}\mathbf{P}(\mathbf{u}_h) \cdot \boldsymbol{\eta} dV + \int_B \rho_0(\bar{\mathbf{b}} - \dot{\mathbf{v}}_h) \cdot \boldsymbol{\eta} dV = 0 \quad (3.73)$$

which of course also has to hold for exact solution \mathbf{u}

$$\int_B \text{Div}\mathbf{P}(\mathbf{u}) \cdot \boldsymbol{\eta} dV + \int_B \rho_0(\bar{\mathbf{b}} - \dot{\mathbf{v}}) \cdot \boldsymbol{\eta} dV = 0 \quad (3.74)$$

The weak form is also known as principle of virtual work in engineering. Since no further assumptions, like existence of a potential are made, the weak form is applicable to general problems such as inelastic materials, friction, non-conservative loading, etc. By partial integration of the first term in (3.74), application of the divergence theorem and introduction of the traction boundary condition, the weak form of linear momentum

$$G(\varphi, \boldsymbol{\eta}) = \int_B \mathbf{P} : \text{Grad}\boldsymbol{\eta} dV - \int_B \rho_0(\bar{\mathbf{b}} - \dot{\mathbf{v}}) \cdot \boldsymbol{\eta} dV - \int_{\partial B_\sigma} \bar{\mathbf{t}} \cdot \boldsymbol{\eta} dA = 0 \quad (3.75)$$

is obtained. The gradient of the test function $\boldsymbol{\eta}$ can also be interpreted as the directional derivative of the deformation gradient $D\mathbf{F} \cdot \boldsymbol{\eta}$ also known as variation $\delta\mathbf{F}$ of the deformation gradient. In the weak form (3.75), the first Piola-Kirchhoff stress tensor can be replaced through $\mathbf{P} = \mathbf{F}\mathbf{S}$ by the second Piola-Kirchhoff stress tensor leading to

$$\mathbf{P} : \text{Grad}\boldsymbol{\eta} = \mathbf{S} : \mathbf{F}^T \text{Grad}\boldsymbol{\eta} = \mathbf{S} : \frac{1}{2} (\mathbf{F}^T \text{Grad}\boldsymbol{\eta} + \text{Grad}^T \boldsymbol{\eta} \mathbf{F}) = \mathbf{S} : \delta\mathbf{E} \quad (3.76)$$

where the fact has been used that the scalar product of a symmetrical tensor (here \mathbf{S}) with an antisymmetric part of a tensor is zero. $\delta\mathbf{E}$ denotes the variation of the Green-Lagrange strain tensor which is obtained via the directional derivative (Wriggers, 2008)

$$\begin{aligned} D\mathbf{E} \cdot \boldsymbol{\eta} &= \frac{d}{d\alpha} \frac{1}{2} [\mathbf{F}^T(\boldsymbol{\varphi} + \alpha\boldsymbol{\eta})\mathbf{F}(\boldsymbol{\varphi} + \alpha\boldsymbol{\eta}) - \mathbf{1}] |_{\alpha=0} \\ &= \frac{d}{d\alpha} \frac{1}{2} [[\text{Grad}(\boldsymbol{\varphi} + \alpha\boldsymbol{\eta})]^T \text{Grad}(\boldsymbol{\varphi} + \alpha\boldsymbol{\eta}) - \mathbf{1}] |_{\alpha=0} \\ &= \frac{1}{2} [(\text{Grad}\boldsymbol{\eta})^T \mathbf{F} + \mathbf{F}^T (\text{Grad}\boldsymbol{\eta})] = \delta\mathbf{E} \end{aligned} \quad (3.77)$$

Using (3.76), equation (3.75) can be rewritten as

$$G(\varphi, \boldsymbol{\eta}) = \int_B \mathbf{S} : \delta\mathbf{E} dV - \int_B \rho_0(\bar{\mathbf{b}} - \dot{\mathbf{v}}) \cdot \boldsymbol{\eta} dV - \int_{\partial B_\sigma} \bar{\mathbf{t}} \cdot \boldsymbol{\eta} dA = 0 \quad (3.78)$$

The first term in (3.78) denotes the internal virtual work, also called stress divergence term.

3.5.2 Weak form of linear momentum in the current configuration

The transformation of the weak form (3.75) to the current or spatial configuration is performed by kinematical operations in which the base vectors are push forward to the configuration $\varphi(B)$. With the transformation $\boldsymbol{\sigma} = \frac{1}{J}\mathbf{P}\mathbf{F}^T$ of the first Piola-Kirchhoff stress tensor to the Cauchy stress tensor, see (3.53), and considering (3.19) we can write equation (3.76) as

$$\mathbf{P} : \text{Grad}\boldsymbol{\eta} = J\boldsymbol{\sigma}\mathbf{F}^{-T} : \text{Grad}\boldsymbol{\eta} = J\boldsymbol{\sigma} : \text{Grad}\boldsymbol{\eta}\mathbf{F}^{-1} = J\boldsymbol{\sigma} : \text{grad}\boldsymbol{\eta} \quad (3.79)$$

Furthermore, from (3.4) $dv = JdV$ follows which is equivalent to $\rho = \rho_0 J$. With these relations, the weak form (3.75) can be written in terms of the current configuration

$$g(\boldsymbol{\varphi}, \boldsymbol{\eta}) = \int_{\varphi(B)} \boldsymbol{\sigma} : \text{grad}\boldsymbol{\eta} dv - \int_{\varphi(B)} \rho(\bar{\mathbf{b}} - \dot{\mathbf{v}}) \cdot \boldsymbol{\eta} dv - \int_{\varphi(\partial B_\sigma)} \mathbf{t} \cdot \boldsymbol{\eta} da = 0 \quad (3.80)$$

In this relations, equation (3.52) has been used to transform the traction vector $\bar{\mathbf{t}}$ to $\varphi(B)$. The symmetry of the Cauchy stress tensor facilitates the replacement of the spatial gradient of the test function $\boldsymbol{\eta}$ by its symmetric part. Hence with the definition

$$\nabla^S \boldsymbol{\eta} = \frac{1}{2}(\text{grad}\boldsymbol{\eta} + \text{grad}^T \boldsymbol{\eta}) \quad (3.81)$$

the weak form follows with respect to the spatial configuration

$$g(\boldsymbol{\varphi}, \boldsymbol{\eta}) = \int_{\varphi(B)} \boldsymbol{\sigma} : \nabla^S \boldsymbol{\eta} dv - \int_{\varphi(B)} \rho(\bar{\mathbf{b}} - \dot{\mathbf{v}}) \cdot \boldsymbol{\eta} dv - \int_{\varphi(\partial B_\sigma)} \hat{\mathbf{t}} \cdot \boldsymbol{\eta} da = 0 \quad (3.82)$$

This relation is, in a formal sense, equivalent to the principle of virtual work of the geometrically linear theory. But here the integral, the stress and virtual strain measures have to be evaluated with respect to the current configuration. Due to this, the nonlinearities do appear, however hidden (Wriggers, 2008).

3.6 Linearizations

Nonlinearities appear in continuum mechanics due to different phenomena. In this respect, geometrical nonlinearities can be mentioned which occur due to the nonlinear strain measures such as the Green-Lagrange strain tensor. Physical nonlinearities stem from nonlinear constitutive behavior like elasto-plastic or visco-plastic response. Further, nonlinearities are related to one-sided or unilateral geometrical constraints as appear in contact problems. These lead to variational inequalities and hence include nonlinear effects.

Linearizations of the associated models have to be derived for several reasons when the

initial or boundary values are solved. At one hand, the linearization process can be applied to derive approximate theories which can still be solved analytically. This is, e.g. the case for the theory of linear elasticity or for first and second order beam, plate and shell theories. On the other hand, linearizations are needed within the algorithmic treatment of the solution process for the nonlinear boundary value problems. This is, e.g. the case for finite element methods where Newton-Raphson algorithms are employed to solve the nonlinear algebraic equation systems.

The directional derivative of the function f at $\bar{\mathbf{x}}$ in the direction of the vector \mathbf{u} is defined by (Bonet and Wood, 2008)

$$\frac{d}{d\alpha}[f(\bar{\mathbf{x}} + \alpha\mathbf{u})]|_{\alpha=0} \quad (3.83)$$

where α is a scalar parameter. Due to the fact that $\bar{\mathbf{x}} + \alpha\mathbf{u}$ describes a straight line in \mathcal{R}^3 , the directional derivative measures the increment of the function f in the direction of this straight line at point $\bar{\mathbf{x}}$. The directional derivative can be computed using the chain rule

$$\frac{d}{d\alpha}[f(\bar{\mathbf{x}} + \alpha\mathbf{u})]|_{\alpha=0} = \left[\frac{\partial f(\bar{\mathbf{x}} + \alpha\mathbf{u})}{\partial \mathbf{x}} \cdot \frac{\partial(\bar{\mathbf{x}} + \alpha\mathbf{u})}{\partial \alpha} \right] |_{\alpha=0} = \frac{\partial f(\mathbf{x})}{\partial \mathbf{x}} \cdot \mathbf{u} \quad (3.84)$$

A comparison of the coefficients yields the result

$$\frac{d}{d\alpha}[f(\bar{\mathbf{x}} + \alpha\mathbf{u})]|_{\alpha=0} = \bar{D}f \cdot \mathbf{u} = \bar{D}f[\mathbf{u}] \quad (3.85)$$

The directional derivative can be generalized for functional spaces in a formal way to obtain the linear part of the mapping \mathbf{G} at $\bar{\mathbf{x}}$:

$$\mathbf{L}[\mathbf{G}]_{x=\bar{x}} = \bar{\mathbf{G}} + \bar{D}\mathbf{G} \cdot \mathbf{u} \quad (3.86)$$

To simplify notation the directional derivative is written instead of $\bar{D}\mathbf{G} \cdot \mathbf{u}$ in the following in the short form $\Delta\bar{\mathbf{G}}$. Here the bar denotes evaluation at $\bar{\mathbf{x}}$.

3.6.1 Linearization of kinematical quantities

The linearization of different kinematical relations is derived in this section (Bonet and Wood, 2008).

Linearized deformation gradient

Consider a small displacement $\mathbf{u}(\mathbf{x})$ from the current configuration $\mathbf{x} = \varphi_t(\mathbf{X}) = \varphi(\mathbf{X}, t)$ as shown in Figure 3.1. The deformation gradient \mathbf{F} can be linearized in the direction

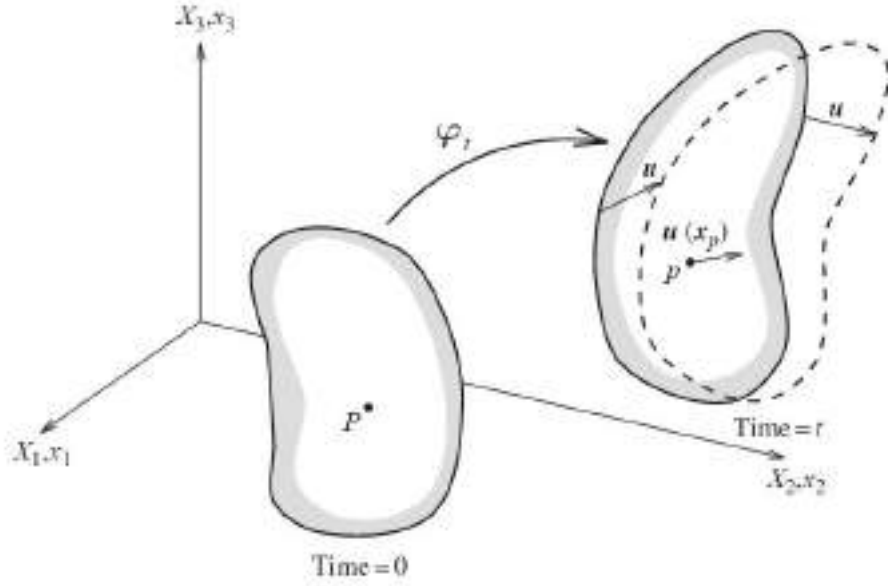


Figure 3.1: Linearized kinematics.

of \mathbf{u} at this position as

$$\begin{aligned}
 D\mathbf{F} \cdot \mathbf{u} &= \frac{d}{d\alpha} [\mathbf{F}(\mathbf{x} + \alpha\mathbf{u})] |_{\alpha=0} \\
 &= \frac{d}{d\alpha} |_{\alpha=0} \frac{\partial(\mathbf{x} + \alpha\mathbf{u})}{\partial\mathbf{X}} \\
 &= \frac{d}{d\alpha} |_{\alpha=0} \left(\frac{\partial\mathbf{x}}{\partial\mathbf{X}} + \alpha \frac{\partial\mathbf{u}}{\partial\mathbf{X}} \right) \\
 &= \frac{\partial\mathbf{u}}{\partial\mathbf{X}} = \text{Grad}\mathbf{u} \\
 &= (\text{grad}\mathbf{u})\mathbf{F} = (\nabla\mathbf{u})\mathbf{F}
 \end{aligned} \tag{3.87}$$

Linearized strain

Using Equation (3.87) and the product rule, the Green-Lagrange strain can be linearized at the current configuration in the direction \mathbf{u} as

$$\begin{aligned}
 D\mathbf{E}[\mathbf{u}] &= \frac{1}{2} (\mathbf{F}^T D\mathbf{F}[\mathbf{u}] + D\mathbf{F}^T[\mathbf{u}]\mathbf{F}) \\
 &= \frac{1}{2} [\mathbf{F}^T \nabla\mathbf{u}\mathbf{F} + \mathbf{F}^T (\nabla\mathbf{u})^T \mathbf{F}] \\
 &= \frac{1}{2} \mathbf{F}^T [\nabla\mathbf{u} + (\nabla\mathbf{u}^T)] \mathbf{F}
 \end{aligned} \tag{3.88}$$

Note that half the tensor inside [] is the small strain tensor $\boldsymbol{\varepsilon}$, and, therefore, $D\mathbf{E}[\mathbf{u}]$ can be interpreted as the pull back of the small strain tensor $\boldsymbol{\varepsilon}$ as

$$D\mathbf{E}[\mathbf{u}] = \mathbf{F}^T \boldsymbol{\varepsilon} \mathbf{F} \tag{3.89}$$

In particular, if the linearization of \mathbf{E} is performed at the initial material configuration, that is, when $\mathbf{x} = \mathbf{X}$ and therefore $\mathbf{F} = \mathbf{I}$, then

$$D\mathbf{E}_0[\mathbf{u}] = \boldsymbol{\varepsilon} \quad (3.90)$$

Similarly, the right and left Cauchy-Green deformation tensors, the inverse Cauchy-Green tensor and Jacobi determinant can be linearized to give, respectively

$$DC[\mathbf{u}] = 2\mathbf{F}^T \boldsymbol{\varepsilon} \mathbf{F} \quad (3.91)$$

$$D\mathbf{b}[\mathbf{u}] = (\nabla \mathbf{u})\mathbf{b} + \mathbf{b}(\nabla \mathbf{u})^T \quad (3.92)$$

$$DC^{-1}[\mathbf{u}] = -2\mathbf{F}^{-1} \boldsymbol{\varepsilon} \mathbf{F}^{-T} \quad (3.93)$$

$$DJ[\mathbf{u}] = J \operatorname{div} \mathbf{u} = J \operatorname{tr} \boldsymbol{\varepsilon} \quad (3.94)$$

Linearization of Almansi strain tensor

The linearization of spatial vectors and tensors is derived by a pull back of the spatial objects to the initial configuration. In this configuration, the linearization is performed and the linearized object then is push forward to the spatial configuration. This procedure can now be applied to linearize the Almansi strain tensor. With the pull back of the strain tensor, the linearization

$$D\mathbf{e}[\mathbf{u}] = \mathbf{F}^{-T} \{D\mathbf{E}[\mathbf{u}]\} \mathbf{F}^{-1} = \boldsymbol{\varepsilon} \quad (3.95)$$

is obtained.

3.6.2 Linearization of constitutive equations

The linearization of constitutive equations can be determined for elastic materials simply by linearizing the equations. For inelastic constitutive equations, the linearization for the continuous case can be derived; however in the framework of the finite element method a time integration has to be applied to evaluate the differential evolution equations describing such materials. Due to that, the linearization depends also upon the integration algorithm. Hence these linearizations cannot be derived without the knowledge of the integration algorithms. For a more general overview see e.g. Simo and Hughes (1998).

The elastic constitutive equation describes the dependence of the 2nd Piola-Kirchhoff stress tensor on the right Cauchy-Green tensor. The linearization of this constitutive relation gives

$$\mathbf{L}[\mathbf{S}] = \bar{\mathbf{S}} + \bar{D}\mathbf{S}[\mathbf{u}] = \bar{\mathbf{S}} + \Delta \bar{\mathbf{S}} \quad (3.96)$$

However, linearization of the constitutive equation yields:

$$\Delta \bar{\mathbf{S}} = \mathbb{D}[\Delta \bar{\mathbf{E}}] = \mathbb{D} : \Delta \bar{\mathbf{E}} \quad (3.97)$$

where \mathbb{D} is a fourth order tensor. This relation has the same structure as the incremental constitutive equation. The only difference is that the time derivatives have to be exchanged by the directional derivatives.

The transformation of (3.97) to the current configuration can be formulated with the Lie-derivative of the Kirchhoff stress tensor (3.64). This derivative is given in index notation as

$$(\mathcal{L}_v \boldsymbol{\tau})_{ij} = F_{iI} \dot{S}_{IJ} F_{jJ} \quad (3.98)$$

With the time derivative of the right Cauchy-Green tensor, see (3.9) and (3.29),

$$\dot{C}_{KL} = 2F_{kK} d_{kl} F_{lL} \quad (3.99)$$

the final result can be expressed by

$$(\mathcal{L}_v \boldsymbol{\tau})_{ij} = F_{iI} F_{jJ} F_{kK} F_{lL} \mathbb{D}_{IJKL} d_{kl} \quad (3.100)$$

where \mathbf{d} is the rate of deformation tensor. Since each basis vector of the incremental constitutive tensor \mathbb{D} in (3.100) is transformed to the current configuration, the spatial incremental constitutive tensor \mathbb{C} can be introduced as

$$\mathbb{C}_{ijkl} = \frac{1}{J} F_{iI} F_{jJ} F_{kK} F_{lL} \mathbb{D}_{IJKL} \quad (3.101)$$

Hence equation (3.100) can be reformulated with this relation

$$\frac{1}{J} (\mathcal{L}_v \boldsymbol{\tau})_{ij} = \mathbb{C}_{ijkl} d_{kl}, \quad \frac{1}{J} \mathcal{L}_v \boldsymbol{\tau} = \mathbb{C} : \mathbf{d} \quad (3.102)$$

Often the Jaumann stress rate, defined in (3.65), is used in the literature to describe elasto-plastic material behavior. Hence the incremental constitutive equation (3.102) will be rewritten for the Jaumann stress rate. Using (3.66) the relation

$$\begin{aligned} \frac{1}{J} \overset{\Delta}{\boldsymbol{\tau}} &= \mathbb{C} : \mathbf{d} + \boldsymbol{\sigma} \mathbf{d} + \mathbf{d} \boldsymbol{\sigma} \\ \frac{1}{J} \overset{\Delta}{\tau}_{ij} &= \mathbb{C}_{ijkl} d_{kl} + \sigma_{ik} d_{kj} + d_{ik} \sigma_{kj} \end{aligned} \quad (3.103)$$

follows which can be abbreviated by placing d_{kl} outside the brackets

$$\frac{1}{J} \overset{\Delta}{\tau}_{ij} = \mathbb{C}^J_{ijkl} d_{kl} \quad \text{with} \quad \mathbb{C}^J_{ijkl} = \mathbb{C}_{ijkl} + \delta_{il} \sigma_{jk} + \delta_{ik} \sigma_{jl} \quad (3.104)$$

Equation (3.104) is from the physical point of view equivalent to (3.102).

3.6.3 Linearization of weak form

The solutions of nonlinear initial boundary value problems in solid mechanics can be obtained in general only by employing approximate solution techniques. Since many of these methods like the finite element method rely on a variational formulation of the field equations, the basis for numerical methods are provided by the weak forms of the associated field equations. A discretization of the weak form leads to a set of nonlinear algebraic equations.

For the solution of the set of nonlinear equations, many different algorithms are known. Often Newton's method is applied since it possesses the advantage of a quadratic convergence close to the solution point. In case of Newton's method, an improved solution is obtained from the Taylor series expansion of the nonlinear equation at the already computed approximate solution. This Taylor expansion corresponds in finite element applications to the linearization of the weak form, or in solid mechanics to the linearization of the principle of virtual work, and can be obtained by the directional derivative discussed above. Such linearization will be computed here. The linearization will be stated first for the weak form with respect to the initial configuration (3.75). In general, the linearization at a deformation state of the solid is computed which is in equilibrium. This state will be denoted by $\bar{\varphi}$.

The linear part of the weak form is given by

$$\mathbf{L}[G]_{\varphi=\bar{\varphi}} = G(\bar{\varphi}, \boldsymbol{\eta}) + DG(\bar{\varphi}, \boldsymbol{\eta}) \cdot \Delta \mathbf{u} \quad (3.105)$$

The operator $G(\bar{\varphi}, \boldsymbol{\eta})$ corresponds to (3.75), just the deformation $\bar{\varphi}$ is inserted instead of φ . By assuming that the load is conservative the directional derivative of G can be computed in the direction of $\Delta \mathbf{u}$ by only taking the first term in (3.75) into account

$$DG(\bar{\varphi}, \boldsymbol{\eta}) \cdot \Delta \mathbf{u} = \int_B [D\mathbf{P}(\bar{\varphi}) \cdot \Delta \mathbf{u}] \cdot \text{Grad} \boldsymbol{\eta} dV \quad (3.106)$$

hence all other terms do not depend upon the deformation. The linearization of the first Piola-Kirchhoff stress tensor yields with $\mathbf{P} = \mathbf{F}\mathbf{S}$

$$DG(\bar{\varphi}, \boldsymbol{\eta}) \cdot \Delta \mathbf{u} = \int_B \{ \text{Grad} \Delta \mathbf{u} \bar{\mathbf{S}} + \bar{\mathbf{F}} [D\mathbf{S}(\bar{\varphi}) \cdot \Delta \mathbf{u}] \} \cdot \text{Grad} \boldsymbol{\eta} dV \quad (3.107)$$

Terms with a bar have to be evaluated at the deformation state $\bar{\varphi}$. The linearization of the second Piola-Kirchhoff stress tensor can be expressed as:

$$D\mathbf{S}(\bar{\varphi}) \cdot \Delta \mathbf{u} = \mathbb{D}[\Delta \bar{\mathbf{E}}] \quad (3.108)$$

where the last term is the linearization of the Green-Lagrange strain tensor \mathbf{E} at $\bar{\varphi}$.

At the state $\bar{\varphi}$, The use of (3.108) in (3.107) completes the linearization

$$DG(\bar{\varphi}, \boldsymbol{\eta}) \cdot \Delta \mathbf{u} = \int_B \{ \text{Grad} \Delta \mathbf{u} \bar{\mathbf{S}} + \bar{\mathbf{F}} \mathbb{D}[\Delta \bar{\mathbf{E}}] \cdot \Delta \mathbf{u} \} \cdot \text{Grad} \boldsymbol{\eta} dV \quad (3.109)$$

Note that $\bar{\mathbb{D}}$ has also to be evaluated at state $\bar{\varphi}$. By applying the trace operation to the second term and by using the symmetry of $\bar{\mathbb{D}}$, a more compact form of (3.109) can be found

$$DG(\bar{\varphi}, \boldsymbol{\eta}).\Delta\mathbf{u} = \int_B \{ \text{Grad}\Delta\mathbf{u}\bar{\mathbf{S}}\text{Grad}\boldsymbol{\eta} + \delta\bar{\mathbf{E}}\bar{\mathbb{D}}[\Delta\bar{\mathbf{E}}] \} dV \quad (3.110)$$

Here the symmetry in $\boldsymbol{\eta}$ and $\Delta\mathbf{u}$ can be observed which results from the linearization operation. The first term in (3.110) is often named initial stress term since the stresses at the given state appear directly. The second term contains, besides the incremental constitutive tensor $\bar{\mathbb{D}}$, the variation of the Green-Lagrange strain tensor $\delta\bar{\mathbf{E}} = \frac{1}{2}(\bar{\mathbf{F}}^T \text{Grad}\boldsymbol{\eta} + \text{Grad}^T \boldsymbol{\eta} \bar{\mathbf{F}})$ and the increment of the Green-Lagrange strain tensor $\Delta\bar{\mathbf{E}} = \frac{1}{2}(\bar{\mathbf{F}}^T \text{Grad}\Delta\mathbf{u} + \text{Grad}^T \Delta\mathbf{u} \bar{\mathbf{F}})$.

The linearization of the principle of virtual work can be obtained in terms of the current configuration by a push forward of the linearization (3.110) to the already computed configuration $\bar{\varphi}$. Using the transformations for the linearization of the Green-Lagrange strain tensor (3.89), which resulted as push forward in $\nabla_x^S \Delta\mathbf{u}$ ($= \bar{\boldsymbol{\varepsilon}}$), it follows for the second term in (3.110)

$$\int_B \nabla_x^S \boldsymbol{\eta} \cdot \bar{\mathbb{C}}[\nabla_x^S \Delta\mathbf{u}] J dV \quad (3.111)$$

In this equations, the fourth order tensor $\bar{\mathbb{C}}$ can be computed by the transformation (3.101) from $\bar{\mathbb{D}}$.

The first term in (3.110) can be directly recast with $\bar{\boldsymbol{\tau}} = \mathbf{F}\bar{\mathbf{S}}\mathbf{F}^T$ as

$$\text{Grad}\Delta\mathbf{u}\bar{\mathbf{S}}.\text{Grad}\boldsymbol{\eta} = \text{Grad}\Delta\mathbf{u}\bar{\mathbf{F}}^{-1}\bar{\boldsymbol{\tau}}\bar{\mathbf{F}}^{-1}.\text{Grad}\boldsymbol{\eta} = (\overline{\text{grad}}\Delta\mathbf{u})\bar{\boldsymbol{\tau}}.\overline{\text{grad}}\boldsymbol{\eta} \quad (3.112)$$

This results in the linearization with respect to the known current configuration $\bar{\varphi}$ where all quantities have to be evaluated at $\bar{\varphi}$

$$Dg(\bar{\varphi}, \boldsymbol{\eta}).\Delta\mathbf{u} = \int_B \{ (\overline{\text{grad}}\Delta\mathbf{u})\bar{\boldsymbol{\tau}}.\overline{\text{grad}}\boldsymbol{\eta} + J\nabla_x^S \boldsymbol{\eta} \cdot \bar{\mathbb{C}}[\nabla_x^S \Delta\mathbf{u}] \} dV \quad (3.113)$$

The integral (3.113) can now be referred to the current configuration with the relation $d\bar{v} = \bar{J}dV$, such that

$$Dg(\bar{\varphi}, \boldsymbol{\eta}).\Delta\mathbf{u} = \int_{\bar{\varphi}(B)} \{ (\overline{\text{grad}}\Delta\mathbf{u})\bar{\boldsymbol{\sigma}} : \overline{\text{grad}}\boldsymbol{\eta} + \nabla_x^S \boldsymbol{\eta} : \bar{\mathbb{C}}[\nabla_x^S \Delta\mathbf{u}] \} d\bar{v} \quad (3.114)$$

is obtained.

The deformation state $\bar{\varphi}$ to which the formulation is referred is not known and can only be obtained within the nonlinear solution process by an update of all deformation states in a successive manner. Hence relation (3.114) is known in the literature also as updated Lagrange formulation, see e.g. Bathe (1996).

With the above given linearizations all relations needed within the Newton method are available as well as for formulations with respect to the initial configuration as with respect to the current configuration. These linearizations are basis for finite element simulations.

3.7 Finite element formulation

A finite element discretization may be constructed by dividing the body into finite elements. Accordingly, we have

$$\Omega \approx \Omega_h = \sum_e \Omega_e \quad (3.115)$$

where Ω_e is the domain of an individual element, e , and Ω_h is the domain covered by all the elements. We note that, in general, Ω_h is an approximation to the domain of the real body. With this approximation the integrals in the variational equation may be approximated as

$$\int_{\Omega} (\cdot) dv \approx \int_{\Omega_h} (\cdot) dv = \sum_e \int_{\Omega_e} (\cdot) dv \quad (3.116)$$

An approximate variational solution may be developed by writing trial solutions and test functions for the motions and virtual displacements, respectively. Adopting an isoparametric formulation, we may write for a typical element

$$\mathbf{X} = N_I(\boldsymbol{\zeta}) \mathbf{X}^I \quad I = 1, 2, \dots, nen \quad (3.117)$$

where nen is the number of nodes defining an element, I are node labels for the element, $N_I(\boldsymbol{\zeta})$ are shape functions for node I which maintain suitable continuity between contiguous elements and \mathbf{X}^I are the coordinates for node I . Similarly, we may write approximations for the current configuration as

$$\mathbf{x} = N_I(\boldsymbol{\zeta}) \mathbf{x}^I \quad I = 1, 2, \dots, nen \quad (3.118)$$

the displacements as

$$\mathbf{u} = N_I(\boldsymbol{\zeta}) \mathbf{u}^I \quad I = 1, 2, \dots, nen \quad (3.119)$$

the incremental displacements as

$$\Delta \mathbf{u} = N_I(\boldsymbol{\zeta}) \Delta \mathbf{u}^I \quad I = 1, 2, \dots, nen \quad (3.120)$$

and the virtual displacements as

$$\boldsymbol{\eta} = N_I(\boldsymbol{\zeta}) \boldsymbol{\eta}^I \quad I = 1, 2, \dots, nen \quad (3.121)$$

Also, time dependence is included in the nodal parameters for the current position and displacements.

Substituting (3.117)–(3.121) into (3.82), we obtain the basic finite element formulation

$$\mathbf{f}^{int} - \mathbf{f}^{ext} = \mathbf{M} \ddot{\mathbf{u}} \quad (3.122)$$

where

$$\mathbf{f}_I^{int} = \sum_e \int_{\Omega_e} \mathbf{B}_I^T \boldsymbol{\sigma} dv \quad (3.123)$$

$$\mathbf{f}_I^{ext} = \sum_e \int_{\Omega_e} N_I \rho \bar{\mathbf{b}} dv + \sum_e \int_{\partial\Omega_e} N_I \mathbf{t} ds \quad (3.124)$$

$$\mathbf{M}_{IJ} = \sum_e \int_{\Omega_e} N_I \rho N_J dv \mathbf{1} \quad (3.125)$$

where the \mathbf{B}_I matrix describes the transformation from the virtual displacements, $\boldsymbol{\eta}^I$ to the $\delta\boldsymbol{\varepsilon}$. Solution of this set of equations together with satisfying the material constitution and the displacement boundary conditions, yields the solution to the problem. A common solution procedure is to use a Newton-type solution method and solve a sequence of linear problems. Accordingly, in a Newton-type method we write the momentum equation as

$$\mathbf{R} = \mathbf{f}^{int} - \mathbf{f}^{ext} - \mathbf{M}\ddot{\mathbf{u}} = \mathbf{0} \quad (3.126)$$

According to (3.113), a linearization of this set of equations gives

$$\mathbf{M}\Delta\ddot{\mathbf{u}} + \mathbf{K}_t\Delta\mathbf{u} = \mathbf{R} \quad (3.127)$$

where

$$\mathbf{K}_t = \mathbf{K}^g + \mathbf{K}^m \quad (3.128)$$

and the geometric stiffness matrix \mathbf{K}^g and material tangent matrix \mathbf{K}^m are computed by (3.114) as:

$$(\mathbf{K}^g)_{IJ} = \sum_e \int_{\Omega_e} \text{tr}(\nabla N_I^T [\boldsymbol{\sigma}] \nabla N_J) dv \mathbf{1} \quad (3.129)$$

$$(\mathbf{K}^m)_{IJ} = \sum_e \int_{\Omega_e} \mathbf{B}_I^T [\mathbf{C}] \mathbf{B}_J dv \quad (3.130)$$

where we have used $[\cdot]$ to denote the matrix form of a tensorial quantity.

The crucial step in the outline given above which remains to be addressed concerns the computation of the stress field $\boldsymbol{\sigma}$ within a typical element. However, the element internal force vector given by (3.123) is evaluated by numerical quadrature formula, i.e:

$$\mathbf{f}_e^{int} = \sum_{l=1}^{n_{int}} \mathbf{B}_e^T \boldsymbol{\sigma}(\mathbf{x}, t)|_{\mathbf{x}=\mathbf{x}_e^l} w^l dv_e \quad (3.131)$$

where $\mathbf{x}_e^l \in \Omega_e$ denotes a quadrature point, w^l is the corresponding weight, and n_{int} is the number of quadrature points for element Ω_e .

The important conclusion to be extracted from expression (3.131) is that the stress within an element Ω_e is required only at discrete points; typically the quadrature points \mathbf{x}_e^l of the element (Simo and Hughes, 1998).

We highlight that, according to the above fact, we will restrict our numerical discussions, in the following chapters, to computation of the stress and tangent matrix at a point level (Gauss point).

Chapter 4

Constitutive modeling: small deformation regime

4.1 Introduction

Depending on the amount of strain, or local deformation, the analysis of deformation is subdivided into three deformation theories:

Finite strain theory, also called large strain theory deals with deformations in which both rotations and strains are arbitrarily large. In this case, the undeformed and deformed configurations of the continuum are significantly different and a clear distinction has to be made between them.

Infinitesimal strain theory, also called small strain theory or small deformation theory where strains and rotations are both small. In this case, the undeformed and deformed configurations of the body can be assumed identical.

Large-rotation theory, which assumes small strains but large rotations and displacements.

In each of these theories the strain is then defined differently. The engineering strain is the most common definition applied to materials used in mechanical and structural engineering, which are subjected to very small deformations. On the other hand, for some materials, e.g. elastomers and polymers, subjected to large deformations, the engineering definition of strain is not applicable, thus other more complex definitions of strain are required. In this chapter we review some three-dimensional SMA constitutive models within the infinitesimal theory framework. Focusing only on primary effects, we recast all models in a simple form, called *basic model*. Afterward, we develop a class of constitutive models and show that it includes some models available in the literature. We focus on a specific member of the proposed class and comparing with the available

models, in theoretical formulation and numerical results, we show its capabilities in capturing SMAs behavior under multiaxial non-proportional loadings. Extension of small strain models into the finite strain deformation as well as large rotation regime is the subject of the next chapter.

4.2 Some models available in the literature

4.2.1 Model proposed by Souza et al. (1998)

The model proposed by Souza et al. is developed within the theory of irreversible thermodynamics in the realm of a small-deformation regime. Accordingly, at each instant the thermodynamical state of a homogenized volume element is described by a set of external (controllable) and internal variables. Moreover, given proper potentials and following classical arguments, it is possible to compute the quantities thermodynamically conjugate to both the external and the internal variables. Such a model utilizes an additive decomposition of the total strain into an elastic and an inelastic (traceless) part, as usual in the case of small strains:

$$\boldsymbol{\varepsilon} = \boldsymbol{\varepsilon}^e + \boldsymbol{\varepsilon}^{in} \quad (4.1)$$

It is convenient to split the strain, $\boldsymbol{\varepsilon}$, and the stress, $\boldsymbol{\sigma}$, as follows:

$$\boldsymbol{\varepsilon} = \boldsymbol{e} + \frac{\theta}{3}\mathbf{1} \quad (4.2)$$

$$\boldsymbol{\sigma} = \boldsymbol{s} + p\mathbf{1} \quad (4.3)$$

where \boldsymbol{e} is the deviatoric strain; $\theta = \text{tr}(\boldsymbol{\varepsilon})$ is the volumetric strain; \boldsymbol{s} is the deviatoric stress; $p = \text{tr}(\boldsymbol{\sigma})/3$ is the volumetric stress, in general indicated as pressure. In this study, the second-order identity tensor is denoted by $\mathbf{1}$.

Souza et al. choose the strain, $\boldsymbol{\varepsilon}$, split in its volumetric and deviatoric components, and the absolute temperature, T , as control variables and a second-order tensor, $\boldsymbol{\varepsilon}^{in}$, indicated as transformation strain, as internal variable. Assumed to be traceless, $\boldsymbol{\varepsilon}^{in}$ (which is equal to its deviatoric part, \boldsymbol{e}^{in}) is a measure of the strain associated to the phase transformation and, in particular, to the conversion from austenite or multiple-variant martensite (twinned) to the single-variant martensite (detwinned). Accordingly, the norm of \boldsymbol{e}^{in} should be bounded between zero, for the case of a material without oriented martensite, and a maximum value ε_L , for the case in which the material is fully transformed in single variant oriented martensite, i.e.:

$$\|\boldsymbol{e}^{in}\| \leq \varepsilon_L \quad (4.4)$$

where $\|\cdot\|$ is the Euclidean norm, defined as $\|\mathbf{A}\| = (\mathbf{A} : \mathbf{A})^{\frac{1}{2}}$, while $\mathbf{A} : \mathbf{B} = A_{ij}B_{ij}$. Henceforth, Souza et al. set the free-energy equal to:

$$\Psi(\theta, \mathbf{e}, T, \mathbf{e}^{in}) = \frac{1}{2}K\theta^2 + G\|\mathbf{e} - \mathbf{e}^{in}\|^2 + \tau_M(T)\|\mathbf{e}^{in}\| + \frac{1}{2}h\|\mathbf{e}^{in}\|^2 + \mathcal{I}_{\varepsilon_L}(\|\mathbf{e}^{in}\|) \quad (4.5)$$

where K and G are the bulk and the shear moduli; $\tau_M(T)$ is a proper function of temperature and h defines the phase transformation hardening. We assume $\tau_M(T)$ in the form $\tau_M(T) = \beta\langle T - T_0 \rangle$ where β is a material parameter, T_0 a reference temperature and $\langle \cdot \rangle$ the positive part function, defined as:

$$\langle a \rangle = \begin{cases} a & \text{if } a > 0 \\ 0 & \text{otherwise} \end{cases} \quad (4.6)$$

Moreover, in equation (4.5) we use the indicator function $\mathcal{I}_{\varepsilon_L}$ defined as

$$\mathcal{I}_{\varepsilon_L}(\|\mathbf{e}^{in}\|) = \begin{cases} 0 & \text{if } \|\mathbf{e}^{in}\| \leq \varepsilon_L \\ +\infty & \text{otherwise} \end{cases} \quad (4.7)$$

in order to enforce inequality constraint (4.4). Following classical arguments, it is possible to compute the quantities thermodynamically conjugate to the volumetric and the deviatoric components of the strain, θ and \mathbf{e} , and to the transformation strain, \mathbf{e}^{in} . In particular, we have:

$$p = \frac{\partial \Psi}{\partial \theta} = K\theta \quad (4.8)$$

$$\mathbf{s} = \frac{\partial \Psi}{\partial \mathbf{e}} = 2G(\mathbf{e} - \mathbf{e}^{in}) \quad (4.9)$$

$$\mathbf{x}^{in} = -\frac{\partial \Psi}{\partial \mathbf{e}^{in}} = \mathbf{s} - \mathbf{x} \quad (4.10)$$

with \mathbf{x}^{in} indicated in the following as *transformation stress* where:

$$\mathbf{x} = [\tau_M(T) + h\|\mathbf{e}^{in}\| + \gamma] \frac{\mathbf{e}^{in}}{\|\mathbf{e}^{in}\|} \quad (4.11)$$

The variable γ results from the indicator function subdifferential $\partial \mathcal{I}_{\varepsilon_L}(\|\mathbf{e}^{in}\|)$ and it is defined as:

$$\begin{cases} \gamma = 0 & \text{if } \|\mathbf{e}^{in}\| < \varepsilon_L \\ \gamma \geq 0 & \text{if } \|\mathbf{e}^{in}\| = \varepsilon_L \end{cases} \quad (4.12)$$

It is interesting to observe that the quantity \mathbf{x} in equation (4.11) plays a role similar to the so-called *back-stress* in classical plasticity and, accordingly, \mathbf{x}^{in} can be identified as a relative stress. The mechanical dissipation inequality reduces to

$$D^{mech} = \boldsymbol{\sigma} : \dot{\boldsymbol{\varepsilon}} - (\dot{\Psi} + \eta\dot{T}) = \mathbf{x}^{in} : \dot{\mathbf{e}}^{in} \geq 0 \quad (4.13)$$

To satisfy the second law of thermodynamics or the mechanical dissipation inequality (4.13), we choose the following flow rule for the internal variable:

$$\dot{\mathbf{e}}^{in} = \dot{\zeta} \frac{\mathbf{x}^{in}}{\|\mathbf{x}^{in}\|} \quad (4.14)$$

To describe phase transformation evolution, we choose a J_2 type limit function f defined as:

$$f = \|\mathbf{x}^{in}\| - R \quad (4.15)$$

where the material parameter R is the elastic region radius. The model is finally completed by the classical Kuhn-Tucker and consistency conditions, respectively, as follows:

$$\dot{\zeta} \geq 0, \quad f \leq 0, \quad \dot{\zeta} f = 0 \quad (4.16)$$

$$\dot{\zeta} \geq 0, \quad \dot{f} \leq 0, \quad \dot{\zeta} \dot{f} = 0 \quad \text{if} \quad f = 0 \quad (4.17)$$

We then summarize the basic Souza (coincides with the original Souza model) model in Table 4.1

Table 4.1: Basic Souza model

External variables: ε, T
Internal variable: \mathbf{e}^{in}
Stress quantities:
$\mathbf{s} = 2G(\mathbf{e} - \mathbf{e}^{in})$
$\mathbf{x} = [\tau_M(T) + h\ \mathbf{e}^{in}\ + \gamma] \frac{\mathbf{e}^{in}}{\ \mathbf{e}^{in}\ }$
$\mathbf{x}^{in} = \mathbf{s} - \mathbf{x}$
with
$\begin{cases} \gamma \geq 0 & \text{if } \ \mathbf{e}^{in}\ = \varepsilon_L \\ \gamma = 0 & \text{otherwise} \end{cases}$
Evolution equation:
$\dot{\mathbf{e}}^{in} = \dot{\zeta} \frac{\mathbf{x}^{in}}{\ \mathbf{x}^{in}\ }$
Limit function:
$f = \ \mathbf{x}^{in}\ - R$
Kuhn-Tucker conditions:
$f \leq 0, \quad \dot{\lambda} \geq 0, \quad \dot{\lambda} f = 0$

4.2.2 Model proposed by Panico and Brinson (2007)

In this section we present the small strain constitutive model proposed by Panico and Brinson (2007). The stress-induced martensite fraction, z_σ is related to the inelastic strain as follows:

$$z_\sigma = \frac{\|\boldsymbol{\varepsilon}^{in}\|}{\sqrt{\frac{3}{2}}\gamma_0} \quad (4.18)$$

where γ is the maximum uniaxial transformation strain ($\gamma_0 = \sqrt{\frac{2}{3}}\varepsilon_L$). From (4.18) the rate of martensite volume fraction can be written as:

$$\dot{z}_\sigma = \frac{\boldsymbol{\varepsilon}^{in} : \dot{\boldsymbol{\varepsilon}}^{in}}{\sqrt{\frac{3}{2}}\gamma_0\|\boldsymbol{\varepsilon}^{in}\|} \quad (4.19)$$

It is assumed that the rate of inelastic strain is due to transformation of the parent phase and to reorientation of the previously developed oriented martensite, i.e.:

$$\dot{\boldsymbol{\varepsilon}}^{in} = \dot{\boldsymbol{\varepsilon}}^{tr} + \dot{\boldsymbol{\varepsilon}}^{re} \quad (4.20)$$

where $\dot{\boldsymbol{\varepsilon}}^{tr}$ and $\dot{\boldsymbol{\varepsilon}}^{re}$ are the transformation and reorientation strain rate tensors, respectively.

Also, the total martensite fraction, z , is obtained as the sum of stress-induced and temperature-induced parts:

$$z = z_\sigma + z_T, \quad 0 \leq z \leq 1, \quad 0 \leq z_\sigma \leq 1, \quad 0 \leq z_T \leq 1 \quad (4.21)$$

where z_T represents the temperature-induced martensite fraction.

Since the reorientation strain term does not contribute to the variation of the martensite volume fraction, the condition $\boldsymbol{\varepsilon}^{in} : \dot{\boldsymbol{\varepsilon}}^{re} = 0$ has to be imposed. Then equation (4.19) becomes:

$$\dot{z}_\sigma = \frac{\boldsymbol{\varepsilon}^{in} : \dot{\boldsymbol{\varepsilon}}^{tr}}{\sqrt{\frac{3}{2}}\gamma_0\|\boldsymbol{\varepsilon}^{in}\|} \quad (4.22)$$

Considering stress-induced martensite fraction, z_σ , and temperature-induced martensite fraction, z_T , as internal variables together with $\boldsymbol{\varepsilon}^e$ and T as control variables, the following classical expression for the Helmholtz free energy function of the three-phase system is adopted:

$$\begin{aligned} \psi(\boldsymbol{\varepsilon}^e, T, z_\sigma, z_T) = & \frac{1}{2\rho} \boldsymbol{\varepsilon}^e : \mathbb{L} : \boldsymbol{\varepsilon}^e + u_0^A - T\eta_0^A - z_T(\Delta u_0 - T\Delta\eta_0) \\ & + z_\sigma \langle T\Delta\eta_0 - \Delta u_0 \rangle + c_\nu \left[(T - T_0) - T \ln \left(\frac{T}{T_0} \right) \right] + \Delta\psi \end{aligned} \quad (4.23)$$

where ρ is the material density, \mathbb{L} is the isotropic elasticity tensor assumed to be the same for all phases. The energy and entropy differences $\Delta u_0 = u_0^A - u_0^M$ and $\Delta\eta_0 = \eta_0^A - \eta_0^M$

have been adopted where u_0^A and u_0^M are the specific free energies of austenite and martensite, η_0^A and η_0^M are the specific entropies of austenite and martensite. Moreover, c_ν is the specific heat at constant volume, $\Delta\psi$ is the so-called configurational energy originated by the phase mixture.

The configurational energy is assumed to depend only on z_σ according to the following quadratic form:

$$\Delta\psi = \frac{1}{2}H_\sigma z_\sigma^2 \quad (4.24)$$

where H_σ is a material parameter governing the initial hardening during the phase transformation.

The rest of the formulation follows standard arguments, so it is not reported here and the reader is referred to Panico and Brinson (2007) for more details. The final form of the constitutive model is summarized as follows:

- Stress quantities

$$\left\{ \begin{array}{l} \boldsymbol{\sigma} = \mathbb{L} : (\boldsymbol{\varepsilon} - \boldsymbol{\varepsilon}^{in}) \\ \bar{\boldsymbol{x}} = \frac{\rho}{\sqrt{\frac{3}{2}}\gamma_0} [\langle T\Delta\eta_0 - \Delta u_0 \rangle + H_\sigma z_\sigma] \frac{\boldsymbol{\varepsilon}^{in}}{\|\boldsymbol{\varepsilon}^{in}\|} \\ \boldsymbol{x}^{tr} = \boldsymbol{s} - \bar{\boldsymbol{x}} \\ \boldsymbol{x}^{re} = \boldsymbol{s} \\ x^T = -\rho(T\Delta\eta_0 - \Delta u_0) \end{array} \right. \quad (4.25)$$

- Evolution equations

$$\begin{aligned} \dot{\boldsymbol{\varepsilon}}^{in} &= \dot{\lambda}_{tr}\boldsymbol{x}^{tr} + \dot{\lambda}_{re}\hat{\mathbb{I}} : \boldsymbol{x}^{re} \\ \dot{z}_T &= \dot{\lambda}_T \boldsymbol{x}^T \end{aligned} \quad (4.26)$$

- Limit functions

$$\begin{aligned} f_{tr} &= \|\boldsymbol{x}^{tr}\| - y_{tr}(z_\sigma) \\ f_{re} &= \frac{1}{2}\boldsymbol{x}^{re} : \hat{\mathbb{I}} : \boldsymbol{x}^{re} - y_{re} \\ f_T &= \begin{cases} x^T - y_T^f(z_T) & \text{if } \dot{z}_T > 0 \\ -x^T - y_T^r(z_T) & \text{if } \dot{z}_T < 0 \end{cases} \end{aligned} \quad (4.27)$$

- Kuhn-Tucker conditions

$$\begin{aligned} f_{tr} &\leq 0, \quad \dot{\lambda}_{tr} \geq 0, \quad \dot{\lambda}_{tr} f_{tr} = 0 \\ f_{re} &\leq 0, \quad \dot{\lambda}_{re} \geq 0, \quad \dot{\lambda}_{re} f_{re} = 0 \\ f_T &\leq 0, \quad \dot{\lambda}_T \geq 0, \quad \dot{\lambda}_T f_T = 0 \end{aligned} \quad (4.28)$$

- Martensite volume fractions

$$z_\sigma = \frac{\|\boldsymbol{\varepsilon}^{in}\|}{\sqrt{\frac{3}{2}}\gamma_0}, \quad 0 \leq z_\sigma \leq 1, \quad 0 \leq z_T \leq 1, \quad 0 \leq z_T + z_\sigma \leq 1 \quad (4.29)$$

In the equations above, the fourth-order tensor $\hat{\mathbb{I}}$ is defined as:

$$\hat{\mathbb{I}} = \mathbb{I} - \frac{\boldsymbol{\varepsilon}^{in}}{\|\boldsymbol{\varepsilon}^{in}\|} \otimes \frac{\boldsymbol{\varepsilon}^{in}}{\|\boldsymbol{\varepsilon}^{in}\|} \quad (4.30)$$

where \mathbb{I} is the fourth-order identity tensor. Moreover, y_{re} is a material parameter which controls the reorientation process, while $y_{tr}(z_\sigma)$ is a function that governs the kinematics of the phase transformation and is assumed to have the following form:

$$y_{tr}(z_\sigma) = \begin{cases} A^f z_\sigma - B^f z_\sigma \ln(1 - z_\sigma) + C^f & \text{if } \dot{z}_\sigma > 0 \\ A^r (1 - z_\sigma) - B^r (1 - z_\sigma) \ln(z_\sigma) + C^r & \text{if } \dot{z}_\sigma < 0 \end{cases} \quad (4.31)$$

with $A^{f,r}, B^{f,r}, C^{f,r}$ material parameters. Dependency of y_{tr} on the stress-induced martensite fraction, z_σ , through a logarithmic function ensures that $0 \leq z_\sigma \leq 1$. The functions $y^f(z_T)$ and $y^r(z_T)$ have the following expressions:

$$\begin{cases} y_T^f(z_T) = c^f z_T \\ y_T^r(z_T) = Y_{T_0}^r + \bar{\sigma} + c^r (1 - z_T) \end{cases} \quad (4.32)$$

with $\bar{\sigma} = \sqrt{\frac{3}{2} \mathbf{s} : \mathbf{s}}$, while c^f , c^r and $Y_{T_0}^r$ are material parameters.

4.2.3 A basic model extracted from Panico-Brinson model

In order to obtain the basic model, we ignore temperature-induced terms. For simplicity, we use the following definitions:

$$\tau_M(T) = \frac{\rho}{\sqrt{3/2}\gamma_0} \langle T \Delta\eta_0 - \Delta u_0 \rangle = \beta \langle T - T_0 \rangle \quad (4.33)$$

$$\varepsilon_L = \sqrt{3/2}\gamma_0 \quad (4.34)$$

$$h = \frac{2\rho H_\sigma}{3\gamma_0^2} \quad (4.35)$$

which yields

$$\beta = \frac{\rho \Delta\eta_0}{\sqrt{3/2}\gamma_0} = \frac{\rho \Delta\eta_0}{\varepsilon_L} \quad (4.36)$$

$$T_0 = \frac{\Delta u_0}{\Delta\eta_0} \quad (4.37)$$

We then summarize the basic Panico-Brinson model in Table 4.2

4.2.4 A modified Panico-Brinson model

In the original work of Panico and Brinson (2007), they have used a logarithmic function to enforce the inelastic strain norm constraint (4.4). Moreover they use different

Table 4.2: Basic model obtained from Panico-Brinson model

External variables: ε, T
Internal variable: e^{in}

Stress quantities:

$$\mathbf{s} = 2G(\mathbf{e} - \mathbf{e}^{in})$$

$$\bar{\mathbf{x}} = [\tau_M(T) + h\|\mathbf{e}^{in}\|] \frac{\boldsymbol{\varepsilon}^{in}}{\|\boldsymbol{\varepsilon}^{in}\|}$$

$$\mathbf{x}^{tr} = \mathbf{s} - \bar{\mathbf{x}}$$

$$\mathbf{x}^{re} = \hat{\mathbb{I}} : \mathbf{s}$$

Evolution equation:

$$\dot{\mathbf{e}}^{in} = \dot{\lambda}_{tr}\mathbf{x}^{tr} + \dot{\lambda}_{re}\mathbf{x}^{re}$$

Limit functions:

$$f_{tr} = \|\mathbf{x}^{tr}\| - y_{tr}(z_\sigma)$$

$$f_{re} = \|\mathbf{x}^{re}\| - y_{re}$$

$$\text{with } y_{tr}(z_\sigma) = \begin{cases} A^f z_\sigma - B^f z_\sigma \ln(1 - z_\sigma) + C^f & \text{if } \dot{z}_\sigma > 0 \\ A^r (1 - z_\sigma) - B^r (1 - z_\sigma) \ln(z_\sigma) + C^r & \text{if } \dot{z}_\sigma < 0 \end{cases}$$

$$\text{and } z_\sigma = \frac{\|\mathbf{e}^{in}\|}{\varepsilon_L}$$

Kuhn-Tucker conditions:

$$f_{tr} \leq 0, \dot{\lambda}_{tr} \geq 0, \dot{\lambda}_{tr} f_{tr} = 0$$

$$f_{re} \leq 0, \dot{\lambda}_{re} \geq 0, \dot{\lambda}_{re} f_{re} = 0$$

functions in forward and reverse phase transformations. However, in the Souza model, instead of using a logarithmic function, they use the indicator function which is more interesting from a numerical point of view. They also use one limit function for both forward and reverse transformations which simplifies considerably the solution algorithm. To these reasons, we are interested to recast the basic Panico and Brinson model in a simple form similar to Souza model. It can also be considered as the modified Souza model, where we have split the inelastic strain into transformation and reorientation parts. Following this approach, we derive the model equations and propose the modified basic Panico-Brinson constitutive model in Table 4.3.

4.2.5 Model proposed by Lagoudas (2008)

Lagoudas and his coworkers have used an SMA model in several works. They have assumed that for the forward phase transformation from austenite to martensite ($\dot{z} > 0$) the transformation strain will form in the direction of the deviatoric stress. During the reverse transformation from martensite to the parent austenitic phase ($\dot{z} < 0$), the

Table 4.3: Modified basic Panico-Brinson model

External variables: $\boldsymbol{\varepsilon}, T$

Internal variable: \boldsymbol{e}^{in}

Stress quantities:

$$\boldsymbol{s} = 2G(\boldsymbol{e} - \boldsymbol{e}^{in})$$

$$\boldsymbol{x} = [\tau_M(T) + h\|\boldsymbol{e}^{in}\| + \gamma] \frac{\boldsymbol{\varepsilon}^{in}}{\|\boldsymbol{\varepsilon}^{in}\|}$$

$$\boldsymbol{x}^{tr} = \boldsymbol{s} - \boldsymbol{x}$$

$$\boldsymbol{x}^{re} = \hat{\mathbb{I}} : \boldsymbol{s}$$

with

$$\begin{cases} \gamma \geq 0 & \text{if } \|\boldsymbol{e}^{in}\| = \varepsilon_L \\ \gamma = 0 & \text{otherwise} \end{cases}$$

Evolution equation:

$$\dot{\boldsymbol{e}}^{in} = \dot{\lambda}_{tr}\boldsymbol{x}^{tr} + \dot{\lambda}_{re}\boldsymbol{x}^{re}$$

Limit functions:

$$f_{tr} = \|\boldsymbol{x}^{tr}\| - R^{tr}$$

$$f_{re} = \|\boldsymbol{x}^{re}\| - R^{re}$$

Kuhn-Tucker conditions:

$$f_{tr} \leq 0, \dot{\lambda}_{tr} \geq 0, \dot{\lambda}_{tr}f_{tr} = 0$$

$$f_{re} \leq 0, \dot{\lambda}_{re} \geq 0, \dot{\lambda}_{re}f_{re} = 0$$

transformation strain will be recovered proportionally to the existing transformation strain at the reversal point (\boldsymbol{e}^{t-r}) from forward to the reverse transformation (Lagoudas, 2008). We introduce the basic Lagoudas model as summarized in Table 4.4.

4.3 Proposing a class of SMA constitutive models

Selecting an appropriate set of internal variables as macroscopic consequences of the micro-structural changes is the first fundamental issue of phenomenological modeling (Haupt, 2002). In fact, introduction and definition of such internal variables would play a crucial role in arriving at a physically sound constitutive formulation with a simple and consistent structure. Since internal variables are related to micro-structural mechanisms, the definition of their evolution equations is the second fundamental issue of phenomenological modeling and they should be well established with relevant physical considerations (Xiao et al., 2006).

Focusing on shape memory alloys, since the martensitic phase transformation is the basic

Table 4.4: Basic Lagoudas model

External variables: ε, T

Internal variable: z

Stress quantities:

$$\mathbf{s} = 2G(\mathbf{e} - \mathbf{e}^{in})$$

$$\bar{x} = \tau_M(T) + h\varepsilon_L z_\sigma$$

$$x^{tr} = \mathbf{s} : \mathbf{n} - \bar{x}$$

with

$$\mathbf{e}^{in} = (\varepsilon_L z) \mathbf{n} \text{ and } \mathbf{n} = \begin{cases} \frac{\mathbf{s}}{\|\mathbf{s}\|} & \text{if } \dot{z}_\sigma > 0 \\ \frac{\mathbf{e}^{t-r}}{\|\mathbf{e}^{t-r}\|} & \text{if } \dot{z}_\sigma < 0 \end{cases}$$

Evolution equation:

$$\dot{z}_\sigma = \dot{\zeta} \frac{\partial f}{\partial x^{tr}} = \dot{\zeta} \frac{x^{tr}}{|x^{tr}|}$$

Limit function:

$$f = |x^{tr}| - R^{tr}$$

Kuhn-Tucker conditions:

$$f \leq 0, \dot{\lambda} \geq 0, \dot{\lambda} f = 0$$

micro-structural property, in order to incorporate the growth, orientation and reorientation of variants, an appropriate set of internal variables should be able to represent at least a scalar and a directional information (Luig and Bruhns, 2008). So, on one hand, a set of scalar variables is not adequate for a simple description of the material behavior due to the loss of explicit directional information, while, on the other hand, models that have used tensorial internal variables seem to be more successful since they explicitly include simple directional information. In most of the previously proposed models, inelastic strain has been considered as a unique internal variable; following these approaches, in general, the norm of the inelastic strain represents the scalar martensite amount and its direction represents the preferred direction of the variants. Accordingly, in this class of models scalar and directional informations are tightly interconnected, possibly leading to a somehow more limited or constrained modeling approach.

To give more freedom, a different set of internal variables is proposed with an emphasis on reorientation. A measure of the amount of stress-induced martensite is chosen as a scalar internal variable, being related to the amount of inelastic strain due to stress-induced phase transformation, while the average direction of different variants (or preferred direction of variants) is chosen as a tensorial internal variable, representing the inelastic strain direction. So, using a standard literature terminology (Bouvet et al.,

2004; Panico and Brinson, 2007) the internal variables may be clearly interpreted as phase transformation and variant reorientation; in this way, transformation and reorientation can be hopefully described with more flexibility.

4.3.1 Constitutive model development

From a physical point of view, the application of a thermo-mechanical load activates the phase transformation and the preferred martensite variants start to nucleate or shrink (Otsuka and Wayman, 1998). Changing the load direction, another set of variants, that are in the new preferred direction with respect to the applied stress, starts to nucleate and previous variants may grow or shrink depending on the available stress for that direction (this phenomenon is known in the literature as simultaneous forward and reverse transformation under non-proportional loading (see, e.g., Bouvet et al. (2004) and Lim and McDowell (1999)). In the phenomenological framework, we consider the average behavior of variants as the behavior of an equivalent single variant. So when the load direction changes, this equivalent single variant rotates to a new preferred direction.

In general the inelastic strain $\boldsymbol{\varepsilon}^{in}$ should include the description of several physical phenomena, ranging, for example, from permanent plasticity and phase transformation up to void generation and fracture. However, in the following we neglect all inelastic phenomena except reversible martensitic phase transformations which are then the only physics to be described by $\boldsymbol{\varepsilon}^{in}$.

Moreover, keeping in mind all the preliminary shape memory alloy material descriptions, in the following we assume to use $\boldsymbol{\varepsilon}^{in}$ as the only internal variable in the model. However, we do not treat $\boldsymbol{\varepsilon}^{in}$ as a unique second-order tensor variable, but we clearly distinguish between its norm and direction with the aim of getting more freedom in the modeling. Besides this distinction, the position of non-introducing other microstructures describing variables leads to obtain a model which is able only to give a very simplified representation of the phenomena occurring at the material micro-mechanical level. In particular there is no attempt to include in the modeling the description of each single martensite variant as well as to obtain a good representation of phenomena such as the phase transformation between single variants.

Accordingly, the choice of dealing with only one second-order tensor internal variable (even decomposed, as mentioned, into its norm and direction) allows only to distinguish between a generic (parent) phase to which no macroscopic strain is associated and a generic (product) phase to which a homogenized macroscopic strain can be associated. This perspective is similar to other effective modeling approaches as the one proposed in Souza et al. (1998).

According to our previous discussion we now introduce a scalar internal variable q and a tensorial internal variable \mathbf{N} such that:

$$\boldsymbol{\varepsilon}^{in} = q\mathbf{N} \quad (4.38)$$

with

$$\|\mathbf{N}\| = 1 \quad (4.39)$$

According to (4.38) and (4.39), it is clear that, supposing $q \geq 0$, we have

$$\|\boldsymbol{\varepsilon}^{in}\| = q \quad (4.40)$$

Hence, introducing the material parameter ε_L corresponding to the maximum transformation strain reached at the end of the transformation during a uniaxial test, we require

$$0 \leq q \leq \varepsilon_L \quad (4.41)$$

Taking time derivative of equation (4.38), we obtain:

$$\dot{\boldsymbol{\varepsilon}}^{in} = \dot{q}\mathbf{N} + q\dot{\mathbf{N}} \quad (4.42)$$

which somehow naturally induces to introduce the following positions:

$$\dot{\boldsymbol{\varepsilon}}^{tr} = \dot{q}\mathbf{N} \quad (4.43)$$

$$\dot{\boldsymbol{\varepsilon}}^{re} = q\dot{\mathbf{N}} \quad (4.44)$$

and using another classical terminology available in the literature, we can interpret equations (4.43) and (4.44) as pure transformation and pure reorientation rates, respectively. Accordingly, we can read equation (4.42) as an additive decomposition of the inelastic strain rate as:

$$\dot{\boldsymbol{\varepsilon}}^{in} = \dot{\boldsymbol{\varepsilon}}^{tr} + \dot{\boldsymbol{\varepsilon}}^{re} \quad (4.45)$$

Relation (4.45) is interesting since it states that the inelastic strain evolution induced by the reversible martensite phase transformation is due to two contributions, one from pure transformation and another one from pure reorientation. We also notice that relation (4.45) is the same as assumed in Panico and Brinson (2007) (see equation (4.20)). Moreover, following (4.45), pure transformation has no effect on the preferred (or average) direction of martensite variants and pure reorientation affects only the direction of variants without directly affecting the amount of martensite. Clearly, also if uncoupled in terms of evolution with respect to their contribution to inelastic strain, the two processes could be related and interconnected through a proper choice of limit functions, as discussed in the following.

Helmholtz free energy function

The model assumes the total strain $\boldsymbol{\varepsilon}$ and the absolute temperature T as control variables, the amount of martensite q and the average direction of martensite variants \mathbf{N} as internal variables. Assuming $\boldsymbol{\varepsilon}^{in}$ to be traceless, the free energy density function Ψ for a polycrystalline SMA material is then expressed as the convex potential (Souza et al., 1998)

$$\begin{aligned} \Psi(\theta, \mathbf{e}, T, q, \mathbf{N}, \lambda) = & \frac{1}{2}K\theta^2 + G\|\mathbf{e} - q\mathbf{N}\|^2 + \tau_M(T)q \\ & + \frac{1}{2}hq^2 + \mathcal{I}_{0,\varepsilon_L}(q) + \kappa(\|\mathbf{N}\| - 1) \end{aligned} \quad (4.46)$$

In equation (4.46) we also use the indicator function $\mathcal{I}_{0,\varepsilon_L}$ defined as

$$\mathcal{I}_{0,\varepsilon_L}(q) = \begin{cases} 0 & \text{if } 0 \leq q \leq \varepsilon_L \\ +\infty & \text{otherwise} \end{cases} \quad (4.47)$$

in order to enforce inequality constraint (4.41), while the Lagrange multiplier κ is the constraint force to enforce equality constraint (4.39).

Starting from the adopted free energy density function Ψ presented in equation (4.46) and following standard arguments, we can derive the constitutive equations

$$\left\{ \begin{array}{l} p = \frac{\partial \Psi}{\partial \theta} = K\theta \\ \mathbf{s} = \frac{\partial \Psi}{\partial \mathbf{e}} = 2G(\mathbf{e} - q\mathbf{N}) \\ \eta = -\frac{\partial \Psi}{\partial T} = -q \frac{\tau_M(T)}{|T - T_0|} \\ Q = -\frac{\partial \Psi}{\partial q} = \mathbf{s} : \mathbf{N} - (\tau_M(T) + hq + \gamma) \\ \mathbf{X} = -\frac{\partial \Psi}{\partial \mathbf{N}} = q\mathbf{s} - \kappa\mathbf{N} \\ \bar{K} = -\frac{\partial \Psi}{\partial \kappa} = -\|\mathbf{N}\| + 1 = 0 \end{array} \right. \quad (4.48)$$

The thermodynamic forces Q and \mathbf{X} are associated to the internal variables q and \mathbf{N} , while \bar{K} is the thermodynamic force associated to κ . The variable γ results from the indicator function subdifferential $\partial \mathcal{I}_{0,\varepsilon_L}(q)$ and it is defined as

$$\gamma = \partial \mathcal{I}_{0,\varepsilon_L}(q) = \begin{cases} \gamma_1 \leq 0 & \text{if } q = 0 \\ 0 & \text{if } 0 < q < \varepsilon_L \\ \gamma_2 \geq 0 & \text{if } q = \varepsilon_L \end{cases} \quad (4.49)$$

Evolution equations for the internal variables

According to (4.48), the mechanical dissipation inequality reduces to

$$D^{mech} = \boldsymbol{\sigma} : \dot{\boldsymbol{\varepsilon}} - (\dot{\Psi} + \eta\dot{T}) = Q\dot{q} + \mathbf{X} : \dot{\mathbf{N}} \geq 0 \quad (4.50)$$

To satisfy the second law of thermodynamics or the mechanical dissipation inequality (4.50), we choose the following flow rules for the internal variables:

$$\begin{cases} \dot{q} &= \dot{\lambda}_{tr} Q &= \dot{\lambda}_{tr} (\mathbf{s} : \mathbf{N} - \tau_M(T) - hq - \gamma) \\ \dot{\mathbf{N}} &= \dot{\lambda}_{re} \mathbf{X} &= \dot{\lambda}_{re} (q\mathbf{s} - \kappa\mathbf{N}) \end{cases} \quad (4.51)$$

where $\dot{\lambda}_{tr}$ and $\dot{\lambda}_{re}$ are non-negative consistency parameters.

Moreover, double contracting both sides of equation (4.51)₂ with \mathbf{N} , applying constraint (4.39) and noting that $\mathbf{N} : \dot{\mathbf{N}} = 0$ (from time differentiation of $\|\mathbf{N}\| = 1$), allow to compute the Lagrange multiplier κ as:

$$\kappa = q\mathbf{s} : \mathbf{N} \quad (4.52)$$

Substituting expression (4.52) for the Lagrange multiplier in the definition (4.48)₅ for the thermodynamic force \mathbf{X} , we obtain:

$$\mathbf{X} = q(\mathbf{s} - (\mathbf{s} : \mathbf{N})\mathbf{N}) = q(\mathbb{I} - \mathbf{N} \otimes \mathbf{N})\mathbf{s} = q\mathbf{Y} \quad (4.53)$$

where \mathbb{I} is the fourth-order identity tensor and $\mathbf{Y} = (\mathbb{I} - \mathbf{N} \otimes \mathbf{N})\mathbf{s}$ is the stress component normal to \mathbf{N} .

We now aim at presenting a general form of limit functions for internal variables q and \mathbf{N} ; to this end, we will use the following identities:

$$\begin{cases} (Q\mathbf{N}) : (\dot{q}\mathbf{N}) &= Q\dot{q} \\ \mathbf{Y} : \mathbf{N} &= 0 \\ \dot{\mathbf{N}} : \mathbf{N} &= 0 \end{cases} \quad (4.54)$$

In the dissipation inequality (4.50), only the component of the thermodynamic forces contributing to dissipation (i.e., those components that are in the direction of evolution) are present and other components do not appear, but using (4.54) it is possible to rewrite (4.50) in a more general, but equivalent, form as :

$$D^{mech} = (Q\mathbf{N} + k(q)\mathbf{Y}) : (\dot{q}\mathbf{N}) + q(\mathbf{Y} + \tilde{k}(q)Q\mathbf{N}) : \dot{\mathbf{N}} \geq 0 \quad (4.55)$$

Relation (4.55) shows that $Q\mathbf{N} + k(q)\mathbf{Y}$ is the thermodynamic force conjugate to the transformation strain, but since according to (4.54)₂ the work done by its normal component is zero it can be ignored. There is a similar discussion for the reorientation part. The point is that although only the component of thermodynamic force in the

direction of evolution affects the dissipation, both components of force contribute in the nucleation of corresponding internal variable.

We use a simple example for clarifying and explaining the nucleation mechanism (to define the limit function for transformation), and investigate the dissipation in a moving block with mass m under coulomb friction in a horizontal surface. The dissipated energy is only due to horizontal component of force (similar to relation (4.50)). Now we study the condition of motion (Nucleation), by increasing the horizontal force up to the maximum friction force, the motion starts. Friction force at this time is proportional to the force normal to the contact surface which is affected by the vertical component of the applied force. So, both components of the force contribute to motion (nucleation) although only the horizontal component contributes to dissipation. In other words, the normal component affects the motion condition by changing the threshold level of resistance against motion.

Now, using relation (4.55) we may define evolution equations as follows:

$$\begin{cases} \dot{q}\mathbf{N} &= \dot{\lambda}_{tr}(Q\mathbf{N} + k(q)\mathbf{Y}) \\ q\dot{\mathbf{N}} &= \dot{\lambda}_{re}(\mathbf{Y} + \tilde{k}(q)Q\mathbf{N}) \end{cases} \quad (4.56)$$

Double contracting both sides of (4.56) with \mathbf{N} and using (4.54), we obtain:

$$\begin{cases} \dot{q} &= \dot{\lambda}_{tr}Q \\ \tilde{k}(q)Q &= 0 \end{cases} \quad (4.57)$$

so the evolution equations can be written as:

$$\begin{cases} \dot{q} &= \dot{\lambda}_{tr}Q \\ q\dot{\mathbf{N}} &= \dot{\lambda}_{re}\mathbf{Y} \end{cases} \quad (4.58)$$

Evolution equations (4.51) and (4.58) differ since in (4.51) $q\mathbf{Y}$ is the thermodynamic force of $\dot{\mathbf{N}}$, while in (4.58) \mathbf{Y} represents the thermodynamic force for $q\dot{\mathbf{N}}$ (i.e., for the reorientation strain rate). Although definitions (4.51) and (4.58) are equivalent from a mathematical point of view (since they both satisfy the dissipation inequality), we prefer the latter from a physical point of view.

According to (4.58), the mechanical dissipation inequality (4.55) reduces to:

$$D^{mech} = \dot{\lambda}_{tr}Q^2 + \dot{\lambda}_{re}\mathbf{Y} : \mathbf{Y} \geq 0 \quad (4.59)$$

Limit functions

To describe phase transformation and reorientation evolutions, we choose two limit functions F^{tr} and F^{re} defined as:

$$\begin{cases} F^{tr}(q, Q, \mathbf{Y}) &= \|Q\mathbf{N} + k(q)\mathbf{Y}\| - R^{tr}(q) = \sqrt{Q^2 + k^2(q)\|\mathbf{Y}\|^2} - R^{tr}(q) \\ F^{re}(q, Q, \mathbf{Y}) &= \|\mathbf{Y}\| - R^{re}(q) \end{cases} \quad (4.60)$$

We remark that, $R^{tr}(q)$ represents the radius of the elastic domain to activate pure transformation, while the term $k(q)$ reflects the effect of reorientation on transformation. Moreover, $R^{re}(q)$ represents a threshold value for the component of stress in the direction normal to the preferred direction of variants to activate the variant reorientation.

The limit function F^{re} affects reorientation by controlling the component of stress normal to the preferred direction of variants and the limit function F^{tr} affects transformation by controlling the transformation thermodynamic force components in the preferred direction of variants, \mathbf{N} , and $k(q)\mathbf{Y}$ normal to that direction.

Also, for generality we assume that transformation affects reorientation and define an interaction function $\bar{k}(q)$ which leads to redefined evolution equations as:

$$\begin{cases} \dot{q} &= \dot{\lambda}_{tr}Q \\ q\dot{\mathbf{N}} &= (\dot{\lambda}_{re} + \bar{k}(q)\dot{\lambda}_{tr})\mathbf{Y} \end{cases} \quad (4.61)$$

According to (4.61), it can be concluded that only the component of stress in the preferred direction of variants evolves phase transformation and variant preferred direction changes only through the component of stress orthogonal to its direction.

Considering (4.61), the mechanical dissipation inequality (4.50) reduces to:

$$D^{mech} = \dot{\lambda}_{tr}Q^2 + (\dot{\lambda}_{re} + \bar{k}(q)\dot{\lambda}_{tr})\mathbf{Y} : \mathbf{Y} \geq 0 \quad (4.62)$$

The model is finally completed by the classical Kuhn-Tucker and consistency conditions, respectively, as follows:

$$\begin{cases} \dot{\lambda}_{tr} \geq 0, F^{tr} \leq 0, \dot{\lambda}_{tr}F^{tr} = 0 \\ \dot{\lambda}_{re} + \bar{k}(q)\dot{\lambda}_{tr} \geq 0, F^{re} \leq 0, (\dot{\lambda}_{re} + \bar{k}(q)\dot{\lambda}_{tr})F^{re} = 0 \end{cases} \quad (4.63)$$

$$\begin{cases} \dot{\lambda}_{tr} \geq 0, \dot{F}^{tr} \leq 0, \dot{\lambda}_{tr}\dot{F}^{tr} = 0 & \text{if } F^{tr} = 0 \\ \dot{\lambda}_{re} + \bar{k}(q)\dot{\lambda}_{tr} \geq 0, \dot{F}^{re} \leq 0, (\dot{\lambda}_{re} + \bar{k}(q)\dot{\lambda}_{tr})\dot{F}^{re} = 0 & \text{if } F^{re} = 0 \end{cases} \quad (4.64)$$

which also guarantee the positiveness of the energy dissipation (4.62).

Summary of proposed class of constitutive equations

We now summarize the material law in the time-continuous frame as follows:

$$\left\{ \begin{array}{l} p = K\theta \\ \mathbf{s} = 2G(\mathbf{e} - q\mathbf{N}) \\ Q = \mathbf{s} : \mathbf{N} - (\tau_M(T) + hq + \gamma) \\ \mathbf{Y} = \mathbf{s} - (\mathbf{s} : \mathbf{N})\mathbf{N} \\ \dot{q} = \dot{\lambda}_{tr}Q \\ q\dot{\mathbf{N}} = (\dot{\lambda}_{re} + \bar{k}(q)\dot{\lambda}_{tr})\mathbf{Y} \\ F^{tr} = \sqrt{Q^2 + k^2(q)\|\mathbf{Y}\|^2} - R^{tr}(q) \\ F^{re} = \|\mathbf{Y}\| - R^{re}(q) \\ \dot{\lambda}_{tr} \geq 0, F^{tr} \leq 0, \dot{\lambda}_{tr}F^{tr} = 0 \\ \dot{\lambda}_{re} + \bar{k}(q)\dot{\lambda}_{tr} \geq 0, F^{re} \leq 0, (\dot{\lambda}_{re} + \bar{k}(q)\dot{\lambda}_{tr})F^{re} = 0 \end{array} \right. \quad (4.65)$$

To decide on the form of interaction functions $k(q)$ and $\bar{k}(q)$ together with $F^{tr}(q)$ and $F^{re}(q)$, experimental observations should be considered.

Adopting a slightly different notation, we present an equivalent form of equations (4.65) expressed in terms of the internal variable \mathbf{e}^{in} , which is more consistent with different papers in the literature, such as Panico and Brinson (2007); Souza et al. (1998). To this end, we substitute q with $\|\mathbf{e}^{in}\|$ and \mathbf{N} with $\frac{\mathbf{e}^{in}}{\|\mathbf{e}^{in}\|}$ in (4.65) and use relation (4.42) to find $\dot{\mathbf{e}}^{in}$, which results in:

$$\left\{ \begin{array}{l} p = K\theta \\ \mathbf{s} = 2G(\mathbf{e} - \mathbf{e}^{in}) \\ \mathbf{x}^{in} = \mathbf{s} - \mathbf{x} \\ \mathbf{Y} = \mathbf{s} - (\mathbf{s} : \mathbf{N})\mathbf{N} \\ \mathbf{x} = (\tau_M(T) + h\|\mathbf{e}^{in}\| + \gamma)\frac{\mathbf{e}^{in}}{\|\mathbf{e}^{in}\|} \\ \dot{\mathbf{e}}^{in} = \dot{\lambda}_{tr}\mathbf{x}^{in} + (\dot{\lambda}_{re} + (\bar{k}(q) - 1)\dot{\lambda}_{tr})\mathbf{Y} \\ F^{tr} = \|\mathbf{x}^{in} + (k(q) - 1)\mathbf{Y}\| - R^{tr}(q) \\ F^{re} = \|\mathbf{Y}\| - R^{re}(q) \end{array} \right. \quad (4.66)$$

4.3.2 Identification and comparison of some models belonging to the proposed general class

To properly show the features of the modeling approach up to now presented, we now try to identify some models belonging to the general class (4.65) which has also been previously discussed in the literature. We can rewrite the models in a unified format, consistent with the notation of section 4.3. To this end, we substitute q instead of $\|\mathbf{e}^{in}\|$

and \mathbf{N} instead of $\frac{\mathbf{e}^{in}}{\|\mathbf{e}^{in}\|}$ in the previously discussed models in Section 4.2. Moreover, we propose a new model considering no effect on reorientation due to transformation. In particular we consider three different models organized as following:

- **Model 1.** This model, proposed by Souza et al. (1998), is characterized by a simple reorientation mechanism and can be considered as a particular member of class of models introduced in Section 4.3, obtained for:

$$k(q) = 1, \quad \bar{k}(q) = 1, \quad R^{tr}(q) = R^{tr}, \quad R^{re}(q) \rightarrow +\infty \quad (4.67)$$

According to (4.67) we conclude that the limit function F^{re} is always negative which results in $\dot{\lambda}_{re} = 0$. In other words, in Model 1 this surface is never activated. Also this model considers the effect of reorientation on transformation ($k(q) \neq 0$) and since it is assumed that $\bar{k}(q) \neq 0$, reorientation is affected by transformation.

- **Model 2.** This model, we introduced as modified basic Panico-Brinson model, can be interpreted either as an extension of Model 1 (including a more flexible description of reorientation mechanism) or as a modification of the model by Panico and Brinson (2007) we presented in Section 4.2.4. This model is also a particular member of the general class of models previously discussed, obtained for:

$$k(q) = 1, \quad \bar{k}(q) = 1, \quad R^{tr}(q) = R^{tr}, \quad R^{re}(q) = R^{re} \quad (4.68)$$

A saturation limit for the component of stress normal to direction \mathbf{N} is present, but similar to Model 1, orientation is affected by transformation part $\bar{K}(q) \neq 0$.

- **Model 3.** This new model (Arghavani et al., 2010c) is a member of the general class introduced before, but no effect on reorientation due to transformation is considered. The proposed model is obtained for:

$$k(q) = 1, \quad \bar{k}(q) = 0, \quad R^{tr}(q) = R^{tr}, \quad R^{re}(q) = R^{re} \quad (4.69)$$

For simplicity we have chosen $k(q) = 1$.

Although other choices are possible, we have chosen the above mentioned form for Model 3, under the assumption that transformation has no effect on reorientation. Moreover for simplicity, we have assumed that R^{tr} and R^{re} are constants, instead of general functions of the martensite amount, while, e. g., in Panico and Brinson (2007), R^{tr} is considered as a function of martensite fraction.

The evolution equations and limit functions for the three models are:

- **Model 1.**

$$\begin{cases} \dot{q} &= \dot{\lambda}_{tr} Q \\ q\dot{\mathbf{N}} &= \dot{\lambda}_{tr} \mathbf{Y} \\ F^{tr} &= \sqrt{Q^2 + \|\mathbf{Y}\|^2} - R^{tr} \end{cases} \quad (4.70)$$

- **Model 2.**

$$\begin{cases} \dot{q} &= \dot{\lambda}_{tr} Q \\ q\dot{\mathbf{N}} &= (\dot{\lambda}_{re} + \dot{\lambda}_{tr}) \mathbf{Y} \\ F^{tr} &= \sqrt{Q^2 + \|\mathbf{Y}\|^2} - R^{tr} \\ F^{re} &= \|\mathbf{Y}\| - R^{re} \end{cases} \quad (4.71)$$

- **Model 3.**

$$\begin{cases} \dot{q} &= \dot{\lambda}_{tr} Q \\ q\dot{\mathbf{N}} &= \dot{\lambda}_{re} \mathbf{Y} \\ F^{tr} &= \sqrt{Q^2 + \|\mathbf{Y}\|^2} - R^{tr} \\ F^{re} &= \|\mathbf{Y}\| - R^{re} \end{cases} \quad (4.72)$$

From the comparison of the models, the first observation is that in both Model 1 and Model 2 the evolution equation for \mathbf{N} is coupled to the evolution equation of q , while in Model 3 the independency of the evolution of \mathbf{N} from $\dot{\lambda}_{tr}$ decouples the reorientation from transformation.

The second observation is about limit functions; in fact, Model 1 has a unique limit function, while Model 2 and Model 3 have two distinct limit functions.

The interesting point is that, all of the above mentioned differences appear only under non-proportional loading conditions. We may observe that, in the case of proportional loading, by definition $\mathbf{N} = \mathbf{s}/\|\mathbf{s}\|$, hence $\mathbf{Y} = \mathbf{0}$ and $\dot{\lambda}_{re} = 0$; so the proposed model (4.65) reduces to:

$$\begin{cases} Q &= \|\mathbf{s}\| - (\tau_M(T) + hq + \gamma) \\ \dot{q} &= \dot{\lambda}_{tr} Q \\ F^{tr} &= |Q| - R^{tr}(q) \end{cases} \quad (4.73)$$

Accordingly, for a proportional loading, the preferred variant direction coincides with the deviatoric stress direction and the only unknown, i.e., the martensite amount q , can be computed by (4.73).

Now, comparing equations (4.65)₇ and (4.73)₃ we can also get some insights on how non-proportional loadings affect the model response. In fact, according to (4.73)₃, the hysteresis size in a proportional loading is constant and is equal to R^{tr} , while loading non-proportionality reduces the hysteresis size, as given by (4.65)₇, of an amount directly

related to $\|\mathbf{Y}\|$, up to a maximum value of R^{re} ; this change in the hysteresis size can be interpreted as the reorientation effect on the transformation. On the other hand, due to the simple limit function adopted for reorientation and based on assuming a constant threshold value for $\|\mathbf{Y}\|$ to activate reorientation, we conclude that pure transformation does not affect reorientation.

4.4 Comparison of models with each other and with experimental data

In this section we perform several uniaxial and multiaxial proportional and nonproportional numerical tests to demonstrate the ability of the presented model (Model 3) to capture the main features of SMA mechanical behavior. All of the results are presented for three models introduced in Section 4.3.2. Since the results of all models for proportional loading are the same, the figures for proportional loading case are presented only for Model 3.

As the aim of this work is to show the model behavior without focusing on algorithmic problems, backward-Euler integration algorithm with small time steps is used for the solution of the examples, and a solution to the nonlinear system is found by means of the function *fsolve* implemented in the Optimization Toolbox of the program *MATLAB*[®]. The present section deals with several uniaxial and multiaxial proportional as well as non-proportional loading conditions. In particular, Section 4.4.1 presents the results for uniaxial tests at three different temperatures to show the model capability of reproducing basic effects such as pseudo-elasticity and shape memory effect. Section 4.4.2 presents the results for multiaxial combined tension-torsion proportional tests with two different proportionality factors. Section 4.4.3 presents the results for several non-proportional loading paths comparing them also with experimental data available in the literature. For all the simulations discussed in Section 4.4.1 and in Section 4.4.2 as well as for the first set of simulations discussed in Section 4.4.3, we adopt the material parameters reported in Table 4.5. It is worthful to note that no value is attributed to R^{re} since this parameter is not significant for the case of proportional loadings. Moreover, material parameters reported in Table 4.5 do not specifically describe any alloy since they are not deduced from experimental data, but simply looking at similar material parameters presented in the literature (Helm and Haupt, 2003; Panico and Brinson, 2007). The chosen material parameters correspond to the following characteristic temperatures $M_f^0 = 306$, $M_s^0 = 310$, $A_s^0 = 317$ and $A_f^0 = 319$ (Panico and Brinson, 2007) where M_s^0 , M_f^0 , A_s^0 and A_f^0 are martensite start, martensite finish, austenite start and austenite finish temperatures at stress-free condition, respectively. For simulation of the

Table 4.5: Material parameters used in the numerical tests (Panico and Brinson, 2007).

parameter	value	unit
E	68400	MPa
ν	0.36	-
h	369.35	MPa
ε_L	4.65	%
β	8.165	MPa K ⁻¹
T_0	310	K
R^{tr}	72.6	MPa
R^{re}	10	MPa

non-proportional loading paths in Section 4.4.3, the material parameters are directly identified from experimental data available in the literature and they are discussed in that section. Finally, in all examples we assume the material to be initially in a generic parent phase ($q = 0$).

Before starting to present the model performance, we wish to point out that we tried to present as much as possible a wide and complete set of loading situations. Unfortunately, in the literature, there is no corresponding set of experimental data on a unique material (this is the reason for dealing with two sets of material data in Section 4.4.3 as discussed above), as well as there is no other macro-modeling paper addressing all the extensive sets of loading conditions reported here. Finally connected to the large variety of situations considered, we cannot absolutely claim that the proposed model is adequate and satisfactory in all the tests, but we try to clearly and honestly address model performance in particular in comparison with what is currently available in the literature.

4.4.1 Uniaxial tests

We start considering uniaxial loading-unloading at the three different constant temperatures of 300, 320 and 340 K and up to a maximum stress value of 600 MPa. As shown in Figure 4.1, the model is able to reproduce the characteristic hysteresis loops of SMAs both in tension and compression. Furthermore, critical transformation stress increases with temperature, as experimentally observed. Then, to test the model reproduction of the shape memory effect, we simulate a thermo-mechanical loading (see Figure 4.2). At a temperature of 300 K, the material is loaded up to a maximum stress of 250 MPa, so it fully transforms to oriented martensite. Keeping the temperature constant and unloading to zero stress results in a mechanically unrecoverable residual strain, which

can be however recovered after heating the material above the austenite finish temperature. Finally, cooling the strain-free material to the initial temperature does not alter its strain or stress state. Sharp increase of stress over the plateau in Figures 4.1 and 4.2 is also predicted by the model as it is only due to elastic behavior of stress-induced martensite phase in the saturated case (fully transformed to martensite) and no phase transformation can occur anymore.

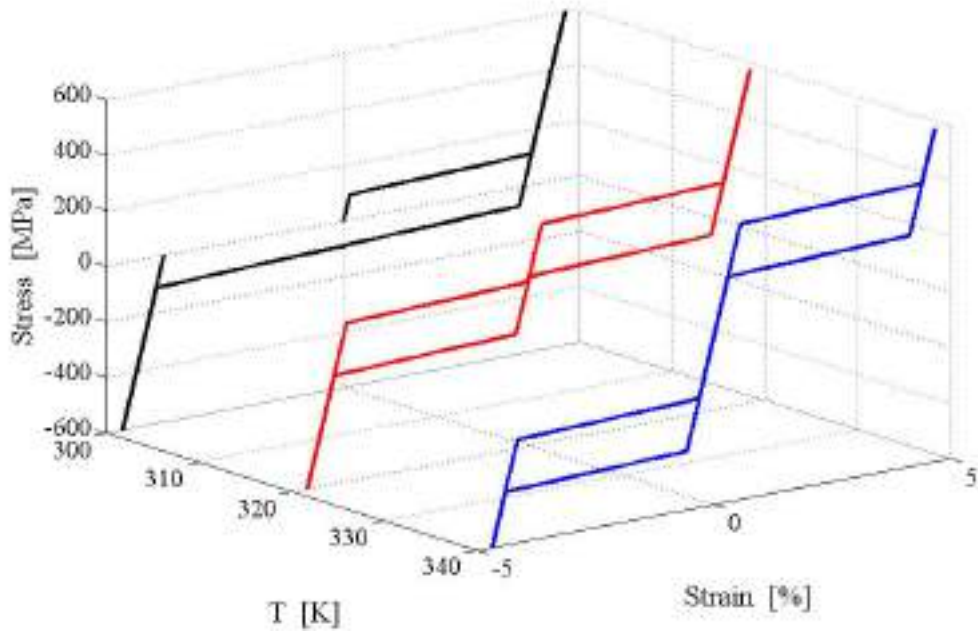


Figure 4.1: Model response for tension-compression uniaxial loading at constant temperature.

4.4.2 Multiaxial proportional tests

Following the idea of Sittner et al. (1995) we now investigate the model predictions in the super-elastic range under two different proportional loading paths characterized by the same equivalent stress (defined as $\sigma_{eq} = \sqrt{\sigma^2 + 3\tau^2}$), but with different proportionality factors. In particular, we set the temperature equal to 330 K and, as suggested by Sittner et al. (1995), we consider two paths, presented in Figure 4.3, such that in path 1 tension is governing, while in path 2 shear is governing. Figures 4.4 and 4.5 show the model response under these loading paths, which qualitatively reproduces experimentally observed material response.

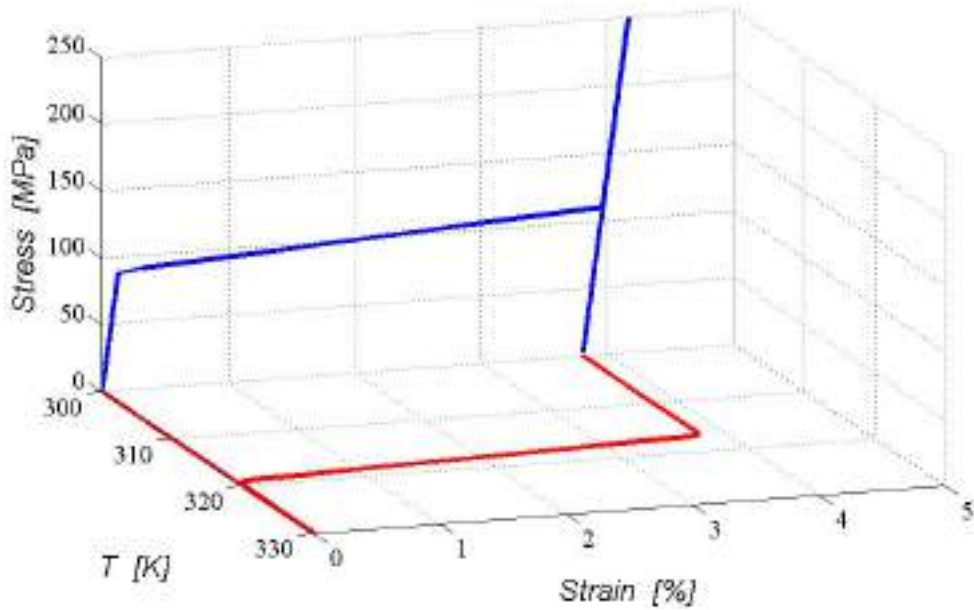


Figure 4.2: Model reproduction of the shape memory effect.

4.4.3 Multiaxial non-proportional tests

We now start investigating the model predictions for non-proportional loadings, still focusing on the material super-elastic range. Accordingly, in all the examples proposed in the following, the test temperature is set to 320 K, for which a super-elastic behavior is expected.

Following the recently published experimental study by Grabe and Bruhns (2009) we start considering a tension-shear test, where stresses are varied in the range ± 250 MPa following a squared-shaped history, as reported in Figure 4.6a. Since during the first tension loading segment, the material fully transforms to oriented martensite, the en-

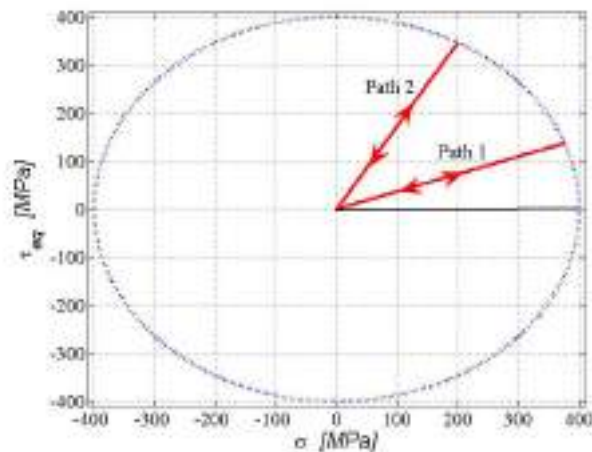


Figure 4.3: Stress path in proportional loading ($\tau_{eq} = \sqrt{3}\tau$, $\tan(\alpha) = \frac{\sqrt{3}\tau}{\sigma}$, $\alpha = \frac{\pi}{9}, \frac{\pi}{3}$).

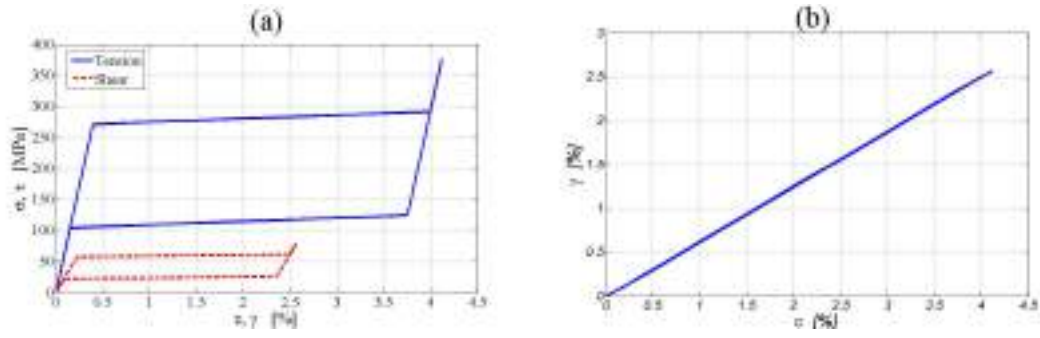


Figure 4.4: Model prediction for proportional path 1: a) stress-strain curves, b) axial-shear strain response.

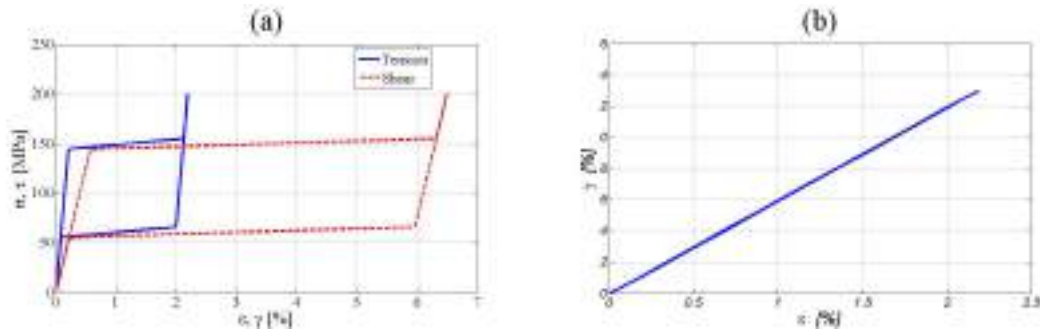


Figure 4.5: Model prediction for proportional path 2: a) stress-strain curves, b) axial-shear strain response.

tire subsequent part of the loading only involves reorientation. A comparison between predictions of the proposed model and the model discussed by Auricchio and Petrini (2002) (in the following, we refer to this model as AP (2002)) is presented in Figure 4.6b. Circle and triangle symbols in Figure 4.6b correspond to points A to G in the stress path for the proposed and for the AP (2002) models, respectively.

It is interesting to observe that in the proposed model, an increase of the value corresponding to the material parameter R^{re} would produce a clockwise rotation of the response path, while there is no equivalent material parameter in AP (2002) to tune the response path rotation. The rotation of the response path has also been observed in the experimental study by Grabe and Bruhns (2009).

Now, we compare the model prediction with experimental data available in the literature. For this purpose we employ the results of tension-torsion experiments with thin wall specimens of CuAlZnMn polycrystalline SMAs reported by Sittner et al. (1995). Since the model discussed in the previous section has been based on an idealized SMA behavior, ignoring asymmetric behavior in tension-compression, subloops, non-constant hysteresis size, etc., only an approximate description of the experimentally observed behavior is possible, and so the comparison between the model prediction and the experimental data will be discussed from a qualitative point of view. We identify material

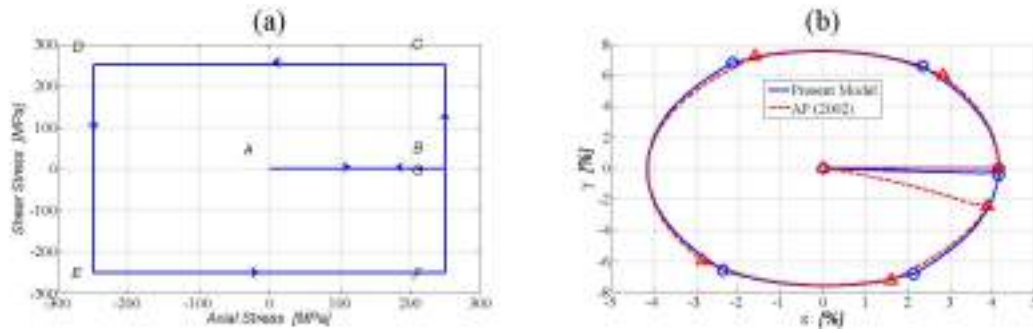


Figure 4.6: Biaxial non-proportional loading: a) axial-shear stress path, b) comparison of model predictions for axial-shear strain response.

parameters (reported in Table 4.6) using the experimental data reported by Sittner et al. (1995) for proportional tension and torsion tests (Figure 4.7). Figures 4.7a and 4.7b show the corresponding model predictions.

Table 4.6: Material parameters adopted for Sittner et al. (1995) experiment.

parameter	value	unit
E	30700	MPa
ν	0.35	-
h	11000	MPa
ε_L	4.9	%
τ_M	150	MPa
T	285	K
R^{tr}	63.3	MPa

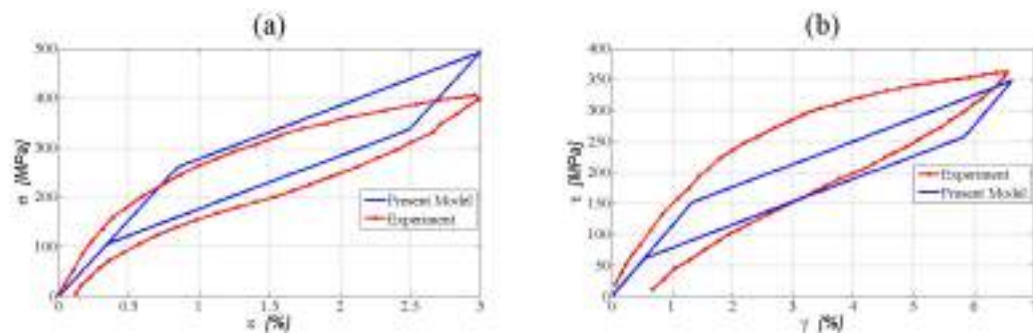


Figure 4.7: Model prediction compared to the experimental data by Sittner et al. (1995): a) uniaxial tension, b) torsion.

After material parameter identification, we simulate some of the combined non-proportional loading paths proposed and experimentally realized in Sittner et al. (1995). Figure 4.8a shows a biaxial non-proportional stress path. Initially, an axial stress of 240 MPa is ap-

plied and then the shear stress is increased up to approximately 195 MPa, while tension is kept constant. During stages 3 and 4, first tension and then shear are sequentially unloaded, respectively.

Figures 4.8b, 4.8c, 4.8d show the comparison between the predictions of the proposed model, of the model presented by Auricchio and Petrini (2002) (referred to as AP (2002)) and the model presented by Panico and Brinson (2007) (referred to as PB (2007)) with the experimental data in terms of shear strain versus normal strain, normal stress versus normal strain and shear stress versus shear strain, respectively. A qualitatively good agreement between experiments and simulations is obtained for the proposed model, which is able to reproduce the main characteristics of the experimentally observed behaviors. This is particularly true for the coupling between axial and shear strains both in stages 2 and 3.

Moreover, the proposed model can predict the crossing in the shear response observed

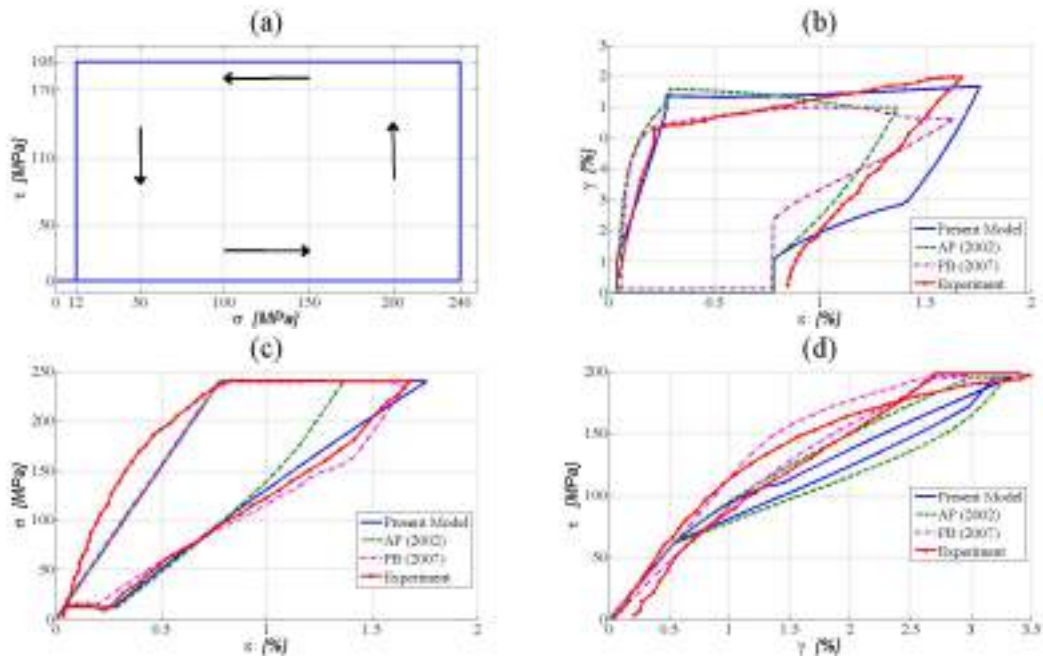


Figure 4.8: Comparison between model predictions and experimental data (Sittner et al., 1995): a) non-proportional biaxial tension-shear path, b) axial-shear strain response, c) axial stress-axial strain response, d) shear stress-shear strain response.

experimentally in Figure 4.8d . Although there is a good qualitative agreement between the proposed model and experimental data, some drawbacks are observed, for example in the second stage of loading, where the coupling effect is not completely in agreement with experiments. This can be partially due to the very simple structure of the proposed model, i.e. assuming R^{re} as a constant material parameter. In order to investigate more this drawback, we present the simulation results along with comparison with AP (2002) and experimental data for two other non-proportional loading paths proposed by Sit-

tner et al. (1995). Accordingly, Figures 4.9 and 4.10 present the results for triangle- and L-shaped stress paths, respectively.

The proposed model captures the basic features of material response to the mentioned loading situations although some differences can be clearly noted if compared to the AP (2002) model. This aspect should be investigated in future studies.

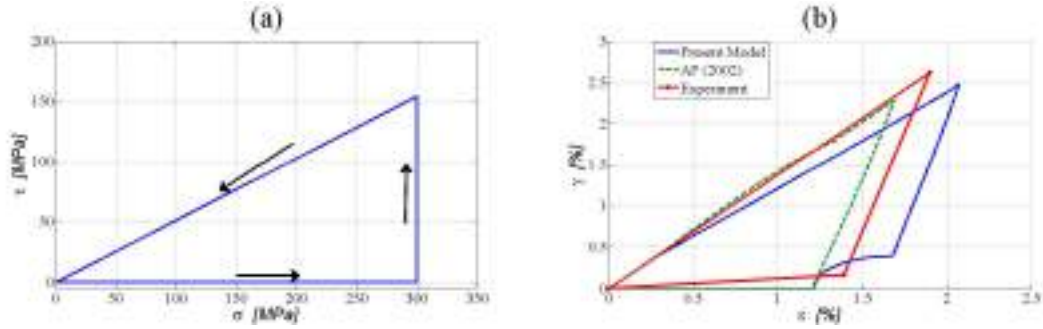


Figure 4.9: Proposed model prediction and comparison with AP (2002) and experimental results (Sittner et al., 1995): a) axial-shear triangle-shaped stress path, b) axial-shear strain response.

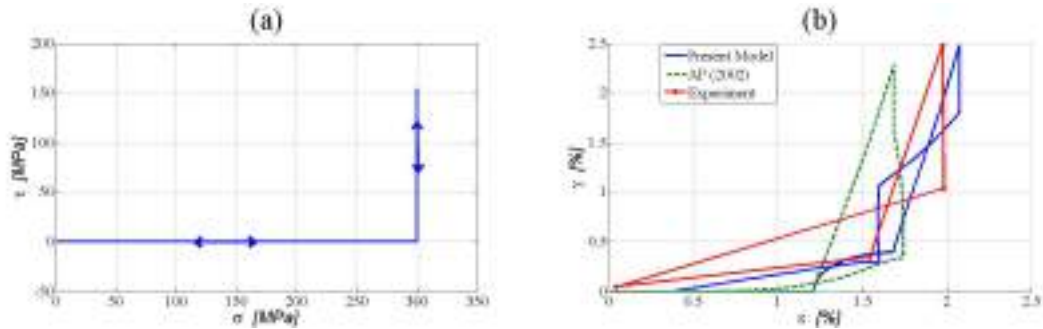


Figure 4.10: Proposed model prediction and comparison with AP (2002) and experimental results (Sittner et al., 1995): a) axial-shear L-shaped stress path, b) axial-shear strain response.

We finally consider the experimental data reported by Bouvet et al. (2002) and Bouvet et al. (2004) on a tubular CuAlBe specimen. In particular, focusing only on experimental tension test data, we choose the material parameters reported in Table 4.7. Figure 4.11 shows a comparison between the proposed model response and experimental data. Using only uniaxial data it is clearly not possible to set a value for the reorientation activation threshold, which is the only parameter left to be determined.

Biaxial tension/compression-internal pressure tests have been performed on tubular CuAlBe specimens to investigate the effects of non-proportionality of the loading path on the super-elastic behavior of SMAs (Bouvet et al., 2002). Since we are using an

Table 4.7: Material parameters adopted for (Bouvet et al., 2002, 2004) experiment.

parameter	value	unit
E	75000	MPa
ν	0.3	-
h	4233	MPa
ε_L	5.85	%
τ_M	51	MPa
T	305	K
R^{tr}	16	MPa

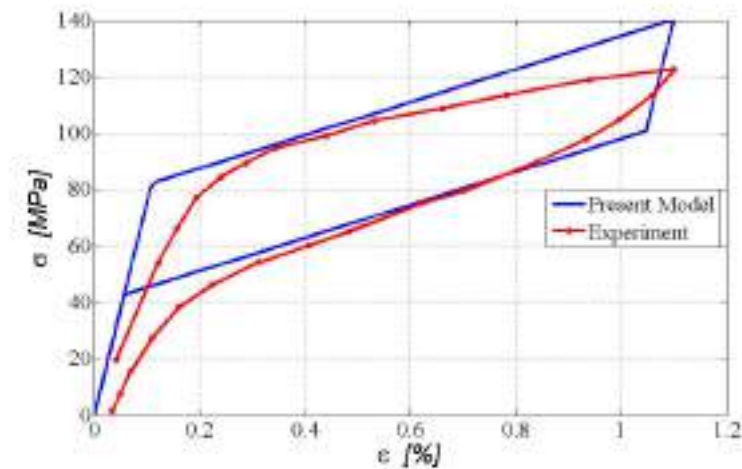


Figure 4.11: Uniaxial tension behavior predicted by the model and comparison with experimental results from Bouvet et al. (2004)

idealized model, experimental data are chosen to reduce tension-compression asymmetry effects, although the material elastic behavior is transversely isotropic ($E_r = 84$ GPa, $E_z = 68$ GPa (Bouvet et al., 2002)). So we concentrate only on the qualitative behavior. With the selected material parameters, we try to reproduce the material response under a non-proportional biaxial tension-internal pressure loading. Figure 4.12a shows a non-proportional biaxial tension test, in which initially a tension stress of 140 MPa in the axial direction is applied, and then an internal pressure is applied to increase the hoop tension stress up to 140 MPa, while the axial tension is kept constant. Then, sequentially, axial tension and internal pressure are removed.

A good correlation between the proposed model predictions and the experimental data is observed for $R^e = R^{tr}$. Figures 4.12b, 4.12c and 4.12d present the comparison between the present model prediction, AP (2002) model prediction and experimental results (Bouvet et al., 2002), respectively in terms of axial versus hoop strain (Figure 4.12b), axial strain versus axial stress (Figure 4.12c), hoop strain versus hoop stress (Figure 4.12d). The model prediction for the axial direction is in good qualitative

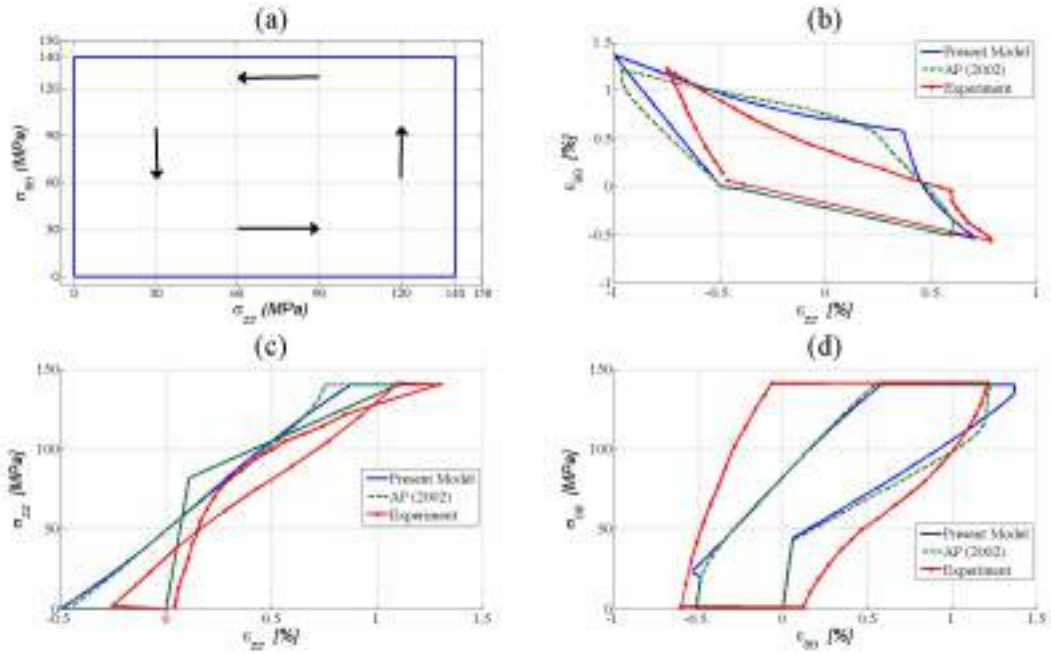


Figure 4.12: Comparison between simulation and experimental results (Bouvet et al., 2002): a) non-proportional biaxial loading path, b) corresponding strain path, c) axial stress-strain curve, d) hoop stress-strain curve.

agreement with the experimental data, but there is a discrepancy with the experiments in the prediction for the hoop direction.

We then consider another set of experimental data, reported in Bouvet et al. (2004), obtained on the same CuAlBe specimen. Figure 4.13a shows the loading path, which is identical to the one considered in the previous test (Figure 4.12a) but it is now applied in the reverse direction (i.e., in Figure 4.13a it is clockwise while in Figure 4.12a it is counter-clockwise).

Figures 4.13b, 4.13c and 4.13d present the comparison between the present model and AP (2002) predictions and experimental results (Bouvet et al., 2004). As a reference we also include the digitized data related to the model proposed in Bouvet et al. (2004) (referred to as BE (2004)), which takes into account the tension-compression asymmetry and the return point memory effects.

A good correlation between the proposed model predictions and the experimental data is again observed for $R^{re} = R^{tr}$. This equality can be interpreted as the macroscopic consequence of microscopic simultaneous forward and reverse transformation, which can link the phase transformation parameter to the reorientation one. We do not limit the model to this case, but this will be the subject of future studies.

According to all the tests reported, we may conclude that the proposed model can describe the reorientation phenomenon in SMAs under non-proportional loading in a good

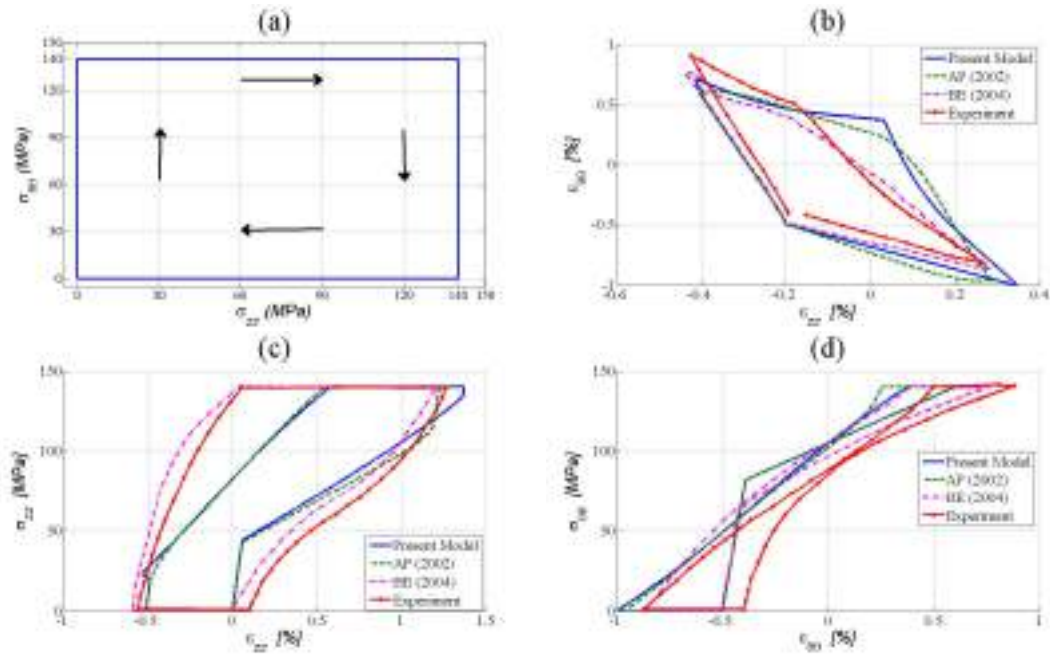


Figure 4.13: Comparison between simulation and experimental results (Bouvet et al., 2004): a) non-proportional biaxial loading path, b) corresponding strain path, c) axial stress-strain curve, d) hoop stress-strain curve.

qualitative way, but it needs some improvements, such as considering the material parameter R^{re} as a function of q , which will be the subject of future works.

Since the internal variables are somehow related to micro-mechanical phenomena, we can find similar concepts if compared with micro-mechanics-based studies. For example the thermodynamic forces and the dissipation inequality arising from the present model are in correlation with analogous expressions in Levitas and Ozsoy (2009). Deriving limit functions motivated by micro-mechanical studies (e.g., Sun and Hwang (1993a); Levitas and Stein (1997); Levitas and Ozsoy (2009)) is an interesting subject for future studies which if adopted, could improve the proposed model capabilities.

4.5 Summary

In this chapter we presented some new features of modeling SMAs behavior under non-proportional loading. A new set of internal variables were introduced; these variables are more physical and in a clear way describe phase transformation and reorientation. It was shown that transformation evolves only by the component of stress in the direction of preferred direction of variants q and only the component of stress normal to the preferred direction affects evolution of variants preferred direction.

The presented formulation has some benefits from numerical point of view, free of regularization can be considered as the most important one. Comparison of the proposed model predictions with experimental data under different non-proportional loading shows a good qualitative agreement which verifies the proposed model capability in capturing the reorientation phenomenon. Moreover, we showed that all models predict the same behavior under a proportional loading and the differences between models are exhibited under non-proportional loadings.

The proposed model has also some drawbacks and needs improvements. Improving the simple model presented in this paper by considering asymmetric behavior, subloops, non-constant hysteresis parameters and etc. can improve the prediction of shape memory alloys behavior under non-proportional loading which could be the subject of future work.

We finally highlight that, reviewing some available models and introducing a class of constitutive models based on the proposed set of internal variables has clarified several aspects of constitutive modeling of shape memory alloys under multiaxial (non-proportional) loading. Introducing an idealized behavior and the concept of the basic constitutive model helped to focus on the most important features of SMAs behavior and to include other less important features (secondary effects) after developing a basic constitutive model.

As a conclusion, we can observe that one of the most important features which still needs considerable research is capturing reorientation behavior under non-proportional loadings. The proposed member of the introduced class, investigated in this work, can be an appropriate start point.

Chapter 5

Constitutive modeling: finite deformation regime

5.1 Introduction

Most devices based on shape memory alloys experience both finite deformations (very large rotations and moderate strains, i.e. in the range of 10-15% for polycrystals (Otsuka and Wayman, 1998)) and non-proportional loading conditions in engineering applications. For example, with reference to biomedical applications, stent structures are usually designed to significantly reduce their diameter during the insertion into a catheter; thereby, large rotations combined with moderate strains occur and the use of a finite deformation scheme is preferred.

Several experimental studies show that the so-called variant reorientation can be assumed as the main phenomenon in non-proportional loadings of SMAs (Bouvet et al., 2002; Grabe and Bruhns, 2009; Helm, 2001; Lim and McDowell, 1999; Sittner et al., 1995). Recently, Grabe and Bruhns (2009) have conducted several multiaxial experiments on polycrystalline NiTi within a wide temperature range, showing the strong nonlinearity as well as the path dependencies of the response and highlighting the presence of reorientation processes for complex loading paths.

These experimental observations, as well as situations experienced by SMAs in real engineering applications, call for the development of 3D SMA constitutive models, taking into account both finite strain and variant reorientation under general loading conditions (multiaxial non-proportional loadings). To this end, in this chapter, based on the principles of continuum thermodynamics with internal variables, several three-dimensional finite strain phenomenological constitutive models are proposed. The proposed finite-strain models took their basis from the constitutive models in the small strain regime discussed in Chapter 4.

We extend the small strain models proposed by Panico and Brinson (2007) and Souza et al. (1998) to the finite strain regime. The finite strain constitutive model derivation is based on the multiplicative decomposition of the deformation gradient into elastic and inelastic parts.

We remark that the extension of a small strain constitutive model into the finite strain regime yields a variety of problems. There are many possible formulations the linearization of which properly recovers the small strain model. But the theoretical concepts deviate noticeably from each other. Considering this point, besides proposing finite strain models based on Green-Lagrange strain measure, we propose a constitutive model based on the logarithmic or Hencky strain measure known as an interesting physical measure of strain. Moreover, we show how it is possible to extend a constitutive model developed within the small-deformation regime into the large rotations (but small strains) regime.

5.2 Literature review: finite strain SMA constitutive models

Finite deformation SMA constitutive models available in the literature (Arghavani et al., 2010b,d; Auricchio, 2001; Auricchio and Taylor, 1997; Christ and Reese, 2009; Evangelista et al., 2009; Helm, 2001; Müller and Bruhns, 2006; Pethö, 2001; Reese and Christ, 2008; Thamburaja, 2010; Ziolkowski, 2007) have been mainly developed by extending small strain constitutive models. The approach in most of the cases is based on the multiplicative decomposition of the deformation gradient into an elastic and an inelastic or transformation part (Auricchio, 2001; Christ and Reese, 2009; Evangelista et al., 2009; Helm, 2001; Pethö, 2001; Reese and Christ, 2008; Ziolkowski, 2007; ?), although there are some models in the literature which have utilized an additive decomposition of the strain rate tensor into an elastic and an inelastic part (Müller and Bruhns, 2006). In the following, we mention some of the finite deformation SMA constitutive models currently available in the literature.

The model by ? is apparently the first macroscopic SMA constitutive model taking into account finite deformation pseudo-elasticity. Disregarding the first invariant of stress, this model reduces to Raniecki and LExcellent (1994) model (R_L model) when linearized. Pethö (2001) decomposes the total deformation gradient into elastic, plastic, and phase transformation parts, describing elasticity using an integrable hypo-elastic model based on the logarithmic rate. Ziolkowski (2007) extends a version of the R_L model (Raniecki and LExcellent, 1994, 1998) to the large deformation regime, considering thermo-mechanical coupling effects. A multiplicative decomposition of the deformation gradient is also proposed by Helm (Helm, 2001; Helm and Haupt, 2003) and

Reese and Christ (Christ and Reese, 2009; Reese and Christ, 2008). Evangelista et al. (2009) and Arghavani et al. (2010b) have extended the small strain model proposed by Souza et al. (1998) and discussed in Auricchio and Petrini (2002, 2004a) to the finite deformation regime. Recently, Thamburaja (2010) has developed a finite-deformation-based, thermo-mechanically-coupled and non-local phenomenological SMA model which is able to determine the position and motion of austenite-martensite interfaces during phase transformations.

While all the above mentioned references use a multiplicative decomposition of the deformation gradient, Müller and Bruhns (2006) utilize an additive decomposition of the strain rate tensor into an elastic and a phase transformation part. In particular, they extend the R_L small strain model (Raniecki and Lexcellent, 1998) to take into account finite deformations and finally reach a rate constitutive model in terms of the logarithmic spin tensor. Bernardini and Pence (2004) have also proposed a finite strain constitutive model within the framework of multifield theories. Moreover, some large strain non-phenomenological models have been proposed in the literature (see e.g., Idesman et al. (1999); Levitas (1998); Pan et al. (2007); Stein and Sagar (2008); Stupkiewicz and Petryk (2006); Thamburaja (2005); Thamburaja and Anand (2001)).

As stated above, finite strain constitutive models are often based on successful small strain ones. Along this line, the model proposed by Souza et al. (1998) as well as the recently proposed three-dimensional model by Panico and Brinson (2007), based on the classical framework of thermodynamics of irreversible processes, represent suitable candidates to be extended to the finite strain regime. In particular, they are interesting for their capability to model both pseudo-elasticity and shape memory effect, as well as description of martensite reorientation under non-proportional loading conditions. It can be an important In this chapter, we first present a finite strain extension of the small strain model proposed by Panico and Brinson (2007). The small strain constitutive model proposed by Souza et al. (1998) has a simple formulation compared with the model proposed by Panico and Brinson which is a great advantage from computational point of view. This features motivate us to develop the finite strain extension of the model proposed by Souza et al. (1998).

5.3 Kinematics description

Following a well-established approach adopted in plasticity (Haupt, 2002; Lubarda, 2001) and already used for SMAs (Auricchio, 2001; Christ and Reese, 2009; Helm, 2001; Pethö, 2001; Reese and Christ, 2008; Ziolkowski, 2007; ?), we assume a multiplicative decomposition of the deformation gradient into an elastic part \mathbf{F}^e , defined with respect

to an intermediate configuration, and an inelastic one \mathbf{F}^{in} , defined with respect to the reference configuration. Accordingly:

$$\mathbf{F} = \mathbf{F}^e \mathbf{F}^{in} \quad (5.1)$$

Since experimental evidences indicate that the inelastic flow due to phase transformation is nearly isochoric, we have to impose $\det(\mathbf{F}^{in}) = 1$, which after taking the time derivative results in:

$$\text{tr}(\mathbf{d}^{in}) = 0 \quad (5.2)$$

where $\mathbf{d}^{in} = \text{sym}(\dot{\mathbf{F}}^{in} \mathbf{F}^{in})$. We define $\mathbf{C}^e = \mathbf{F}^{eT} \mathbf{F}^e$ and $\mathbf{C}^{in} = \mathbf{F}^{inT} \mathbf{F}^{in}$ as the elastic and the inelastic right Cauchy-Green deformation tensors and using definition (5.1), we obtain:

$$\mathbf{C}^e = \mathbf{F}^{in-T} \mathbf{C} \mathbf{F}^{in-1} \quad (5.3)$$

Taking the time derivative of equation (5.3) and using (3.26), the material time derivative of the elastic right Cauchy-Green deformation tensor is obtained as:

$$\dot{\mathbf{C}}^e = -\mathbf{l}^{inT} \mathbf{C}^e + \mathbf{F}^{in-T} \dot{\mathbf{C}} \mathbf{F}^{in-1} - \mathbf{C}^e \mathbf{l}^{in} \quad (5.4)$$

The inelastic Green-Lagrange strain tensor is then defined as:

$$\mathbf{E}^{in} = \frac{\mathbf{C}^{in} - \mathbf{1}}{2} \quad (5.5)$$

5.4 Finite strain extension of Panico and Brinson model

We use the multiplicative decomposition of the deformation gradient into elastic and inelastic parts, along with an additive decomposition of the inelastic strain rate tensor into transformation and reorientation parts to derive the finite strain extension of constitutive model proposed by Panico and Brinson (2007).

To this end, analogously to (4.18), we also define the stress-induced martensite fraction as (Christ and Reese, 2009; Reese and Christ, 2008):

$$z_\sigma = \frac{\|\mathbf{E}^{in}\|}{\varepsilon_L} \quad (5.6)$$

we recall that $\varepsilon_L = \sqrt{\frac{3}{2}}\gamma$ is a material parameter.

In order to satisfy the principle of material objectivity, the Helmholtz free energy has to depend on \mathbf{F}^e only through the elastic right Cauchy-Green deformation tensor; it is moreover assumed to be a function of the stress- and temperature-induced martensite

fractions and the temperature in the following form¹ (Christ and Reese, 2009; Reese and Christ, 2008):

$$\Psi = \Psi(\mathbf{C}^e, z_\sigma, z_T, T) = \frac{1}{\rho_0} W(\mathbf{C}^e) + \psi(z_\sigma, z_T, T) \quad (5.7)$$

where ρ_0 is the reference density and $W(\mathbf{C}^e)$ is a hyperelastic strain energy function (per unit undeformed volume). In addition, we assume $W(\mathbf{C}^e)$ to be an isotropic function of \mathbf{C}^e and to be the same for austenite and martensite phases; it can be therefore expressed as:

$$W(\mathbf{C}^e) = W(I_{\mathbf{C}^e}, II_{\mathbf{C}^e}, III_{\mathbf{C}^e}) \quad (5.8)$$

where $I_{\mathbf{C}^e}, II_{\mathbf{C}^e}, III_{\mathbf{C}^e}$ are the invariants of \mathbf{C}^e . We also define ψ (per unit mass) in the following form (see also equation (4.23)):

$$\begin{aligned} \psi(z_\sigma, z_T, T) = & u_0^A - T\eta_0^A - z_T(\Delta u_0 - T\Delta\eta_0) + z_\sigma \langle T\Delta\eta_0 - \Delta u_0 \rangle \\ & + c_\nu \left[(T - T_0) - T \ln \left(\frac{T}{T_0} \right) \right] + \frac{1}{2} H_\sigma z_\sigma^2 \end{aligned} \quad (5.9)$$

where the meaning of the material parameters is the same as in Chapter 4.

According to (5.6), the time derivative of the stress-induced martensite fraction is given as:

$$\dot{z}_\sigma = \frac{\mathbf{E}^{in}}{\varepsilon_L \|\mathbf{E}^{in}\|} : \dot{\mathbf{E}}^{in} \quad (5.10)$$

where $\dot{\mathbf{E}}^{in}$ is expressed as (see equation (3.29)):

$$\dot{\mathbf{E}}^{in} = \mathbf{F}^{inT} \mathbf{d}^{in} \mathbf{F}^{in} \quad (5.11)$$

Substituting (5.11) into (5.10) and using the relations $\mathbf{C}^{in} = \mathbf{F}^{inT} \mathbf{F}^{in}$, $\mathbf{b}^{in} = \mathbf{F}^{in} \mathbf{F}^{inT}$ and (5.5), we obtain:

$$\dot{z}_\sigma = \frac{\mathbf{F}^{in} \mathbf{E}^{in} \mathbf{F}^{inT}}{\varepsilon_L \|\mathbf{E}^{in}\|} : \mathbf{d}^{in} = \frac{\mathbf{b}^{in^2} - \mathbf{b}^{in}}{2\varepsilon_L \|\mathbf{E}^{in}\|} : \mathbf{d}^{in} \quad (5.12)$$

We now decompose additively \mathbf{d}^{in} into a component \mathbf{d}^{tr} coaxial with $(\mathbf{b}^{in^2} - \mathbf{b}^{in})^D$ and a component \mathbf{d}^{re} normal to $(\mathbf{b}^{in^2} - \mathbf{b}^{in})^D$, where the superscript D indicates the deviator of a tensor ($\mathbf{A}^D = \mathbf{A} - \frac{1}{3}(\text{tr}\mathbf{A})\mathbf{1}$), i.e.:

$$\mathbf{d}^{in} = \mathbf{d}^{tr} + \mathbf{d}^{re} \quad (5.13)$$

with

$$\mathbf{d}^{tr} = (\mathbf{d}^{in} : \bar{\mathbf{n}}) \bar{\mathbf{n}}, \quad \mathbf{d}^{re} = \mathbf{d}^{in} - (\mathbf{d}^{in} : \bar{\mathbf{n}}) \bar{\mathbf{n}} \quad (5.14)$$

¹To be consistent with the small strain model (Panico and Brinson, 2007), we express the free energy in terms of energy per unit mass.

and

$$\bar{\mathbf{n}} = \frac{\left(\mathbf{b}^{in2} - \mathbf{b}^{in}\right)^D}{\left\|\left(\mathbf{b}^{in2} - \mathbf{b}^{in}\right)^D\right\|} \quad (5.15)$$

Using (5.2) and (5.14) we may also conclude that

$$tr(\mathbf{d}^{tr}) = 0, \quad tr(\mathbf{d}^{re}) = 0 \quad (5.16)$$

which is consistent with the experimental evidences of (nearly) isochoric conditions under forward and reverse transformation, as well as during reorientation.

Combining (5.12) and (5.13), we obtain

$$\dot{z}_\sigma = \frac{\mathbf{b}^{in2} - \mathbf{b}^{in}}{2\varepsilon_L \|\mathbf{E}^{in}\|} : (\mathbf{d}^{tr} + \mathbf{d}^{re}) = \frac{\left(\mathbf{b}^{in2} - \mathbf{b}^{in}\right)^D}{2\varepsilon_L \|\mathbf{E}^{in}\|} : (\mathbf{d}^{tr} + \mathbf{d}^{re}) \quad (5.17)$$

According to (5.14) the \mathbf{d}^{re} component does not contribute to the variation of martensite fraction, but only produces a reorientation of the inelastic strain according to the local stress state and consequently, it can be considered as the reorientation part of \mathbf{d}^{in} , while the component \mathbf{d}^{tr} can be considered as the transformation part².

In this way, equation (5.17) reduces to

$$\dot{z}_\sigma = \frac{\left(\mathbf{b}^{in2} - \mathbf{b}^{in}\right)^D}{2\varepsilon_L \|\mathbf{E}^{in}\|} : \mathbf{d}^{tr} = \frac{\mathbf{b}^{in2} - \mathbf{b}^{in}}{2\varepsilon_L \|\mathbf{E}^{in}\|} : \mathbf{d}^{tr} \quad (5.18)$$

Now we use the Clausius-Duhem inequality form of the second law of thermodynamics:

$$\frac{1}{\rho_0} \mathbf{S} : \dot{\mathbf{E}} - \left(\dot{\Psi} + \eta \dot{T}\right) \geq 0 \quad (5.19)$$

Substituting (5.7) into (5.19), after multiplication by ρ_0 , we obtain

$$\mathbf{S} : \frac{1}{2} \dot{\mathbf{C}} - \frac{\partial W}{\partial \mathbf{C}^e} : \dot{\mathbf{C}}^e - \rho_0 \frac{\partial \psi}{\partial z_\sigma} \dot{z}_\sigma - \rho_0 \frac{\partial \psi}{\partial z_T} \dot{z}_T - \rho_0 \left(\eta + \frac{\partial \psi}{\partial T} \right) \dot{T} \geq 0 \quad (5.20)$$

Thus, substituting (5.4) and (5.18) into (5.20), after some mathematical manipulations, we obtain:

$$\begin{aligned} & \left(\mathbf{S} - 2\mathbf{F}^{in-1} \frac{\partial W}{\partial \mathbf{C}^e} \mathbf{F}^{in-T} \right) : \frac{1}{2} \dot{\mathbf{C}} - \rho_0 \left(\eta + \frac{\partial \psi}{\partial T} \right) \dot{T} + \\ & \left(\frac{\partial W}{\partial \mathbf{C}^e} \mathbf{C}^e + \mathbf{C}^e \frac{\partial W}{\partial \mathbf{C}^e} \right) : \mathbf{l}^{in} - \rho_0 \frac{\partial \psi}{\partial z_\sigma} \frac{\mathbf{b}^{in2} - \mathbf{b}^{in}}{2\varepsilon_L \|\mathbf{E}^{in}\|} : \mathbf{d}^{tr} - \rho_0 \frac{\partial \psi}{\partial z_T} \dot{z}_T \geq 0 \end{aligned} \quad (5.21)$$

²This interpretation makes clear the reason for the name choice of the coaxial and normal components as, respectively, \mathbf{d}^{tr} and \mathbf{d}^{re} .

We now use the isotropic property of $W(\mathbf{C}^e)$, implying that \mathbf{C}^e and $\frac{\partial W}{\partial \mathbf{C}^e}$ are coaxial, i.e.:

$$\frac{\partial W}{\partial \mathbf{C}^e} \mathbf{C}^e = \mathbf{C}^e \frac{\partial W}{\partial \mathbf{C}^e} \quad (5.22)$$

Substituting (5.22) into (5.21), we obtain:

$$\begin{aligned} \left(\mathbf{S} - 2\mathbf{F}^{in-1} \frac{\partial W}{\partial \mathbf{C}^e} \mathbf{F}^{in-T} \right) : \frac{1}{2} \dot{\mathbf{C}} - \rho_0 \left(\eta + \frac{\partial \psi}{\partial T} \right) \dot{T} + 2\mathbf{C}^e \frac{\partial W}{\partial \mathbf{C}^e} : \mathbf{l}^{in} \\ - \rho_0 \frac{\partial \psi}{\partial z_\sigma} \frac{\mathbf{b}^{in2} - \mathbf{b}^{in}}{2\varepsilon_L \|\mathbf{E}^{in}\|} : \mathbf{d}^{tr} - \rho_0 \frac{\partial \psi}{\partial z_T} \dot{z}_T \geq 0 \end{aligned} \quad (5.23)$$

Following standard arguments, we finally conclude that:

$$\begin{cases} \mathbf{S} = 2\mathbf{F}^{in-1} \frac{\partial W}{\partial \mathbf{C}^e} \mathbf{F}^{in-T} \\ \eta = -\frac{\partial \psi}{\partial T} \end{cases} \quad (5.24)$$

and

$$\tilde{\mathbf{M}} : \mathbf{d}^{in} - \tilde{\mathbf{N}} : \mathbf{d}^{tr} + X_T \dot{z}_T \geq 0 \quad (5.25)$$

where

$$\begin{cases} \tilde{\mathbf{M}} = 2\mathbf{C}^e \frac{\partial W}{\partial \mathbf{C}^e} \\ \tilde{\mathbf{N}} = \rho_0 \frac{\partial \psi}{\partial z_\sigma} \frac{\mathbf{b}^{in2} - \mathbf{b}^{in}}{2\varepsilon_L \|\mathbf{E}^{in}\|} = \rho_0 [\langle T \Delta \eta_0 - \Delta u_0 \rangle + H_\sigma z_\sigma] \frac{\mathbf{b}^{in2} - \mathbf{b}^{in}}{2\varepsilon_L \|\mathbf{E}^{in}\|} \\ X_T = -\rho_0 \frac{\partial \psi}{\partial z_T} = -\rho_0 (T \Delta \eta_0 - \Delta u_0) \end{cases} \quad (5.26)$$

Combining equations (5.13) and (5.25), the dissipation inequality can be written as:

$$\tilde{\mathbf{M}} : \mathbf{d}^{re} + (\tilde{\mathbf{M}} - \tilde{\mathbf{N}}) : \mathbf{d}^{tr} + X_T \dot{z}_T \geq 0 \quad (5.27)$$

Evolution equations and limit functions

In order to satisfy the second law of thermodynamics (5.27), we may define the following evolution equations:

$$\begin{cases} \dot{\mathbf{d}}^{tr} = \dot{\lambda}_{tr} (\tilde{\mathbf{M}} - \tilde{\mathbf{N}})^D \\ \dot{\mathbf{d}}^{re} = \dot{\lambda}_{re} \tilde{\mathbb{I}} : \tilde{\mathbf{M}}^D \\ \dot{z}^T = \dot{\lambda}_T X_T \end{cases} \quad (5.28)$$

where the fourth order tensor $\tilde{\mathbb{I}}$ is defined as:

$$\tilde{\mathbb{I}} = \mathbb{I} - \bar{\mathbf{n}} \otimes \bar{\mathbf{n}} \quad (5.29)$$

We note that definition (5.28)₂ together with (5.29) ensures that $\mathbf{d}^{re} : \bar{\mathbf{n}} = 0$.

In order to describe phase transformation, reorientation and twinned martensite evolutions, we choose three limit functions F_{tr} , F_{re} and F_T as:

$$\begin{aligned} F_{tr} &= \|(\tilde{\mathbf{M}} - \tilde{\mathbf{N}})^D\| - Y_{tr}(z_\sigma) \\ F_{re} &= \frac{1}{2} \tilde{\mathbf{M}}^D : \tilde{\mathbb{I}} : \tilde{\mathbf{M}}^D - Y_{re} \\ F_T &= \begin{cases} X^T - Y_T^f(z_T) & \text{if } \dot{z}_T > 0 \\ -X^T - Y_T^r(z_T) & \text{if } \dot{z}_T < 0 \end{cases} \end{aligned} \quad (5.30)$$

where Y_{re} is a material parameter controlling the reorientation process, while $Y_{tr}(z_\sigma)$ is a function governing the kinetics of the phase transformation. We assume functions $Y_{tr}(z_\sigma)$ and $Y_T^f(z_T)$ to have the same form as in the small strain formulation (see (4.31) and (4.32₁)). Moreover, we assume the following form for Y_T^r :

$$Y_T^r(z_T) = Y_{T0}^r + \tilde{\sigma} + c^r(1 - z_T) \quad (5.31)$$

with $\tilde{\sigma} = \sqrt{\frac{3}{2}(\mathbf{J}\mathbf{s}) : (\mathbf{J}\mathbf{s})}$.

Similarly to plasticity, the consistency parameters and the limit functions satisfy the Kuhn-Tucker conditions:

$$\begin{aligned} F_{tr} &\leq 0, \quad \dot{\lambda}_{tr} \geq 0, \quad \dot{\lambda}_{tr} F_{tr} = 0 \\ F_{re} &\leq 0, \quad \dot{\lambda}_{re} \geq 0, \quad \dot{\lambda}_{re} F_{re} = 0 \\ F_T &\leq 0, \quad \dot{\lambda}_T \geq 0, \quad \dot{\lambda}_T F_T = 0 \end{aligned} \quad (5.32)$$

5.4.1 Representation with respect to the reference configuration

In the previous section, using a multiplicative decomposition of the deformation gradient into elastic and inelastic parts, we derived a finite strain constitutive model for SMAs. But while \mathbf{F} and \mathbf{F}^{in} are related to the reference configuration, \mathbf{F}^e has been defined with respect to an intermediate configuration. It is however necessary to recast all equations in terms of quantities described with respect to the reference configuration, so that all quantities are Lagrangian.

Since a hyperelastic strain energy function $W(\mathbf{C}^e)$ has been introduced in terms of \mathbf{C}^e (i.e. with respect to the intermediate configuration), we first investigate it.

As introduced in (5.8), W depends on \mathbf{C}^e only through its invariants. But the invariants of \mathbf{C}^e are equal to those of $\mathbf{C}\mathbf{C}^{in-1}$, as we show for the first invariant (the same can be shown also for the second and the third invariants in a similar way):

$$I_{\mathbf{C}^e} = tr(\mathbf{C}^e) = tr(\mathbf{F}^{in-T} \mathbf{C} \mathbf{F}^{in-1}) = tr(\mathbf{C} \mathbf{F}^{in-1} \mathbf{F}^{in-T}) = tr(\mathbf{C} \mathbf{C}^{in-1}) = I_{\mathbf{C}\mathbf{C}^{in-1}} \quad (5.33)$$

Since we assumed W to be an isotropic function of \mathbf{C}^e , considering representation theorem it can be written in the following form (Ogden, 1984):

$$\frac{\partial W}{\partial \mathbf{C}^e} = \alpha_1 \mathbf{1} + \alpha_2 \mathbf{C}^e + \alpha_3 \mathbf{C}^{e2} \quad (5.34)$$

where $\alpha_i = \alpha_i(I_{\mathbf{C}^e}, II_{\mathbf{C}^e}, III_{\mathbf{C}^e})$. Substituting (5.34) into (5.24) and using (5.3), we conclude that:

$$\mathbf{S} = 2 \left(\alpha_1 \mathbf{C}^{in-1} + \alpha_2 \mathbf{C}^{in-1} \mathbf{C} \mathbf{C}^{in-1} + \alpha_3 \mathbf{C}^{in-1} \left(\mathbf{C} \mathbf{C}^{in-1} \right)^2 \right) \quad (5.35)$$

which expresses the second Piola-Kirchhoff stress tensor in terms of quantities computed with respect to the reference configuration.

In order to find the Lagrangian form of the tensorial evolution equation, we combine (5.28) with (5.13) and substituting it into (5.11), we obtain:

$$\dot{\mathbf{E}}^{in} = \mathbf{F}^{inT} \left(\dot{\lambda}_{tr} \left(\tilde{\mathbf{M}} - \tilde{\mathbf{N}} \right)^D + \dot{\lambda}_{re} \tilde{\mathbb{I}} : \tilde{\mathbf{M}}^D \right) \mathbf{F}^{in} \quad (5.36)$$

or equivalently,

$$\dot{\mathbf{C}}^{in} = 2 \dot{\lambda}_{tr} \mathbf{F}^{inT} \left(\tilde{\mathbf{M}} - \tilde{\mathbf{N}} \right)^D \mathbf{F}^{in} + 2 \dot{\lambda}_{re} \mathbf{F}^{inT} \tilde{\mathbb{I}} : \tilde{\mathbf{M}}^D \mathbf{F}^{in} \quad (5.37)$$

We now consider the first term in the definition of the tensorial internal variable in (5.37), which is related to the transformation. To this end we compute:

$$\mathbf{F}^{inT} \tilde{\mathbf{M}} \mathbf{F}^{in} = (\mathbf{F}^{in} \mathbf{C}^e \mathbf{F}^{in}) (\mathbf{F}^{in-1} 2 \frac{\partial W}{\partial \mathbf{C}^e} \mathbf{F}^{in-T}) \mathbf{C}^{in} = \mathbf{C} \mathbf{S} \mathbf{C}^{in} \quad (5.38)$$

and

$$\mathbf{F}^{inT} \tilde{\mathbf{N}} \mathbf{F}^{in} = \rho_0 \frac{\partial \psi}{\partial z_\sigma} \frac{\mathbf{C}^{in3} - \mathbf{C}^{in2}}{2 \varepsilon_L \|\mathbf{E}^{in}\|} = \mathbf{C}^{in} \left(\frac{\rho_0}{\varepsilon_L} \frac{\partial \psi}{\partial z_\sigma} \frac{\mathbf{E}^{in}}{\|\mathbf{E}^{in}\|} \right) \mathbf{C}^{in} = \mathbf{C}^{in} \mathbf{X} \mathbf{C}^{in} \quad (5.39)$$

where we have defined:

$$\mathbf{X} = \frac{\rho_0}{\varepsilon_L} \frac{\partial \psi}{\partial z_\sigma} \frac{\mathbf{E}^{in}}{\|\mathbf{E}^{in}\|} \quad (5.40)$$

We now define:

$$\mathbf{Y} \mathbf{C}^{in} = \mathbf{F}^{inT} (\tilde{\mathbf{M}} - \tilde{\mathbf{N}}) \mathbf{F}^{in} \quad (5.41)$$

and obtain from (5.38)-(5.41) the asymmetric tensor \mathbf{Y} as follows:

$$\mathbf{Y} = \mathbf{C} \mathbf{S} - \mathbf{C}^{in} \mathbf{X} \quad (5.42)$$

Moreover, we have:

$$\begin{aligned} \mathbf{F}^{inT} (\tilde{\mathbf{M}} - \tilde{\mathbf{N}})^D \mathbf{F}^{in} &= \mathbf{F}^{inT} \left(\tilde{\mathbf{M}} - \tilde{\mathbf{N}} - \frac{1}{3} \text{tr}(\tilde{\mathbf{M}} - \tilde{\mathbf{N}}) \mathbf{1} \right) \mathbf{F}^{in} = \\ &= (\mathbf{C} \mathbf{S} \mathbf{C}^{in} - \mathbf{C}^{in} \mathbf{X} \mathbf{C}^{in} - \frac{1}{3} \text{tr}(\mathbf{C} \mathbf{S}) \mathbf{C}^{in} + \frac{1}{3} \text{tr}(\mathbf{C}^{in} \mathbf{X}) \mathbf{C}^{in}) = \mathbf{Y}^D \mathbf{C}^{in} \end{aligned} \quad (5.43)$$

yielding

$$(\tilde{\mathbf{M}} - \tilde{\mathbf{N}})^D = \mathbf{F}^{in-T} \mathbf{Y}^D \mathbf{F}^{inT} \quad (5.44)$$

and

$$\|\underline{\mathbf{Y}^D}\|^2 = (\tilde{\mathbf{M}} - \tilde{\mathbf{N}})^D : (\tilde{\mathbf{M}} - \tilde{\mathbf{N}})^{DT} = \mathbf{Y}^D : \mathbf{Y}^{DT} = \|\underline{\mathbf{Y}^D}\|^2 \quad (5.45)$$

where $\|\cdot\|$ is the norm operator, defined as³ $\|\mathbf{A}\| = (\mathbf{A} : \mathbf{A}^T)^{\frac{1}{2}}$

The second term in the evolution equation (5.37) can be rewritten in a similar way as:

$$\mathbf{F}^{inT} (\tilde{\mathbb{I}} : \tilde{\mathbf{M}}^D) \mathbf{F}^{in} = (\tilde{\mathbb{I}} : \mathbf{M}^D) \mathbf{C}^{in} \quad (5.46)$$

where

$$\mathbf{M} = \mathbf{C} \mathbf{S} \quad (5.47)$$

$$\tilde{\mathbb{I}} = \mathbb{I} - \tilde{\mathbf{H}} \otimes \tilde{\mathbf{H}} \quad (5.48)$$

$$\tilde{\mathbf{H}} = \frac{(\mathbf{C}^{in2} - \mathbf{C}^{in})^D}{\|(\mathbf{C}^{in2} - \mathbf{C}^{in})^D\|} \quad (5.49)$$

It can also be shown that:

$$\tilde{\mathbf{M}}^D : \tilde{\mathbb{I}} : \tilde{\mathbf{M}}^D = \mathbf{M}^D : \tilde{\mathbb{I}} : \mathbf{M}^D \quad (5.50)$$

Finally using (3.55), we obtain

$$(\mathbf{J} \mathbf{s}) : (\mathbf{J} \mathbf{s}) = \|\underline{(\mathbf{C} \mathbf{S})^D}\|^2 \quad (5.51)$$

showing that in (5.31) we can express $\tilde{\sigma}$ in terms of quantities defined with respect to the reference configuration.

Table 5.1 finally summarizes the finite deformation extension of Panico and Brinson (2007) constitutive model, written in terms of Lagrangian quantities only.

³ We remark that the norm operator $\|\cdot\|$ is different from the Frobenius norm (defined as $\|\mathbf{A}\| = (\mathbf{A} : \mathbf{A})^{\frac{1}{2}}$), but is an admissible operator and satisfies the objectivity requirement as it can be shown by using the transformation rule of second order tensors, i.e., $A_{ij}^* = \Omega_{ik} \Omega_{jl} A_{kl}$ ($\mathbf{\Omega}$ being a proper orthogonal tensor), to obtain:

$$\mathbf{A}^* : \mathbf{A}^{*T} = A_{ij}^* A_{ji}^* = \Omega_{ik} \Omega_{jl} A_{kl} \Omega_{jm} \Omega_{in} A_{mn} = (\Omega_{ik} \Omega_{in}) (\Omega_{jl} \Omega_{jm}) (A_{kl} A_{mn}) = \delta_{nk} \delta_{ml} A_{kl} A_{mn} = A_{kl} A_{lk} = \mathbf{A} : \mathbf{A}^T$$

Moreover, both norm definitions yield the same result for a symmetric tensor. Finally, the adopted norm has already been used in several works (see, e.g., Christ and Reese (2009)).

Remark: To be consistent with the small strain constitutive model development approach by Panico and Brinson, in this Section we used $\{\mathbf{C}^e, T\}$ and $\{z_\sigma, z_T\}$ as control and internal variables, respectively. But we prefer to consider $\{\mathbf{C}, T\}$ and $\{\mathbf{C}^{in}, z_T\}$ as control and internal variables, respectively, as the final form of constitutive model confirms this. To this end, in Appendix A, we have developed finite strain constitutive model considering $\{\mathbf{C}, T\}$ as control variables as well as $\{\mathbf{C}^{in}, z_T\}$ as internal ones showing that both approaches lead to the same constitutive equations.

5.4.2 Linearization of the finite deformation SMA model

In this section, we derive the linearized form of the constitutive equations proposed in Section 5.7.3 and show that it reduces to the small strain constitutive model in Panico and Brinson (2007). Since we have obtained the model by extending the small strain model, this reduction is expected, however it is a very simple approach to check the correctness of the developed finite strain model.

The infinitesimal strain tensor is defined as:

$$\boldsymbol{\varepsilon} = \frac{1}{2} \left(\nabla \mathbf{u} + (\nabla \mathbf{u})^T \right) \quad (5.52)$$

According to the definition of displacement vector, $\mathbf{u} = \mathbf{x} - \mathbf{X}$, we have:

$$\nabla \mathbf{u} = \mathbf{F} - \mathbf{1} \quad (5.53)$$

Substituting \mathbf{F} from (5.53) into (5.52), we find the relation between the Green-Lagrange strain tensor and the infinitesimal strain tensor as:

$$\mathbf{E} = \boldsymbol{\varepsilon} + \frac{1}{2} (\nabla \mathbf{u})^T (\nabla \mathbf{u}) \quad (5.54)$$

Neglecting higher order terms, we then obtain the linearized form of kinematic quantities as

$$\begin{aligned} \mathbf{E} &\simeq \boldsymbol{\varepsilon}, & \mathbf{C} &= \mathbf{1} + 2\mathbf{E} \simeq \mathbf{1} + 2\boldsymbol{\varepsilon} \\ \mathbf{E}^{in} &\simeq \boldsymbol{\varepsilon}^{in}, & \mathbf{C}^{in} &= \mathbf{1} + 2\mathbf{E}^{in} \simeq \mathbf{1} + 2\boldsymbol{\varepsilon}^{in} \\ \mathbf{C}^{in^2} - \mathbf{C}^{in} &\simeq 2\boldsymbol{\varepsilon}^{in} \end{aligned} \quad (5.55)$$

Also, it can be shown that stress quantities have the following linearized form:

$$\begin{aligned} \mathbf{S} &\simeq tr(\boldsymbol{\varepsilon}) \boldsymbol{\sigma} = \frac{\rho_0}{\rho} \boldsymbol{\sigma} \simeq \boldsymbol{\sigma} \\ \mathbf{CS} &\simeq \boldsymbol{\sigma} \\ \mathbf{X} &\simeq \rho \frac{1}{\varepsilon_L} \frac{\partial \psi}{\partial z_\sigma} \frac{\boldsymbol{\varepsilon}^{in}}{\|\boldsymbol{\varepsilon}^{in}\|} = \bar{\mathbf{x}} \\ \mathbf{Y}^D &\simeq \mathbf{s} - \bar{\mathbf{x}} = \mathbf{x}^{tr} \\ \mathbf{M}^D &\simeq \mathbf{s} = \mathbf{x}^{re} \\ X^T &= -\rho_0 (T \Delta \eta_0 - \Delta u_0) \simeq x_T \end{aligned} \quad (5.56)$$

In finite elasticity, it is usually supposed that for a hyperelastic material, the strain energy function $W(\mathbf{C}^e)$ reduces to the strain energy of a Hookean elastic material in the small strain regime (Ogden, 1984). Therefore, we may conclude that independently on the functional form of $W(\mathbf{C}^e)$ (e.g., Saint-Venant Kirchhoff type, Neo-Hookean, Mooney-Rivlin, Ogden, etc.), the linearized form reads as:

$$W \simeq \frac{1}{2}\lambda(\text{tr}(\boldsymbol{\varepsilon}^e))^2 + \mu\text{tr}(\boldsymbol{\varepsilon}^e{}^2) \quad (5.57)$$

where λ and μ are Lamè constants.

Applying the linearized forms in (5.55)-(5.57) to the finite deformation constitutive model of Section 5.4.1 readily gives the same constitutive model proposed in Panico and Brinson (2007).

5.5 Finite strain extension of Souza model

We use a multiplicative decomposition of the deformation gradient and present a thermodynamically consistent finite strain extension of Souza model. As stated before, to satisfy the principle of material objectivity, the Helmholtz free energy has to depend on \mathbf{F}^e only through the elastic right Cauchy-Green deformation tensor; it is moreover assumed to be a function of the transformation right Cauchy-Green deformation tensor and of the temperature, T , in the following form:

$$\Psi = \Psi(\mathbf{C}^e, \mathbf{C}^{in}, T) = W(\mathbf{C}^e) + \psi^{in}(\mathbf{E}^{in}, T) \quad (5.58)$$

We remark that in proposing decomposition (5.58), we have assumed the same material behavior for the austenite and martensite phases. In addition, we assume $W(\mathbf{C}^e)$ to be an isotropic function of \mathbf{C}^e . We also define ψ^{in} in the following form (Auricchio and Petrini, 2002; Souza et al., 1998):

$$\psi^{in}(\mathbf{E}^{in}, T) = \tau_M(T)\|\mathbf{E}^{in}\| + \frac{1}{2}h\|\mathbf{E}^{in}\|^2 + \mathcal{I}_{\varepsilon_L}(\|\mathbf{E}^{in}\|) \quad (5.59)$$

similarly to small strain model, $\tau_M(T) = \beta\langle T - T_0 \rangle$ and β , T_0 and h are material parameters. We also use the indicator function $\mathcal{I}_{\varepsilon_L}$ defined as:

$$\mathcal{I}_{\varepsilon_L}(\|\mathbf{E}^{in}\|) = \begin{cases} 0 & \text{if } \|\mathbf{E}^{in}\| \leq \varepsilon_L \\ +\infty & \text{otherwise} \end{cases} \quad (5.60)$$

to satisfy the constraint on the transformation strain norm, i.e.:

$$\|\mathbf{E}^{in}\| \leq \varepsilon_L \quad (5.61)$$

We now use Clausius-Duhem inequality form of the second law of thermodynamics (per unit undeformed volume):

$$\mathbf{S} : \frac{1}{2}\dot{\mathbf{C}} - (\dot{\Psi} + \eta\dot{T}) \geq 0 \quad (5.62)$$

Substituting (5.58) into (5.62), we obtain:

$$\mathbf{S} : \frac{1}{2}\dot{\mathbf{C}} - \left(\frac{\partial W}{\partial \mathbf{C}^e} : \dot{\mathbf{C}}^e + \frac{\partial \psi^{in}}{\partial \mathbf{E}^{in}} : \dot{\mathbf{E}}^{in} + \frac{\partial \psi^{in}}{\partial T} \dot{T} \right) - \eta\dot{T} \geq 0 \quad (5.63)$$

Now, substituting (5.4) into (5.63), after some mathematical manipulations, we obtain:

$$\left(\mathbf{S} - 2\mathbf{F}^{in-1} \frac{\partial W}{\partial \mathbf{C}^e} \mathbf{F}^{in-T} \right) : \frac{1}{2}\dot{\mathbf{C}} + 2\mathbf{C}^e \frac{\partial W}{\partial \mathbf{C}^e} : \mathbf{l}^{in} - \mathbf{X} : \dot{\mathbf{E}}^{in} - \left(\eta + \frac{\partial \psi^{in}}{\partial T} \right) \dot{T} \geq 0 \quad (5.64)$$

where

$$\mathbf{X} = h\mathbf{E}^{in} + (\tau_M(T) + \gamma) \mathbf{N} \quad (5.65)$$

and

$$\mathbf{N} = \frac{\mathbf{E}^{in}}{\|\mathbf{E}^{in}\|} \quad (5.66)$$

The positive variable γ results from the indicator function subdifferential $\partial \mathcal{I}_{\varepsilon_L}(\|\mathbf{E}^{in}\|)$ and it is such that:

$$\begin{cases} \gamma \geq 0 & \text{if } \|\mathbf{E}^{in}\| = \varepsilon_L \\ \gamma = 0 & \text{otherwise} \end{cases} \quad (5.67)$$

In deriving (5.64) we have used the isotropic property of $W(\mathbf{C}^e)$, implying that \mathbf{C}^e and $\frac{\partial W}{\partial \mathbf{C}^e}$ are coaxial. Following standard arguments, we finally conclude:

$$\begin{cases} \mathbf{S} = 2\mathbf{F}^{in-1} \frac{\partial W}{\partial \mathbf{C}^e} \mathbf{F}^{in-T} \\ \eta = -\frac{\partial \psi^{in}}{\partial T}, \end{cases} \quad (5.68)$$

Using a classical property of second-order tensor double contraction, i.e., $\mathbf{A} : (\mathbf{BC}) = \mathbf{B} : (\mathbf{AC}^T) = \mathbf{C} : (\mathbf{B}^T \mathbf{A})$, we conclude:

$$\mathbf{X} : \dot{\mathbf{E}}^{in} = \left(\mathbf{F}^{in} \mathbf{X} \mathbf{F}^{inT} \right) : \mathbf{d}^{in} \quad (5.69)$$

In deriving (5.69) we have used the following relation:

$$\dot{\mathbf{E}}^{in} = \mathbf{F}^{inT} \mathbf{d}^{in} \mathbf{F}^{in} \quad (5.70)$$

Substituting (5.68) and (5.69) into (5.64) and taking advantage of the symmetry of $\mathbf{C}^e \frac{\partial W}{\partial \mathbf{C}^e}$, the dissipation inequality can be written as:

$$(\mathbf{P} - \mathbf{K}) : \mathbf{d}^{in} \geq 0 \quad (5.71)$$

where

$$\begin{cases} \mathbf{P} &= 2\mathbf{C}^e \frac{\partial W}{\partial \mathbf{C}^e} \\ \mathbf{K} &= \mathbf{F}^{in} \mathbf{X} \mathbf{F}^{inT} \end{cases} \quad (5.72)$$

To satisfy the second law of thermodynamics, (5.71), we define the following evolution equation:

$$\mathbf{d}^{in} = \dot{\zeta} \frac{(\mathbf{P} - \mathbf{K})^D}{\|(\mathbf{P} - \mathbf{K})^D\|} \quad (5.73)$$

Moreover, we highlight that (5.73) satisfies the inelastic deformation incompressibility condition (5.2).

To describe phase transformation, we choose the following limit function:

$$f = \|(\mathbf{P} - \mathbf{K})^D\| - R \quad (5.74)$$

where the material parameter R is the elastic region radius. Similarly to plasticity, we also introduce the consistency parameter and the limit function satisfying the Kuhn-Tucker conditions:

$$f \leq 0, \quad \dot{\zeta} \geq 0, \quad \dot{\zeta} f = 0 \quad (5.75)$$

In conclusion, the constitutive model in the finite deformation regime can be finally summarized as follows:

- Stress quantities:

$$\begin{aligned} \mathbf{S} &= 2\mathbf{F}^{in-1} \frac{\partial W}{\partial \mathbf{C}^e} \mathbf{F}^{in-T} \\ \mathbf{P} &= 2\mathbf{C}^e \frac{\partial W}{\partial \mathbf{C}^e} \\ \mathbf{X} &= h\mathbf{E}^{in} + (\tau_M + \gamma) \mathbf{N} \\ \mathbf{K} &= \mathbf{F}^{in} \mathbf{X} \mathbf{F}^{inT} \end{aligned}$$

- Evolution equation:

$$\mathbf{d}^{in} = \dot{\zeta} \frac{(\mathbf{P} - \mathbf{K})^D}{\|(\mathbf{P} - \mathbf{K})^D\|}$$

- Limit function:

$$f = \|(\mathbf{P} - \mathbf{K})^D\| - R$$

- Kuhn-Tucker conditions:

$$f \leq 0, \quad \dot{\zeta} \geq 0, \quad \dot{\zeta} f = 0$$

5.5.1 Representation with respect to the reference configuration.

We now recast all equations in terms of \mathbf{C} (control variable) and \mathbf{C}^t (internal variable) which are described with respect to the reference configuration.

As it has already been shown in 5.4.1, considering the isotropic property of W , we can express the second Piola-Kirchhoff stress tensor in terms of quantities computed with respect to the reference configuration as follows:

$$\mathbf{S} = 2 \left(\alpha_1 \mathbf{C}^{in-1} + \alpha_2 \mathbf{C}^{in-1} \mathbf{C} \mathbf{C}^{in-1} + \alpha_3 \mathbf{C}^{in-1} \left(\mathbf{C} \mathbf{C}^{in-1} \right)^2 \right) \quad (5.76)$$

In order to find the Lagrangian form of the evolution equation, we follow an approach similar to one we used in Section 5.4.1 and obtain:

$$\mathbf{F}^{inT} (\mathbf{P} - \mathbf{K}) \mathbf{F}^{in} = \mathbf{Y} \mathbf{C}^{in} \quad (5.77)$$

where

$$\mathbf{Y} = \mathbf{C} \mathbf{S} - \mathbf{C}^{in} \mathbf{X} \quad (5.78)$$

Now, we can express the limit function and the evolution equation as:

$$f = \|\underline{\mathbf{Y}^D}\| - R \quad (5.79)$$

and

$$\dot{\mathbf{C}}^{in} = 2 \dot{\zeta} \frac{\mathbf{Y}^D}{\|\underline{\mathbf{Y}^D}\|} \mathbf{C}^{in} = \dot{\zeta} \mathbf{A} = \dot{\zeta} \mathbf{A}_1 \mathbf{C}^{in} \quad (5.80)$$

where

$$\mathbf{A} = 2 \frac{\mathbf{Y}^D}{\|\underline{\mathbf{Y}^D}\|} \mathbf{C}^{in} \quad \text{and} \quad \mathbf{A}_1 = 2 \frac{\mathbf{Y}^D}{\|\underline{\mathbf{Y}^D}\|} \quad (5.81)$$

5.5.2 A singularity-free, continuous definition for \mathbf{N}

We note that, according to (5.66), the variable \mathbf{N} is not defined for the case of vanishing transformation strain. Despite some discussions in the paper by Auricchio and Petrini (2002)⁴, regularization schemes have extensively been used in the literature to overcome this problem. For example, Helm and Haupt (2003) propose the following regularization scheme also used in (Auricchio et al., 2007, 2009c; Christ and Reese, 2009; Panico and Brinson, 2007; Reese and Christ, 2008):

$$\|\underline{\mathbf{E}^{in}}\| = \sqrt{\|\mathbf{E}^{in}\|^2 + \delta} \quad (5.82)$$

⁴ Auricchio and Petrini (2002) tried to define a non-singular equation in the small-strain regime. However, the approach is completely different from the one followed herein which is based on a well-defined \mathbf{N} . In fact, in Auricchio and Petrini (2002) a non-singular variable corresponding to limit function f (or, equivalently, the linearized form of $\|\mathbf{Y}\|$) is presented.

where δ is a user defined parameter (typical value: 10^{-7}) and a bar over the norm operator denoted the regularization. In Auricchio and Petrini (2004a) and adopted also in (Auricchio and Petrini, 2004b; Evangelista et al., 2009), another proposed regularization scheme is as follows:

$$\overline{\|\mathbf{E}^{in}\|} = \|\mathbf{E}^{in}\| - \frac{d^{\frac{d+1}{d}}}{d-1} (\|\mathbf{E}^{in}\| + d)^{\frac{d-1}{d}} \quad (5.83)$$

where d is again a user defined parameter (typical value: 0.02). Regularization schemes (5.82) and (5.83) are indeed equivalent, despite they have different forms.

While using a regularization scheme has some advantages in removing singularity in \mathbf{N} and in giving a smooth transition from austenitic to martensitic phase and vice versa with a quite simple approach, it has however the disadvantage of transforming a large part of the elastic region into a region of nonlinear material response. For example, in the simple case of uniaxial loading, when the regularized scheme (5.82) is used, for the $(\mathbf{CS}_e)^D$ values in the interval of $[0, \tau_M - R]$ the limit function is positive and it is assumed that material response is nonlinear; however, from physical point of view, its response should be elastic and there is no need to solve a nonlinear system. We can see that this interval increases with increasing temperatures and is zero for the case of $\tau_M - R < 0$ which occurs for the SME case.

This significantly increases the solution time and consequently decreases the numerical efficiency, especially for boundary value problems in which considerable part of the structure remains elastic (e.g., a stent structure). In the following, motivated by the work by Arghavani et al. (2010c) in the small-strain regime, we suggest to avoid a regularized form for $\|\mathbf{E}^{in}\|$ and to deal with the case of vanishing transformation strain through a careful analytical study of the limiting conditions. We start investigating a condition in which \mathbf{E}^{in} starts to evolve from a zero value (indicated in the following as *Nucleation*), i.e., $\mathbf{E}^{in} = \mathbf{0}$ with $\overline{\|\dot{\mathbf{E}}^{in}\|} > 0$. Substituting $\mathbf{C}^{in} = \mathbf{1}$ into (5.78) (also see (5.65) and (5.76)) we conclude that $\mathbf{Y}^D = (\mathbf{CS}_e)^D$. We now consider (5.80) which yields:

$$\dot{\mathbf{E}}^{in} = \frac{1}{2} \dot{\mathbf{C}}^{in} = \dot{\zeta} \frac{(\mathbf{CS}_e)^D}{\|(\mathbf{CS}_e)^D\|} \quad (5.84)$$

where $\mathbf{S}_e = 2(\alpha_1 \mathbf{1} + \alpha_2 \mathbf{C} + \alpha_3 \mathbf{C}^2)$ is the stress obtained from (5.76) substituting $\mathbf{1}$ in place of \mathbf{C}^{in} . According to (5.84), the transformation strain, \mathbf{E}^{in} , nucleates in the $(\mathbf{CS}_e)^D$ direction.

We now investigate the case when transformation strain vanishes from a nonzero value (indicated in the following as *Completion*), i.e., $\mathbf{E}^{in} = \mathbf{0}$ ($\mathbf{C}^{in} = \mathbf{1}$) with $\overline{\|\dot{\mathbf{E}}^{in}\|} < 0$. Since $\|\mathbf{E}^{in}\| = 0$, we conclude that adopting any arbitrary direction \mathbf{N} leads to $\mathbf{E}^{in} = \mathbf{0}$. As stated in Arghavani et al. (2010c) (for a small-strain case), we select this direction as the $(\mathbf{CS}_e)^D$ direction which also guarantees continuity. Therefore, we revise the variable

\mathbf{N} in the following form:

$$\mathbf{N} = \begin{cases} \frac{(\mathbf{CS}_e)^D}{\|(\mathbf{CS}_e)^D\|} & \text{if } \|\mathbf{E}^{in}\| = 0 \\ \frac{\mathbf{E}^{in}}{\|\mathbf{E}^{in}\|} & \text{if } \|\mathbf{E}^{in}\| \neq 0 \end{cases} \quad (5.85)$$

Equation (5.85) means that in the case of non-vanishing transformation strain, \mathbf{N} is the direction of the inelastic strain tensor while in the vanishing case, it is defined as the direction of stress tensor $(\mathbf{CS}_e)^D$ which still is definite for the case of $(\mathbf{CS}_e)^D = \mathbf{0}$, as the direction of a tensor (or a vector) is independent from its value or norm. However, it needs some consideration in numerical implementation which would be addressed in Section 6.2.3.

We note that according to the above discussion, the tensor \mathbf{N} and consequently the tensor \mathbf{X} are well-defined, non-singular and continuous.

Finally, Table 5.2 summarizes the time-continuous finite-strain constitutive model, written only in terms of Lagrangian quantities.

5.6 An approach to fully symmetrize the derived constitutive models

We observe that due to the asymmetry of \mathbf{CS} , the quantity \mathbf{Y} is not symmetric. The asymmetric tensor \mathbf{Y} also appears in the constitutive equations proposed in (Arghavani et al., 2010b,d; Christ and Reese, 2009; Evangelista et al., 2009; Reese and Christ, 2008). To this end, we present an alternative formulation which is in terms of symmetric tensors only. According to (5.76), we may write:

$$\mathbf{CS} = 2 \left(\alpha_1 \mathbf{CC}^{in-1} + \alpha_2 \left(\mathbf{CC}^{in-1} \right)^2 + \alpha_3 \left(\mathbf{CC}^{in-1} \right)^3 \right) \quad (5.86)$$

Equation (5.86) shows that the asymmetry in \mathbf{CS} is due to the asymmetric term \mathbf{CC}^{in-1} . We now present the following identity

$$\mathbf{CC}^{in-1} = \mathbf{U}^{in} \left(\mathbf{U}^{in-1} \mathbf{CU}^{in-1} \right) \mathbf{U}^{in-1} = \mathbf{U}^{in} \tilde{\mathbf{C}} \mathbf{U}^{in-1} \quad (5.87)$$

where

$$\tilde{\mathbf{C}} = \mathbf{U}^{in-1} \mathbf{CU}^{in-1} \quad (5.88)$$

Substituting (5.87) into (5.86), we obtain:

$$\mathbf{CS} = \mathbf{U}^{in} \tilde{\mathbf{C}} \tilde{\mathbf{S}} \mathbf{U}^{in-1} \quad (5.89)$$

where,

$$\tilde{\mathbf{S}} = 2 \left(\alpha_1 \mathbf{1} + \alpha_2 \tilde{\mathbf{C}} + \alpha_3 \tilde{\mathbf{C}}^2 \right) \quad (5.90)$$

Moreover, due to the coaxiality of \mathbf{C}^{in} and \mathbf{X} , we may write:

$$\mathbf{C}^{in} \mathbf{X} = \mathbf{U}^{in} \mathbf{C}^{in} \mathbf{X} \mathbf{U}^{in-1} \quad (5.91)$$

Substituting (5.89) and (5.91) into (5.78), we obtain:

$$\mathbf{Y} = \mathbf{U}^{in} \tilde{\mathbf{Y}} \mathbf{U}^{in-1} \quad (5.92)$$

where $\tilde{\mathbf{Y}}$ is defined as:

$$\tilde{\mathbf{Y}} = \tilde{\mathbf{C}} \tilde{\mathbf{S}} - \mathbf{C}^{in} \mathbf{X} \quad (5.93)$$

Using the property $\text{tr} \left(\mathbf{U}^{in} \tilde{\mathbf{Y}} \mathbf{U}^{in-1} \right) = \text{tr}(\tilde{\mathbf{Y}})$, we also obtain:

$$\mathbf{Y}^D = \mathbf{U}^{in} \tilde{\mathbf{Y}}^D \mathbf{U}^{in-1} \quad (5.94)$$

We now substitute (5.94) into (5.79) and (5.80) and obtain (5.95) and (5.96), respectively, as follows:

$$\mathbf{Y}^D : \mathbf{Y}^{DT} = \tilde{\mathbf{Y}}^D : \tilde{\mathbf{Y}}^D, \quad \text{or} \quad f = \|\mathbf{Y}^D\| - R = \|\tilde{\mathbf{Y}}^D\| - R \quad (5.95)$$

and

$$\dot{\mathbf{C}}^{in} = 2\dot{\zeta} \mathbf{U}^{in} \frac{\tilde{\mathbf{Y}}^D}{\|\tilde{\mathbf{Y}}^D\|} \mathbf{U}^{in} \quad (5.96)$$

We remark that in the proposed formulation we can express \mathbf{S} as:

$$\mathbf{S} = \mathbf{U}^{in-1} \tilde{\mathbf{S}} \mathbf{U}^{in-1} \quad (5.97)$$

Finally, we summarize the proposed improved time-continuous finite-strain constitutive models in Table 5.3.

We may compare the original and the proposed alternative time-continuous forms summarized in Tables 5.2 and 5.3, respectively. It is clearly observed that, in the proposed alternative constitutive model, all quantities are symmetric and the norm operator argument is also a symmetric tensor.

5.7 A kinematic hardening constitutive model based on Hencky strain

5.7.1 Motivation

The logarithmic strain, sometimes referred to as true or natural strain, introduced by Hencky (1928) and also called Hencky strain, is a favored measure of strain due to its

remarkable properties at large deformations in solid mechanics, materials science and metallurgy. A remarkable property is that among all finite strain measures, only the spherical and the deviatoric parts of the Hencky strain can, in an additive manner, separate the volumetric deformation and the isochoric deformation from the total deformation, whereas the just-mentioned two deformation modes are inseparably coupled with each other in either of the spherical part and the deviatoric part of any other strain measure (Xiao et al., 2004).

Moreover, the logarithmic strain possesses certain intrinsic far-reaching properties that establish its favored position in all possible strain measures. One reason of such properties was clarified by disclosing an important relation, i.e., the Eulerian logarithmic strain is the unique strain measure that its corotational rate (associated with the so-called logarithmic spin) is the strain rate tensor. In other words, the strain rate tensor, \mathbf{d} , is the corotational rate of the Hencky strain tensor associated with the logarithmic spin tensor. Such a result has been introduced by Reinhardt and Dubey (1995) as D-rate and by Xiao et al. (1997) as log-rate. The work-conjugate pair of Eulerian Hencky strain and Cauchy stress, being natural or true strain and stress measures, respectively, are of most interest in constitutive modeling beyond the small strain regime (Xiao et al., 2006).

For its considerable advantages, logarithmic strain has been used in constitutive modeling of solids by many authors (see, e.g., Bruhns et al. (1999); Criscione et al. (2000); Lin and Schomburg (2003); Miehe et al. (2002); Müller and Bruhns (2006); Naghdabadi et al. (2005); Peric et al. (1992); Reinhardt and Dubey (1996); Xiao et al. (2000, 2001); Xiao and Chen (2002); Yeganeh and Naghdabadi (2006)).

There has also been a lot of effort in the literature using Green-Lagrange strain and the second Piola-Kirchhoff stress which are finite strain and stress as well as work-conjugate measures in nonlinear solid mechanics. However, the physical meaning of Green-Lagrange strain is not precise and direct unless the magnitude is small. Sometimes Green-Lagrange strain is called an energy-measure strain (Pai et al., 1998) to emphasize that it is not a physical or true measure.

Recently, Darijani and Naghdabadi (2010) have reconsidered the strain measure definition to satisfy the consistency requirements: 1) strain should go to $+\infty$ when stretch goes to $+\infty$, 2) strain should go to $-\infty$ when stretch goes to zero. As discussed by Darijani and Naghdabadi, the well known Seth-Hill strain measures do not satisfy the both requirements simultaneously⁵. We emphasize that the Hencky strain, belonging to both Seth-Hill and Darijani-Naghdabadi measures, is the only member of Seth-Hill class that satisfies both requirements.

There are still more motivations to develop a Hencky-strain based constitutive model.

⁵For example, Green-Lagrange strain measure, $\mathbf{E} = \frac{1}{2}(\mathbf{U}^2 - \mathbf{1}) \rightarrow -\frac{1}{2}\mathbf{1}$ when $\mathbf{U} \rightarrow \mathbf{0}$

For example, for a Hookean-type constitutive relation, only the Hencky-based one is useful at moderately large elastic stretches (Anand, 1979, 1986). Another motivation is related to the physical kinematical constraints, for example, in shape memory alloys (SMAs), to capture the transformation-induced strain saturation, it is necessary to define a kinematical constraint on the inelastic true strain norm. This constraint has yet been enforced through the Green–Lagrange strain norm, which is not physical; however, it is reasonable for small strains, large rotation deformations. Moreover, the incompressibility constraint takes a very simple form when Hencky strain is used (Xiao et al., 2004).

To this end, based on the Hencky strain, we develop a finite strain constitutive model.

5.7.2 Constitutive model development

A multiplicative decomposition of \mathbf{F} into dilatational and distortional parts is defined as:

$$\mathbf{F} = (J^{1/3}\mathbf{1}) \bar{\mathbf{F}} = J^{1/3} \bar{\mathbf{F}} \quad (5.98)$$

where $\det(\bar{\mathbf{F}}) = 1$. The terms $J^{1/3}\mathbf{1}$ and $\bar{\mathbf{F}}$ are associated, respectively, with volume-changing and volume-preserving deformations of the material (Holzapfel, 2000).

Then, the right and left Cauchy-Green deformation tensors are, respectively, defined as:

$$\begin{aligned} \mathbf{C} &= \mathbf{F}^T \mathbf{F} = \mathbf{U}^2 = J^{2/3} \bar{\mathbf{F}}^T \bar{\mathbf{F}} = J^{2/3} \bar{\mathbf{C}} = J^{2/3} \bar{\mathbf{U}}^2 \\ \mathbf{b} &= \mathbf{F} \mathbf{F}^T = \mathbf{V}^2 = J^{2/3} \bar{\mathbf{F}} \bar{\mathbf{F}}^T = J^{2/3} \bar{\mathbf{b}} = J^{2/3} \bar{\mathbf{V}}^2 \end{aligned} \quad (5.99)$$

where $\det(\bar{\mathbf{C}}) = \det(\bar{\mathbf{U}}) = 1$ and $\det(\bar{\mathbf{b}}) = \det(\bar{\mathbf{V}}) = 1$.

The material and spatial Hencky (or logarithmic) strain tensors \mathbf{H} and \mathbf{h} read, respectively, as (Lubarda, 2001)⁶

$$\begin{aligned} \mathbf{H} &= \log \mathbf{U} = \frac{1}{2} \log \mathbf{C} = \bar{\mathbf{H}} + \frac{1}{3} \theta \mathbf{1} \\ \mathbf{h} &= \log \mathbf{V} = \frac{1}{2} \log \mathbf{b} = \bar{\mathbf{h}} + \frac{1}{3} \theta \mathbf{1} \end{aligned} \quad (5.100)$$

where

$$\theta = \log(J), \quad \bar{\mathbf{H}} = \log \bar{\mathbf{U}} = \frac{1}{2} \log \bar{\mathbf{C}}, \quad \bar{\mathbf{h}} = \log \bar{\mathbf{V}} = \frac{1}{2} \log \bar{\mathbf{b}} \quad (5.101)$$

Moreover, the velocity gradient tensor \mathbf{l} is given as:

$$\mathbf{l} = \dot{\mathbf{F}} \mathbf{F}^{-1} = \bar{\mathbf{l}} + \frac{1}{3} \dot{\theta} \mathbf{1} \quad (5.102)$$

⁶The material and spatial Hencky strains are computed through spectral decomposition, i.e.,

$$\mathbf{H} = \sum_{i=1}^3 \log(\lambda_i) \mathbf{e}_i \otimes \mathbf{e}_i \quad \text{and} \quad \mathbf{h} = \sum_{i=1}^3 \log(\lambda_i) \tilde{\mathbf{e}}_i \otimes \tilde{\mathbf{e}}_i$$

where λ_i are the three principal stretches (possibly repeated), while \mathbf{e}_i and $\tilde{\mathbf{e}}_i$ are the corresponding principal directions of the right and left stretch tensors, respectively.

where

$$\bar{\mathbf{l}} = \dot{\bar{\mathbf{F}}}\bar{\mathbf{F}}^{-1} \quad (5.103)$$

The symmetric and skew symmetric parts of \mathbf{l} supply, respectively, the strain rate tensor \mathbf{d} and the vorticity tensor \mathbf{w} , i.e.:

$$\begin{aligned} \mathbf{d} &= \text{sym}(\mathbf{l}) = \bar{\mathbf{d}} + \frac{1}{3}\dot{\theta}\mathbf{1} \\ \mathbf{w} &= \text{skew}(\mathbf{l}) = \bar{\mathbf{w}} \end{aligned} \quad (5.104)$$

where $\bar{\mathbf{d}} = \text{sym}(\bar{\mathbf{l}})$ and $\bar{\mathbf{w}} = \text{skew}(\bar{\mathbf{l}})$, while $\text{sym}(\mathbf{A}) = (1/2)(\mathbf{A} + \mathbf{A}^T)$ and $\text{skew}(\mathbf{A}) = (1/2)(\mathbf{A} - \mathbf{A}^T)$ compute the symmetric and skew symmetric parts of an arbitrary tensor \mathbf{A} , respectively.

As we introduced in Chapter 3, corotational rate of an Eulerian tensor \mathbf{A} associated with the rotating frame having spin Ω^* is defined as (see (3.36)):

$$\overset{\circ}{\mathcal{A}} = \dot{\mathcal{A}} - \Omega^* \mathcal{A} + \mathcal{A} \Omega^* \quad (5.105)$$

where $\dot{\mathcal{A}}$ is the material time derivative of \mathcal{A} associated with the fixed frame and $\overset{\circ}{\mathcal{A}}$ is the corotational rate of \mathcal{A} (Ghavam and Naghdabadi, 2007; Xiao et al., 1997).

We now double contract both sides of (5.105) with an arbitrary second-order symmetric tensor \mathcal{B} ; assuming \mathcal{A} symmetric and after some mathematical manipulation, we obtain:

$$\overset{\circ}{\mathcal{A}} : \mathcal{B} = \dot{\mathcal{A}} : \mathcal{B} + 2\Omega^* : (\mathcal{A}\mathcal{B}) \quad (5.106)$$

If \mathcal{A} and \mathcal{B} are coaxial (besides being symmetric), $\mathcal{A}\mathcal{B}$ is also symmetric and its double contraction with the skew-symmetric tensor Ω^* vanishes. Therefore, we conclude the following identity for any arbitrary spin tensor Ω^* :

$$\text{if } \mathcal{A} \text{ and } \mathcal{B} \text{ are symmetric and coaxial} \Rightarrow \dot{\mathcal{A}} : \mathcal{B} = \overset{\circ}{\mathcal{A}} : \mathcal{B} \quad (5.107)$$

The corotational rate of the Eulerian (or spatial) Hencky strain \mathbf{h} associated with the so-called logarithmic spin⁷ Ω^{log} is identical to the Eulerian stretching \mathbf{d} , and \mathbf{h} is the only strain enjoying this property (Xiao et al., 1997). According to (5.105), this means:

$$\overset{\circ}{\mathbf{h}}^{log} = \dot{\mathbf{h}} - \Omega^{log} \mathbf{h} + \mathbf{h} \Omega^{log} = \mathbf{d} \quad (5.108)$$

We now use the multiplicative decomposition of the deformation gradient into elastic and inelastic parts and, defining Helmholtz strain energy function in terms of elastic and inelastic Hencky strains, we develop a thermodynamically-consistent finite strain kinematic hardening constitutive model. We utilize the deformation gradient decomposition into volumetric and distortional parts, as follows:

$$\begin{aligned} \mathbf{F}^e &= J^{e\frac{1}{3}} \bar{\mathbf{F}}^e \\ \mathbf{F}^{in} &= J^{in\frac{1}{3}} \bar{\mathbf{F}}^{in} \end{aligned} \quad (5.109)$$

⁷In this study, only the existence of such spin is utilized and the explicit form of Ω^{log} is not needed; however we refer to e.g., Ghavam and Naghdabadi (2007); Reinhardt and Dubey (1995); Xiao et al. (1997) for more details.

where $J^e = \det(\mathbf{F}^e)$, $J^{in} = \det(\mathbf{F}^{in})$ and $\det(\bar{\mathbf{F}}^e) = \det(\bar{\mathbf{F}}^{in}) = 1$.

Similarly, we may define the following tensors:

$$\begin{aligned}
\mathbf{C}^e &= \mathbf{F}^{eT} \mathbf{F}^e, & \bar{\mathbf{C}}^e &= \bar{\mathbf{F}}^{eT} \bar{\mathbf{F}}^e, & \mathbf{b}^e &= \mathbf{F}^e \mathbf{F}^{eT}, & \bar{\mathbf{b}}^e &= \bar{\mathbf{F}}^e \bar{\mathbf{F}}^{eT} \\
\mathbf{C}^{in} &= \mathbf{F}^{inT} \mathbf{F}^{in}, & \bar{\mathbf{C}}^{in} &= \bar{\mathbf{F}}^{inT} \bar{\mathbf{F}}^{in}, & \mathbf{b}^{in} &= \mathbf{F}^{in} \mathbf{F}^{inT}, & \bar{\mathbf{b}}^{in} &= \bar{\mathbf{F}}^{in} \bar{\mathbf{F}}^{inT} \\
\mathbf{U}^e &= \mathbf{C}^{e1/2}, & \bar{\mathbf{U}}^e &= \bar{\mathbf{C}}^{e1/2}, & \mathbf{V}^e &= \mathbf{b}^{e1/2}, & \bar{\mathbf{V}}^e &= \bar{\mathbf{b}}^{e1/2} \\
\mathbf{U}^{in} &= \mathbf{C}^{in1/2}, & \bar{\mathbf{U}}^{in} &= \bar{\mathbf{C}}^{in1/2}, & \mathbf{V}^{in} &= \mathbf{b}^{in1/2}, & \bar{\mathbf{V}}^{in} &= \bar{\mathbf{b}}^{in1/2} \\
\mathbf{H}^e &= \log \mathbf{U}^e, & \bar{\mathbf{H}}^e &= \log \bar{\mathbf{U}}^e, & \mathbf{H}^{in} &= \log \mathbf{U}^{in}, & \bar{\mathbf{H}}^{in} &= \log \bar{\mathbf{U}}^{in}
\end{aligned} \tag{5.110}$$

Combining (5.1) and (5.109), we obtain:

$$\mathbf{F} = (J^e J^{in})^{\frac{1}{3}} \bar{\mathbf{F}}^e \bar{\mathbf{F}}^{in} = J^{\frac{1}{3}} \bar{\mathbf{F}} \tag{5.111}$$

where

$$J = J^e J^{in} \quad \text{and} \quad \bar{\mathbf{F}} = \bar{\mathbf{F}}^e \bar{\mathbf{F}}^{in} \tag{5.112}$$

Substituting (5.112) into (5.104)₁, we obtain:

$$\bar{\mathbf{d}} = \dot{\bar{\mathbf{F}}} \bar{\mathbf{F}}^{-1} = \bar{\mathbf{d}}^e + \text{sym} \left(\bar{\mathbf{F}}^{e\bar{l}^{in}} \bar{\mathbf{F}}^{e-1} \right) \quad \text{and} \quad \theta = \theta^e + \theta^{in} \tag{5.113}$$

where, $\bar{\mathbf{d}}^e = \text{sym} \left(\dot{\bar{\mathbf{F}}}^e \bar{\mathbf{F}}^{e-1} \right)$, $\bar{l}^{in} = \dot{\bar{\mathbf{F}}}^{in} \bar{\mathbf{F}}^{in-1}$, $\theta^e = \log(J^e)$ and $\theta^{in} = \log(J^{in})$.

In order to satisfy the principle of material objectivity, the Helmholtz free energy has to depend on \mathbf{F}^e only through the elastic right stretch tensor; it is moreover assumed to be a function of \mathbf{F}^{in} through the inelastic right stretch tensor and of the temperature⁸, T . Finally, we express the Helmholtz free energy per unit undeformed volume, decomposed additively in the following form:

$$\begin{aligned}
\Psi &= \Psi \left(\theta^e, \theta^{in}, \bar{\mathbf{H}}^e, \bar{\mathbf{H}}^{in}, T \right) = \phi^e(\theta^e) + \psi^e(\bar{\mathbf{H}}^e) + \phi^{in}(\theta^{in}) + \psi^{in}(\bar{\mathbf{H}}^{in}, T) \\
&= W^e(\mathbf{H}^e) + W^{in}(\mathbf{H}^{in}, T)
\end{aligned} \tag{5.114}$$

where $W^e(\mathbf{H}^e)$ is a hyperelastic strain energy function decomposed into $\phi^e(\theta^e)$ and $\psi^e(\bar{\mathbf{H}}^e)$, representing the volumetric and distortional elastic strain energies due to the elastic material deformations, respectively. Similarly, the term $W^{in}(\mathbf{H}^{in}, T)$ represents the additional amount of stored energy due to inelastic hardening (e.g., phase transformation, plastic hardening and so on), decomposed into volumetric and isochoric parts $\phi^{in}(\theta^{in})$ and $\psi^{in}(\bar{\mathbf{H}}^{in})$, respectively. For simplicity we do not consider the isotropic hardening effect, knowing that it can be easily included in the proposed constitutive model.

In this study, we assume $\psi^e(\bar{\mathbf{H}}^e)$ and $\psi^{in}(\bar{\mathbf{H}}^{in}, T)$ to be isotropic functions of $\bar{\mathbf{H}}^e$ and

⁸We remark that we do not consider a fully thermo-mechanical coupled model. In this way, the Helmholtz free energy should be more properly referred to as a temperature-parameterized function.

$\bar{\mathbf{H}}^{in}$, respectively⁹. Therefore, ψ^e and ψ^{in} can be expressed as functions of their argument invariants. Since, the Lagrangian and Eulerian Hencky strains have the same invariants, we can express the Helmholtz free energy as a function of the Eulerian Hencky strains, i.e.,:

$$\begin{aligned}\Psi\left(\theta^e, \theta^{in}, \bar{\mathbf{H}}^e, \bar{\mathbf{H}}^{in}, T\right) &= \Psi\left(\theta^e, \theta^{in}, \bar{\mathbf{h}}^e, \bar{\mathbf{h}}^{in}, T\right) \\ &= \phi^e(\theta^e) + \psi^e(\bar{\mathbf{h}}^e) + \phi^{in}(\theta^{in}) + \psi^{in}(\bar{\mathbf{h}}^{in}, T)\end{aligned}\quad (5.115)$$

We now use Clausius-Duhem inequality form of the second law of thermodynamics:

$$J\boldsymbol{\sigma} : \mathbf{d} - (\dot{\Psi} + \eta\dot{T}) = \boldsymbol{\tau} : \mathbf{d} - (\dot{\Psi} + \eta\dot{T}) \geq 0 \quad (5.116)$$

where $\boldsymbol{\tau} = J\boldsymbol{\sigma}$ is the Kirchhoff stress tensor.

Moreover, we make use of (5.104)₁ and the additive decomposition of the Kirchhoff stress tensor $\boldsymbol{\tau}$ into a hydrostatic part $p^*\mathbf{1}$ and a deviatoric part: $\mathbf{s}^* = \boldsymbol{\tau} - p^*\mathbf{1}$, where $p^* = \text{tr}(\boldsymbol{\tau})/3$, and rewrite (5.116) as:

$$p^*\dot{\theta} + \mathbf{s}^* : \bar{\mathbf{d}} - (\dot{\Psi} + \eta\dot{T}) \geq 0 \quad (5.117)$$

We now substitute (5.113) and (5.115) into (5.117) to obtain:

$$\begin{aligned}p^*\left(\dot{\theta}^e + \dot{\theta}^{in}\right) + \mathbf{s}^* : \left[\bar{\mathbf{d}}^e + \text{sym}\left(\bar{\mathbf{F}}^e \bar{\mathbf{t}}^{in} \bar{\mathbf{F}}^{e-1}\right)\right] \\ - \left(\frac{\partial \phi^e}{\partial \theta^e} \dot{\theta}^e + \frac{\partial \psi^e}{\partial \bar{\mathbf{h}}^e} : \dot{\bar{\mathbf{h}}}^e + \frac{\partial \phi^{in}}{\partial \theta^{in}} \dot{\theta}^{in} + \frac{\partial \psi^{in}}{\partial \bar{\mathbf{h}}^{in}} : \dot{\bar{\mathbf{h}}}^{in} + \frac{\partial \psi^{in}}{\partial T} \dot{T}\right) - \eta\dot{T} \geq 0\end{aligned}\quad (5.118)$$

As a consequence of isotropy, the symmetric tensors $\bar{\mathbf{h}}^e$ and $\partial \psi^e / \partial \bar{\mathbf{h}}^e$ as well as the symmetric tensors $\bar{\mathbf{h}}^{in}$ and $\partial \psi^{in} / \partial \bar{\mathbf{h}}^{in}$ are coaxial. According to (5.107), we can replace the time derivative of elastic and inelastic Hencky strains appearing in (5.118) with any corotational rate in the form of (5.105). We particularly make use of the corresponding logarithmic spin tensors, i.e., $\boldsymbol{\Omega}^{log-e}$ and $\boldsymbol{\Omega}^{log-in}$, which according to (5.108) result in¹⁰:

$$\frac{\partial \psi^e}{\partial \bar{\mathbf{h}}^e} : \dot{\bar{\mathbf{h}}}^e = \frac{\partial \psi^e}{\partial \bar{\mathbf{h}}^e} : (\bar{\mathbf{h}}^e)^\circ{}^{log-e} = \frac{\partial \psi^e}{\partial \bar{\mathbf{h}}^e} : \bar{\mathbf{d}}^e \quad (5.119)$$

⁹We refer to Henann and Anand (2009) and Gurtin and Anand (2005) for more details on objectivity as well as isotropy requirements.

¹⁰ According to the work by Xiao et al. (1997), the logarithmic spin $\boldsymbol{\Omega}^{log}$ is introduced as:

$$\boldsymbol{\Omega}^{log}(\mathbf{F}) = \mathbf{w} + \sum_{i,j=1, i \neq j}^m \left[\left(\frac{1 + (b_i/b_j)}{1 - (b_i/b_j)} + \frac{2}{\log(b_i/b_j)} \right) \mathbf{P}_i d\mathbf{P}_j \right]$$

where $b_i = \lambda_i^2$ are the eigenvalues of the left Cauchy-Green deformation tensor and \mathbf{P}_i are the eigenprojections subordinate to eigenvalues $\lambda_i > 0$. According to this relation, knowing the deformation gradient $\mathbf{F}(t)$, the logarithmic spin $\boldsymbol{\Omega}^{log}(\mathbf{F})$ can be computed. We now consider the multiplicative decomposition of the deformation gradient and introduce the logarithmic spins $\boldsymbol{\Omega}^{log-e}$ and $\boldsymbol{\Omega}^{log-in}$ as

and

$$\frac{\partial\psi^{in}}{\partial\bar{\mathbf{h}}^{in}} : \dot{\bar{\mathbf{h}}}^{in} = \frac{\partial\psi^{in}}{\partial\bar{\mathbf{h}}^{in}} : (\overset{\circ}{\bar{\mathbf{h}}^{in}})^{log-in} = \frac{\partial\psi^{in}}{\partial\bar{\mathbf{h}}^{in}} : \bar{\mathbf{d}}^{in} \quad (5.120)$$

where superscripts "log-e" and "log-in" represent the corotational rate associated with the logarithmic spins during the elastic and inelastic deformations, $\bar{\mathbf{F}}^e$ and $\bar{\mathbf{F}}^{in}$, respectively.

Substituting (5.119) and (5.120) into (5.118), after some mathematical manipulations, we obtain:

$$\begin{aligned} & \left(p^* - \frac{\partial\phi^e}{\partial\theta^e} \right) \dot{\theta}^e + \left(\mathbf{s}^* - \frac{\partial\psi^e}{\partial\bar{\mathbf{h}}^e} \right) : \bar{\mathbf{d}}^e + \left(p^* - \frac{\partial\phi^{in}}{\partial\theta^{in}} \right) \dot{\theta}^{in} \\ & + \left(\bar{\mathbf{F}}^{eT} \mathbf{s}^* \bar{\mathbf{F}}^{e-T} - \frac{\partial\psi^{in}}{\partial\bar{\mathbf{h}}^{in}} \right) : \bar{\mathbf{l}}^{in} - \left(\eta + \frac{\partial\psi^{in}}{\partial T} \right) \dot{T} \geq 0 \end{aligned} \quad (5.121)$$

In deriving (5.121) we have used the symmetric property of both \mathbf{s}^* and $\frac{\partial\psi^{in}}{\partial\bar{\mathbf{h}}^{in}}$ implying, respectively:

$$\mathbf{s}^* : \text{sym} \left(\bar{\mathbf{F}}^e \bar{\mathbf{l}}^{in} \bar{\mathbf{F}}^{e-1} \right) = \mathbf{s}^* : \left(\bar{\mathbf{F}}^e \bar{\mathbf{l}}^{in} \bar{\mathbf{F}}^{e-1} \right) = \bar{\mathbf{l}}^{in} : \left(\bar{\mathbf{F}}^{eT} \mathbf{s}^* \bar{\mathbf{F}}^{e-T} \right) \quad (5.122)$$

and

$$\frac{\partial\psi^{in}}{\partial\bar{\mathbf{h}}^{in}} : \bar{\mathbf{d}}^{in} = \frac{\partial\psi^{in}}{\partial\bar{\mathbf{h}}^{in}} : \bar{\mathbf{l}}^{in} \quad (5.123)$$

Following standard arguments (Haupt, 2002; Ottosen and Ristinmaa, 2005), from (5.121) we may conclude¹¹

$$p^* = \frac{\partial\phi^e}{\partial\theta^e}, \quad \mathbf{s}^* = \frac{\partial\psi^e}{\partial\bar{\mathbf{h}}^e}, \quad \eta = -\frac{\partial\psi^{in}}{\partial T} \quad (5.124)$$

leading to the following simplified Clausius-Duhem inequality:

$$\left(p^* - \frac{\partial\phi^{in}}{\partial\theta^{in}} \right) \dot{\theta}^{in} + \left(\bar{\mathbf{F}}^{eT} \mathbf{s}^* \bar{\mathbf{F}}^{e-T} - \frac{\partial\psi^{in}}{\partial\bar{\mathbf{h}}^{in}} \right) : \bar{\mathbf{l}}^{in} \geq 0 \quad (5.125)$$

follows:

$$\boldsymbol{\Omega}^{log-e} = \boldsymbol{\Omega}^{log}(\bar{\mathbf{F}}^e) \quad \text{and} \quad \boldsymbol{\Omega}^{log-in} = \boldsymbol{\Omega}^{log}(\bar{\mathbf{F}}^{in})$$

The relations above confirm the existence of such spins. However, in this work, we do not need the explicit forms of $\boldsymbol{\Omega}^{log-e}$ and $\boldsymbol{\Omega}^{log-in}$.

¹¹ In the work by Xiao et al. (2000), they use the hypoelastic constitutive model $\mathbf{d}^e = \overset{\circ}{(\partial\Sigma/\partial\boldsymbol{\pi})}^{log-e}$, where Σ is a complementary hyperelastic potential and $\boldsymbol{\pi} = \mathbf{R}\boldsymbol{\Pi}\mathbf{R}^T$ is the Eulerian stress while $\boldsymbol{\Pi}$ is the work-conjugate stress measure of the Lagrangean logarithmic strain \mathbf{H} . However, the corresponding hypoelastic constitutive model of this work, when written in the framework of Xiao et al. (2000) work, takes the form $\mathbf{d}^e = \overset{\circ}{(\partial\Sigma/\partial\boldsymbol{\pi})}^{log-e}$. It is noted that regarding the fact that $\mathbf{d}^e = \overset{\circ}{\mathbf{h}}^e{}^{log-e}$, we can write $\overset{\circ}{\mathbf{h}}^e{}^{log-e} = \overset{\circ}{(\partial\Sigma/\partial\boldsymbol{\pi})}^{log-e}$ which can be integrated to yield $\mathbf{h}^e = \partial\Sigma/\partial\boldsymbol{\pi}$. This shows that, the hypoelastic form used in this work can be reduced to a hyperelastic constitutive model as observed in (5.124)_{1,2}.

Considering (5.124)₂ and the isotropic property of ψ^e , it can be shown that $\bar{\mathbf{F}}^{eT} \mathbf{s}^* \bar{\mathbf{F}}^{e-T}$ is a symmetric tensor (see equation (B.6) in the Appendix). Therefore, equation (5.125) reads as:

$$q\dot{\theta}^{in} + \boldsymbol{\alpha} : \bar{\mathbf{d}}^{in} \geq 0 \quad (5.126)$$

where the scalar and tensorial relative stresses, q and $\boldsymbol{\alpha}$, are defined as:

$$\begin{aligned} q &= p^* - \frac{\partial \phi^{in}}{\partial \theta^{in}} = \frac{\partial \phi^e}{\partial \theta^e} - \frac{\partial \phi^{in}}{\partial \theta^{in}} \\ \boldsymbol{\alpha} &= \mathbf{m} - \mathbf{x} \end{aligned} \quad (5.127)$$

with

$$\mathbf{m} = \bar{\mathbf{F}}^{eT} \mathbf{s}^* \bar{\mathbf{F}}^{e-T}, \quad \mathbf{x} = \frac{\partial \psi^{in}}{\partial \bar{\mathbf{h}}^{in}} \quad (5.128)$$

To satisfy the second law of thermodynamics (5.126), following Ottosen and Ristinmaa (2005), we introduce the convex potential $G(\boldsymbol{\alpha}, q)$ and define the following evolution equations:

$$\bar{\mathbf{d}}^{in} = \zeta \frac{\partial G(\boldsymbol{\alpha}, q)}{\partial \boldsymbol{\alpha}} \quad \text{and} \quad \dot{\theta}^{in} = \zeta \frac{\partial G(\boldsymbol{\alpha}, q)}{\partial q} \quad (5.129)$$

where λ is the consistency parameter.

Moreover, we consider a yield or limit function as follows:

$$F = f(\boldsymbol{\alpha}, q) - R \quad (5.130)$$

where the material parameter R is the elastic region radius.

Similarly to plasticity, the consistency parameter and the limit function (or yield function) satisfy the Kuhn-Tucker conditions:

$$F \leq 0, \quad \dot{\zeta} \geq 0, \quad \dot{\zeta} F = 0 \quad (5.131)$$

Accordingly, the finite strain, non-associative constitutive model can be summarized as:

- Stress-like quantities

$$\begin{aligned} p^* &= \frac{\partial \phi^e}{\partial \theta^e}, \quad q = \frac{\partial \phi^e}{\partial \theta^e} - \frac{\partial \phi^{in}}{\partial \theta^{in}}, \quad \mathbf{s}^* = \frac{\partial \psi^e}{\partial \bar{\mathbf{h}}^e}, \\ \mathbf{m} &= \bar{\mathbf{F}}^{eT} \mathbf{s}^* \bar{\mathbf{F}}^{e-T}, \quad \mathbf{x} = \frac{\partial \psi^{in}}{\partial \bar{\mathbf{h}}^{in}}, \quad \boldsymbol{\alpha} = \mathbf{m} - \mathbf{x} \end{aligned}$$

- Limit function

$$F = f(\boldsymbol{\alpha}, q) - R$$

- Potential function

$$G = G(\boldsymbol{\alpha}, q)$$

- Evolution equations

$$\bar{\mathbf{d}}^{in} = \dot{\zeta} \frac{\partial G(\boldsymbol{\alpha}, q)}{\partial \boldsymbol{\alpha}} \quad \text{and} \quad \dot{\theta}^{in} = \dot{\zeta} \frac{\partial G(\boldsymbol{\alpha}, q)}{\partial q}$$

- Kuhn-Tucker conditions

$$F \leq 0, \quad \dot{\zeta} \geq 0, \quad \dot{\zeta} F = 0$$

5.7.3 Representation with respect to the reference configuration

In the above formulation, \mathbf{F}^e is defined with respect to an intermediate configuration. Accordingly, tensor \mathbf{s} has been defined with respect to the current configuration, while tensors \mathbf{m} , \mathbf{x} , $\boldsymbol{\alpha}$ and $\bar{\mathbf{d}}^{in}$ have been defined with respect to the intermediate configuration. Thus, we recast all equations in terms of quantities defined with respect to the reference configuration, allowing to express all equations in a Lagrangian form.

As already stated, ψ^e depends on $\bar{\mathbf{h}}^e$ only through its invariants which are the same as those of $\bar{\mathbf{H}}^e$. Since $\bar{\mathbf{H}}^e = 1/2 \log(\bar{\mathbf{C}}^e)$, it is clear that the invariants of $\bar{\mathbf{H}}^e$ can be expressed in terms of the invariants of $\bar{\mathbf{C}}^e$ which are equal to those of $\bar{\mathbf{U}}^{in-1} \bar{\mathbf{C}} \bar{\mathbf{U}}^{in-1}$. In fact, for the first invariant, the following identity holds:

$$I_{\bar{\mathbf{C}}^e} = \text{tr}(\bar{\mathbf{C}}^e) = \text{tr}(\bar{\mathbf{F}}^{in-T} \bar{\mathbf{C}} \bar{\mathbf{F}}^{in-1}) = \text{tr}(\bar{\mathbf{U}}^{in-1} \bar{\mathbf{C}} \bar{\mathbf{U}}^{in-1}) \quad (5.132)$$

and similar relations hold for the second and the third invariants. Therefore, we conclude that the invariants of $\bar{\mathbf{h}}^e$ are equal to those of an elastic-like strain tensor $\boldsymbol{\mathcal{H}}^e$ defined as:

$$\boldsymbol{\mathcal{H}}^e = \frac{1}{2} \log(\bar{\mathbf{U}}^{in-1} \bar{\mathbf{C}} \bar{\mathbf{U}}^{in-1}) \quad (5.133)$$

Considering the isotropic property of ψ^e and according to the representation theorem, we now write (Ogden, 1984; Ottosen and Ristinmaa, 2005):

$$\frac{\partial \psi^e}{\partial \bar{\mathbf{h}}^e} = \alpha_1 \mathbf{1} + 2\alpha_2 \bar{\mathbf{h}}^e + 4\alpha_3 \bar{\mathbf{h}}^{e2} \quad (5.134)$$

where

$$\alpha_i = \alpha_i(I_{\bar{\mathbf{h}}^e}, II_{\bar{\mathbf{h}}^e}, III_{\bar{\mathbf{h}}^e}) = \alpha_i(I_{\boldsymbol{\mathcal{H}}^e}, II_{\boldsymbol{\mathcal{H}}^e}, III_{\boldsymbol{\mathcal{H}}^e}); \quad (5.135)$$

It can be shown that (see equation (B.9) in the Appendix):

$$\bar{\mathbf{h}}^e = \frac{1}{2} \bar{\mathbf{F}}^{-T} \log(\bar{\mathbf{C}} \bar{\mathbf{C}}^{in-1}) \bar{\mathbf{F}}^T \quad (5.136)$$

We now substitute (5.136) into (5.134) and the result into (5.124)₂ which leads to:

$$\mathbf{s}^* = \bar{\mathbf{F}}^{-T} \mathbf{M}^* \bar{\mathbf{F}}^T \quad (5.137)$$

where we have defined $\mathbf{M}^* = \alpha_1 \mathbf{1} + \alpha_2 \log(\bar{\mathbf{C}}\bar{\mathbf{C}}^{in^{-1}}) + \alpha_3 \left(\log(\bar{\mathbf{C}}\bar{\mathbf{C}}^{in^{-1}})\right)^2$.

We now pull back the quantities \mathbf{m} and \mathbf{x} , where they live in the intermediate configuration, to the reference configuration. To this end, we use the identity $\bar{\mathbf{F}}^{e^T} \bar{\mathbf{h}}^e \bar{\mathbf{F}}^{e^{-T}} = \bar{\mathbf{H}}^e$ (see equation (B.5) in the Appendix) as well as the following identity (see equation (B.10) in the Appendix):

$$\bar{\mathbf{F}}^{in^T} \bar{\mathbf{H}}^e \bar{\mathbf{F}}^{in} = \frac{1}{2} \log(\bar{\mathbf{C}}\bar{\mathbf{C}}^{in^{-1}}) \bar{\mathbf{C}}^{in} \quad (5.138)$$

and conclude:

$$\bar{\mathbf{F}}^{in^T} \mathbf{m} \bar{\mathbf{F}}^{in} = \mathbf{M}^* \bar{\mathbf{C}}^{in} \quad (5.139)$$

We observe that tensor \mathbf{M}^* is unsymmetric. In order to obtain a constitutive model in which all quantities are symmetric, we follow the proposed approach in Section 5.6 and utilize the following identity (see equation (B.12) in the Appendix):

$$\log(\bar{\mathbf{C}}\bar{\mathbf{C}}^{in^{-1}}) = \bar{\mathbf{U}}^{in} \log\left(\bar{\mathbf{U}}^{in^{-1}} \bar{\mathbf{C}} \bar{\mathbf{U}}^{in^{-1}}\right) \bar{\mathbf{U}}^{in^{-1}} \quad (5.140)$$

and express tensor \mathbf{M}^* as:

$$\mathbf{M}^* = \bar{\mathbf{U}}^{in} \mathbf{Q} \bar{\mathbf{U}}^{in^{-1}} \quad (5.141)$$

where the symmetric tensor \mathbf{Q} is expressed as:

$$\mathbf{Q} = \alpha_1 \mathbf{1} + 2\alpha_2 \mathcal{H}^e + 4\alpha_3 \mathcal{H}^{e^2} \quad (5.142)$$

Comparing (5.142) and (5.134), and considering (5.135), we use the representation theorem and express (5.142) as:

$$\mathbf{Q} = \frac{\partial \psi^e(\mathcal{H}^e)}{\mathcal{H}^e} \quad (5.143)$$

We now substitute (5.141) into (5.139), which yields:

$$\bar{\mathbf{F}}^{in^T} \mathbf{m} \bar{\mathbf{F}}^{in} = \bar{\mathbf{U}}^{in} \mathbf{Q} \bar{\mathbf{U}}^{in} \quad (5.144)$$

Using the isotropic property of ψ^{in} , following a similar approach, we obtain:

$$\mathbf{x} = \frac{\partial \psi^{in}}{\partial \bar{\mathbf{h}}^{in}} = \beta_1 \mathbf{1} + \beta_2 \bar{\mathbf{h}}^{in} + \beta_3 \bar{\mathbf{h}}^{in^2} \quad (5.145)$$

where

$$\beta_i = \beta_i(I_{\bar{\mathbf{h}}^{in}}, II_{\bar{\mathbf{h}}^{in}}, III_{\bar{\mathbf{h}}^{in}}, T) = \beta_i(I_{\bar{\mathbf{H}}^{in}}, II_{\bar{\mathbf{H}}^{in}}, III_{\bar{\mathbf{H}}^{in}}, T) \quad (5.146)$$

We now use the identity $\bar{\mathbf{F}}^{in^T} \bar{\mathbf{h}}^{in} \bar{\mathbf{F}}^{in} = \bar{\mathbf{H}}^{in} \bar{\mathbf{C}}^{in}$ to obtain:

$$\bar{\mathbf{F}}^{in^T} \mathbf{x} \bar{\mathbf{F}}^{in} = \mathbf{X} \bar{\mathbf{C}}^{in} \quad (5.147)$$

where

$$\mathbf{X} = \beta_1 \mathbf{1} + \beta_2 \bar{\mathbf{H}}^{in} + \beta_3 \bar{\mathbf{H}}^{in^2} \quad (5.148)$$

Similarly, comparing (5.148) and (5.145) and considering (5.146), we can express (5.148) as:

$$\mathbf{X} = \frac{\partial \psi^{in}(\bar{\mathbf{H}}^{in})}{\partial \bar{\mathbf{H}}^{in}} \quad (5.149)$$

Since \mathbf{X} and $\bar{\mathbf{U}}^{in}$ are coaxial, the following identity holds:

$$\mathbf{X} = \bar{\mathbf{U}}^{in} \mathbf{X} \bar{\mathbf{U}}^{in^{-1}} \quad (5.150)$$

Substituting (5.150) into (5.147), we obtain:

$$\bar{\mathbf{F}}^{inT} \mathbf{x} \bar{\mathbf{F}}^{in} = \bar{\mathbf{U}}^{in} \mathbf{X} \bar{\mathbf{U}}^{in} \quad (5.151)$$

Combining (5.144) and (5.151), we finally conclude:

$$\bar{\mathbf{F}}^{inT} \boldsymbol{\alpha} \bar{\mathbf{F}}^{in} = \bar{\mathbf{F}}^{inT} (\mathbf{m} - \mathbf{x}) \bar{\mathbf{F}}^{in} = \bar{\mathbf{U}}^{in} \mathbf{Z} \bar{\mathbf{U}}^{in} \quad (5.152)$$

where

$$\mathbf{Z} = \mathbf{Q} - \mathbf{X} \quad (5.153)$$

Using (5.152), we obtain:

$$\bar{\mathbf{F}}^{inT} \boldsymbol{\alpha}^n \bar{\mathbf{F}}^{in} = \bar{\mathbf{U}}^{in} \mathbf{Z}^n \bar{\mathbf{U}}^{in} \quad \text{and} \quad \text{tr}(\boldsymbol{\alpha}^n) = \text{tr}(\mathbf{Z}^n) \quad (5.154)$$

where n is a non-negative integer number. Equation (5.154)₂ means that the invariants of $\boldsymbol{\alpha}$ and \mathbf{Z} are the same.

We now assume $G(\boldsymbol{\alpha}, q)$ and $F(\boldsymbol{\alpha}, q)$ to be isotropic functions of $\boldsymbol{\alpha}$ which means that they are expressed only in terms of the invariants of $\boldsymbol{\alpha}$ which are equal to those of \mathbf{Z} . Therefore, we present the Lagrangian form of the potential and limit functions, respectively, as follows:

$$G = G(\mathbf{Z}, q) \quad \text{and} \quad F = f(\mathbf{Z}, q) - R \quad (5.155)$$

In order to obtain the evolution equation in a Lagrangian form, we use relation $\dot{\bar{\mathbf{C}}}^{in} = 2\bar{\mathbf{F}}^{inT} \dot{\bar{\mathbf{d}}}^{in} \bar{\mathbf{F}}^{in}$ and (5.129) to obtain:

$$\dot{\bar{\mathbf{C}}}^{in} = 2\dot{\bar{\mathbf{F}}}^{inT} \frac{\partial G(\boldsymbol{\alpha}, q)}{\partial \boldsymbol{\alpha}} \bar{\mathbf{F}}^{in} \quad (5.156)$$

Considering the isotropic property of $G(\boldsymbol{\alpha}, q)$, the following identity holds (see equation (B.16) in the Appendix):

$$\bar{\mathbf{F}}^{inT} \frac{\partial G(\boldsymbol{\alpha}, q)}{\partial \boldsymbol{\alpha}} \bar{\mathbf{F}}^{in} = \bar{\mathbf{U}}^{in} \frac{\partial G(\mathbf{Z}, q)}{\partial \mathbf{Z}} \bar{\mathbf{U}}^{in} \quad (5.157)$$

Finally, substituting (5.157) into (5.156), we obtain the Lagrangian form of the tensorial evolution equation as follows:

$$\dot{\bar{\mathbf{C}}}^{in} = 2\dot{\bar{\mathbf{U}}}^{in} \frac{\partial G(\mathbf{Z}, q)}{\partial \mathbf{Z}} \bar{\mathbf{U}}^{in} \quad (5.158)$$

Moreover, the scalar internal variable evolution is stated as:

$$\dot{\theta}^{in} = \dot{\zeta} \frac{\partial G(\mathbf{Z}, q)}{\partial q} \quad (5.159)$$

The second Piola-Kirchhoff stress tensor \mathbf{S} is obtained from the Kirchhoff stress tensor as:

$$\mathbf{S} = \mathbf{F}^{-1} \boldsymbol{\tau} \mathbf{F}^{-T} \quad (5.160)$$

Substituting (5.111) and $\boldsymbol{\tau} = \mathbf{s}^* + p^* \mathbf{1}$ into (5.160) yields:

$$\mathbf{S} = J^{-2/3} \left(p \bar{\mathbf{C}}^{-1} + \bar{\mathbf{F}}^{-1} \mathbf{s} \bar{\mathbf{F}}^{-T} \right) \quad (5.161)$$

Substituting (5.124)₁ and (5.137) into (5.161), we obtain:

$$\mathbf{S} = J^{-2/3} \left(\dot{\phi}^e \bar{\mathbf{C}}^{-1} + \bar{\mathbf{C}}^{-1} \mathbf{M}^* \right) \quad (5.162)$$

where, $\dot{\phi}^e = \partial \phi^e / \partial \theta^e$.

We now substitute (5.141) into (5.162) and obtain the second Piola-Kirchhoff stress tensor as follows¹² :

$$\mathbf{S} = J^{-2/3} \bar{\mathbf{C}}^{-1} \left(\dot{\phi}^e \mathbf{1} + \bar{\mathbf{U}}^{in} \mathbf{Q} \bar{\mathbf{U}}^{in^{-1}} \right) \quad (5.163)$$

We finally summarize the time-continuous finite-strain constitutive model, written only in terms of Lagrangian quantities in Table 5.4.

It is interesting that the proposed finite strain and the corresponding small strain (when the proposed model is linearized) constitutive models have similar forms, thanks to the Hencky strain. In particular, when linearized, the elastic-like strain tensor $\boldsymbol{\mathcal{H}}^e$ is reduced to small-strain elastic strain tensor, i.e.,

$$\boldsymbol{\mathcal{H}}^e \simeq \boldsymbol{\varepsilon} - \boldsymbol{\varepsilon}^{in} + \text{higher order terms} \simeq \boldsymbol{\varepsilon}^e \quad (5.164)$$

where $\boldsymbol{\varepsilon}$, $\boldsymbol{\varepsilon}^e$ and $\boldsymbol{\varepsilon}^{in}$ are, respectively, the total, elastic and inelastic small strain tensors. Equation (5.164) makes clear the reason for choosing the name "elastic-like strain tensor" for $\boldsymbol{\mathcal{H}}^e$.

5.7.4 Proposing a Hencky-based SMA constitutive model

We now particularize the inelastic model presented in Sections 5.4 to shape memory alloys.

We remark that in the constitutive models based on the multiplicative decomposition of the deformation gradient, Green-Lagrange strain has been used as a strain measure

¹²According to equation (5.163), the so-called Mandel stress is $\mathbf{C}\mathbf{S} = \dot{\phi}^e \mathbf{1} + \bar{\mathbf{U}}^{in} \mathbf{Q} \bar{\mathbf{U}}^{in^{-1}} = \bar{\mathbf{U}}^{in} (\dot{\phi}^e \mathbf{1} + \mathbf{Q}) \bar{\mathbf{U}}^{in^{-1}}$ which is, in general, an asymmetric tensor.

and in most cases the obtained constitutive models are in a Lagrangian form. In the approaches based on the use of Green-Lagrange strain, one critical point is introducing a relation between martensite volume fraction, z , and the norm of the Green-Lagrange strain measure¹³ (since $0 \leq z \leq 1$ it can be considered as a constraint on the inelastic strain). While the martensite fraction is a physical quantity, the Green-Lagrange strain is not a physical measure of strain. Considering this point, the proposed finite strain model which is based on the true strain is preferred.

On the other hand, in the constitutive models in which logarithmic strain is used as a (physical) strain measure, the additive decomposition of the strain rate tensor is adopted and the final form of the constitutive equations are Eulerian and objective rates should be used. For example, Müller and Bruhns (2004, 2006) have used a corotational rate associated to the logarithmic spin in their formulations.

In this section, we use the logarithmic strain as a physical measure of strain and based on the multiplicative decomposition of the deformation gradient we present a constitutive model in a Lagrangian form. We develop a finite-strain SMA model by extending the small-strain constitutive model proposed by Souza et al. (1998).

Strain energy function forms

We now assume the following forms for the elastic strain energy functions¹⁴:

$$\phi^e(\theta^e) = \frac{1}{2}K\theta^{e2}, \quad \psi^e(\bar{\mathbf{h}}^e) = \mu \|\bar{\mathbf{h}}^e\|^2 \quad (5.165)$$

where K and μ are the material parameters.

Since experimental evidence indicates that phase transformation-induced deformations in SMAs are nearly isochoric, we have to impose $\det(\mathbf{F}^{in}) = 1$, which after taking the time derivative results in:

$$\text{tr}(\mathbf{d}^{in}) = 0 \quad (5.166)$$

Therefore, $J^{in} = 1$ (or $\theta^{in} = 0$) is a known quantity. For this reason, without loss of generality, we can assume $\phi^{in}(\theta^{in}) = 0$. In the following, for simplicity, we denote all inelastic quantities without a bar symbol.

In order to describe SMAs behavior, we use the following form for ψ^{in} (Arghavani et al., 2010b; Souza et al., 1998):

$$\psi^{in} = \psi^{in}(\mathbf{h}^{in}, T) = \tau_M \|\mathbf{h}^{in}\| + \frac{1}{2}h_k \|\mathbf{h}^{in}\|^2 + \mathcal{I}_{\varepsilon_L}(\|\mathbf{h}^{in}\|) \quad (5.167)$$

¹³It has been defined in several works (Arghavani et al., 2010d; Christ and Reese, 2009; Evangelista et al., 2009; Helm and Haupt, 2003; Reese and Christ, 2008) as $z = \frac{\|\mathbf{E}^{in}\|}{\varepsilon_L}$, (see also equation (5.6)) where ε_L is a material parameter related to the maximum transformation strain.

¹⁴This is a Hookean-type strain energy function in terms of Hencky strain. It is also known as Hencky model in the literature (see e.g., Xiao and Chen (2002)).

where the material parameter h_k is the kinematic hardening parameter. In equation (5.167) we use the indicator function $\mathcal{I}_{\varepsilon_L}$ defined as:

$$\mathcal{I}_{\varepsilon_L}(\|\mathbf{h}^{in}\|) = \begin{cases} 0 & \text{if } \|\mathbf{h}^{in}\| \leq \varepsilon_L \\ +\infty & \text{otherwise} \end{cases} \quad (5.168)$$

to satisfy the constraint on the transformation strain norm,i.e.:

$$\|\mathbf{h}^{in}\| \leq \varepsilon_L \quad (5.169)$$

For a kinematic hardening plasticity, we can assume a quadratic form for ψ^{in} , denoted by ψ^p :

$$\psi^{in} = \psi^p(\mathbf{h}^p, T) = \frac{1}{2}h_k\|\mathbf{h}^p\|^2 \quad (5.170)$$

Comparing the above equation and (5.167), we can conclude that a SMA constitutive model is reduced to a kinematic hardening plasticity model, when $\tau_M(T) = 0$ (or $T < T_0$) and $\varepsilon_L \rightarrow \infty$. To this reason, The proposed SMA constitutive model is capable to describe associated von-Mises type kinematic hardening plasticity.

We assume an associated case ($F = G$) and consider a von-Mises type limit (yield) function as:

$$F(\mathbf{Z}, q) = \|\mathbf{Z}\| - R \quad (5.171)$$

We now compute the strain energy functions derivative as follows:

$$\dot{\phi}^e = \frac{\partial \phi^e}{\partial \theta^e} = K\theta^e, \quad \frac{\partial \psi^e}{\partial \bar{\mathbf{h}}^e} = 2\mu \bar{\mathbf{h}}^e \quad (5.172)$$

which yields

$$\alpha_1 = 0, \quad \alpha_2 = \mu, \quad \alpha_3 = 0 \quad (5.173)$$

and accordingly:

$$\mathbf{Q} = \mu \log \left(\mathbf{U}^{in-1} \bar{\mathbf{C}} \mathbf{U}^{in-1} \right) = 2\mu \mathcal{H}^e \quad (5.174)$$

In a similar approach, we obtain

$$\frac{\partial \psi^{in}}{\partial \mathbf{h}^{in}} = h_k \mathbf{h}^{in} + (\tau_M(T) + \gamma) \frac{\mathbf{h}^{in}}{\|\mathbf{h}^{in}\|} \quad (5.175)$$

The positive variable γ results from the indicator function subdifferential $\partial \mathcal{I}_{\varepsilon_L}(\mathbf{h}^{in})$ and it is defined as:

$$\begin{cases} \gamma \geq 0 & \text{if } \|\mathbf{H}^{in}\| = \varepsilon_L \\ \gamma = 0 & \text{if } \|\mathbf{H}^{in}\| < \varepsilon_L \end{cases} \quad (5.176)$$

We then conclude:

$$\beta_1 = 0, \quad \beta_2 = h_k + \frac{\tau_M(T) + \gamma}{\|\mathbf{H}^{in}\|}, \quad \beta_3 = 0 \quad (5.177)$$

In equations (5.176) and (5.177), we have also used the property of $\|\mathbf{h}^{in}\| = \|\mathbf{H}^{in}\|$. Substituting (5.177) into (5.148), we obtain:

$$\mathbf{X} = h_k \mathbf{H}^{in} + (\tau_M(T) + \gamma) \mathbf{N} \quad (5.178)$$

where $\mathbf{N} = \mathbf{H}^{in} / \|\mathbf{H}^{in}\|$.

Presentation of a well-defined form

In an approach similar to 5.5.2, we start investigating a condition in which \mathbf{H}^{in} starts to evolve from a zero value (indicated in the following as *Nucleation*), i.e., $\mathbf{H}^{in} = \mathbf{0}$ with $\|\dot{\mathbf{H}}^{in}\| > 0$. Substituting $\mathbf{U}^{in} = \mathbf{1}$ into (5.153) we conclude that $\mathbf{Z} = \mathbf{Q}_e$. We now consider the evolution equation which yields:

$$\dot{\mathbf{C}}^{in} = 2\dot{\zeta} \frac{\mathbf{Q}_e}{\|\mathbf{Q}_e\|} \quad (5.179)$$

where $\mathbf{Q}_e = \mu \log(\bar{\mathbf{C}}) = 2\mu \bar{\mathbf{H}}$ is obtained from (5.174) substituting $\mathbf{1}$ in place of \mathbf{U}^{in} . According to (5.179), the transformation strain, $\mathbf{H}^{in} = \frac{1}{2} \log(\mathbf{C}^{in}) \simeq \frac{1}{2}(\mathbf{C}^{in} - \mathbf{1})$, nucleates in the \mathbf{Q}_e direction.

We now investigate the case when transformation strain vanishes from a nonzero value (indicated in the following as *Completion*), i.e., $\mathbf{H}^{in} = \mathbf{0}$ ($\mathbf{U}^{in} = \mathbf{1}$) with $\|\dot{\mathbf{H}}^{in}\| < 0$. Since $\|\mathbf{H}^{in}\| = 0$, we conclude that adopting any arbitrary direction \mathbf{N} leads to $\mathbf{H}^{in} = \mathbf{0}$. We select this direction as the \mathbf{Q}_e direction which also guarantees continuity. Therefore, we revise the variable \mathbf{N} in the following form:

$$\mathbf{N} = \begin{cases} \frac{\mathbf{Q}_e}{\|\mathbf{Q}_e\|} & \text{if } \|\mathbf{H}^{in}\| = 0 \\ \frac{\mathbf{H}^{in}}{\|\mathbf{H}^{in}\|} & \text{if } \|\mathbf{H}^{in}\| \neq 0 \end{cases} \quad (5.180)$$

We note that according to the above discussion, the tensor \mathbf{N} and consequently the tensor \mathbf{X} are well-defined, non-singular and continuous.

We finally summarize the proposed finite strain constitutive model for shape memory alloys in Table 5.5. We recall that, for simplicity, all inelastic quantities are denoted without a bar symbol.

5.8 Extension into large rotation, small strain regime

5.8.1 Introduction

In this section, we deal with the special case of large rotation but small strains. There are several reasons for doing so, but the principal one is simplicity. Using the restrictions of small strain it is possible to keep much of the classical theory. To this end, we develop a constitutive model in the finite deformation regime and emphasize that its domain of application is limited by a priori kinematic assumptions, i.e.:

Displacements and rotations may be arbitrarily large; but strains must be small.

5.8.2 Kinematics description

For the important case of large rotations and small strains, we can use the polar decomposition as $\mathbf{F} = \mathbf{R}\mathbf{U}$, where \mathbf{R} is the rotation and \mathbf{U} is the right stretch tensor (the stretch written on the reference configuration). If we write the principal stretches in terms of nominal principal strains,

$$\lambda_i = 1 + \varepsilon_i, \quad (i = 1, 2, 3) \quad (5.181)$$

The right stretch tensor can be written as:

$$\mathbf{U} = \sum_{i=1}^3 (1 + \varepsilon_i) \mathbf{N}_i \otimes \mathbf{N}_i = \mathbf{1} + \boldsymbol{\varepsilon} \quad (5.182)$$

where $\boldsymbol{\varepsilon}$ is the (engineering) strain in the small deformation theory. The deformation gradient can be then written as:

$$\mathbf{F} = \mathbf{R}(\mathbf{1} + \boldsymbol{\varepsilon}) \quad (5.183)$$

and the inverse deformation gradient can be approximated by:

$$\mathbf{F}^{-1} = (\mathbf{1} + \boldsymbol{\varepsilon})^{-1} \mathbf{R}^T = (\mathbf{1} - \boldsymbol{\varepsilon}) \mathbf{R}^T \quad (5.184)$$

We note that, for the small strain case, all entries in $\boldsymbol{\varepsilon}$ are very much smaller than one. In addition,

$$J = \det(\mathbf{F}) = \det(\mathbf{R})\det(\mathbf{1} + \boldsymbol{\varepsilon}) = 1 + \text{tr}(\boldsymbol{\varepsilon}) + O(\varepsilon^2) \approx 1 + \text{tr}(\boldsymbol{\varepsilon}) \quad (5.185)$$

The relation between time derivative of strain tensor and stretching tensor can be obtained in a similar approach. To this end, we first compute the velocity gradient tensor as:

$$\mathbf{l} = \dot{\mathbf{F}}\mathbf{F}^{-1} \approx \dot{\mathbf{R}}\mathbf{R}^T + \mathbf{R}\dot{\boldsymbol{\varepsilon}}(\mathbf{1} - \boldsymbol{\varepsilon})\mathbf{R}^T \approx \dot{\mathbf{R}}\mathbf{R}^T + \mathbf{R}\dot{\boldsymbol{\varepsilon}}\mathbf{R}^T \quad (5.186)$$

We now use the relation $\mathbf{d} = \text{sym}(\mathbf{l})$ and conclude:

$$\mathbf{d} = \mathbf{R}\dot{\boldsymbol{\varepsilon}}\mathbf{R}^T \quad (5.187)$$

The relation between the time rate of Green-Lagrange strain and the stretching tensor is simplified to:

$$\dot{\mathbf{E}} = \mathbf{F}^T \mathbf{d}\mathbf{F} = (\mathbf{1} + \boldsymbol{\varepsilon})\mathbf{R}^T \mathbf{d}\mathbf{R}(\mathbf{1} + \boldsymbol{\varepsilon}) \approx \mathbf{R}^T \mathbf{d}\mathbf{R} \quad (5.188)$$

Comparing (5.187) and (5.188), we conclude:

$$\dot{\mathbf{E}} = \dot{\boldsymbol{\varepsilon}} \quad (5.189)$$

Which simply states that, for a small strain, large rotation case, the engineering strain rate and the rate of Green-Lagrange strain are approximately the same.

Moreover, for the case of large rotations and small strains, we can decompose additively the Green-Lagrange strain tensor (Crisfield, 1997):

$$\mathbf{E} = \mathbf{E}^e + \mathbf{E}^{in} \quad (5.190)$$

According to relations (5.188)-(5.190), we can conclude:

$$\dot{\mathbf{E}}^e = \mathbf{R}^T \mathbf{d}^e \mathbf{R} \quad \text{and} \quad \dot{\mathbf{E}}^{in} = \mathbf{R}^T \mathbf{d}^{in} \mathbf{R} \quad (5.191)$$

The second Piola-Kirchhoff stress is then readily interpreted as a rotated stress:

$$\mathbf{S} \approx (1 + O(\varepsilon))(\mathbf{1} - \boldsymbol{\varepsilon})\mathbf{R}^T \boldsymbol{\sigma} \mathbf{R}(\mathbf{1} - \boldsymbol{\varepsilon})^T \quad (5.192)$$

Neglecting terms of order strain compared to unity (since this is the small-strain approximation), we conclude that:

$$\mathbf{S} = \mathbf{R}^T \boldsymbol{\sigma} \mathbf{R} \quad (5.193)$$

This result gives a very simple physical interpretation of the second Piola-Kirchhoff stress for small strains but arbitrarily large rotations: the components of \mathbf{S} are the rotated components of $\boldsymbol{\sigma}$. That is, the components of \mathbf{S} are the stress components, associated with directions in the reference configuration.

Finally, Table 5.6 summarizes the obtained results under the assumption of large rotations and small strains.

5.8.3 Extension of Souza model to large rotation regime: Lagrangian formulation

According to the preliminaries presented in Section 5.8.2, we conclude that for the case of small strains, large rotations, the Souza model is extended just using the Green-Lagrange strain in place of $\boldsymbol{\varepsilon}$ and the second Piola-Kirchhoff stress (rotated stress) in place of $\boldsymbol{\sigma}$. Formulated in a Lagrangian framework, we then summarize the basic Souza model extension for the case of large rotation, small strain in Table 5.7. We remark that we denote with superscript D the deviatoric part of a tensor.

5.8.4 Extension of Souza model to large rotation regime: Eulerian formulation

In order to transform the constitutive model summarized in Table 5.7 to the current configuration (i.e., Eulerian formulation), we use the standard approach introduced in Chapter 3. However, we here use the approximation of strains being small and simplify the final relations. To this end, we first address some preliminaries.

Equality of all strain measures under small strain assumption

We note that under the assumption of small strains, we can use the following approximation:

$$\frac{1}{\alpha}(\lambda^\alpha - 1) \approx \lambda - 1 \approx \log(\lambda) \quad (5.194)$$

Applying the above approximation to (3.16) and then to (3.15), we obtain the following results which are valid only under the assumption of small strains:

$$\mathbf{E}^\alpha \approx \log(\mathbf{U}) = \mathbf{H} \quad \text{and} \quad \mathbf{e}^\alpha \approx \log(\mathbf{V}) = \mathbf{h} \quad (5.195)$$

Moreover, since $\mathbf{V} = \mathbf{R}\mathbf{U}\mathbf{R}^T$, we have:

$$\mathbf{e}^\alpha = \mathbf{R}\mathbf{E}^\alpha\mathbf{R}^T \quad (5.196)$$

We now combine (5.195) and (5.196) to obtain:

$$\mathbf{R}\mathbf{E}^\alpha\mathbf{R}^T = \mathbf{h} \quad (5.197)$$

Relation (5.197) means that under the assumption of strains being small, any rotated Lagrangian strain approximately represents the Eulerian Hencky strain.

Equality of all spin tensors under small strain assumption

According to Xiao et al. (1998), any objective spin tensor can be written as:

$$\boldsymbol{\Omega}^* = \mathbf{w} + \nu_1 \text{skew}(\mathbf{b}\mathbf{d}) + \nu_2 \text{skew}(\mathbf{b}^2\mathbf{d}) + \nu_3 \text{skew}(\mathbf{b}\mathbf{d}\mathbf{b}^2) \quad (5.198)$$

where ν_1, ν_2, ν_3 are functions of principal invariants of \mathbf{b} . Under the assumption of small strains, we have:

$$\mathbf{b} \approx \mathbf{1} + 2\mathbf{h} \quad \text{and} \quad \mathbf{b}^2 \approx \mathbf{1} + 4\mathbf{h} \quad \text{where} \quad \|\mathbf{h}\| = O(\varepsilon) \quad (5.199)$$

Substituting (5.199) into (5.198) and ignoring higher order terms, we observe that the skew-symmetric terms in (5.198) vanish. Thus, we can conclude that under the assumption of strains being small, all spins yield the same result. For example, the Jaumann,

Green-Naghdi and logarithmic rates are approximately the same. We show this fact for Green-Naghdi spin, knowing that the relation between \mathbf{w} and $\mathbf{\Omega} = \dot{\mathbf{R}}\mathbf{R}^T$ is given as:

$$\mathbf{w} - \mathbf{\Omega} = \frac{1}{2}\mathbf{R}(\dot{\mathbf{U}}\mathbf{U}^{-1} - \mathbf{U}^{-1}\dot{\mathbf{U}})\mathbf{R}^T \quad (5.200)$$

According to (5.182), we can write:

$$\dot{\mathbf{U}}\mathbf{U}^{-1} - \mathbf{U}^{-1}\dot{\mathbf{U}} = \dot{\boldsymbol{\varepsilon}}(\mathbf{1} - \boldsymbol{\varepsilon}) - (\mathbf{1} - \boldsymbol{\varepsilon})\dot{\boldsymbol{\varepsilon}} \approx \dot{\boldsymbol{\varepsilon}} - \dot{\boldsymbol{\varepsilon}} = \mathbf{0} \quad (5.201)$$

Constitutive model development

We now use the above approximations and transform the constitutive equations of Section 5.8.3 to the current configuration. To this end, we multiply all equations from left and right by \mathbf{R} and \mathbf{R}^T , respectively. We then use the following relations:

$$\mathbf{R}\mathbf{S}^D\mathbf{R}^T = \mathbf{s}, \quad \mathbf{R}\mathbf{E}^{in}\mathbf{R}^T = \mathbf{h}^{in}, \quad \mathbf{R}\mathbf{X}\mathbf{R}^T = \mathbf{x}, \quad \mathbf{R}\mathbf{X}^{in}\mathbf{R}^T = \mathbf{x}^{in} \quad (5.202)$$

where

$$\mathbf{x} = [\tau_M(T) + h\|\mathbf{h}^{in}\| + \gamma] \frac{\mathbf{h}^{in}}{\|\mathbf{h}^{in}\|} \quad (5.203)$$

We now consider the evolution equation. Multiplying the evolution equation from left and right by \mathbf{R} and \mathbf{R}^T , respectively, we obtain:

$$\mathbf{R}\dot{\mathbf{E}}^{in}\mathbf{R}^T = \dot{\zeta} \frac{\mathbf{x}^{in}}{\|\mathbf{x}^{in}\|} \quad (5.204)$$

According to (5.191)₂, we now substitute \mathbf{d}^{in} in place of $\mathbf{R}\dot{\mathbf{E}}^{in}\mathbf{R}^T$. However, we know that \mathbf{d}^{in} is the objective rate of Eulerian Hencky strain associated with the logarithmic spin. Since the strains are assumed to be small, we can use any objective rate in place of logarithmic spin. For simplicity, we use the Jaumann rate and finally obtain the following evolution equation:

$$\overset{\Delta}{\mathbf{h}}^{in} = \dot{\zeta} \frac{\mathbf{x}^{in}}{\|\mathbf{x}^{in}\|} \quad (5.205)$$

We now summarize in Table 5.8 the Eulerian extension of Souza model into large rotation, small strain regime.

5.9 Summary

In this chapter, we used a multiplicative decomposition of the deformation gradient into elastic and inelastic parts to extend two small strain constitutive models, i.e., the model by Panico and Brinson (2007) and the model by Souza et al. (1998), into finite strain

regime. We first extended the model by Panico and Brinson (2007) decomposing the inelastic strain rate tensor into transformation and reorientation parts. Based on the Green-Lagrange strain tensor, we then extended the Souza model. We observed that in the final (Lagrangian) equations an asymmetric Mandel stress appears; however we used a mathematical identity to recast all equations in a fully symmetric form. We then extended the Souza model through use of Hencky strain. To this end, we first developed a constitutive model in a general framework and then specialized it to the Souza model. Following this approach, we simply showed that the finite extension of a small strain model is not unique. We finally extended the original Souza model to the large rotation, but small strain, regime.

Table 5.1: Finite strain extension of Panico and Brinson (2007) constitutive model

External variables: \mathbf{C}, T

Internal variable: \mathbf{C}^{in}

Stress quantities:

$$\mathbf{S} = 2 \left(\alpha_1 \mathbf{C}^{in-1} + \alpha_2 \mathbf{C}^{in-1} \mathbf{C} \mathbf{C}^{in-1} + \alpha_3 \mathbf{C}^{in-1} (\mathbf{C} \mathbf{C}^{in-1})^2 \right)$$

$$\mathbf{Y} = \mathbf{C} \mathbf{S} - \mathbf{C}^{in} \mathbf{X}$$

$$\mathbf{M} = \mathbf{C} \mathbf{S}$$

$$\mathbf{X} = \rho_0 [\langle T \Delta \eta_0 - \Delta u_0 \rangle + H_\sigma z_\sigma] \frac{\mathbf{E}^{in}}{\|\mathbf{E}^{in}\|}$$

$$X^T = -\rho_0 (T \Delta \eta_0 - \Delta u_0)$$

Evolution equations:

$$\dot{\mathbf{C}}^{in} = \left(2\dot{\lambda}_{tr} \mathbf{Y}^D + 2\dot{\lambda}_{re} \tilde{\mathbb{I}} : \mathbf{M}^D \right) \mathbf{C}^{in}$$

$$\dot{z}_T = \dot{\lambda}_T X^T$$

Limit functions:

$$F_{tr} = \|\mathbf{Y}^D\| - Y_{tr}(z_\sigma)$$

$$F_{re} = \frac{1}{2} \mathbf{M}^D : \tilde{\mathbb{I}} : \mathbf{M}^D - Y_{re}$$

$$f_T = \begin{cases} X_T - Y_T^f(z_T) & \text{if } \dot{z}_T > 0 \\ -X_T - Y_T^r(z_T) & \text{if } \dot{z}_T < 0 \end{cases}$$

Kuhn-Tucker conditions:

$$F_{tr} \leq 0, \quad \dot{\lambda}_{tr} \geq 0, \quad \dot{\lambda}_{tr} F_{tr} = 0$$

$$F_{re} \leq 0, \quad \dot{\lambda}_{re} \geq 0, \quad \dot{\lambda}_{re} F_{re} = 0$$

$$F_T \leq 0, \quad \dot{\lambda}_T \geq 0, \quad \dot{\lambda}_T F_T = 0$$

Martensite volume fractions:

$$z_\sigma = \frac{\|\mathbf{E}^{in}\|}{\varepsilon_L}, \quad 0 \leq z_\sigma \leq 1, \quad 0 \leq z_T \leq 1, \quad 0 \leq z_T + z_\sigma \leq 1$$

Table 5.2: Finite-strain extension of Souza model.

External variables: \mathbf{C}, T

Internal variable: \mathbf{C}^{in}

Stress quantities:

$$\mathbf{S} = 2 \left(\alpha_1 \mathbf{C}^{in-1} + \alpha_2 \mathbf{C}^{in-1} \mathbf{C} \mathbf{C}^{in-1} + \alpha_3 \mathbf{C}^{in-1} \left(\mathbf{C} \mathbf{C}^{in-1} \right)^2 \right)$$

$$\mathbf{Y} = \mathbf{C} \mathbf{S} - \mathbf{C}^{in} \mathbf{X}$$

$$\mathbf{X} = h \mathbf{E}^{in} + (\tau_M + \gamma) \mathbf{N}$$

with

$$\begin{cases} \gamma \geq 0 & \text{if } \|\mathbf{E}^{in}\| = \varepsilon_L \\ \gamma = 0 & \text{if } \|\mathbf{E}^{in}\| < \varepsilon_L \end{cases}$$

and

$$\mathbf{N} = \begin{cases} \frac{(\mathbf{C} \mathbf{S}_e)^D}{\|(\mathbf{C} \mathbf{S}_e)^D\|} & \text{if } \|\mathbf{E}^{in}\| = 0 \\ \frac{\mathbf{E}^{in}}{\|\mathbf{E}^{in}\|} & \text{if } \|\mathbf{E}^{in}\| \neq 0 \end{cases}$$

where $\mathbf{E}^{in} = (\mathbf{C}^{in} - \mathbf{1}) / 2$

Evolution equation:

$$\dot{\mathbf{C}}^{in} = 2 \dot{\zeta} \frac{\mathbf{Y}^D}{\|\mathbf{Y}^D\|} \mathbf{C}^{in}$$

Limit function:

$$f = \|\mathbf{Y}^D\| - R$$

Kuhn-Tucker conditions:

$$f \leq 0, \quad \dot{\zeta} \geq 0, \quad \dot{\zeta} f = 0$$

Table 5.3: Finite-strain extension of Souza model: proposed fully symmetric form.

External variables: C, T

Internal variable: C^{in}

Stress quantities:

$$\mathbf{S} = \mathbf{U}^{in-1} \tilde{\mathbf{S}} \mathbf{U}^{in-1}$$

$$\tilde{\mathbf{S}} = 2 \left(\alpha_1 \mathbf{1} + \alpha_2 \tilde{\mathbf{C}} + \alpha_3 \tilde{\mathbf{C}}^2 \right)$$

$$\tilde{\mathbf{Y}} = \tilde{\mathbf{C}} \tilde{\mathbf{S}} - C^{in} \mathbf{X}$$

$$\mathbf{X} = h \mathbf{E}^{in} + (\tau_M + \gamma) \mathbf{N}$$

with

$$\begin{cases} \gamma \geq 0 & \text{if } \|\mathbf{E}^t\| = \varepsilon_L \\ \gamma = 0 & \text{otherwise} \end{cases}$$

and

$$\mathbf{N} = \frac{\mathbf{E}^{in}}{\|\mathbf{E}^{in}\|}, \quad \tilde{\mathbf{C}} = \mathbf{U}^{in-1} \mathbf{C} \mathbf{U}^{in-1}$$

where $\mathbf{E}^{in} = (\mathbf{C}^{in} - \mathbf{1}) / 2$

Evolution equation:

$$\dot{\mathbf{C}}^{in} = 2 \dot{\zeta} \mathbf{U}^{in} \frac{\tilde{\mathbf{Y}}^D}{\|\tilde{\mathbf{Y}}^D\|} \mathbf{U}^{in}$$

Limit function:

$$f = \|\tilde{\mathbf{Y}}^D\| - R$$

Kuhn-Tucker conditions:

$$f \leq 0, \quad \dot{\zeta} \geq 0, \quad \dot{\zeta} f = 0$$

Table 5.4: Finite-strain Hencky-based kinematic hardening constitutive model

External variables: \bar{C}, θ, T

Internal variables: $\bar{U}^{in}, \theta^{in}$

Stress quantities:

$$\mathbf{Q} = \frac{\partial \psi^e(\mathcal{H}^e)}{\partial \mathcal{H}^e} \quad \mathbf{X} = \frac{\partial \psi^{in}(\bar{\mathbf{H}}^{in})}{\partial \bar{\mathbf{H}}^{in}} \quad \mathbf{Z} = \mathbf{Q} - \mathbf{X} \quad q = \phi^e - \phi^{in}$$

with

$$\bar{\mathbf{H}}^{in} = \log(\bar{\mathbf{U}}^{in}), \quad \mathcal{H}^e = \frac{1}{2} \log(\bar{\mathbf{U}}^{in-1} \bar{\mathbf{C}} \bar{\mathbf{U}}^{in-1})$$

and

$$\dot{\phi}^e = \partial \phi^e / \partial \theta^e, \quad \dot{\phi}^{in} = \partial \phi^{in} / \partial \theta^{in} \quad \text{and} \quad \theta^e = \theta - \theta^{in},$$

Limit function:

$$F = f(\mathbf{Z}, q) - R$$

Potential function:

$$G = G(\mathbf{Z}, q)$$

Evolution equations:

$$\dot{\bar{\mathbf{C}}}^{in} = 2\dot{\zeta} \bar{\mathbf{U}}^{in} \frac{\partial G(\mathbf{Z}, q)}{\partial \mathbf{Z}} \bar{\mathbf{U}}^{in} \quad \text{and} \quad \dot{\theta}^{in} = \dot{\zeta} \frac{\partial G(\mathbf{Z}, q)}{\partial q}$$

Kuhn-Tucker conditions:

$$F \leq 0, \quad \dot{\zeta} \geq 0, \quad \dot{\zeta} F = 0$$

Table 5.5: Finite-strain Hencky-based extension of Souza model

External variables: \bar{C}, J, T

Internal variable: U^{in}

Stress quantities:

$$\mathbf{Q} = \mu \log \left(U^{in-1} \bar{C} U^{in-1} \right) = 2\mu \mathcal{H}^e$$

$$\mathbf{X} = h_k \mathbf{H}^{in} + (\tau_M(T) + \gamma) \mathbf{N}$$

$$\mathbf{Z} = \mathbf{Q} - \mathbf{X}$$

$$\mathbf{S} = J^{-2/3} \bar{C}^{-1} \left(K \log(J) \mathbf{1} + U^{in} \mathbf{Q} U^{in-1} \right)$$

with

$$\mathbf{H}^{in} = \log(U^{in}), \quad \mathcal{H}^e = \frac{1}{2} \log \left(U^{in-1} \bar{C} U^{in-1} \right)$$

$$\mathbf{N} = \begin{cases} \frac{\mathbf{Q}_e}{\|\mathbf{Q}_e\|} & \text{if } \|\mathbf{H}^{in}\| = 0 \\ \frac{\mathbf{H}^{in}}{\|\mathbf{H}^{in}\|} & \text{if } \|\mathbf{H}^{in}\| \neq 0 \end{cases}$$

$$\mathbf{Q}^e = 2\mu \bar{\mathbf{H}}$$

Evolution equation:

$$\dot{\mathbf{C}}^{in} = 2\dot{\zeta} U^{in} \frac{\mathbf{Z}}{\|\mathbf{Z}\|} U^{in}$$

Limit function:

$$F = \|\mathbf{Z}\| - R$$

Kuhn-Tucker conditions:

$$F \leq 0, \quad \dot{\zeta} \geq 0, \quad \dot{\zeta} F = 0$$

Table 5.6: Simplified relations under the assumption of large rotations and small strains

Kinematics:

deformation gradient: $\mathbf{F} = \mathbf{R}(\mathbf{1} + \boldsymbol{\varepsilon})$

Jacobian (determinant): $J = 1 + \text{tr}(\boldsymbol{\varepsilon})$

stretching tensor: $\mathbf{d} = \mathbf{R}\dot{\boldsymbol{\varepsilon}}\mathbf{R}^T$

vorticity tensor: $\mathbf{w} = \dot{\mathbf{R}}\mathbf{R}^T$

additive decomposition: $\mathbf{d} = \mathbf{d}^e + \mathbf{d}^{in}$

additive decomposition: $\mathbf{E} = \mathbf{E}^e + \mathbf{E}^{in}$

elastic G-L strain rate: $\dot{\mathbf{E}}^e = \mathbf{R}^T \mathbf{d}^e \mathbf{R}$

inelastic G-L strain rate: $\dot{\mathbf{E}}^{in} = \mathbf{R}^T \mathbf{d}^{in} \mathbf{R}$

Stress:

second Piola-Kirchhoff stress: $\mathbf{S} = \mathbf{R}^T \boldsymbol{\sigma} \mathbf{R}$

Energy:

conjugate pairs: $\mathbf{S} : \dot{\mathbf{E}} = J \boldsymbol{\sigma} : \mathbf{d}$

Table 5.7: Extension of Souza model to large rotation regime: Lagrangian formulation

External variables: \mathbf{E}, T

Internal variable: \mathbf{E}^{in}

Stress quantities:

$$\mathbf{S} = 2G(\mathbf{E}^D - \mathbf{E}^{in}) + K \operatorname{tr}(\mathbf{E}) \mathbf{1}$$

$$\mathbf{X} = [\tau_M(T) + h \|\mathbf{E}^{in}\| + \gamma] \frac{\mathbf{E}^{in}}{\|\mathbf{E}^{in}\|}$$

$$\mathbf{X}^{in} = \mathbf{S}^D - \mathbf{X}$$

with

$$\begin{cases} \gamma \geq 0 & \text{if } \|\mathbf{E}^{in}\| = \varepsilon_L \\ \gamma = 0 & \text{otherwise} \end{cases}$$

Evolution equation:

$$\dot{\mathbf{E}}^{in} = \dot{\zeta} \frac{\mathbf{X}^{in}}{\|\mathbf{X}^{in}\|}$$

Limit function:

$$f = \|\mathbf{X}^{in}\| - R$$

Kuhn-Tucker conditions:

$$f \leq 0, \quad \dot{\lambda} \geq 0, \quad \dot{\lambda} f = 0$$

Table 5.8: Extension of Souza model to large rotation regime: Eulerian formulation

External variables: \mathbf{h}, T

Internal variable: \mathbf{h}^{in}

Stress quantities:

$$\mathbf{s} = 2G(\bar{\mathbf{h}} - \mathbf{h}^{in})$$

$$\mathbf{x} = [\tau_M(T) + h\|\mathbf{h}^{in}\| + \gamma] \frac{\mathbf{h}^{in}}{\|\mathbf{h}^{in}\|}$$

$$\mathbf{x}^{in} = \mathbf{s} - \mathbf{x}$$

with

$$\begin{cases} \gamma \geq 0 & \text{if } \|\mathbf{h}^{in}\| = \varepsilon_L \\ \gamma = 0 & \text{otherwise} \end{cases}$$

Evolution equation:

$$\dot{\mathbf{h}}^{in} = \zeta \frac{\mathbf{x}^{in}}{\|\mathbf{x}^{in}\|}$$

Limit function:

$$f = \|\mathbf{x}^{in}\| - R$$

Kuhn-Tucker conditions:

$$f \leq 0, \dot{\lambda} \geq 0, \dot{\lambda}f = 0$$

Chapter 6

Numerical implementation: time-discretization and solution algorithms

6.1 Introduction

In chapters 4 and 5 we developed several SMA constitutive models at small and finite deformation regimes, respectively. In this chapter, we present the numerical counterpart and propose different time integration and solution algorithms. We mainly discuss the numerical implementation of finite deformation extensions of Souza model developed in Chapter 5 and avoid presenting too much details for small deformation part. This is due to the fact that most part of the current discussion at finite deformation regime can be applied to the small deformation regime as well. Moreover, details on small deformation Souza model can be found in Souza et al. (1998) and Auricchio and Petrini (2002, 2004a).

To this end, we first develop the time-discrete form of the constitutive equations. We then develop solution algorithm and address construction of consistent tangent matrix. We remark that due to similarity in discussions for different models, we first present a detailed discussion for the finite strain extension of Souza model discussed in Section 5.5 and then present a concise discussion for fully symmetric Souza model (Section 5.6), Hencky-based model in a general framework (Section 5.7) and Hencky-based Souza model (Section 5.7.4).

With the aim of increasing computational efficiency, we also present a corotational formulation which is able to compensate rigid body rotations and to use the codes already developed for the small strain constitutive model. In this chapter, we will extensively use abbreviations for different formulations which are summarized in Table

6.1.

Table 6.1: Different formulations and their abbreviations

Model	Abbreviation
Table 4.1	SSSR (Small Strain, Small Rotation)
Table 5.2	GLUS (Green-Lagrange based UnSymmetric)
Table 5.3	GLSY (Green-Lagrange based SYmmetric)
Table 5.4	HSGF (Hencky Strain based General Formulation)
Table 5.5	HSSY (Hencky Strain based SYmmetric)
Table 5.7	SSLR (Small Strain, Large Rotation)

Robustness study of different algorithms as well as comparison of their efficiency and application to the simulation of SMA-based devices is the subject of Chapter 7.

6.2 Numerical implementation of GLUS model

In this section we investigate the numerical solution of the constitutive model derived in Section 5.5 and summarized in Table 5.2, with the final goal of using it within a finite element program. The main task is to apply an appropriate numerical time integration scheme to the evolution equation of the internal variable. In general, implicit schemes are preferred because of their stability at larger time step sizes. Moreover, the present section provides some details about the stress update and the computation of the consistent tangent matrix, which are the two points where the material model is directly connected to the finite element solution procedure.

We now treat the nonlinear problem described in Section 5.5 as an implicit time-discrete deformation-driven problem. Accordingly, we subdivide the time interval of interest $[0, t]$ in sub-increments and we solve the evolution problem over the generic interval $[t_n, t_{n+1}]$ with $t_{n+1} > t_n$. To simplify the notation, we indicate with the subscript n a quantity evaluated at time t_n , and with no subscript a quantity evaluated at time t_{n+1} . Assuming to know the solution and the deformation gradient \mathbf{F}_n at time t_n as well as the deformation gradient \mathbf{F} at time t_{n+1} , the stress and the internal variable should be updated from the deformation history.

Since, the constitutive model is in terms of Lagrangian quantities, from now on, we assume as deformation driver the Green-Lagrange strain (instead of the deformation gradient), and compute the second Piola-Kirchhoff stress tensor. Then, using (3.55), the Cauchy stress is computed. We also derive the material consistent tangent matrix and construct the spatial tangent matrix using the following relation (Wriggers, 2008):

$$\mathbb{C}_{mnlk} = \frac{1}{J} F_{mM} F_{nN} F_{kK} F_{lL} \mathbb{D}_{MNKL} \quad (6.1)$$

where \mathbb{C} and \mathbb{D} are the fourth-order spatial and material consistent tangents, respectively. We remark that the consistent tangent matrix correspond to the Jaumann rate of stress can then be derived according to (3.104). Moreover, in ABAQUS/Standard, for continuum elements, we should report this tangent in the user-defined subroutine UMAT (ABAQUS/Standard, 2008).

6.2.1 Time integration.

Exponential-based integration schemes are frequently applied to problems in plasticity and isotropic inelasticity (Eterovic and Bathe, 1990; Miehe, 1996). The use of the exponential mapping enables to exactly conserve the inelastic volume. Thus, it allows larger time step sizes than any other first-order accurate integration scheme.

Applying the exponential mapping scheme to the evolution equation (5.80), we obtain:

$$\mathbf{C}^{in} = \exp(\Delta\zeta \mathbf{A}_1) \mathbf{C}_n^{in} \quad (6.2)$$

In the above form of the exponential mapping, we need to compute the exponential of an asymmetric tensor, which is a problematic computation due to impossibility of using a spectral decomposition method¹. Accordingly, using the strategy initially proposed in (Christ and Reese, 2009; Reese and Christ, 2008; Vladimirov et al., 2008) and also exploited in (Arghavani et al., 2010a; Evangelista et al., 2009; Vladimirov et al., 2010), we can find an alternative expression where the argument of the exponential operator is a symmetric tensor which can be computed through spectral decomposition. In fact, we can write:

$$\begin{aligned} \exp(\Delta\zeta \mathbf{A}_1) &= \mathbf{1} + \Delta\zeta \mathbf{A}_1 + \frac{\Delta\zeta^2}{2!} \mathbf{A}_1^2 + \dots \\ &= \mathbf{1} + \Delta\zeta \mathbf{A} \mathbf{C}^{in-1} + \frac{\Delta\zeta^2}{2!} \left(\mathbf{A} \mathbf{C}^{in-1} \right)^2 + \dots \\ &= \mathbf{U}^{in} \left(\mathbf{1} + \Delta\zeta \mathbf{U}^{in-1} \mathbf{A} \mathbf{U}^{in-1} + \frac{\Delta\zeta^2}{2!} \left(\mathbf{U}^{in-1} \mathbf{A} \mathbf{U}^{in-1} \right)^2 + \dots \right) \mathbf{U}^{in-1} \\ &= \mathbf{U}^{in} \exp \left(\Delta\zeta \mathbf{U}^{in-1} \mathbf{A} \mathbf{U}^{in-1} \right) \mathbf{U}^{in-1} \end{aligned} \quad (6.3)$$

We now right- and left-multiply (6.2) by \mathbf{C}_n^{in-1} and \mathbf{C}^{in-1} , respectively, to obtain:

$$\mathbf{C}_n^{in-1} = \mathbf{C}^{in-1} \exp(\Delta\zeta \mathbf{A}_1) \quad (6.4)$$

Then, substituting (6.3) into (6.4), we can write the integration formula as (Reese and Christ, 2008):

$$- \mathbf{C}_n^{in-1} + \mathbf{U}^{in-1} \exp \left(\Delta\zeta \mathbf{U}^{in-1} \mathbf{A} \mathbf{U}^{in-1} \right) \mathbf{U}^{in-1} = \mathbf{0} \quad (6.5)$$

¹The exponential of an asymmetric tensor is computed by means of series expansion. However, the exponential of a symmetric tensor can be computed in closed form by means of a spectral decomposition.

which is the time-discrete form associated to (5.80) presented so far in the literature (Christ and Reese, 2009; Evangelista et al., 2009; Reese and Christ, 2008; Vladimirov et al., 2008, 2010).

We now introduce an alternative form of the time-discrete evolution equation (6.5) which improves the numerical efficiency by decreasing the degree of equation nonlinearity. To this end, we left- and right-multiply (6.5) by \mathbf{U}^{in} and obtain:

$$\mathbf{U}^{in} \mathbf{C}_n^{in-1} \mathbf{U}^{in} = \exp\left(\Delta\zeta \mathbf{U}^{in-1} \mathbf{A} \mathbf{U}^{in-1}\right) \quad (6.6)$$

We take the logarithm of both sides of (6.6) and after left- and right-multiplication by \mathbf{U}^{in} , we obtain:

$$-\mathbf{U}^{in} \log\left(\mathbf{U}^{in} \mathbf{C}_n^{in-1} \mathbf{U}^{in}\right) \mathbf{U}^{in} + \Delta\zeta \mathbf{A} = \mathbf{0} \quad (6.7)$$

which can be seen as an alternative form of the time-discrete evolution equation through a logarithmic mapping.

While equations (6.5) and (6.7) are mathematically equivalent, equation (6.7) appears to be less nonlinear and computationally more effective, as shown in Chapter 7 through several numerical examples.

We remark that, to our knowledge, the logarithmic time-discrete form (6.7) (or logarithmic mapping) is presented for the first time in this paper, while the exponential form (6.5) has been extensively investigated in the literature (Christ and Reese, 2009; Evangelista et al., 2009; Reese and Christ, 2008; Vladimirov et al., 2008, 2010). We finally summarize the integration algorithms in Table 6.2.

Table 6.2: Exponential and logarithmic mappings.

Time-continuous form:

$$\dot{\mathbf{C}}^{in} = \dot{\zeta} \mathbf{A} \quad \text{and} \quad \det(\mathbf{C}^{in}) = 1$$

Exponential mapping:

$$-\mathbf{C}_n^{in-1} + \mathbf{U}^{in-1} \exp\left(\Delta\zeta \mathbf{U}^{in-1} \mathbf{A} \mathbf{U}^{in-1}\right) \mathbf{U}^{in-1} = \mathbf{0}$$

Logarithmic mapping:

$$-\mathbf{U}^{in} \log\left(\mathbf{U}^{in} \mathbf{C}_n^{in-1} \mathbf{U}^{in}\right) \mathbf{U}^{in} + \Delta\zeta \mathbf{A} = \mathbf{0}$$

6.2.2 Solution algorithm.

As usual in computational inelasticity problems, to solve the time-discrete constitutive model we use an elastic predictor-inelastic corrector procedure. The algorithm consists of evaluating an elastic trial state, in which the internal variable remains constant, and of verifying the admissibility of the trial function. If the trial state is admissible, the step is elastic; otherwise, the step is inelastic and the transformation internal variable

has to be updated through integration of the evolution equation.

In order to solve the inelastic step, we use another predictor-corrector scheme, that is, we assume $\gamma = 0$ (i.e., we predict an unsaturated transformation strain case with $\|\mathbf{E}^{in}\| \leq \varepsilon_L$) and we solve the following system of nonlinear equations (we refer to this system as *PT1* system):

$$\begin{cases} \mathbf{R}^{in} = -\mathbf{U}^{in} \log \left(\mathbf{U}^{in} \mathbf{C}_n^{in-1} \mathbf{U}^{in} \right) \mathbf{U}^{in} + \Delta\zeta \mathbf{A} = \mathbf{0} \\ R^\zeta = \|\mathbf{Y}^D\| - R = 0 \end{cases} \quad (6.8)$$

If the solution is not admissible (i.e., $\|\mathbf{E}^{in}\|_{PT1} > \varepsilon_L$), we assume $\gamma > 0$ (i.e., we consider a saturated transformation case with $\|\mathbf{E}^{in}\| = \varepsilon_L$) and we solve the following system of nonlinear equations (we refer to this system as *PT2* system):

$$\begin{cases} \mathbf{R}^{in} = -\mathbf{U}^{in} \log \left(\mathbf{U}^{in} \mathbf{C}_n^{in-1} \mathbf{U}^{in} \right) \mathbf{U}^{in} + \Delta\zeta \mathbf{A} = \mathbf{0} \\ R^\zeta = \|\mathbf{Y}^D\| - R = 0 \\ R^\gamma = \|\mathbf{E}^{in}\| - \varepsilon_L = 0 \end{cases} \quad (6.9)$$

Solution of equations (6.8) and (6.9) is, in general, approached through a straightforward Newton-Raphson method and it is not characterized by special difficulties except for the cases in which the transformation strain vanishes. Accordingly, in the following, we specifically focus on the nucleation ($\mathbf{E}_n^{in} = \mathbf{0}$) and completion ($\mathbf{E}^{in} = \mathbf{0}$) cases and construct the solution algorithm.

6.2.3 Considerations on nucleation-completion condition.

We first investigate the trial value of the limit function in the nucleation case, i.e., at the beginning of forward phase transformation, expressed as:

$$f^{TR} = \left| \|\mathbf{C}\mathbf{S}_e\|^D - \tau_M(T) \right| - R = \|\mathbf{C}\mathbf{S}_e\|^D - \tau_M(T) - R > 0 \quad (6.10)$$

where a superscript *TR* indicates a trial value. We may thus introduce the following as *nucleation condition*:

$$\|\mathbf{C}\mathbf{S}_e\|^D > \tau_M(T) + R \quad \text{and} \quad \|\mathbf{E}_n^{in}\| = 0 \quad (6.11)$$

In the solution procedure, when $\|\mathbf{E}_n^{in}\| = 0$ we check the nucleation condition and, if not satisfied, we assume an elastic behavior.

We remark that, to avoid singularity in local system (6.8) for the nucleation case, it is necessary to use a nonzero initial transformation strain. Since, we know the initial transformation strain direction (as discussed in Section 5.5.2), the only unknown for

constructing an initial guess is its norm; if we denote with q its value, we can use the following initial guess for the nucleation case:

$$\mathbf{C}_0^{in} = \mathbf{1} + 2q\mathbf{N}, \quad \mathbf{N} = \frac{(\mathbf{C}\mathbf{S}_e)^D}{\|(\mathbf{C}\mathbf{S}_e)^D\|} \quad (6.12)$$

where a subscript 0 denotes the initial guess. A value of 10^{-4} could be an appropriate choice for q .

We now focus on the completion case, i.e., $\mathbf{E}_n^{in} \neq \mathbf{0}$ but $\mathbf{E}^{in} = \mathbf{0}$, occurring at the end of reverse phase transformation. To this end, we consider equations (6.5) or (6.7) and substitute $\mathbf{C}^{in} = \mathbf{1}$ (as it happens for the completion case) to obtain:

$$\Delta\zeta\mathbf{A} = \log\left(\mathbf{C}_n^{in-1}\right) = -\log\left(\mathbf{C}_n^{in}\right), \quad \mathbf{A} = 2\frac{\mathbf{Y}^D}{\|\mathbf{Y}^D\|}, \quad \mathbf{Y}^D = (\mathbf{C}\mathbf{S}_e)^D - \tau_M\mathbf{N} \quad (6.13)$$

In deriving (6.13)₃, we have used the deviatoric property of \mathbf{N} , i.e., $\mathbf{N}^D = \mathbf{N}$, in accordance with (5.85). Assuming a very small time step size (or the time-continuous form), we can assume $\mathbf{C}_n^{in} \simeq \mathbf{1}$ and, considering (6.13) as well as the continuity of \mathbf{N} , approximate \mathbf{N}^{TR} with (5.85)₁ to obtain the following trial value for the limit function:

$$f^{TR} = \left| \|(\mathbf{C}\mathbf{S}_e)^D\| - \tau_M(T) \right| - R = -\|(\mathbf{C}\mathbf{S}_e)^D\| + \tau_M(T) - R > 0 \quad (6.14)$$

Similarly to the nucleation case, we may now define the following *completion condition*:

$$\|(\mathbf{C}\mathbf{S}_e)^D\| < \tau_M(T) - R \quad \text{and} \quad \|\mathbf{E}_n^{in}\| \neq 0 \quad (6.15)$$

Completion condition (6.15) is consistent with the time-continuous form of the evolution equation; it is then necessary to derive a completion condition consistent with the time-discrete form.

To this end, using equation (6.13)_{1,2} which define the \mathbf{Y}^D direction, and considering the limit function (5.79), we conclude:

$$\mathbf{Y}^D = -R\frac{\log\left(\mathbf{C}_n^{in}\right)}{\|\log\left(\mathbf{C}_n^{in}\right)\|} \quad (6.16)$$

Substituting (6.16) in (6.13)₃, we obtain:

$$(\mathbf{C}\mathbf{S}_e)^D + R\frac{\log\left(\mathbf{C}_n^{in}\right)}{\|\log\left(\mathbf{C}_n^{in}\right)\|} = \tau_M\mathbf{N} \quad (6.17)$$

Finally, taking the norm of both sides of equation (6.17), we define the following *consistent completion condition*:

$$\left\| (\mathbf{C}\mathbf{S}_e)^D + R\frac{\log\left(\mathbf{C}_n^{in}\right)}{\|\log\left(\mathbf{C}_n^{in}\right)\|} \right\| \leq \tau_M, \quad \|\mathbf{E}_n^{in}\| \neq 0 \quad (6.18)$$

Therefore, in the solution procedure we also should check the completion condition and, if it is satisfied, we simply update the internal variable by setting $\mathbf{C}^{in} = \mathbf{1}$.

We remark that in deriving (6.18), we started assuming $\mathbf{C}^{in} = \mathbf{1}$, while in the solution algorithm, we first check condition (6.18) and, if satisfied, we conclude $\mathbf{C}^{in} = \mathbf{1}$. Though from a mathematical point of view this is not proved, we will use condition (6.18) to solve a variety of problems which also confirms its validity.

The last point we discuss in this section is the improvement of the time-integration algorithm robustness by enhancing the Newton-Raphson (NR) method robustness. We remind that, the NR method converges to the solution only when the initial guess is good enough or, in other words, if the initial guess is inside the convergence area. Using a proper initial guess for the system of nonlinear equations, PT1 and PT2, has an important role in the algorithm robustness.

The solution from the previous time-step is apparently a proper initial guess for the PT1 system. We now consider the case of non-admissible PT1 solution ($\|\mathbf{E}^{in}\|_{PT1} > \varepsilon_L$) and seek a proper initial guess for the PT2 system. It could seem that using the previous time-step solution as the initial guess could be again a proper choice. We have done a comprehensive study on the different initial guess effects on the PT2 solution robustness under different loading conditions and the results show that, while using the previous time-step solution as the initial guess, NR converges for proportional loading conditions (usually with a large number of iterations), in most cases it diverges for large time-step sizes and non-proportional loadings.

Another option we propose is to use PT1 solution as the initial guess for PT2. In fact, our experience is that this choice improves the convergence behavior, dramatically reducing the number of iterations.

We have however to remark that, though using the proposed initial guess improves the convergence behavior, it fails in the case of severe non-proportional loading case and large time-step size. To this end, it is necessary to use the well-known techniques for divergence detection (maximum number of iterations, residual norm check, solution norm check) and introduce automatic increment-cutting techniques to reduce the increment size ².

In case of diverging PT2 system, gradually applying the norm constraint (6.9)₃ also improves convergence. This consists of first applying constraint (6.9)₃ and, if NR di-

²We assume \mathbf{C}_n and \mathbf{C}_n^{in} as well as \mathbf{C}_{n+1} to be given and try to compute \mathbf{C}_{n+1}^{in} . We start determining $\mathbf{E}_n = (\mathbf{C}_n - \mathbf{1})/2$ and $\mathbf{E}_{n+1} = (\mathbf{C}_{n+1} - \mathbf{1})/2$ and defining $\Delta\mathbf{E} = \mathbf{E}_{n+1} - \mathbf{E}_n$ as the strain increment. In the solution process we then assume $\mathbf{E} = \mathbf{E}_n + t\Delta\mathbf{E}$ (and compute $\mathbf{C} = 2\mathbf{E} + \mathbf{1}$) and we first solve the equations assuming $t = 1$. If we find out that NR diverges, we half the increment size dividing t by 2 and solve the equations; this process is iterated until NR converges. Then, we use this converged solution as an improved initial guess for NR to solve the original problem. This process can be repeated until solution converges.

verges, halving the projection length ($\|\mathbf{E}^{in}\|_{PT1} - \varepsilon_L$) and continuing this procedure until partially-projected PT2 system solution converges. Then we use the converged solution as the improved initial guess for the fully-projected PT2 system.

6.2.4 Consistent tangent matrix.

In the following, we linearize the nonlinear equations as it is required for the iterative Newton-Raphson method. For brevity, we report the construction of the tangent matrix only for the case of the saturated phase transformation, corresponding to (6.9). Linearizing (6.9), we obtain:

$$\begin{cases} \mathbf{R}^{in} + \mathbf{R}_{,\mathbf{C}^{in}}^{in} : d\mathbf{C}^{in} + \mathbf{R}_{,\Delta\zeta}^{in} d\Delta\zeta + \mathbf{R}_{,\gamma}^{in} d\gamma = \mathbf{0} \\ R^\zeta + R_{,\mathbf{C}^{in}}^\zeta : d\mathbf{C}^{in} + R_{,\Delta\zeta}^\zeta d\Delta\zeta + R_{,\gamma}^\zeta d\gamma = 0 \\ R^\gamma + R_{,\mathbf{C}^{in}}^\gamma : d\mathbf{C}^{in} + R_{,\Delta\zeta}^\gamma d\Delta\zeta + R_{,\gamma}^\gamma d\gamma = 0 \end{cases} \quad (6.19)$$

where subscripts following a comma indicate differentiation with respect to that quantity. The derivatives appearing in the above equation are detailed in Appendix C.

Utilizing the linearized form (6.19), after converting it to matrix form, a system of eight nonlinear scalar equations is solved to obtain $d\mathbf{C}^{in}$, $d\Delta\zeta$ and $d\gamma$ (we refer to this system as the local system and to its solution as the local solution, to distinguish it from the global system of equilibrium equations).

We now address the construction of the tangent tensor consistent with the time-discrete constitutive model. The use of a consistent tensor preserves the quadratic convergence of the Newton-Raphson method for the incremental solution of the global time-discrete problem, as in the framework of a finite element scheme.

The consistent tangent is computed by linearizing the second Piola-Kirchhof tensor, i.e.:

$$d\mathbf{S} = \mathbb{D} : d\mathbf{E} = \mathbb{D} : \frac{1}{2}d\mathbf{C} \quad (6.20)$$

Recalling that \mathbf{S} is a function of \mathbf{C} and \mathbf{C}^{in} , we can write:

$$d\mathbf{S} = \frac{\partial \mathbf{S}}{\partial \mathbf{C}} : d\mathbf{C} + \frac{\partial \mathbf{S}}{\partial \mathbf{C}^{in}} : d\mathbf{C}^{in} \quad (6.21)$$

Recasting (6.21) into a matrix form, we obtain:

$$[d\mathbf{S}] = \left[\frac{\partial \mathbf{S}}{\partial \mathbf{C}} \right] [d\mathbf{C}] + \left[\frac{\partial \mathbf{S}}{\partial \mathbf{C}^{in}} \right] [d\mathbf{C}^{in}] \quad (6.22)$$

where we have used $[\cdot]$ to denote the matrix form of the tensorial argument.

We now consider equation (6.9) as a function of \mathbf{C} , \mathbf{C}^{in} , $\Delta\zeta$ and γ , and then the corresponding linearization gives:

$$\begin{cases} \mathbf{R}_{,\mathbf{C}}^{in} : d\mathbf{C} + \mathbf{R}_{,\mathbf{C}^{in}}^{in} : d\mathbf{C}^{in} + \mathbf{R}_{,\Delta\zeta}^{in} d\Delta\zeta + \mathbf{R}_{,\gamma}^{in} d\gamma = \mathbf{0} \\ R_{,\mathbf{C}}^\zeta : d\mathbf{C} + R_{,\mathbf{C}^{in}}^\zeta : d\mathbf{C}^{in} + R_{,\Delta\zeta}^\zeta d\Delta\zeta + R_{,\gamma}^\zeta d\gamma = 0 \\ R_{,\mathbf{C}}^\gamma : d\mathbf{C} + R_{,\mathbf{C}^{in}}^\gamma : d\mathbf{C}^{in} + R_{,\Delta\zeta}^\gamma d\Delta\zeta + R_{,\gamma}^\gamma d\gamma = 0 \end{cases} \quad (6.23)$$

Recasting (6.23) into a matrix form, we obtain:

$$\begin{bmatrix} d\mathbf{C}^{in} \\ d\zeta \\ d\gamma \end{bmatrix} = - \begin{bmatrix} \mathbf{R}_{,\mathbf{C}^{in}}^{in} & \mathbf{R}_{,\Delta\zeta}^{in} & \mathbf{R}_{,\gamma}^{in} \\ R_{,\mathbf{C}^{in}}^{\zeta} & R_{,\Delta\zeta}^{\zeta} & R_{,\gamma}^{\zeta} \\ R_{,\mathbf{C}^{in}}^{\gamma} & R_{,\Delta\zeta}^{\gamma} & R_{,\gamma}^{\gamma} \end{bmatrix}^{-1} \begin{bmatrix} \mathbf{R}_{,\mathbf{C}}^{in} \\ R_{,\mathbf{C}}^{\zeta} \\ R_{,\mathbf{C}}^{\gamma} \end{bmatrix} [d\mathbf{C}] \quad (6.24)$$

Now, using (6.24), we can compute the matrix $[\mathbb{B}]$ such that:

$$[d\mathbf{C}^{in}] = [\mathbb{B}] [d\mathbf{C}] \quad (6.25)$$

We then substitute (6.25) into (6.22) to obtain the consistent tangent matrix as:

$$[\mathbb{D}] = 2 \left[\frac{\partial \mathbf{S}}{\partial \mathbf{C}} \right] + 2 \left[\frac{\partial \mathbf{S}}{\partial \mathbf{C}^{in}} \right] [\mathbb{B}] \quad (6.26)$$

Table 6.3 finally presents the proposed solution algorithm based on the logarithmic form of the time-discrete evolution equation (6.7) and a *Nucleation – Consistent Completion (NC2)* scheme.

Implementing the proposed solution procedure, we obtain a robust time integration algorithm; in the next chapter we test its robustness for different complicated stress-strain histories and various boundary value problems.

For comparison, in Table 6.4 we also provide the solution algorithm when a regularization scheme (discussed in Section 5.5.2) is used. We remark that in this case the tensor \mathbf{N} is defined as:

$$\mathbf{N} = \frac{\mathbf{E}^{in}}{\|\mathbf{E}^{in}\|} = \frac{\mathbf{E}^{in}}{\sqrt{\|\mathbf{E}^{in}\|^2 + \delta}} \quad (6.27)$$

Remark. Up to now, the relations have been derived in a completely general manner without specifying the form of the Helmholtz free energy W , apart from the fact that it is an isotropic function of \mathbf{C}^e . Despite the hyperelastic strain energy function W can take any well-known form in finite elasticity, for the numerical examples to be discussed in the next sections we use the commonly-used Saint-Venant Kirchhoff strain energy function:

$$W = \frac{\lambda}{2} (\text{tr} \mathbf{E}^e)^2 + \mu \text{tr} \mathbf{E}^e{}^2 \quad (6.28)$$

which yields:

$$\alpha_1 = \frac{\lambda}{4} \left(\mathbf{C} : \mathbf{C}^{in-1} - 3 \right) - \frac{1}{2} \mu, \quad \alpha_2 = \frac{1}{2} \mu, \quad \alpha_3 = 0 \quad (6.29)$$

where λ and μ are the Lamè constants.

Table 6.3: Solution algorithm for GLUS model based on $NC2$ scheme

1. compute $\mathbf{C} = \mathbf{F}^T \mathbf{F}$
 2. compute $(\mathbf{C} \mathbf{S}_e)^D$
 3. **if** $(\|(\mathbf{C} \mathbf{S}_e)^D\| < \tau_M + R$ and $\|\mathbf{E}_n^{in}\| = 0)$ **then**
 - set $\mathbf{C}^{in} = \mathbf{1}$
 - else**
 - use (5.85) and set $\mathbf{C}^{inTR} = \mathbf{C}_n^{in}$ to compute f^{TR} and trial solution
 - if** $(f^{TR} < 0)$ **then**
 - set trial solution as the problem solution, i.e., $\mathbf{C}^{in} = \mathbf{C}^{inTR}$
 - else if** (completion condition (6.18)) **then**
 - set $\mathbf{C}^{in} = \mathbf{1}$
 - else**
 - set $\mathbf{C}_0^{in} = \mathbf{C}_n^{in}$ and $\Delta\zeta_0 = 0$.
 - if** $\|\mathbf{E}_n^{in}\| = 0$ **then** set \mathbf{C}_0^{in} value by (6.12)
 - solve PT1
 - if** $(\|\mathbf{E}^{in}\|_{PT1} < \varepsilon_L)$ **then**
 - set PT1 solution as the solution: i.e., $\mathbf{C}^{in} = \mathbf{C}^{in}_{PT1}$
 - else**
 - set $\mathbf{C}_0^{in} = \mathbf{C}_{PT1}^{in}$, $\Delta\zeta_0 = \Delta\zeta_{PT1}$ and $\gamma_0 = 0$, then solve PT2
 - set $\mathbf{C}^{in} = \mathbf{C}^{in}_{PT2}$
 - end if**
 - end if**
 - end if**
 - end if**
 4. compute second Piola-Kirchhoff stress using (5.76), then Cauchy stress using (3.55)
 5. compute material tangent matrix and then spatial tangent matrix using (6.1)
-

6.3 Numerical implementation of GLSY model

In the above section, we used \mathbf{C}^{in} as unknown in the solution procedure as it has already been done in (Arghavani et al., 2010b; Evangelista et al., 2009; Reese and Christ, 2008). However, according to the GLSY model it seems to be beneficial to use \mathbf{U}^{in} as unknown. To this end, in this section we assume \mathbf{U}^{in} , $\Delta\zeta$ and γ as unknowns which also has already been done in some works (Christ and Reese, 2009; Vladimirov et al., 2008). We then will investigate the effect of the unknown selection on the computational efficiency in Chapter 7.

Table 6.4: Solution algorithm for GLUS model based on *Reg* scheme

-
1. compute $\mathbf{C} = \mathbf{F}^T \mathbf{F}$
 2. set $\mathbf{C}^{inTR} = \mathbf{C}_n^{in}$ to compute f^{TR} and trial solution
 3. **if** ($f^{TR} < 0$) **then**
 - Accept trial solution, i.e., $\mathbf{C}^{in} = \mathbf{C}^{inTR}$
 - else**
 - Solve PT1 system.
 - if** ($\|\mathbf{E}^{in}\|_{PT1} < \varepsilon_L$) **then**
 - Accept PT1 solution, i.e., $\mathbf{C}^{in} = (\mathbf{C}^{in})_{PT1}$
 - else**
 - Set $\mathbf{C}_0^{in} = \mathbf{C}_{PT1}^{in}$, $\Delta\zeta_0 = \Delta\zeta_{PT1}$ and $\gamma_0 = 0$
 - Solve PT2 system and set $\mathbf{C}^{in} = (\mathbf{C}^{in})_{PT2}$
 - end if**
 - end if**
-

Skipping the similar discussions with Section 6.2, we readily present the PT2 systems for GLSY model, as follows:

$$\begin{cases} \mathbf{R}^{in} = -\mathbf{U}^{in} \mathbf{C}_n^{in-1} \mathbf{U}^{in} + \exp(2\Delta\zeta \tilde{\mathbf{W}}) = \mathbf{0} \\ R^\zeta = \|\tilde{\mathbf{Y}}^D\| - R = 0 \\ R^\gamma = \|\mathbf{E}^{in}\| - \varepsilon_L = 0 \end{cases} \quad (6.30)$$

where

$$\tilde{\mathbf{W}} = \frac{\tilde{\mathbf{Y}}^D}{\|\tilde{\mathbf{Y}}^D\|} \quad (6.31)$$

We now linearize the nonlinear equations (6.30) as it is required for the iterative Newton-Raphson method. Linearizing (6.30), we obtain:

$$\begin{cases} \mathbf{R}^{in} + \mathbf{R}_{,\mathbf{U}^{in}}^{in} : d\mathbf{U}^{in} + \mathbf{R}_{,\Delta\zeta}^{in} d\Delta\zeta + \mathbf{R}_{,\gamma}^{in} d\gamma = \mathbf{0} \\ R^\zeta + R_{,\mathbf{U}^{in}}^\zeta : d\mathbf{U}^{in} + R_{,\Delta\zeta}^\zeta d\Delta\zeta + R_{,\gamma}^\zeta d\gamma = 0 \\ R^\gamma + R_{,\mathbf{U}^{in}}^\gamma : d\mathbf{U}^{in} + R_{,\Delta\zeta}^\gamma d\Delta\zeta + R_{,\gamma}^\gamma d\gamma = 0 \end{cases} \quad (6.32)$$

Utilizing the linearized form (6.32), after converting it to matrix form, a system of eight nonlinear scalar equations is obtained that is solved for $d\mathbf{U}^{in}$, $d\Delta\zeta$ and $d\gamma$.

The consistent tangent is computed by linearizing the second Piola-Kirchhof tensor, i.e.:

$$d\mathbf{S} = \mathbb{D} : d\mathbf{E} = \mathbb{D} : \frac{1}{2} d\mathbf{C} \quad (6.33)$$

Recalling that \mathbf{S} is a function of \mathbf{C} and \mathbf{U}^{in} , we can write:

$$d\mathbf{S} = \frac{\partial \mathbf{S}}{\partial \mathbf{C}} : d\mathbf{C} + \frac{\partial \mathbf{S}}{\partial \mathbf{U}^{in}} : d\mathbf{U}^{in} \quad (6.34)$$

Recasting (6.34) into a matrix form, we obtain:

$$[d\mathbf{S}] = \left[\frac{\partial \mathbf{S}}{\partial \mathbf{C}} \right] [d\mathbf{C}] + \left[\frac{\partial \mathbf{S}}{\partial \mathbf{U}^{in}} \right] [d\mathbf{U}^{in}] \quad (6.35)$$

We now consider equation (6.30) as a function of \mathbf{C} , \mathbf{U}^{in} , $\Delta\zeta$ and γ , and then the corresponding linearization gives:

$$\begin{cases} \mathbf{R}_{,\mathbf{C}}^{in} : d\mathbf{C} + \mathbf{R}_{,\mathbf{U}^{in}}^{in} : d\mathbf{U}^{in} + \mathbf{R}_{,\Delta\zeta}^{in} d\Delta\zeta + \mathbf{R}_{,\gamma}^{in} d\gamma = \mathbf{0} \\ R_{,\mathbf{C}}^{\zeta} : d\mathbf{C} + R_{,\mathbf{U}^{in}}^{\zeta} : d\mathbf{U}^{in} + R_{,\Delta\zeta}^{\zeta} d\Delta\zeta + R_{,\gamma}^{\zeta} d\gamma = 0 \\ R_{,\mathbf{C}}^{\gamma} : d\mathbf{C} + R_{,\mathbf{U}^{in}}^{\gamma} : d\mathbf{U}^{in} + R_{,\Delta\zeta}^{\gamma} d\Delta\zeta + R_{,\gamma}^{\gamma} d\gamma = 0 \end{cases} \quad (6.36)$$

Recasting (6.36) into a matrix form, we obtain:

$$\begin{bmatrix} d\mathbf{U}^{in} \\ d\zeta \\ d\gamma \end{bmatrix} = - \begin{bmatrix} \mathbf{R}_{,\mathbf{U}^{in}}^{in} & \mathbf{R}_{,\Delta\zeta}^{in} & \mathbf{R}_{,\gamma}^{in} \\ R_{,\mathbf{U}^{in}}^{\zeta} & R_{,\Delta\zeta}^{\zeta} & R_{,\gamma}^{\zeta} \\ R_{,\mathbf{U}^{in}}^{\gamma} & R_{,\Delta\zeta}^{\gamma} & R_{,\gamma}^{\gamma} \end{bmatrix}^{-1} \begin{bmatrix} \mathbf{R}_{,\mathbf{C}}^{in} \\ R_{,\mathbf{C}}^{\zeta} \\ R_{,\mathbf{C}}^{\gamma} \end{bmatrix} [d\mathbf{C}] \quad (6.37)$$

Now, using (6.37), we can compute the matrix $[\mathbb{B}]$ such that:

$$[d\mathbf{U}^{in}] = [\mathbb{B}] [d\mathbf{C}] \quad (6.38)$$

We then substitute (6.38) into (6.35) to obtain the consistent tangent matrix as:

$$[\mathbb{D}] = 2 \left[\frac{\partial \mathbf{S}}{\partial \mathbf{C}} \right] + 2 \left[\frac{\partial \mathbf{S}}{\partial \mathbf{U}^{in}} \right] [\mathbb{B}] \quad (6.39)$$

6.4 Numerical implementation of HSGF model

Since, the constitutive model is in terms of Lagrangian quantities, from now on, we consider as deformation driver the right Cauchy-Green deformation tensor (instead of the deformation gradient), assuming $\bar{\mathbf{C}}$ and θ are given (control variables).

6.4.1 Time integration.

We use a backward-Euler integration scheme for the scalar internal variable evolution equation (5.159) and obtain:

$$\theta^{in} = \theta_n^{in} + \Delta\zeta \frac{\partial G(\mathbf{Z}, q)}{\partial q} \quad (6.40)$$

where $\Delta\zeta = \zeta - \zeta_n$.

Considering Table 6.2 and the evolution equation (5.158), we conclude:

$$\mathbf{A} = 2\bar{\mathbf{U}}^{in} \frac{\partial G(\mathbf{Z}, q)}{\partial \mathbf{Z}} \bar{\mathbf{U}}^{in} \quad (6.41)$$

We now substitute (6.41) into (6.5) to obtain the time-discrete form of the evolution equation (5.158) based on the exponential mapping:

$$-\bar{\mathbf{C}}_n^{in-1} + \bar{\mathbf{U}}^{in-1} \exp\left(2\Delta\zeta \frac{\partial G(\mathbf{Z}, q)}{\partial \mathbf{Z}}\right) \bar{\mathbf{U}}^{in-1} = \mathbf{0} \quad (6.42)$$

Substituting (6.41) into (6.7), we obtain the time-discrete evolution equation based on the logarithmic mapping:

$$-\bar{\mathbf{U}}^{in} \log\left(\bar{\mathbf{U}}^{in} \bar{\mathbf{C}}_n^{in-1} \bar{\mathbf{U}}^{in}\right) \bar{\mathbf{U}}^{in} + 2\Delta\zeta \bar{\mathbf{U}}^{in} \frac{\partial G(\mathbf{Z}, q)}{\partial \mathbf{Z}} \bar{\mathbf{U}}^{in} = \mathbf{0} \quad (6.43)$$

We now, left- and right- multiply (6.43) by $\bar{\mathbf{U}}^{in-1}$ and obtain the time-discrete form of the evolution equation, based on the logarithmic mapping as follows:

$$-\log\left(\bar{\mathbf{U}}^{in} \bar{\mathbf{C}}_n^{in-1} \bar{\mathbf{U}}^{in}\right) + 2\Delta\zeta \frac{\partial G(\mathbf{Z}, q)}{\partial \mathbf{Z}} = \mathbf{0} \quad (6.44)$$

We finally remark that, since \mathbf{Z} contains logarithmic terms, (6.44) includes only logarithmic terms, while in (6.42) an exponential term exists. The time-discrete evolution equations (6.40) and (6.44) together with the limit (yield) condition (5.155) construct a system of nonlinear equations, i.e.:

$$\begin{cases} -\log\left(\bar{\mathbf{U}}^{in} \bar{\mathbf{C}}_n^{in-1} \bar{\mathbf{U}}^{in}\right) + 2\Delta\zeta \frac{\partial G(\mathbf{Z}, q)}{\partial \mathbf{Z}} = \mathbf{0} \\ -\theta^{in} + \theta_n^{in} + \Delta\zeta \frac{\partial G(\mathbf{Z}, q)}{\partial q} = 0 \\ F(\mathbf{Z}, q) = 0 \end{cases} \quad (6.45)$$

Solution of system of equations (6.45) is, in general, approached through a straightforward Newton-Raphson method to find $\bar{\mathbf{U}}^{in}$, θ^{in} and $\Delta\zeta$.

6.5 Numerical implementation of HSSY model

6.5.1 Solution algorithm.

We substitute (5.171) into (6.7) and obtain the time-discrete tensorial evolution equation as:

$$-\log\left(\bar{\mathbf{U}}^{in} \bar{\mathbf{C}}_n^{in-1} \bar{\mathbf{U}}^{in}\right) + 2\Delta\zeta \frac{\mathbf{Z}}{\|\mathbf{Z}\|} = \mathbf{0} \quad (6.46)$$

Accordingly, the PT2 system takes the following form:

$$\begin{cases} \mathbf{R}^{in} = -\log\left(\mathbf{U}^{in} \mathbf{C}_n^{in-1} \mathbf{U}^{in}\right) + 2\Delta\zeta \mathbf{W} = \mathbf{0} \\ R^\zeta = \|\mathbf{Z}\| - R = 0 \\ R^\gamma = \|\mathbf{H}^{in}\| - \varepsilon_L = 0 \end{cases} \quad (6.47)$$

where

$$\mathbf{W} = \mathbf{Z} / \|\mathbf{Z}\| \quad (6.48)$$

6.5.2 Considerations on nucleation-completion condition.

We first investigate the trial value of the limit function in the nucleation case as:

$$f^{TR} = |||\mathbf{Q}_e|| - \tau_M(T) - R = \|\mathbf{Q}_e\| - \tau_M(T) - R > 0 \quad (6.49)$$

where a subscript TR indicates a trial value. We may thus introduce the following *nucleation condition*:

$$\|\mathbf{Q}_e\| > \tau_M(T) + R \quad \text{and} \quad \|\mathbf{H}_n^{in}\| = 0 \quad (6.50)$$

In the solution procedure, when $\|\mathbf{H}_n^{in}\| = 0$ we check the nucleation condition and if not satisfied, we assume an elastic behavior.

We remark that, to avoid singularity in system (6.47) for the nucleation case, it is necessary to use a nonzero initial (guess) transformation strain. Since, we know the initial transformation strain direction from (5.180), the only unknown for constructing an initial guess is its norm; if we denote with q its value, we can use the following initial guess for the nucleation case:

$$\mathbf{H}_0^{in} = \log(\mathbf{U}_0^{in}) \simeq \mathbf{U}_0^{in} - \mathbf{1} = q\mathbf{N} \implies \mathbf{U}_0^{in} = \mathbf{1} + q\mathbf{N} \quad (6.51)$$

where a subscript 0 denotes the initial guess. A value of 10^{-4} could be an appropriate choice for q .

We now focus on the completion case, i.e., $\mathbf{H}_n^{in} \neq \mathbf{0}$ but $\mathbf{H}^{in} = \mathbf{0}$. To this end, we consider equations (6.42) or (6.44) and substitute $\mathbf{U}^t = \mathbf{1}$ (as it happens for the completion case) to obtain:

$$\Delta\zeta \mathbf{A} = \log\left(\mathbf{C}_n^{in-1}\right) = -2\mathbf{H}_n^{in}, \quad \mathbf{A} = 2\frac{\mathbf{Z}}{\|\mathbf{Z}\|}, \quad \mathbf{Z} = \mathbf{Q}_e - \tau_M\mathbf{N} \quad (6.52)$$

To this end, using (6.52)_{1,2} which define the \mathbf{Z} direction and considering the limit function (5.171), we conclude:

$$\mathbf{Z} = -R\frac{\mathbf{H}_n^{in}}{\|\mathbf{H}_n^{in}\|} = -R\mathbf{N}^{TR} \quad (6.53)$$

substituting (6.53) in (6.52)₃, we obtain:

$$\mathbf{Q}_e + R\mathbf{N}^{TR} = \tau_M\mathbf{N} \quad (6.54)$$

Finally taking the norm of both sides of equation (6.54), we define the following *completion condition*:

$$\|\mathbf{Q}_e + R\mathbf{N}^{TR}\| \leq \tau_M, \quad \|\mathbf{H}_n^{in}\| \neq 0 \quad (6.55)$$

Therefore, in the solution procedure we also should check the completion condition and, if it is satisfied, we simply update the internal variable by setting $\mathbf{U}^{in} = \mathbf{1}$.

Table 6.5 finally presents the branch detection and the solution algorithm.

Table 6.5: Solution algorithm for HSSY model based on *NC2* scheme.

-
1. compute $\mathbf{C} = \mathbf{F}^T \mathbf{F}$ then $J = \sqrt{\det \mathbf{C}}$ and $\bar{\mathbf{C}} = J^{-2/3} \mathbf{C}$
 2. compute \mathbf{Q}_e
 3. **if** ($\|\mathbf{Q}_e\| < \tau_M + R$ and $\|\mathbf{H}_n^{in}\| = 0$) **then**
 - set $\mathbf{U}^{in} = \mathbf{1}$
 - else**
 - use (5.180) and set $\mathbf{U}^{inTR} = \mathbf{U}_n^{in}$ to compute f^{TR} and trial solution
 - if** ($f^{TR} < 0$) **then**
 - set trial solution as the problem solution, i.e., $\mathbf{U}^{in} = \mathbf{U}^{inTR}$
 - else if** (completion condition (6.55)) **then**
 - set $\mathbf{U}^{in} = \mathbf{1}$
 - else**
 - set $\mathbf{U}_0^{in} = \mathbf{U}_n^{in}$ and $\Delta\zeta_0 = 0$.
 - if** $\|\mathbf{H}_n^{in}\| = 0$ **then** set \mathbf{U}_0^{in} value by (6.51)
 - solve PT1
 - if** ($\|\mathbf{H}^{in}\|_{PT1} < \varepsilon_L$) **then**
 - set PT1 solution as the solution: i.e., $\mathbf{U}^{in} = \mathbf{U}^{in}_{PT1}$
 - else**
 - set $\mathbf{U}_0^{in} = \mathbf{U}_{PT1}^{in}$, $\Delta\zeta_0 = \Delta\zeta_{PT1}$ and $\gamma_0 = 0$, then solve PT2
 - set $\mathbf{U}^t = \mathbf{U}^{in}_{PT2}$
 - end if**
 - end if**
 - end if**
-

6.5.3 Consistent tangent matrix.

Linearizing (6.47), we obtain:

$$\begin{cases} \mathbf{R}^{in} + \mathbf{R}_{,\mathbf{U}^{in}}^{in} : d\mathbf{U}^{in} + \mathbf{R}_{,\Delta\zeta}^{in} d\Delta\zeta + \mathbf{R}_{,\gamma}^{in} d\gamma = \mathbf{0} \\ R^\zeta + R_{,\mathbf{U}^{in}}^\zeta : d\mathbf{U}^{in} + R_{,\Delta\zeta}^\zeta d\Delta\zeta + R_{,\gamma}^\zeta d\gamma = 0 \\ R^\gamma + R_{,\mathbf{U}^{in}}^\gamma : d\mathbf{U}^{in} + R_{,\Delta\zeta}^\gamma d\Delta\zeta + R_{,\gamma}^\gamma d\gamma = 0 \end{cases} \quad (6.56)$$

Utilizing the linearized form (6.56), after converting it to a matrix form, a system of eight nonlinear scalar equations is solved to obtain $d\mathbf{U}^{in}$, $d\Delta\zeta$ and $d\gamma$.

We now address the construction of the tangent tensor consistent with the time-discrete constitutive model. The consistent tangent is computed by linearizing the second Piola-Kirchhof tensor, i.e.:

$$d\mathbf{S} = \mathbb{D} : d\mathbf{E} = \frac{1}{2} \mathbb{D} : d\mathbf{C} \quad (6.57)$$

Recalling that \mathbf{S} is a function of J , $\bar{\mathbf{C}}$ and \mathbf{U}^{in} , we can write:

$$d\mathbf{S} = \frac{\partial \mathbf{S}}{\partial J} dJ + \frac{\partial \mathbf{S}}{\partial \bar{\mathbf{C}}} : d\bar{\mathbf{C}} + \frac{\partial \mathbf{S}}{\partial \mathbf{U}^{in}} : d\mathbf{U}^{in} \quad (6.58)$$

The following relations express dJ and $d\bar{\mathbf{C}}$ in terms of $d\mathbf{C}$ (Holzapfel, 2000):

$$dJ = \frac{J^{1/3}}{2} \bar{\mathbf{C}}^{-1} : d\mathbf{C} \quad \text{and} \quad d\bar{\mathbf{C}} = J^{-2/3} \mathbb{P} : d\mathbf{C} \quad (6.59)$$

where,

$$\mathbb{P} = \mathbb{I} - \frac{1}{3} \bar{\mathbf{C}} \otimes \bar{\mathbf{C}}^{-1} \quad (6.60)$$

We now consider equation (6.47) as a function of $\bar{\mathbf{C}}$, \mathbf{U}^{in} , $\Delta\zeta$ and γ , and then the corresponding linearization gives:

$$\begin{cases} \mathbf{R}_{,\bar{\mathbf{C}}}^{in} : d\bar{\mathbf{C}} + \mathbf{R}_{,\mathbf{U}^{in}}^{in} : d\mathbf{U}^{in} + \mathbf{R}_{,\Delta\zeta}^{in} d\Delta\zeta + \mathbf{R}_{,\gamma}^{in} d\gamma = \mathbf{0} \\ \mathbf{R}_{,\bar{\mathbf{C}}}^{\zeta} : d\bar{\mathbf{C}} + \mathbf{R}_{,\mathbf{U}^{in}}^{\zeta} : d\mathbf{U}^{in} + \mathbf{R}_{,\Delta\zeta}^{\zeta} d\Delta\zeta + \mathbf{R}_{,\gamma}^{\zeta} d\gamma = 0 \\ \mathbf{R}_{,\bar{\mathbf{C}}}^{\gamma} : d\bar{\mathbf{C}} + \mathbf{R}_{,\mathbf{U}^{in}}^{\gamma} : d\mathbf{U}^{in} + \mathbf{R}_{,\Delta\zeta}^{\gamma} d\Delta\zeta + \mathbf{R}_{,\gamma}^{\gamma} d\gamma = 0 \end{cases} \quad (6.61)$$

Recasting (6.61) into a matrix form, we obtain:

$$\begin{bmatrix} d\mathbf{U}^{in} \\ d\zeta \\ d\gamma \end{bmatrix} = - \begin{bmatrix} \mathbf{R}_{,\mathbf{U}^{in}}^{in} & \mathbf{R}_{,\Delta\zeta}^{in} & \mathbf{R}_{,\gamma}^{in} \\ \mathbf{R}_{,\mathbf{U}^{in}}^{\zeta} & \mathbf{R}_{,\Delta\zeta}^{\zeta} & \mathbf{R}_{,\gamma}^{\zeta} \\ \mathbf{R}_{,\mathbf{U}^{in}}^{\gamma} & \mathbf{R}_{,\Delta\zeta}^{\gamma} & \mathbf{R}_{,\gamma}^{\gamma} \end{bmatrix}^{-1} \begin{bmatrix} \mathbf{R}_{,\bar{\mathbf{C}}}^{in} \\ \mathbf{R}_{,\bar{\mathbf{C}}}^{\zeta} \\ \mathbf{R}_{,\bar{\mathbf{C}}}^{\gamma} \end{bmatrix} [d\bar{\mathbf{C}}] \quad (6.62)$$

Now, using (6.62), we can compute the matrix $[\mathbb{B}]$ (the matrix form of the fourth-order tensor \mathbb{B}) such that:

$$[d\mathbf{U}^{in}] = [\mathbb{B}] [d\bar{\mathbf{C}}] \quad \text{or} \quad d\mathbf{U}^{in} = \mathbb{B} : d\bar{\mathbf{C}} \quad (6.63)$$

We then substitute (6.59) and (6.63)₂ into (6.58) to obtain the consistent tangent as:

$$\mathbb{D} = J^{1/3} \mathbf{J} \otimes \bar{\mathbf{C}}^{-1} + 2J^{-2/3} (\mathbb{S} + \mathbb{T} : \mathbb{B}) : \mathbb{P} \quad (6.64)$$

where the second-order tensor $\partial \mathbf{S} / \partial J$ as well as the fourth-order tensors $\partial \mathbf{S} / \partial \bar{\mathbf{C}}$ and $\partial \mathbf{S} / \partial \mathbf{U}^{in}$ are denoted by \mathbf{J} , \mathbb{S} and \mathbb{T} , respectively.

6.6 Numerical implementation of SSSR model

We now present concisely the numerical implementation of the original model proposed by Souza et al. (1998) in the small deformation regime (both strain and rotation are assumed to be small) as discussed in Section 4.2.1. The solution algorithm is the same we presented for the GLUS model in Section 6.2. The algorithm, we present here, is

different from that one already presented by Auricchio and Petrini (2002, 2004a) since we use as unknown the inelastic strain in place of transformation strain in the model equations.

We use a backward–Euler integration algorithm to discretized the evolution equation (4.14) as:

$$\mathbf{e}^{in} = \mathbf{e}_n^{in} + \Delta\zeta \widehat{\mathbf{W}} \quad (6.65)$$

where

$$\widehat{\mathbf{W}} = \frac{\mathbf{x}^{in}}{\|\mathbf{x}^{in}\|} \quad (6.66)$$

where the transformation stress \mathbf{x}^{in} has been defined in (4.10) as

$$\mathbf{x}^{in} = \mathbf{s} - \mathbf{x} = 2G(\mathbf{e} - \mathbf{e}^{in}) - [\tau_M(T) + h\|\mathbf{e}^{in}\| + \gamma] \mathbf{N} \quad (6.67)$$

where, we well-define the variable \mathbf{N} as:

$$\mathbf{N} = \begin{cases} \frac{\mathbf{s}}{\|\mathbf{s}\|} & \text{if } \|\mathbf{e}^{in}\| = 0 \\ \frac{\mathbf{e}^{in}}{\|\mathbf{e}^{in}\|} & \text{if } \|\mathbf{e}^{in}\| \neq 0 \end{cases} \quad (6.68)$$

The PT2 system for SSSR model takes then the following form:

$$\begin{cases} \mathbf{R}^{in} = -\mathbf{e}^{in} + \mathbf{e}_n^{in} + \Delta\zeta \widehat{\mathbf{W}} = \mathbf{0} \\ R^\zeta = \|\mathbf{x}^{in}\| - R = 0 \\ R^\gamma = \|\mathbf{e}^{in}\| - \varepsilon_L = 0 \end{cases} \quad (6.69)$$

6.6.1 Consistent tangent matrix.

We now linearize the nonlinear equations (6.69) to obtain:

$$\begin{cases} \mathbf{R}^{in} + \mathbf{R}_{,\mathbf{e}^{in}}^{in} : d\mathbf{e}^{in} + \mathbf{R}_{,\Delta\zeta}^{in} d\Delta\zeta + \mathbf{R}_{,\gamma}^{in} d\gamma = \mathbf{0} \\ R^\zeta + R_{,\mathbf{e}^{in}}^\zeta : d\mathbf{e}^{in} + R_{,\Delta\zeta}^\zeta d\Delta\zeta + R_{,\gamma}^\zeta d\gamma = 0 \\ R^\gamma + R_{,\mathbf{e}^{in}}^\gamma : d\mathbf{e}^{in} + R_{,\Delta\zeta}^\gamma d\Delta\zeta + R_{,\gamma}^\gamma d\gamma = 0 \end{cases} \quad (6.70)$$

Utilizing the linearized form (6.70), after converting it to matrix form, a system of eight nonlinear scalar equations is obtained that is solved for $d\mathbf{e}^{in}$, $d\Delta\zeta$ and $d\gamma$.

We now address the construction of the tangent tensor consistent with the time-discrete constitutive model. The consistent tangent can be computed as a linearization of the stress $\boldsymbol{\sigma}$.

$$d\boldsymbol{\sigma} = \mathbb{D} : d\boldsymbol{\varepsilon} \quad (6.71)$$

Recalling equations (4.8) and (4.9), the linearization of the elastic constitutive relation, in its volumetric and deviatoric component, gives:

$$\begin{aligned} dp\mathbf{1} &= K(\mathbf{1} \otimes \mathbf{1}) : d\boldsymbol{\varepsilon} \\ d\mathbf{s} &= 2G(\mathbb{I} - \frac{d\mathbf{e}^{in}}{d\mathbf{e}})\mathbb{I}_{dev} : d\boldsymbol{\varepsilon} \end{aligned} \quad (6.72)$$

where

$$\begin{aligned}\mathbb{I}_{dev} &= \mathbb{I} - \frac{1}{3}\mathbf{1} \otimes \mathbf{1} \\ d\mathbf{e} &= \mathbb{I}_{dev} : d\boldsymbol{\varepsilon}\end{aligned}\tag{6.73}$$

If we now consider equation (6.69) as function of \mathbf{e} , \mathbf{e}^{in} , $\Delta\zeta$ and γ , then the corresponding linearization gives:

$$\begin{cases} \mathbf{R}_{,\mathbf{e}}^{in} : d\mathbf{e} + \mathbf{R}_{,\mathbf{e}^{in}}^{in} : d\mathbf{e}^{in} + \mathbf{R}_{,\Delta\zeta}^{in} d\Delta\zeta + \mathbf{R}_{,\gamma}^{in} d\gamma = \mathbf{0} \\ R_{,\mathbf{e}}^{\zeta} : d\mathbf{e} + R_{,\mathbf{e}^{in}}^{\zeta} : d\mathbf{e}^{in} + R_{,\Delta\zeta}^{\zeta} d\Delta\zeta + R_{,\gamma}^{\zeta} d\gamma = 0 \\ R_{,\mathbf{e}}^{\gamma} : d\mathbf{e} + R_{,\mathbf{e}^{in}}^{\gamma} : d\mathbf{e}^{in} + R_{,\Delta\zeta}^{\gamma} d\Delta\zeta + R_{,\gamma}^{\gamma} d\gamma = 0 \end{cases}\tag{6.74}$$

Recasting (6.74) into a matrix form, we obtain:

$$\begin{bmatrix} d\mathbf{e}^{in} \\ d\zeta \\ d\gamma \end{bmatrix} = - \begin{bmatrix} \mathbf{R}_{,\mathcal{U}^t}^{in} & \mathbf{R}_{,\Delta\zeta}^{in} & \mathbf{R}_{,\gamma}^{in} \\ R_{,\mathbf{e}^{in}}^{\zeta} & R_{,\Delta\zeta}^{\zeta} & R_{,\gamma}^{\zeta} \\ R_{,\mathbf{e}^{in}}^{\gamma} & R_{,\Delta\zeta}^{\gamma} & R_{,\gamma}^{\gamma} \end{bmatrix}^{-1} \begin{bmatrix} \mathbf{R}_{,\mathbf{e}}^{in} \\ R_{,\mathbf{e}}^{\zeta} \\ R_{,\mathbf{e}}^{\gamma} \end{bmatrix} [d\mathbf{e}]\tag{6.75}$$

Now, using (6.75), we can compute the matrix $[\mathbb{B}]$ such that:

$$[d\mathbf{e}^{in}] = [\mathbb{B}] [d\mathbf{e}]\tag{6.76}$$

We then substitute (6.75) into (6.72) to obtain the consistent tangent matrix as:

$$\mathbb{D} = K(\mathbf{1} \otimes \mathbf{1}) + 2G(\mathbb{I} - \mathbb{B})\mathbb{I}_{dev}\tag{6.77}$$

6.7 Numerical implementation of SSLR model

We now discuss the numerical implementation of SSLR model. The main goal in the implementation is to use as much as possible the same code we already have developed for SSSR model. To this end, based on the developed models in Lagrangian and Eulerian formulations in Section 5.8, we present two methods for such a formulation. In method 1, we first time-discretize the Lagrangian equations and then transform the time-discretized equations to the current formulations. In method 2, we use the Eulerian formulation (it means that we first transform the model equations to the current configuration) and based on an incrementally objective integration algorithm, we develop time-discrete model. We finally show that both methods yield the same result.

6.7.1 Method 1: Time-discretization based on Lagrangian formulation

We use the constitutive model in the time-continuous frame as summarized in Table 5.7. Comparing this model with the SSSR Souza model (summarized in Table 4.1) we find

out that beside they use different stress and strain measures, they are exactly the same. It means that we can use exactly the same code we developed for SSSR model but use as input the Green-Lagrange strain (in place of infinitesimal strain) which gives as output the second Piola-Kirchhoff stress and material tangent matrix (in place of Cauchy stress and spatial tangent matrix). The only point we should clarify is that considering the simplified kinematic assumptions (see Table 5.6) we can transform the material tangent to the spatial one through the following relation:

$$\mathbb{C}_{mnkl} = R_{mM}R_{nN}R_{kK}R_{lL}\mathbb{D}_{MNKL} \quad (6.78)$$

However, in (6.78) we can use, as an approximate, the tensor \mathbf{F} in place of \mathbf{R} (also note that $J \approx 1$). Following this approach we don't need to compute the rotation tensor \mathbf{R} , i.e.:

$$\mathbb{C}_{mnkl} = F_{mM}F_{nN}F_{kK}F_{lL}\mathbb{D}_{MNKL} \quad (6.79)$$

We summarize the SSLR model implementation based on the Lagrangian formulation in Table 6.6.

Table 6.6: Solution algorithm for SSLR model based on Lagrangian formulation.

Inputs (given at a point): \mathbf{F} , \mathbf{F}_n , \mathbf{E}_n^{in}

Outputs (to be computed): $\boldsymbol{\sigma}$, \mathbf{E}^{in} , \mathbb{C}

1. compute $\mathbf{E} = 1/2(\mathbf{F}^T\mathbf{F} - \mathbf{1})$ and $\mathbf{E}_n = 1/2(\mathbf{F}_n^T\mathbf{F}_n - \mathbf{1})$
 2. use SSSR code: set as input $\boldsymbol{\varepsilon} = \mathbf{E}$, $\boldsymbol{\varepsilon}_n = \mathbf{E}_n$ and $\mathbf{e}_n^{in} = \mathbf{E}_n^{in}$ and obtain as outputs \mathbf{S} , \mathbf{E}^{in} and \mathbb{D}
 3. compute the Cauchy stress: $\boldsymbol{\sigma} = \mathbf{R}\mathbf{S}\mathbf{R}^T$
 4. use relation (6.78) or (6.79) and \mathbb{D} to compute \mathbb{C}
 5. use relation (6.1) to compute spatial Jaumann tangent matrix.
-

6.7.2 Method 2: Time-discretization based on Eulerian formulation

For a Lagrangean strain measure, the material time rate is objective. However, for an Eulerian strain measure, to eliminate superimposed rigid rotating motion, the objective corotational rates, such as the Zaremba-Jaumann rate etc., should be accounted for. We then will need an integration algorithm which is, as called in the literature, *incrementally objective* (Simo and Hughes, 1998). Since in this section we are going to time-discretize an Eulerian constitutive model, we first present an appropriate time-integration algorithm. Afterward, we present the time-discrete model as well as the spatial tangent matrix.

Time integration

We recall that we use subscript n to denote the quantities at time t and a quantity without a subscript is computed at time $t + \Delta t$. Moreover we denote with subscript $n + \frac{1}{2}$ the quantities at time $t + \frac{1}{2}\Delta t$. Integrating (3.35) in the time interval $[t, t + \Delta t]$, we obtain:

$$\int_t^{t+\Delta t} \frac{\dot{\widehat{\mathbf{Q}}}(t) \mathcal{A} \widehat{\mathbf{Q}}(t)^T}{(\widehat{\mathbf{Q}}(t) \mathcal{A} \widehat{\mathbf{Q}}(t)^T)} dt = \int_t^{t+\Delta t} \widehat{\mathbf{Q}}(t)^T \overset{\circ}{\mathcal{A}} \widehat{\mathbf{Q}}(t) dt \quad (6.80)$$

We now use mid-point rule to compute the right-hand side integral and obtain:

$$\widehat{\mathbf{Q}}^T \mathcal{A} \widehat{\mathbf{Q}} - \widehat{\mathbf{Q}}_n^T \mathcal{A}_n \widehat{\mathbf{Q}}_n = \widehat{\mathbf{Q}}_{n+\frac{1}{2}}^T \overset{\circ}{\mathcal{A}}_{n+\frac{1}{2}} \widehat{\mathbf{Q}}_{n+\frac{1}{2}} \Delta t \quad (6.81)$$

Multiplying by $\widehat{\mathbf{Q}}$ and $\widehat{\mathbf{Q}}^T$ from left and right, respectively, we obtain:

$$\mathcal{A} = \widehat{\mathbf{Q}} \widehat{\mathbf{Q}}_n^T \mathcal{A}_n \widehat{\mathbf{Q}}_n \widehat{\mathbf{Q}}^T + \widehat{\mathbf{Q}} \widehat{\mathbf{Q}}_{n+\frac{1}{2}}^T \overset{\circ}{\mathcal{A}}_{n+\frac{1}{2}} \widehat{\mathbf{Q}}_{n+\frac{1}{2}} \widehat{\mathbf{Q}}^T \Delta t \quad (6.82)$$

Assuming an updated Lagrangian formulation, we set $\widehat{\mathbf{Q}}_n = \mathbf{1}$ and using the approximation $\widehat{\mathbf{Q}} \widehat{\mathbf{Q}}_{n+\frac{1}{2}}^T \approx \widehat{\mathbf{Q}}_{n+\frac{1}{2}} \widehat{\mathbf{Q}}^T \approx \mathbf{1}$ we obtain:

$$\mathcal{A} = \widehat{\mathbf{Q}} \mathcal{A}_n \widehat{\mathbf{Q}}^T + \overset{\circ}{\mathcal{A}}_{n+\frac{1}{2}} \Delta t \quad (6.83)$$

We now define

$$\Delta \mathcal{A} = \overset{\circ}{\mathcal{A}}_{n+\frac{1}{2}} \Delta t = \int_t^{t+\Delta t} \overset{\circ}{\mathcal{A}} dt \quad (6.84)$$

Substituting (6.84) into (6.83), we obtain the time-integration formula as:

$$\mathcal{A} = \widehat{\mathbf{Q}} \mathcal{A}_n \widehat{\mathbf{Q}}^T + \Delta \mathcal{A} \quad (6.85)$$

Equation (6.85) coincides with the one already proposed by Hughes and Winget (1980) and is known as Hughes-Winget integration algorithm in the literature. This algorithm updates an Eulerian tensor by transforming (or rotating) its old value to the current configuration and then adding its increment in the new configuration.

Application to the SSLR Eulerian Souza model

We now apply the time-integration algorithm (6.85) to (5.205) which yields:

$$\mathbf{h}^{in} = \widehat{\mathbf{Q}} \mathbf{h}_n^{in} \widehat{\mathbf{Q}}^T + \Delta \zeta \frac{\mathbf{x}^{in}}{\|\mathbf{x}^{in}\|} \quad (6.86)$$

Moreover, we can present a similar relation for the total (deviatoric) strain:

$$\bar{\mathbf{h}} = \widehat{\mathbf{Q}} \bar{\mathbf{h}}_n \widehat{\mathbf{Q}}^T + \Delta \bar{\mathbf{h}} \quad (6.87)$$

We now define the problem as: given $\bar{\mathbf{h}}$, θ , \mathbf{h}_n and $\widehat{\mathbf{Q}}$ then compute the updated internal variable \mathbf{h}^{in} (which is used to update stress) and the tangent matrix. Using (6.86) and (6.87) (see also table 5.8), the stress also is given by:

$$\begin{aligned}\mathbf{s} &= 2G(\bar{\mathbf{h}} - \mathbf{h}^{in}) = \widehat{\mathbf{Q}} [2G(\bar{\mathbf{h}}_n - \mathbf{h}_n^{in})] \widehat{\mathbf{Q}}^T + 2G\Delta\bar{\mathbf{h}} + 2G\Delta\zeta \frac{\mathbf{x}^{in}}{\|\mathbf{x}^{in}\|} \\ &\implies \mathbf{s} = \widehat{\mathbf{Q}} \mathbf{s}_n \widehat{\mathbf{Q}}^T + 2G\Delta\bar{\mathbf{h}} + 2G\Delta\zeta \frac{\mathbf{x}^{in}}{\|\mathbf{x}^{in}\|}\end{aligned}\quad (6.88)$$

Accordingly, the PT2 system can be presented as follows:

$$\begin{cases} \mathbf{R}^{in} = -\mathbf{h}^{in} + \widehat{\mathbf{Q}} \mathbf{h}_n^{in} \widehat{\mathbf{Q}}^T + \Delta\zeta \frac{\mathbf{x}^{in}}{\|\mathbf{x}^{in}\|} = \mathbf{0} \\ R^\zeta = \|\mathbf{x}^{in}\| - R = 0 \\ R^\gamma = \|\mathbf{h}^{in}\| - \varepsilon_L = 0 \end{cases}\quad (6.89)$$

where the time-continuous variable $\mathbf{x}^{in} = \mathbf{s} - (\tau_M(T) + h\|\mathbf{h}^{in}\| + \gamma) \frac{\mathbf{h}^{in}}{\|\mathbf{h}^{in}\|}$ takes the following form in the time-discrete frame:

$$\mathbf{x}^{in} = \widehat{\mathbf{Q}} \mathbf{s}_n \widehat{\mathbf{Q}}^T + 2G\Delta\mathbf{e} + 2G\Delta\zeta \frac{\mathbf{x}^{in}}{\|\mathbf{x}^{in}\|} - (\tau_M(T) + h\|\mathbf{h}^{in}\| + \gamma) \frac{\mathbf{h}^{in}}{\|\mathbf{h}^{in}\|}\quad (6.90)$$

We observe that the time-discretized system (6.89) has exactly the same form that SSSR has except one difference: the old variables at time t_n should be rotated to the new configuration. It means that, we can use the small deformation code for the corotational formulation without any need to recoding. We just should rotate the old variables through the rotation tensor $\widehat{\mathbf{Q}}$. In the ABAQUS/Standard, this rotation matrix is passed to the user defined subroutine UMAT through a 3×3 matrix `Drot`. Moreover, the strain tensor \mathbf{h} is provided by the software in the UMAT subroutine.

We remark that, to construct the tangent matrix, we follow exactly the same approach we took for SSSR model. However, here we assume, during the linearization process, the rotation tensor $\widehat{\mathbf{Q}}$ remains constant. Table 6.7 summarizes the solution procedure.

Remark: It is a straightforward procedure to show that if we rotate the time-discrete Lagrangian equations to the current configuration and pay attention that $\mathbf{R}\mathbf{R}_n^T = \widehat{\mathbf{Q}}$, we obtain exactly the same time-discrete Eulerian equations.

6.8 Summary

In this chapter, we presented the time-discrete form of the constitutive models developed in the previous chapters. To this end, we investigated different time-integration

Table 6.7: Solution algorithm for SSLR model based on Eulerian formulation.

Inputs (given at a point): \mathbf{h} , \mathbf{h}_n , \mathbf{h}_n^{in}

Outputs (to be computed): $\boldsymbol{\sigma}$, \mathbf{h}^{in} , \mathbb{C}

1. use SSSR code: set as input $\boldsymbol{\varepsilon} = \mathbf{h}$, $\boldsymbol{\varepsilon}_n = \widehat{\mathbf{Q}}\mathbf{h}_n\widehat{\mathbf{Q}}^T$ and $\mathbf{e}_n^{in} = \widehat{\mathbf{Q}}\mathbf{h}_n^{in}\widehat{\mathbf{Q}}^T$
and obtain as outputs $\boldsymbol{\sigma}$, \mathbf{h}^{in} and \mathbb{C}
 2. compute spatial Jaumann tangent matrix with $\mathbb{C}_{ijkl}^J = \mathbb{C}_{ijkl} + \delta_{ik}\sigma_{jl} + \delta_{il}\sigma_{jk}$.
-

algorithms and introduced a logarithmic mapping. Proposing a nucleation-completion condition, we discussed in detail different solution algorithms. Moreover, we discussed in detail the proper initial guess in the Newton-Raphson method. Finally, we investigated the SSLR formulation which has the advantage of using the previously developed codes for the SSSR model.

Chapter 7

Numerical examples and simulation of SMA-based applications

7.1 Introduction

In this chapter, we study the solution algorithms developed in Chapter 6 from two points of view. We first study the algorithm robustness through several numerical test investigations at a gauss point level and then we compare the computational efficiency of different constitutive models as well as solution algorithms by simulating several boundary value problems. We investigate the simple shear test, uniaxial tension, torsion, a butterfly-shaped strain-controlled path, a box-shaped strain-controlled path and a box-shaped stress-controlled path. All examples are solved for two different time-step sizes, four different integration algorithms and for three or two different temperatures. Moreover, we simulate several boundary value problems, including a spring for three cases of pseudo-elasticity, one-way and two-way shape memory effects, a medical stent for two cases of pseudo-elasticity and shape memory effect, a cantilever beam and a curved beam. We finally simulate an SMA micro-gripper as an interesting application of SMAs.

7.2 Robustness study of different integration algorithms for GLUS model

7.2.1 Numerical examples: Gauss point level investigations

To investigate the robustness and efficiency of the proposed integration algorithm as well as of the solution procedure, we simulate some benchmark tests at the Gauss point

level. Up to now, different benchmark tests have been introduced in the literature; the paths are usually square-, butterfly-, triangle-, circle- or L-shaped (Auricchio and Petrini, 2002, 2004a; Grabe and Bruhns, 2009; Helm, 2001; Lim and McDowell, 1999; Sittner et al., 1995), while they can be either strain- or stress-controlled.

We first investigate the simple shear test, a well-known benchmark test for evaluating a finite strain model. Then, we simulate some uniaxial stress-controlled tension-compression and torsion tests at three different temperatures, varying from pseudo-elasticity to shape memory effect. Afterward, a $(E_{11} - E_{22})$ -controlled butterfly-shaped and a $(E_{11} - E_{12})$ -controlled square-shaped path are simulated. In each simulation we consider two different maximum values for controlling variables as well as two different temperatures, one leading to pseudo-elasticity and the other to shape memory effect. Finally, we present the response paths for stress-controlled butterfly- and square-shaped paths¹.

In order to investigate the algorithm robustness, two different time-step sizes are adopted in each numerical test. Moreover, we report the average number of iterations in PT1 and PT2 for different selected cases to show the convergence behavior (as this information can somehow be related to the algorithm robustness). Averages are computed by dividing the total number of iterations in a test by the total number of calls to the corresponding subroutine.

While we report the results for the logarithmic form of the evolution equation when a *NC2* scheme is adopted in the solution algorithm, we also investigate the convergence behavior for both exponential and logarithmic forms of the evolution equation using both regularized (*Reg*) and *NC2* schemes in the solution algorithm. Following this procedure we consider four different cases: a regularized scheme with exponential mapping (*exp+Reg*), a nucleation-completion scheme with exponential mapping (*exp+NC2*), a regularized scheme with logarithmic mapping (*log+Reg*) and a nucleation-completion scheme with logarithmic mapping (*log+NC2*). It is also possible to compare the local convergence behavior as well as the robustness of different algorithms.

The material properties in Table 7.1, typical of NiTi², are adopted in all the simulations of this section. where E and ν are the elastic modulus and the Poisson ratio, respectively. Details on the material parameters identification can be found in Auricchio et al. (2009a).

¹ We remark that, in this section, we use as a strain measure the Green-Lagrange strain tensor and as a stress measure the second Piola-Kirchhoff stress tensor. Moreover, we highlight that reported results are not physical as we know that the selected measures are not physical measures (see for example Pai et al. (1998)).

²See, for example, www.shape-memory-alloys.com.

Table 7.1: Material properties

E	ν	h	β	T_0	ε_L	R
[GPa]	[-]	[MPa]	[MPaK ⁻¹]	[°C]	[%]	[MPa]
51.7	0.3	750	5.60	-25	7.5	140

Simple shear test

We start simulating a loading-unloading simple shear test at two different temperatures: 37°C for pseudo-elasticity and -25°C for shape memory effect (see Figure 7.1, left). The deformation gradient and the Green-Lagrange strain tensors are expressed in terms of the shear amount κ as follows:

$$\mathbf{F} = \begin{bmatrix} 1 & \kappa & 0 \\ 0 & 1 & 0 \\ 0 & 0 & 1 \end{bmatrix}, \quad \mathbf{E} = \frac{1}{2} \begin{bmatrix} 0 & \kappa & 0 \\ \kappa & \kappa^2 & 0 \\ 0 & 0 & 0 \end{bmatrix}$$

Figure 7.1 (right) shows the results for two different time-step sizes ($0.02s$ and $0.2s$ denoted by the line and the circle symbols, respectively, while the total simulation time is $2s$). The results show the algorithm accuracy as well as the robustness for large time-

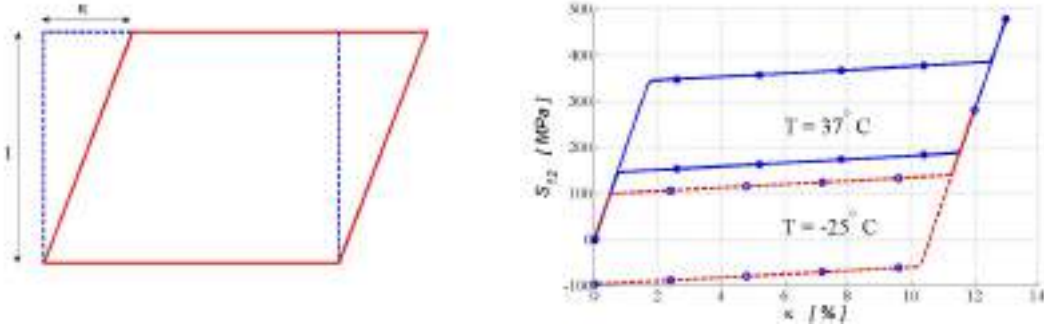


Figure 7.1: Simple shear test: shear deformation (left) and S_{12} component as a function of the shear amount κ (right). Lines denote $dt = 0.02s$ and the circles $dt = 0.2s$.

step sizes. We also observe the model capability of capturing pseudo-elasticity as well as shape memory effect.

Uniaxial tests.

We now simulate tension-compression as well as torsion tests under stress control at three different temperatures, and in particular for $T > A_f$, $M_f < T < A_f$, and $T < M_f$. For the tests with $T < A_f$ we also investigate shape recovery under temperature control. Moreover, we remark that since the term τ_M uses Macaulay brackets, the predictions of any temperature equal to or below M_f would be the same.

Figure 7.2 reports the stress-strain response with a solid line and for the tests with $T < A_f$, the strain recovery with a dashed line. The results show the model capability of capturing pseudo-elasticity and shape memory effect as well as the intermediate behavior.

To check the algorithm robustness we perform the tests with two different stress increments per step: in particular we consider stress increments equal to 150 and 15 MPa in tension-compression tests and equal to 100 and 10 MPa in torsion tests. Points A and B in Figure 7.2, indicate that a load cutting is used in the global solution (equilibrium) to prevent its divergence as the stiffness is abruptly changing³. Table 7.2 shows the convergence results for different formulations in tension-compression tests. We use letters f and c to distinguish the results for the fine and coarse increments, respectively. For each case, a pair of numbers is reported corresponding to PT1 and PT2, respectively. As it is expected, using a *NC2* scheme reduces the average number of iterations. It is interesting to note that using the logarithmic form reduces the number of iterations and this can be interpreted as the result of the reduced nonlinearity of the equations. We do not focus on the efficiency comparison in this section and postpone it to Section 7.2.2, where we compare the CPU time for different boundary value problems (BVPs).

Table 7.2: Convergence results for tension-compression tests.

	exp+Reg	exp+NC2	log+Reg	log+NC2
$37^\circ C$ (f)	6	7	4	4
	4	4	4	4
$37^\circ C$ (c)	8	7	4	4
	4	4	4	4
$-5^\circ C$ (f)	8	4	4	4
	5	4	4	4
$-5^\circ C$ (c)	6	6	4	4
	4	5	4	4
$-25^\circ C$ (f)	6	5	4	4
	4	4	4	4
$-25^\circ C$ (c)	5	4	4	4
	4	4	4	4

³Similarly to increment cutting technique, we can use load-cutting for a stress-controlled problem.

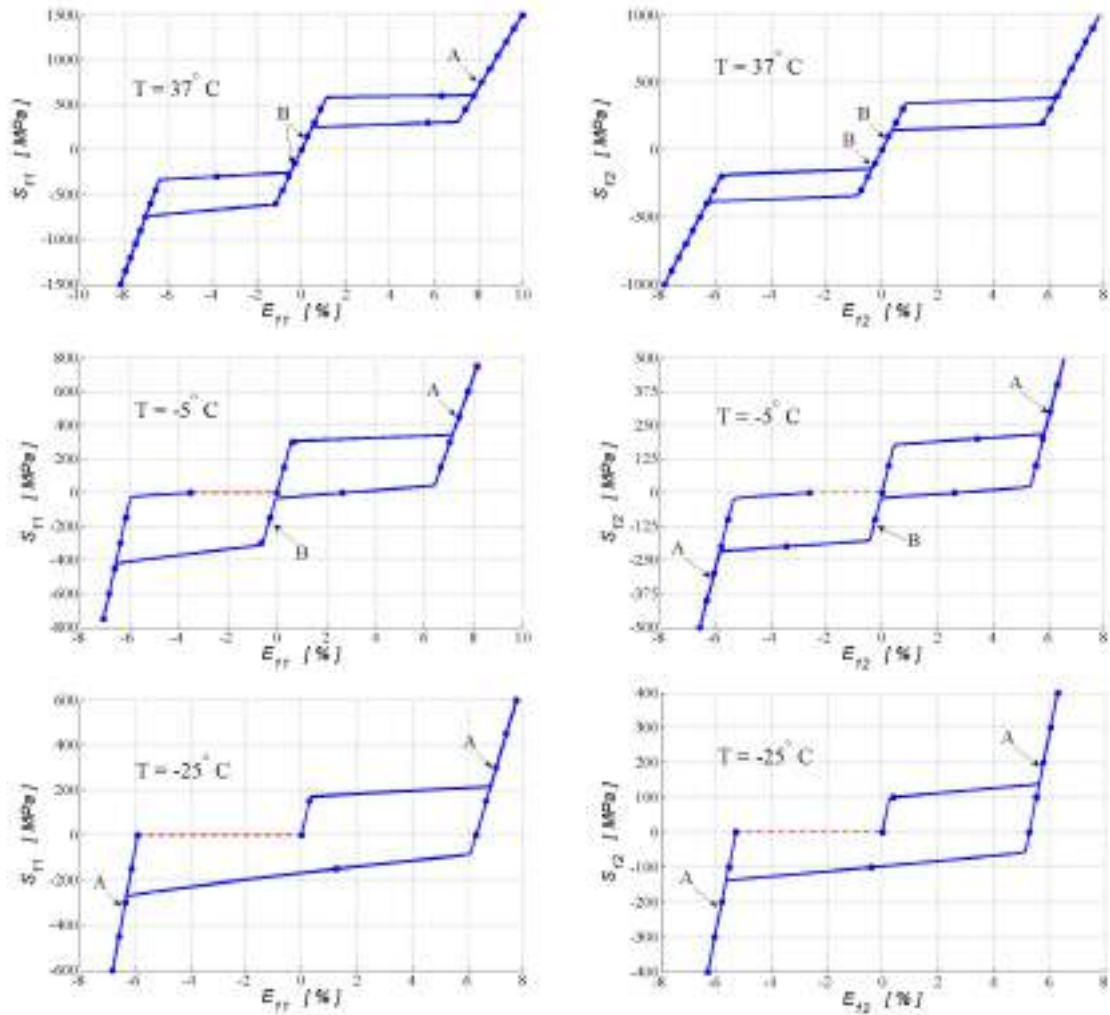


Figure 7.2: Uniaxial tests: tension-compression tests (left) and torsion tests (right) under stress control: $T = 37^{\circ}\text{C}$ (upper); $T = -5^{\circ}\text{C}$ (center); $T = -25^{\circ}\text{C}$ (lower). For $T < A_f$ strain recovery induced by heating is indicated with a dashed-dot line. Stress increment per step during tension-compression tests: 15 MPa (line) and 150 MPa (circles). Stress increment per step during torsion tests: 10 MPa (line) and 100 MPa (circles).

Multiaxial tests.

We now investigate two types of strain-controlled biaxial tests, the first consisting of a butterfly-shaped ($E_{11} - E_{22}$) input, and the second of a square-shaped ($E_{11} - E_{12}$) input. Figure 7.3 shows the strain input as well as the stress output for the butterfly-shaped test. The plots on the left refer to a strain value of 6%, while a 10% strain value is used for plots on the right. The middle and lower plots show the results at $T = 37^{\circ}\text{C}$ (pseudo-elasticity) and $T = -25^{\circ}\text{C}$ (shape memory effect), respectively. All series of tests are performed using two different time step sizes (0.02s and 0.2s, corresponding to the solid line and the circle symbols, respectively), while the total time is 8s.

As we discussed in Section 6.2.2, the implemented algorithm, detects any divergence during a solution process and automatically cuts the increment size. We use a label *IC* to indicate an increment in which cutting takes place and emphasize that the increment size is not the actual size. We avoid reporting intermediate increment results to keep the figures as clear and simple as possible.

We repeat with a similar approach the squared-shape test and report the results in

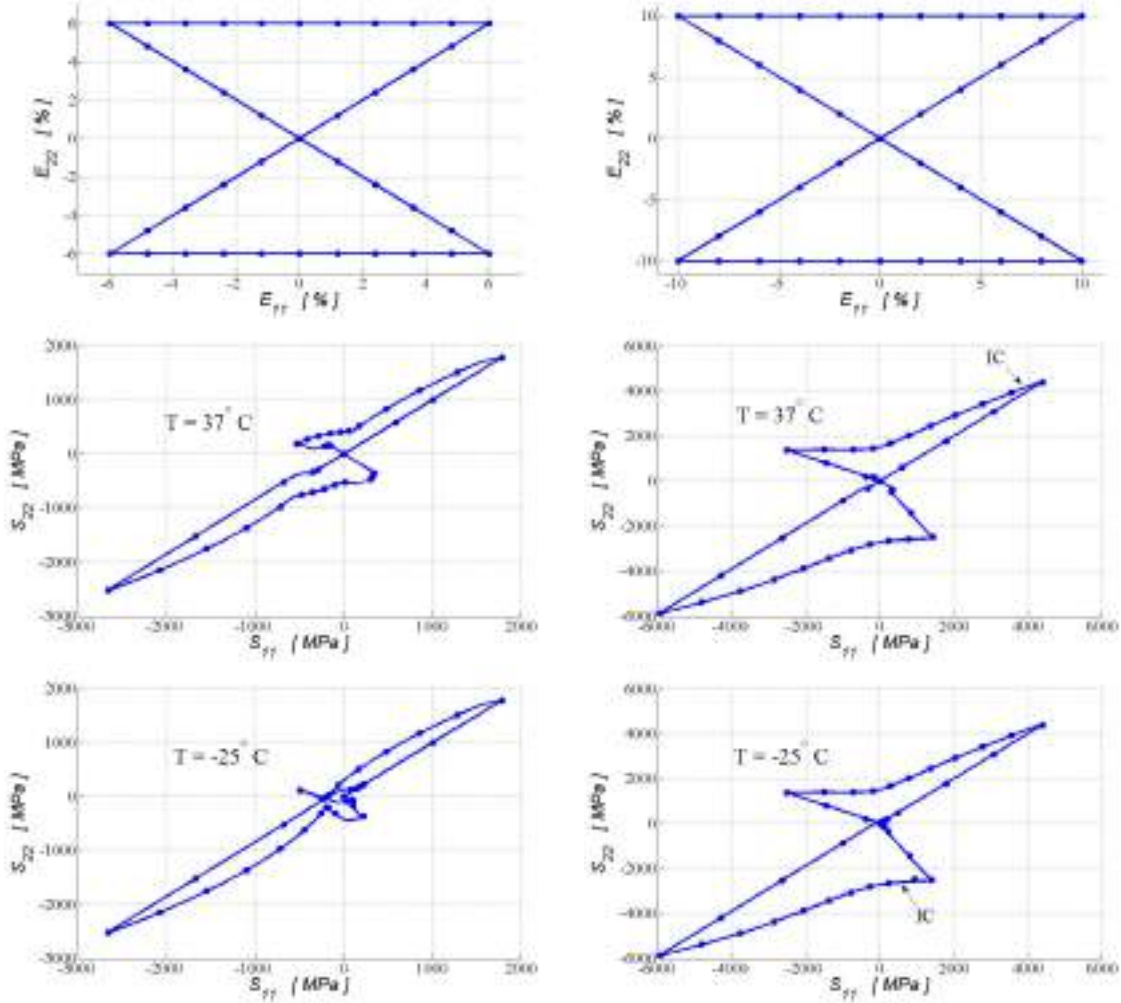


Figure 7.3: Biaxial butterfly-shaped input under strain control up to 6% (upper-left) and 10% (upper-right); stress output at $T = 37^{\circ}\text{C}$ (center) and $T = -25^{\circ}\text{C}$ (lower) for two time step sizes: 0.02s (line) and 0.2s (circles).

Figure 7.4. Tables 7.3 and 7.4 show the convergence results for the stain-controlled biaxial tests. For brevity, we only report the results for the most critical cases, i.e., for 10% strain. It is observed that in terms of convergence, the *NC2* scheme is preferred compared with the *Reg* scheme. As we expected, using a logarithmic form of the evolution equation improves the convergence behavior. Using the logarithmic form improves both robustness and efficiency by decreasing the equation nonlinearity and the number of increment cuttings, as well as the number of iterations.

Table 7.3: Convergence results for the butterfly-shaped path: up to 10% strain.

	exp+Reg	exp+NC2	log+Reg	log+NC2
37°C (f)	8	8	6	6
	11	11	10	10
37°C (c)	11	8	10	7
	9	10	9	10
-25°C (f)	7	7	6	6
	10	10	10	10
-25°C (c)	7	7	7	7
	10	9	10	9

We also repeat the above mentioned tests under stress control. The stress values vary

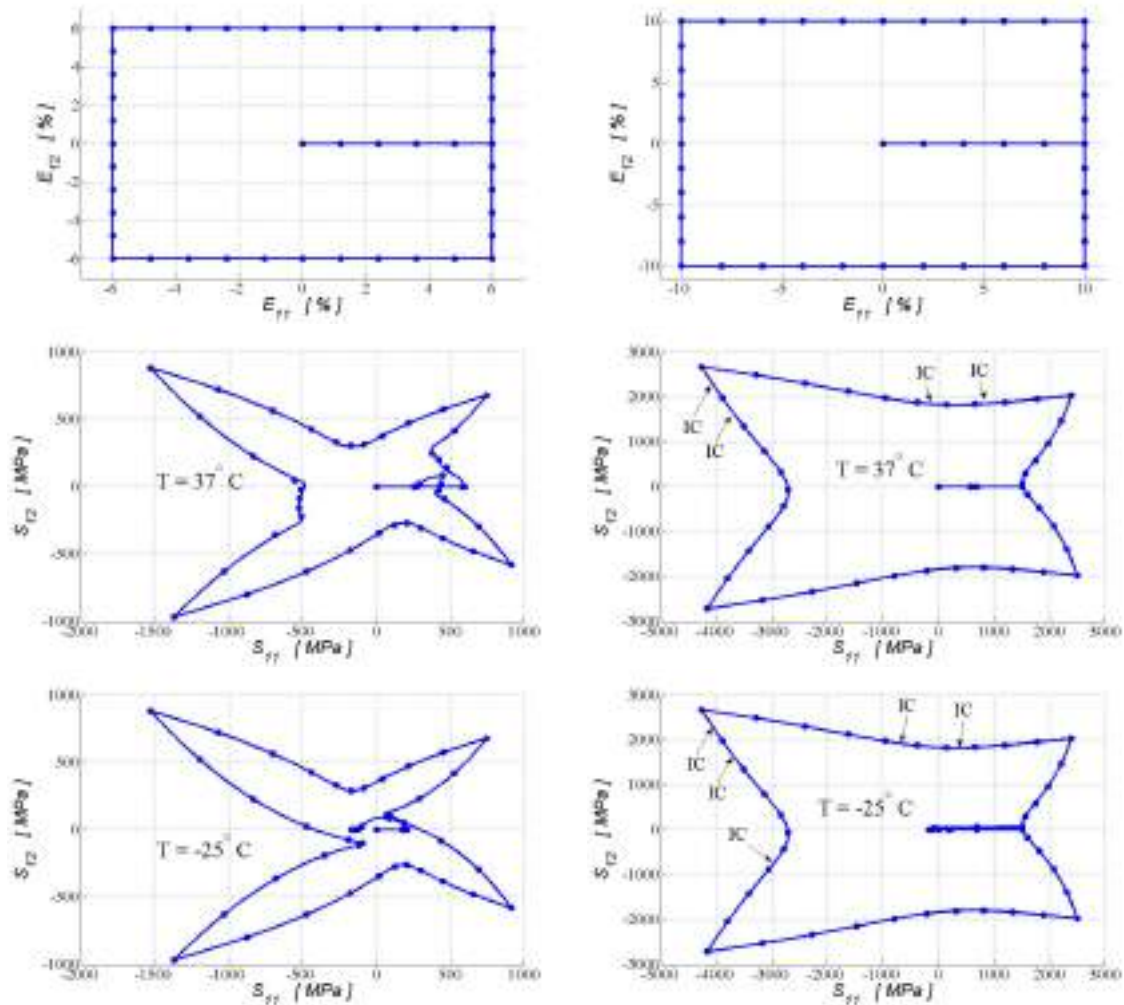


Figure 7.4: Biaxial squared-shaped input under strain control up to 6% (upper-left) and 10% (upper-right); stress output at $T = 37^{\circ}\text{C}$ (center) and $T = -25^{\circ}\text{C}$ (lower) for two time step sizes: 0.02s (line) and 0.2s (circles).

Table 7.4: Convergence results for the squared-shaped path: up to 10% strain.

	exp+Reg	exp+NC2	log+Reg	log+NC2
$37^{\circ}C$ (f)	9	9	8	8
	12	12	12	12
$37^{\circ}C$ (c)	9	9	8	8
	8	7	7	7
$-25^{\circ}C$ (f)	13	13	9	9
	14	14	12	11
$-25^{\circ}C$ (c)	9	9	9	9
	12	13	13	13

between ± 700 MPa. At $T = -25^{\circ}C$, after applying the stress path, we increase the temperature up to A_f , such that the residual strain recovery takes place as shown in the lower part of Figure 7.5 (see the dotted line).

7.2.2 Numerical examples: Boundary value problems

In this section, we solve four boundary value problems to validate the adopted model as well as the proposed integration algorithm and the solution procedure. A helical spring and a medical stent are simulated at two different temperatures to show the model capability of capturing both pseudo-elasticity and shape memory effect. Moreover, we compare the CPU time for both exponential and logarithmic forms of the time-discrete evolution equation, as well as for *Reg* and *NC2* schemes. In all boundary value examples we use the same material properties as in Section 7.2.1. The temperature in pseudo-elastic simulations is set to $37^{\circ}C$ while in shape memory effect simulations a temperature of $-25^{\circ}C$ is adopted.

For all simulations, we use the commercial nonlinear finite element software ABAQUS/Standard, implementing the described algorithm within a user-defined subroutine UMAT.

Helical spring: pseudo-elastic test.

A helical spring (with a wire diameter of $4mm$, a spring external diameter of $24mm$, a pitch size of $12mm$ and with two coils and an initial length of $28mm$) is simulated using 9453 quadratic tetrahedron (C3D10) elements and 15764 nodes. An axial force of $1525N$ is applied to the one end while the other end is completely fixed. The force is increased from zero to its maximum value and unloaded back to zero. Figure 7.6 shows the spring initial geometry, the adopted mesh and the deformed shape under the

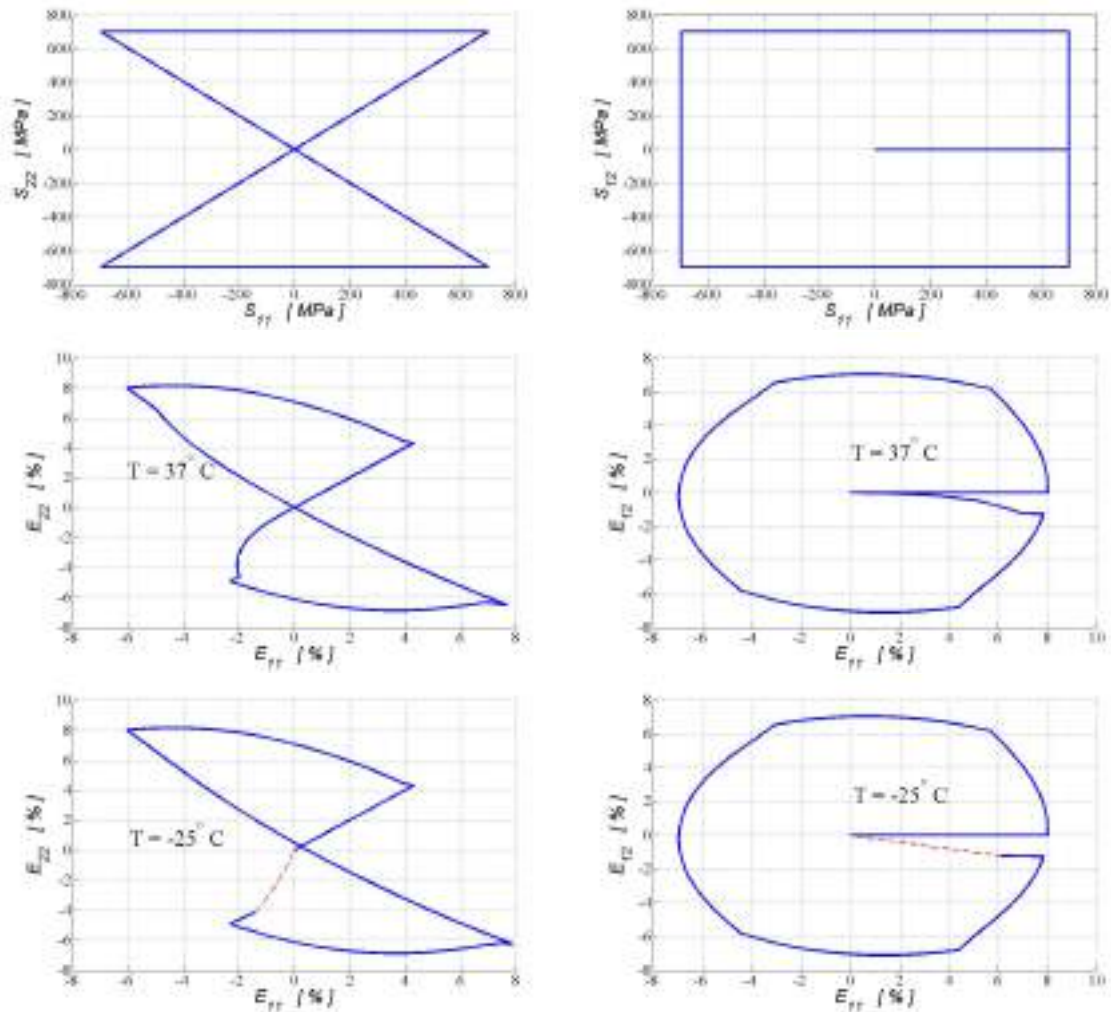


Figure 7.5: Biaxial butterfly-shaped input (upper-left) and squared-shaped input (upper-right) under stress control; strain output at $T = 37^\circ\text{C}$ (centre) and $T = -25^\circ\text{C}$ (lower); strain output (lower) with strain recovery (dotted line) under temperature increment.

maximum force. After unloading, the spring recovers its original shape as it is expected in the pseudo-elastic regime. Figure 7.7 (left) shows the force-displacement diagram. It is observed that the spring shape is fully recovered after load removal.

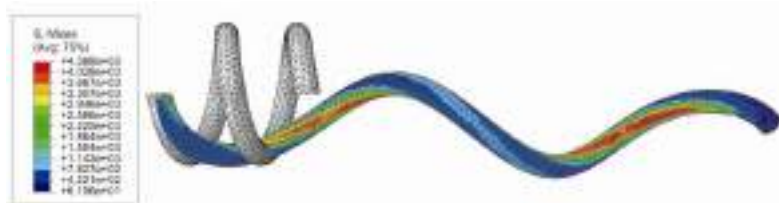


Figure 7.6: Pseudo-elastic spring: comparison of initial geometry and deformed configuration.

Helical spring: shape memory effect test.

We also simulate the same spring of Section 7.2.2 in the case of shape memory effect. An axial force of 427N is applied at $T = -25^\circ\text{C}$ (Figure 7.8, top) and, after unloading, the spring does not recover its initial shape (Figure 7.8, bottom). After heating, up to a temperature of 10°C , the spring recovers its original shape. Figure 7.7 (right) shows the force-displacement-temperature behavior. According to Figure 7.7 (right), heating the spring leads to full recovery of the original shape at $T = A_f$ (0°C) and subsequent heating does not change any more its shape.

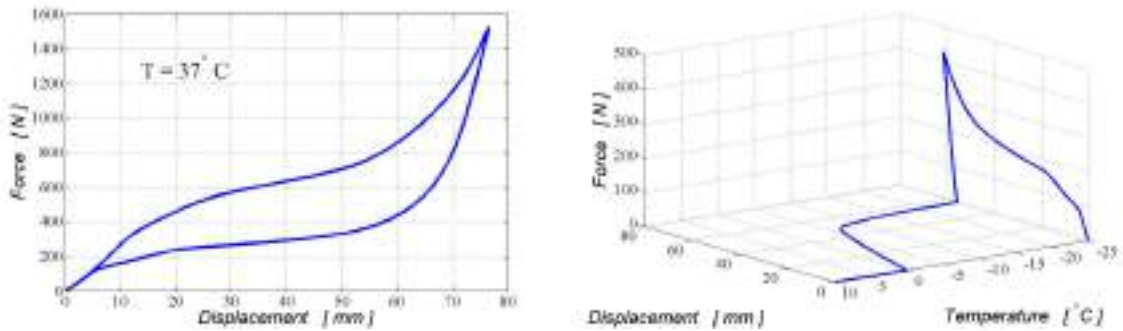


Figure 7.7: Force-displacement diagram for the SMA spring: pseudo-elasticity (left) and shape memory effect (right).

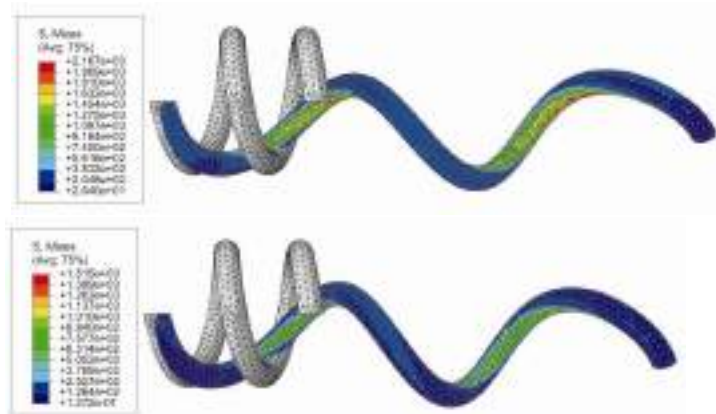


Figure 7.8: Shape memory effect in the simulated spring: deformed shape under maximum load (top) and after unloading (bottom).

Crimping of a medical stent: pseudo-elastic test.

In this example, the crimping of a pseudo-elastic medical stent is simulated. To this end a medical stent with 0.216mm thickness and an initial outer diameter of 6.3mm (Figure 7.9, upper-left) is crimped to an outer diameter of 1.5mm . Utilizing the

ABAQUS/Standard contact module, the contact between the catheter and the stent is considered in the simulation. A radial displacement is applied to the catheter and is then released to reach the initial diameter. In this process, the stent recovers its original shape after unloading. Figure 7.9 (upper-right) shows the stent deformed shape when crimped.

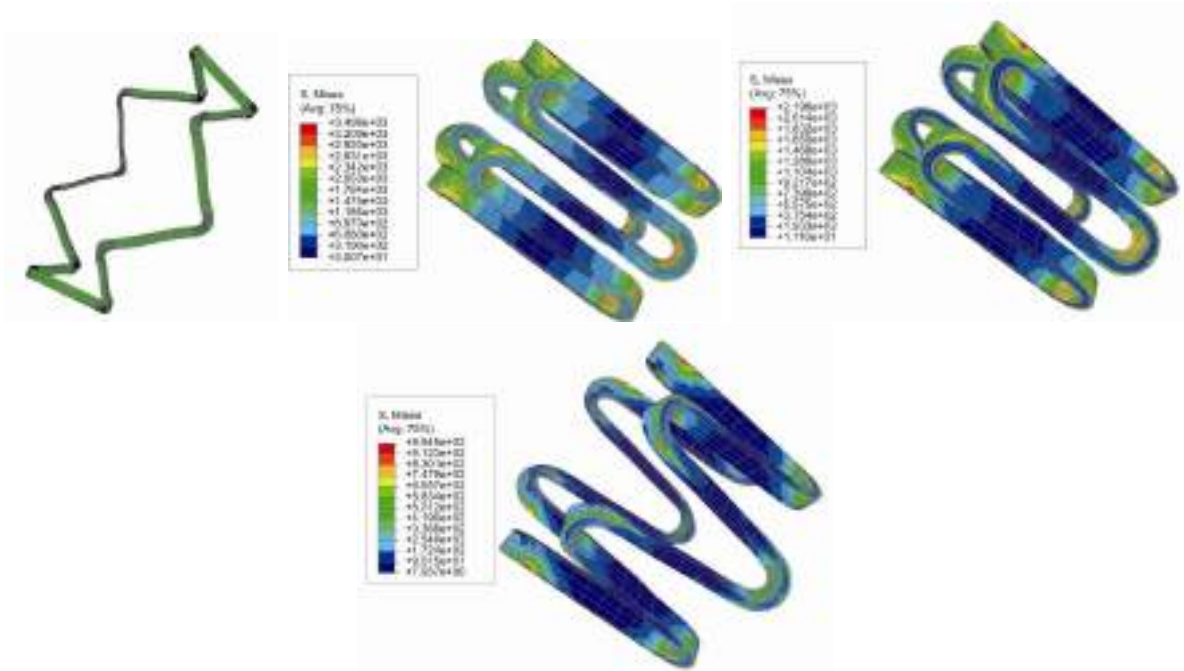


Figure 7.9: Stent crimping: initial geometry (upper-left), crimped shape in PE case (upper-right), crimped shape in SME case (centre) and deformed shape in SME case after uncrimping (lower).

Crimping of a medical stent: shape memory effect test.

In this example, the same stent is crimped at a temperature of $-25^{\circ}C$ as it is shown in Figure 7.9 (center). Due to the low temperature, while the catheter is expanded, the stent remains in a deformed state as shown in Figure 7.9 (lower). The initial shape is however recovered after heating.

7.2.3 Investigation of computational efficiency: comparison of CPU times.

We now compare the CPU times in order to show the efficiency gained by using logarithmic form as well as a nucleation-completion scheme. We remark that we normalize all CPU times with respect to the CPU time for the case of exponential form with a regularized scheme.

We first consider the CPU times for the SME simulations to study the effect of different time-discrete forms. Due to the small elastic regime than in the PE case, we expect approximately the same CPU times for both *Reg* and *NC2* schemes. Therefore, these tests give us an approximation of the gained efficiency due to the use of the logarithmic form of the time-discrete evolution equation. Comparing the simulation CPU times for exponential and logarithmic forms for SME cases reported in Table 7.6, we conclude that using the logarithmic form decreases CPU time of approximately 20% compared with the exponential form.

We now consider the CPU times for PE simulations. As it can be observed in Table 7.6, in all cases, using the *NC2* scheme decreases the CPU time compared with the *Reg* scheme. This decrease depends on the problem and for the simulated problems it varies from 6% (spring and log form) to 21% (stent and log form).

We finally compare the CPU time of the proposed integration algorithm (*log + NC2*) with the previously proposed one (*exp + Reg*). Considering the first and last columns of Table 7.6, we observe that the gained efficiency varies from 19% up to 36%.

Table 7.5: CPU times comparison.

	exp+Reg	exp+NC2	log+Reg	log+NC2
Stent (PE)	1.00	0.84	0.81	0.64
Spring (PE)	1.00	0.89	0.74	0.70
Stent (SME)	1.00	1.01	0.81	0.81
Spring (SME)	1.00	1.02	0.79	0.77

7.3 Comparison of GLUS and GLSY models in terms of computational efficiency

We now compare the CPU times for three cases, i.e., original unsymmetric model in which \mathbf{C}^{in} is considered as unknown (Arghavani et al., 2010b; Evangelista et al., 2009), the original unsymmetric model in which \mathbf{U}^{in} is considered as unknown and the proposed symmetric model in which \mathbf{U}^{in} is considered as unknown. We denote them as *original-C*, *original-U* and *improved*, respectively, in the following.

We remark that we normalize all CPU times with respect to those for the case *original-C* (Arghavani et al., 2010b; Evangelista et al., 2009). Moreover, the models have been programmed in a consistent manner so that reliable comparisons concerning the speed of computation could be obtained.

The simulation CPU times are reported in Table 7.6. From such results we may con-

clude that using \mathbf{U}^{in} instead of \mathbf{C}^{in} , decreases the CPU time of approximately one third compared with that adopted in (Arghavani et al., 2010b; Evangelista et al., 2009).

Moreover, comparing *original-U* and *improved* CPU times, we observe a slightly increased efficiency for the proposed symmetric model.

We finally, conclude that using the proposed symmetric constitutive model and solution algorithm can improve the numerical efficiency in the order of one third when compared with the previously adopted ones in (Arghavani et al., 2010b; Evangelista et al., 2009).

Table 7.6: Normalized CPU time comparison (exp+Reg).

	Spring (PE)	Spring (SME)	Stent (PE)	Stent (SME)
<i>original-C</i>	1.00	1.00	1.00	1.00
<i>original-U</i>	0.68	0.72	0.65	0.72
<i>improved</i>	0.64	0.69	0.63	0.73

7.4 Simulation of some BVPs using HSSY formulation

In this section, we solve some boundary value problems to show the proposed model capabilities as well as the proposed integration algorithm and the solution procedure. A uniaxial test on a cube, crimping of a pseudo-elastic medical stent and a helical spring actuator are simulated to show the model capability of capturing both pseudo-elasticity and shape memory effect.

For all simulations, we use the commercial nonlinear FE software ABAQUS/Standard, implementing the described algorithm within a user-defined subroutine UMAT.

The material properties reported in Table 7.7 are adopted in all the simulations of this section.

Table 7.7: Material properties

E	ν	h	β	T_0	ε_L	R
[GPa]	[-]	[MPa]	[MPaK ⁻¹]	[°C]	[%]	[MPa]
51.7	0.3	1000	5.60	-25	10	140

7.4.1 Uniaxial test

We simulate a single element unit cube under an applied force on one face while the opposite face is fixed. The applied force is increased from zero to a maximum value of 1500 N and subsequently decreased to zero and increased in the opposite direction to a value of 1500 N and finally decreased back to zero. Figures 7.10a and 7.10b show the SMA behavior at 37°C and -25°C, respectively. We observe the pseudo-elastic behavior in Figure 7.10a where the temperature is above the austenite finish temperature while in Figure 7.10b the material does not recover the original shape after unloading; however it can be recovered by heating above the austenite finish temperature (shape memory effect).

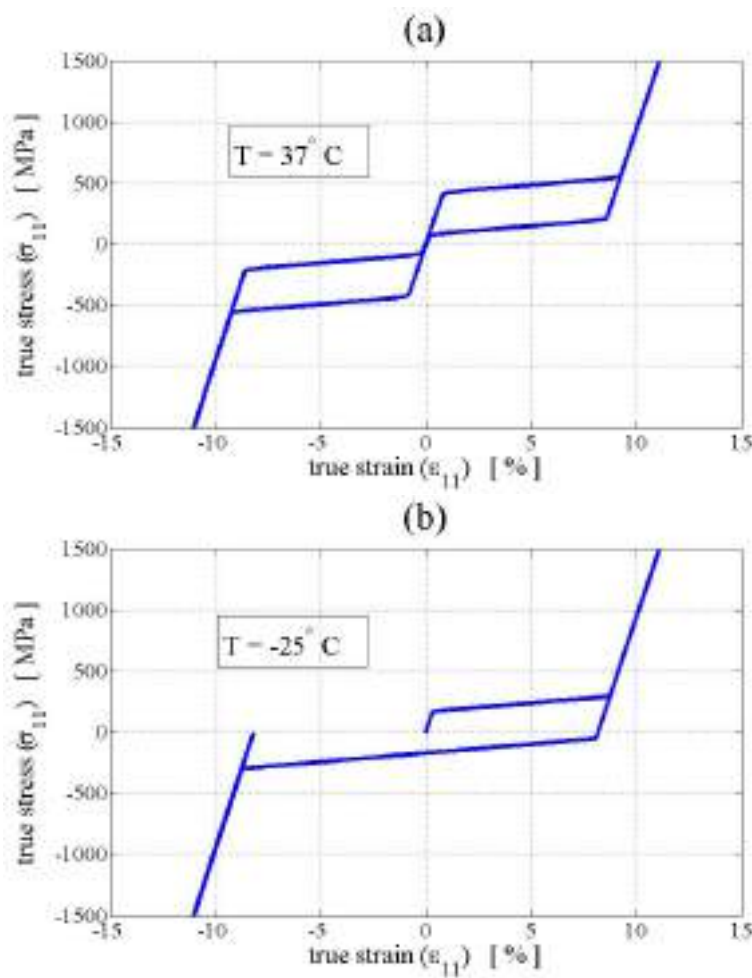


Figure 7.10: Illustration of the material behavior under uni-axial force-controlled test: a) pseudo-elasticity at $T = 37^\circ\text{C}$; b) shape memory effect at $T = -25^\circ\text{C}$.

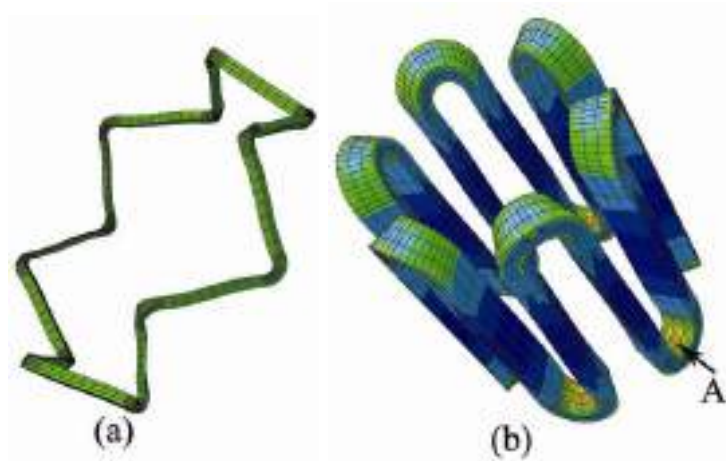


Figure 7.11: Pseudo-elastic stent crimping: a) initial geometry; b) crimped shape

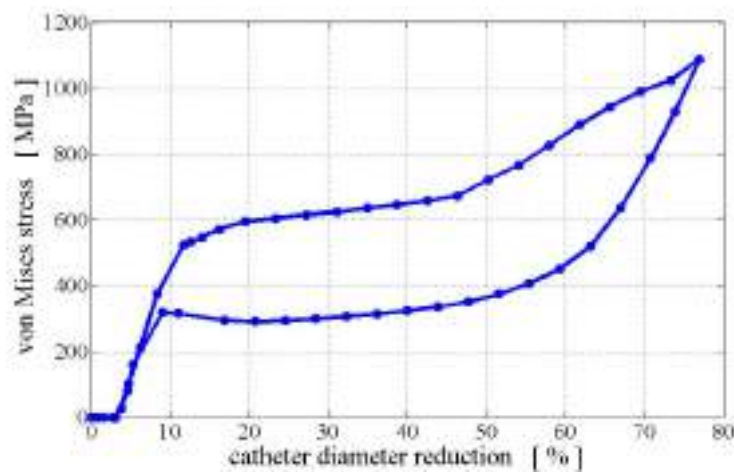


Figure 7.12: von-Mises stress versus percentage of catheter diameter reduction (at point A shown in Figure 7.9b).

7.4.2 Pseudo-elastic stent

In this example, the crimping of the pseudo-elastic medical stent described in Section 7.2.2 is simulated at a temperature of 37°C . Figures 7.11a, b show the stent undeformed and deformed shape when fully crimped, respectively. In this simulation, the stent recovers its original shape after unloading as expected for the pseudo-elastic case. Moreover, Figure 7.12 reports the von-Mises stress at the critical point A (shown in Figure 7.11b) versus the reduction percentage in catheter diameter.

7.4.3 Spring actuator

In order to investigate the shape memory effect, the helical spring described in Section 7.2.2 and shown in Figure 7.13A is simulated. The spring is loaded by a weight $W =$

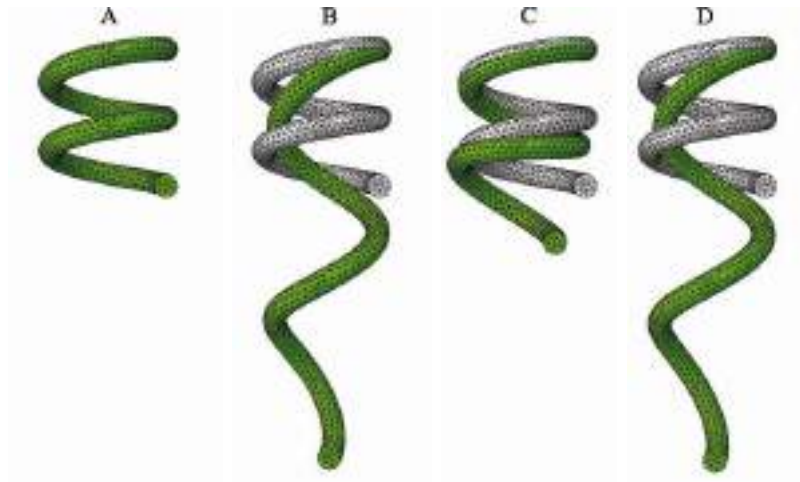


Figure 7.13: Spring actuator: A) initial geometry and mesh; B) deformed shape due to the weight application at $T = -25^{\circ}\text{C}$; C) spring shape recovery and weight lifting due to heating to $T = 75^{\circ}\text{C}$; D) spring stretching due to cooling to $T = -25^{\circ}\text{C}$.

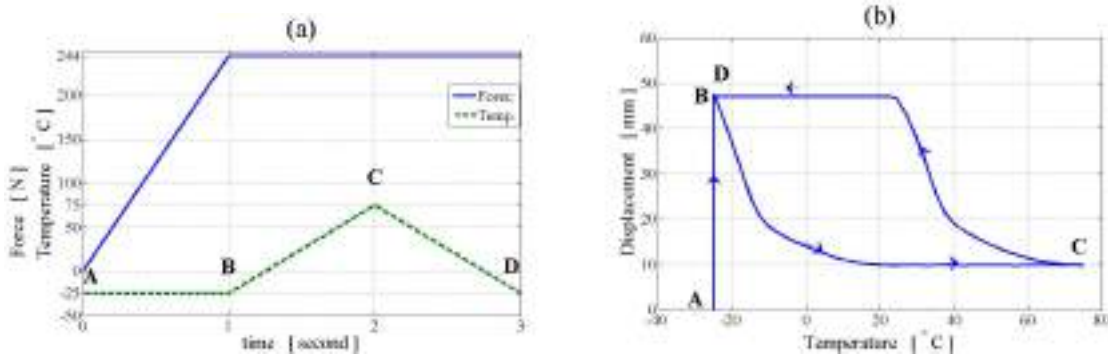


Figure 7.14: a) Loading history during simulation; b) vertical displacement of the lower loaded end of spring versus temperature variation.

244 N in martensite state at $T = -25^{\circ}\text{C}$ (Figure 7.13B), If the stress applied by the weight is less than the alloy recovery stress, heating the material above A_f induces the inverse phase transformation and the spring lifts the weight (Figure 7.13C). Moreover, cooling below M_f the transformation from austenite to martensite takes place and the weight stretches again the spring (Figure 7.13D); accordingly, a repeatable two-way motion takes place.

We remark that in the analysis, we assume that during each time step the temperature is uniform in the material body, i.e., we neglect the thermo-mechanical coupling.

Figure 7.14a shows the loading history during the simulation. In Figure 7.14b, we plot the vertical displacement versus temperature. It is observed that applying a temperature cycle between -25°C and 75°C , the spring actuator traverse a length of 37mm.

7.5 Comparison of SSSR, SSLR and GLUS models

In this section, we are interested to study the large rotation effects. To this end, we simulate several beam bending problems which exhibit very large rotations. We use the material properties in Table 7.8 in all simulations of this section.

Table 7.8: Material properties

E	ν	h	β	T_0	ε_L	R
[GPa]	[-]	[MPa]	[MPaK ⁻¹]	[°C]	[%]	[MPa]
50.0	0.33	3000	3.23	-25	5	100

7.5.1 Simple tension test

We first simulate a simple tension test for a rod with $L = 100mm$, $h = 6mm$ and $b = 8mm$ (Figure 7.15, top) and with an applied displacement at one end (up to $7mm$ which is unloaded to the initial configuration), while another end is fixed (we will then use this geometry as a beam in the next example). Figure 7.15 (down) presents the simulation results as well as different formulation comparisons. According to Figure 7.15 (down), we conclude that all formulations result in approximately the same behavior. For displacements larger than $4mm$, there is a small difference between small-strain and finite-strain formulation results which is due to the cross-sectional area reduction.

7.5.2 Bending of a straight beam

We now simulate a cantilever beam which is loaded at the end by a force $F = 2000N$ and then is unloaded. Figure 7.16 (top) shows the deformed shape when a finite-strain formulation (GLUS) is used. Figure 7.16 (down) shows the force-displacement (component in the direction of the force) curve as well as different formulation comparisons, highlighting the big difference between the small-deformation formulation SSSR and the finite deformation ones (SSLR, GLUS).

7.5.3 Out-of-plane bending of a curved beam

We finally simulate the arc-shaped beam shown in Figure 7.17 (top) with an outer radius of $20mm$, an inner radius of $15mm$ and a thickness of $2mm$ subjected to an

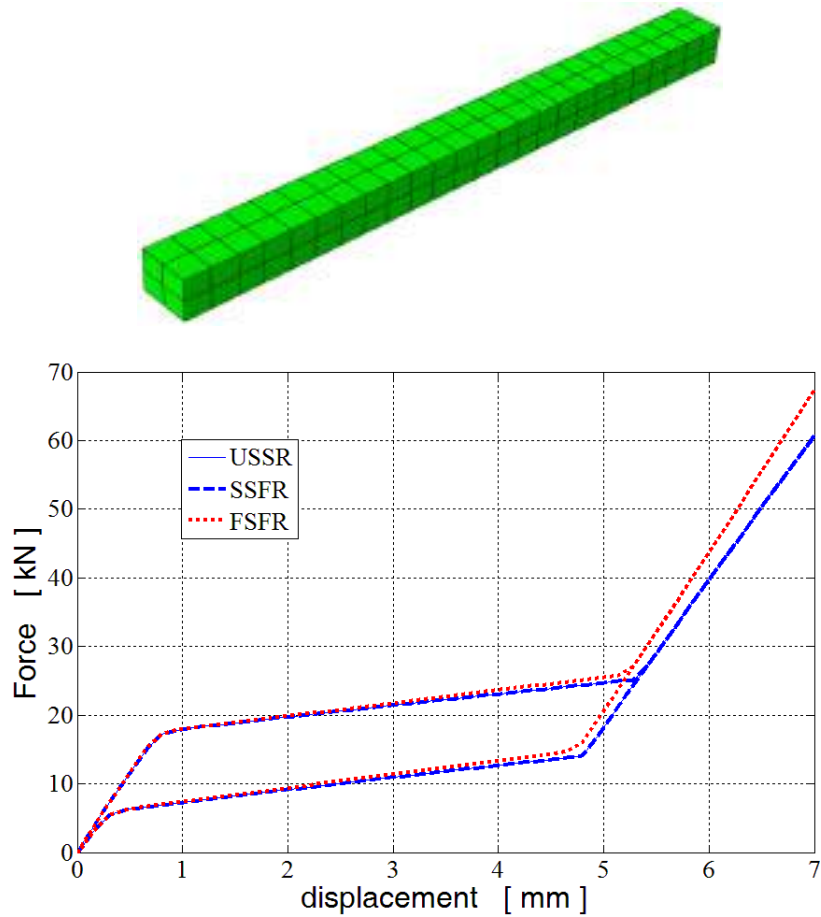


Figure 7.15: Geometry and mesh of the beam(top); force-displacement diagram and comparison of different formulations under tension test (down).

out-of-plane force of $500N$. Figure 7.17 (top) also shows the deformed shape under the maximum force of $500N$. In Figure 7.17 (down), we report the force-displacement diagrams (displacement vector magnitude). We observe that the simulation result of small-deformation formulation SSSR deviates considerably and for this simulation it diverges. However, we stress that this deviation is not surprising, since the small-deformation constitutive model is based on the assumption that the reference and current configurations are approximately the same, while at large deformations this assumption is not valid any more.

This example simply shows the nonlinear geometry effects and highlights the necessity of using a finite deformation constitutive model for SMA-based structures in which usually large rotations are present. In addition, according to the simulation results we conclude that using a small-strain formulation without considering rotation effects, may lead to highly unsatisfactory results. Moreover, using a corotational formulation can improve the results in the same way a full finite-strain formulation can do. While both SSLR and GLUS formulations yield approximately the same results, the computational cost in terms of CPU time is much lower for the corotational formulation. This is an important

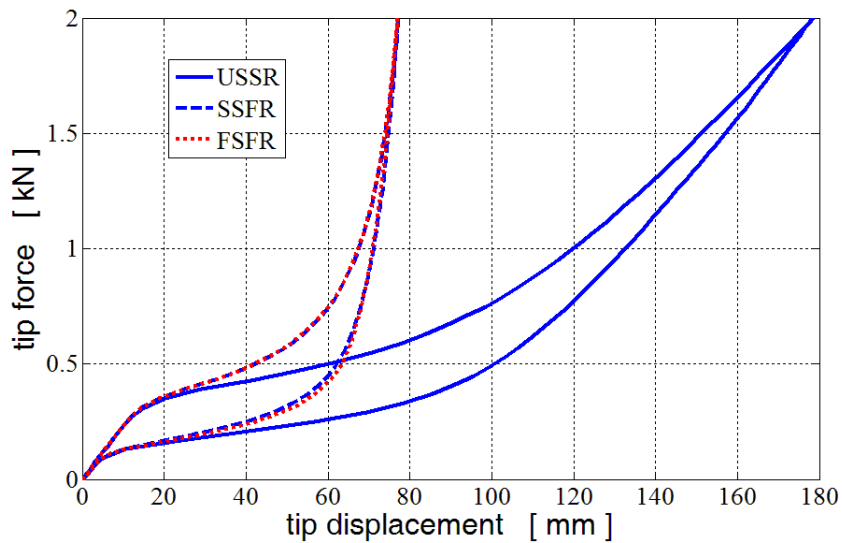
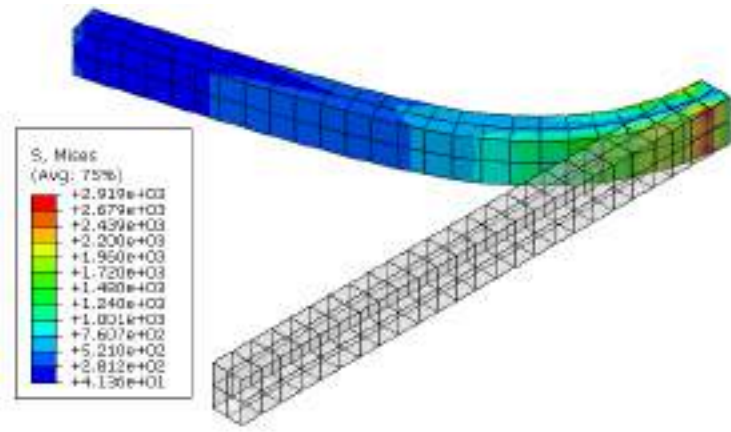


Figure 7.16: The cantilever beam under tip force, deformed shape when GLUS formulation is used (top); comparison of force-tip displacement diagram for different formulations (down).

issue from a computational cost point of view. These findings are in agreement with the results reported by Christ and Reese (2008) where they compare a small-deformation formulation with a finite-strain one; however, the difference (or the error) is mainly due to large rotations.

7.6 Simulation of SMA-based devices: an SMA micro-gripper

The developed computational tool can be used in analysis of SMA micro-actuators and biomedical stent devices. Application of the developed computational tool in simulation of several SMA devices motivates it as an effective tool that can be successfully used in the design, analysis and optimization procedures of SMA devices.

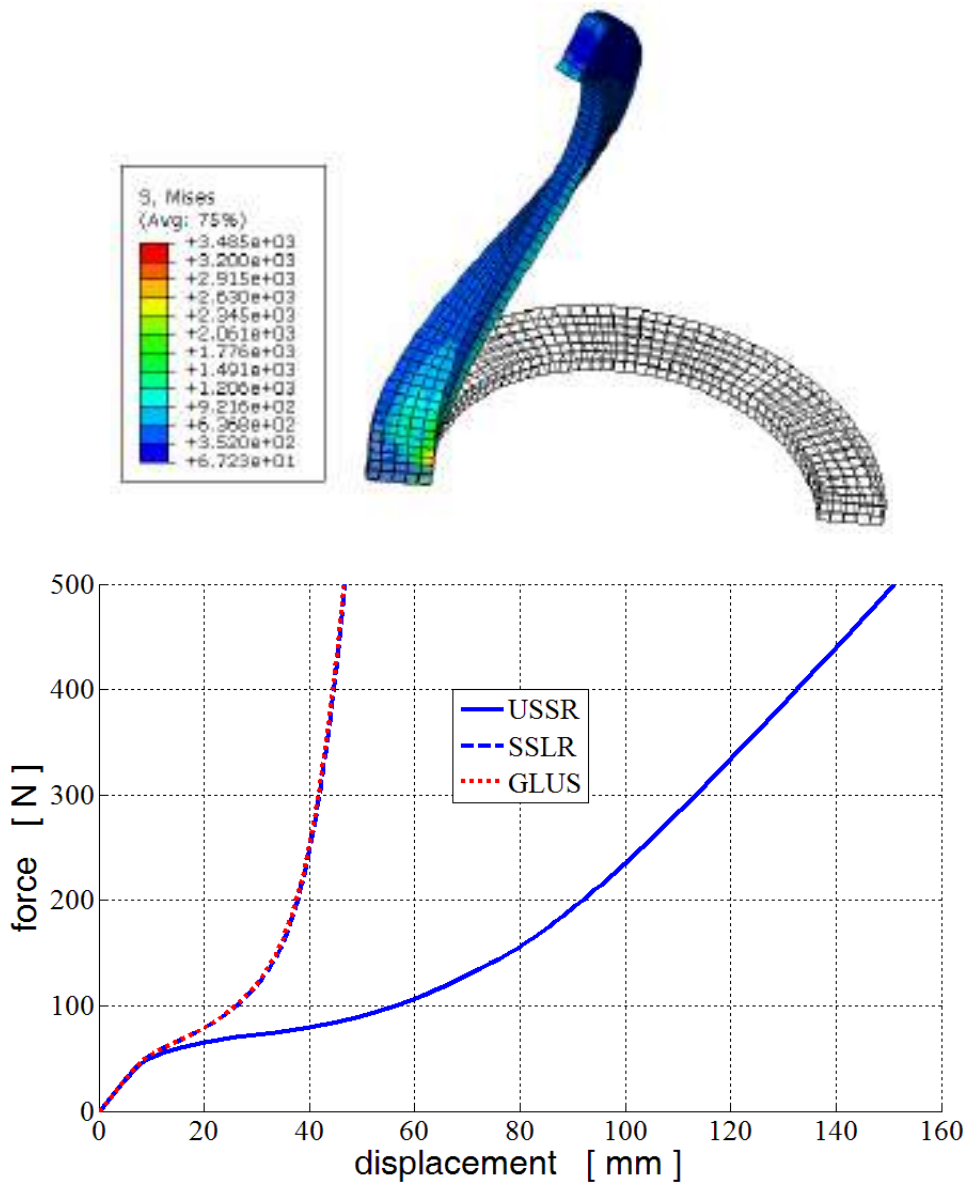


Figure 7.17: Geometry and mesh description of the arc-shaped beam under an out of plane force (top); force-displacement diagram comparison for different formulations (down)

To this end, adopting the material properties reported in Table 7.9, we simulate the SMA micro-gripper shown in Figure 7.18. The micro-gripper geometry is similar to that reported by Kohl (2004) and it has two parts: the upper part (gear actuator) and the lower part (linear actuator). After laser cutting (Figure 7.18a), a pre-deformation of 2mm is applied to the linear actuator, while heating the gear one (Figure 7.18b). From now on, at each time, one actuator is martensitic while another one is austenitic. We now heat the linear actuator to a temperature of $T = 30^\circ\text{C}$ while cooling the gear one to a temperature of $T = -25^\circ\text{C}$ which closes the gripper (Figure 7.18c). If we then heat the gear actuator and cool down the linear one, the gripper would open again (Figure 7.18d). Figure 7.19 shows the micro-gripper when it grips a micro-sample.

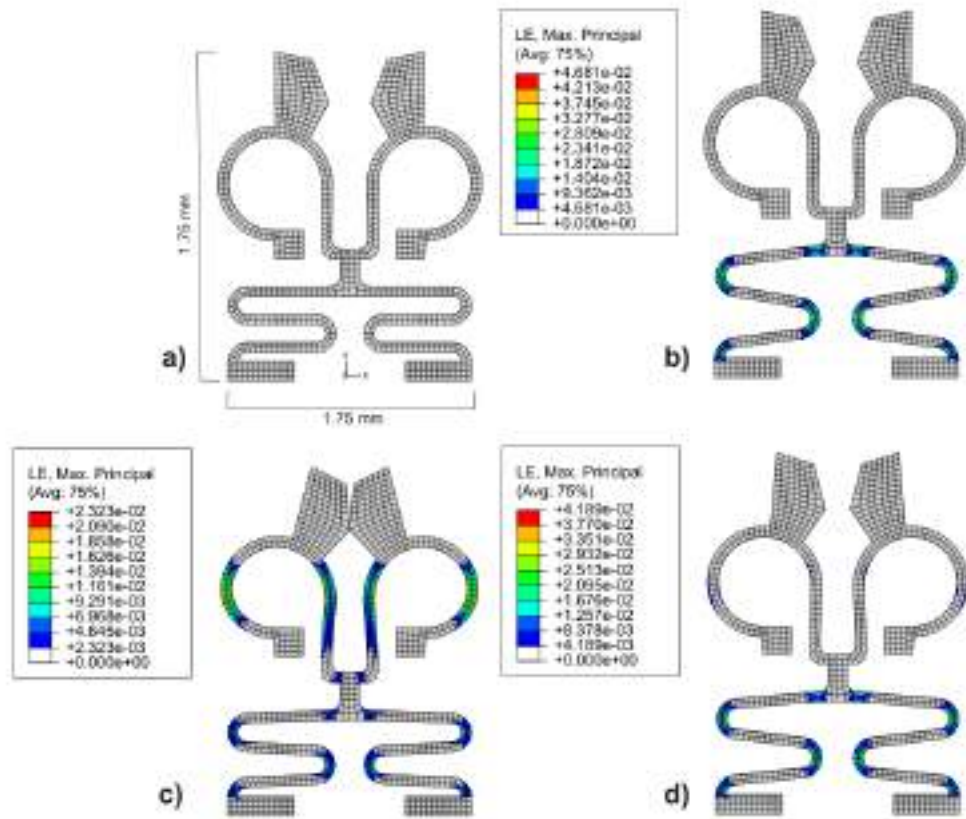


Figure 7.18: An SMA micro-gripper: a) starting configuration; b) memorization step of linear actuator; c) heating of linear actuator and consequent actuation of the gear one; d) heating of gear actuator with consequent re-opening. Contour plot of maximum principal logarithmic strain is reported.

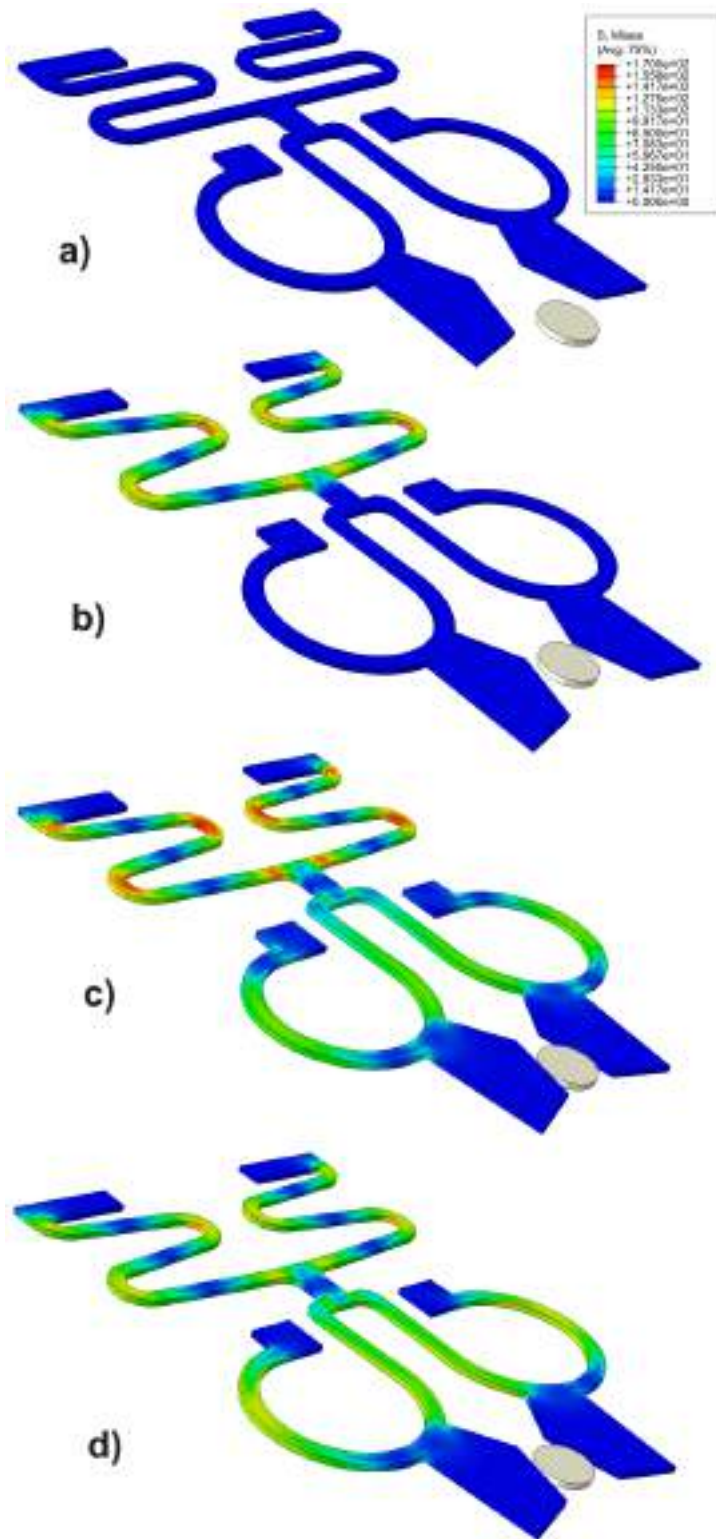


Figure 7.19: Simulation of micro-gripper with a sample: a) starting configuration; b) memorization step; c) heating of linear actuator and sample gripping; d) heating of rotary actuator with consequent re-opening. von Mises stress [MPa] distribution in the micro-gripper are depicted in the contour plot.

Table 7.9: Material properties

E	ν	h	β	T_0	ε_L	R
[GPa]	[-]	[MPa]	[MPaK ⁻¹]	[°C]	[%]	[MPa]
53	0.3	1000	2.5	-25	4	60

7.7 Summary

In this chapter, we presented several numerical examples to study the robustness and efficiency of the developed integration algorithms in Chapter 6. We performed several numerical simulations at the gauss point level to study the robustness of different algorithms. We then simulated several boundary value problems to compare different algorithms efficiency. We also compared different model formulations and simulated several SMA-based devices. The results show that the developed algorithms can be used as a proper and efficient computational tool in design and analysis of SMA structures.

Chapter 8

Summary and conclusions

8.1 Summary

Increasing number of SMA applications calls for developing proper constitutive models as well as computational tools to be used in engineering design, analysis and optimization of SMA structures. However, SMAs exhibit very complicated behavior under different loading conditions. Thus, it is advantageous to know the importance of different phenomena in the simulation of real engineering applications.

To this end, in Chapter 1 we studied the SMA behavior and classified them in two categories: 1. primary effects which include the pseudo-elasticity and shape memory effect under general multiaxial (non-proportional) thermo-mechanical loadings and specifically the variant reorientation under loading non-proportionality; 2. secondary effects which cover other behaviors, being important in the specific applications. A model that can capture only the primary effects is called a basic model. It is usual to add secondary effects into a successful basic model, following straightforward approaches. This fact motivated us to focus only on primary effects in the constitutive modeling, i.e. basic model.

We investigated different SMA constitutive modeling approaches in Chapter 2 and concluded that the approach based on continuum thermodynamics with internal variables is more appropriate for developing phenomenological constitutive models. We then presented a literature review on phenomenological models. We highlighted that appearance of experimental data and the increasing interest in biomedical applications motivated the research toward 3D phenomenological modeling as well as corresponding computational part.

In Chapter 3, we briefly reviewed some preliminaries in nonlinear continuum mechanics and finite element (FE) analysis. We highlighted that, in FE analysis, the material behavior is evaluated at a point (Gauss point); consequently, to implement a constitutive

model into a finite element program, we should supply the stress and the tangent matrix at a point level.

The rest of the research devoted to constitutive modeling at small and finite strain regimes and numerical implementation in FEM. To this end, in Chapter 4, after reviewing some small strain formulations available in the literature, we presented a class of small strain SMA models and showed that several available models can be identified as members of the proposed class of models. With emphasis on non-proportional loading and reorientation, we specifically introduced a model which had the property of decoupling pure reorientation from pure phase transformation.

In Chapter 5, we extended the small strain constitutive models proposed by Panico and Brinson (2007) and Souza et al. (1998) into finite strain regime. The approach was based on the use of a multiplicative decomposition of the deformation gradient into elastic and inelastic parts. We then improved the finite strain extension of Souza model in several aspects, e.g.: well-defining the variables, presenting a fully-symmetric formulation and developing a model based on the Hencky strain measure.

Chapter 6 was totally devoted to numerical implementation of the developed constitutive models. We gave details on time-discretization, integration algorithm and solution schemes. Proposing a nucleation-completion condition, we discussed in detail different solution algorithms. Finally, we investigated a formulation in the large rotation, small strain regime (SSLR) which had the advantage of using the previously developed codes for the infinitesimal model (SSSR).

In chapter 7, we solved several numerical examples to study the robustness of different integration algorithms. In addition, we simulated several SMA applications and compared the computational efficiency of different algorithms. To this end, we compared the finite strain, small strain and finite rotation formulations. For all simulations, we implemented the developed algorithms into a user-defined subroutine UMAT in the non-linear finite element software ABAQUS. The results highlighted that the corotational formulation can yield satisfactory results while it is considerably faster than fully finite strain formulation.

8.2 Conclusions

To incorporate the growth, orientation and reorientation of variants, we introduced an appropriate set of internal variables. This set of internal variables was able to represent a scalar and a directional information. In most of the previously proposed models, inelastic strain had been considered as a unique internal variable. In general, the norm of

the inelastic strain represents the scalar martensite amount and its direction represents the preferred direction of the variants. However, in this work, a measure of the amount of stress-induced martensite was chosen as a scalar internal variable, being related to the amount of the inelastic strain due to the stress-induced phase transformation, while the average direction of different variants (or preferred direction of variants) was chosen as a tensorial internal variable, representing the inelastic strain direction. So, using a standard literature terminology (Bouvet et al., 2004; Panico and Brinson, 2007) the internal variables may be clearly interpreted as phase transformation and variant reorientation. We remarked that from a physical point of view, the application of a thermo-mechanical load activates the phase transformation and the preferred martensite variants start to nucleate or shrink (Otsuka and Wayman, 1998). Changing the load direction, another set of variants, that are in the new preferred direction with respect to the applied stress, starts to nucleate and previous variants may grow or shrink depending on the available stress for that direction (this phenomenon is known in the literature as simultaneous forward and reverse transformation under non-proportional loading (see, e.g., Bouvet et al. (2004) and Lim and McDowell (1999))). In the phenomenological framework, we considered the average behavior of variants as the behavior of an equivalent single variant. So when the load direction changes, this equivalent single variant rotates to a new preferred direction.

We concluded that the component of stress in the preferred direction of variants affects the evolution of phase transformation and variant preferred direction changes only through the component of stress orthogonal to its direction. Based on the introduced set of internal variables, we proposed a class of SMA constitutive models in the small strain regime. We proved that different basic constitutive models predict the same behavior under proportional loading conditions and the differences are highlighted under non-proportional loadings. A good correlation between the proposed model predictions and the experimental data was observed for the case of equal transformation and reorientation region radius ($R^{re} = R^{tr}$). We concluded that this equality can be interpreted as the macroscopic consequence of microscopic simultaneous forward and reverse transformation, which can link the phase transformation parameter to the reorientation one. According to all the test results reported, we also concluded that the results of the proposed had a good qualitative description of the reorientation phenomenon in SMAs under non-proportional loading, however the model needs some improvements. Since the internal variables were somehow related to micro-mechanical phenomena, we saw similar concepts when compared with micro-mechanics-based studies.

Moreover, we showed that using a multiplicative decomposition of the deformation gradient into elastic and inelastic parts together with the isotropic property of energy functions, it is possible to extend small strain constitutive models into finite deforma-

tion regime. In addition, for a complicated model (e.g., model proposed by Panico and Brinson (2007)), we showed that in the finite deformation model development, we should decompose additively the inelastic strain rate tensor into transformation and re-orientation parts, besides the multiplicative decomposition of the deformation gradient into elastic and inelastic parts. We also derived a Hencky-based constitutive model and showed that it has a similar form to the small model. In particular, under proportional loadings, it takes the full similarity, while under non-proportional loadings, the introduced elastic-like strain differs from that in the small strain formulation. Moreover, we extended small strain models into large rotation, small strain regime.

We also presented the time-discrete form of the constitutive equations and introduced different solution algorithms. It was observed that in terms of convergence, the Nucleation-Consistent Completion (*NC2*) scheme is preferred compared with the Regularization (*Reg*) scheme. We also concluded that use of a logarithmic form of the evolution equation improves the convergence behavior. It was shown that the logarithmic form improves both robustness and efficiency by decreasing the equation nonlinearity and the number of increment cuttings as well as the number of iterations. Comparing the simulation CPU times for exponential and logarithmic forms, we concluded that the logarithmic form decreases CPU time of about 20% compared with the exponential form. Also, using the *NC2* scheme decreased the CPU time compared with the *Reg* scheme. This decrease depends on the problem as well as temperature. For the simulated problems it varied from 6% to 21%. We also compared the CPU time of the proposed integration algorithm (*log + NC2*) with the previously proposed one (*exp + Reg*) and observed that the gained efficiency varied from 19% up to 36%. In another study, we concluded that use of \mathbf{U}^{in} instead of \mathbf{C}^{in} , as an unknown in the solution procedure, decreases the CPU time of about one third.

Solving several problems, we highlighted the necessity of using a finite deformation constitutive model for SMA-based structures in which usually large rotations are present. We concluded that using a small-strain formulation without considering rotation effects, may lead to highly unsatisfactory results. Moreover, it was shown that using a large rotation formulation can improve the results in the same way a full finite-strain formulation can do. We stress that while both SSLR (small strain, large rotation) and GLUS (finite strain and large rotation) formulations yielded approximately the same results, the computational cost in terms of CPU time was much lower for the SSLR formulation which is an important issue from a computational cost point of view. We presented several numerical examples to study the robustness and efficiency of the developed integration algorithms. The results showed that the developed algorithms can be used as a proper and efficient computational tool in design and analysis of SMA structures.

8.3 Future research directions

In this research, we studied three subjects: Constitutive modeling under non-proportional loading and variant reorientation, extension of small strain models into finite deformation regime and numerical implementation in FEM. However, additional research and developments are needed in order to obtain a general reliable constitutive model as well as an effective computational tool. From the modeling point of view the suggested extensions and improvements for future research are as follows:

- More investigation of the proposed general class of models and specially the limit functions and evolution equations and comparison with more experimental data.
- Modeling of temperature-induced phase transformation to develop more accurate models for description of the shape memory effect.
- According to the ever increasing number of SMA applications, modeling of secondary effects can be an interesting subject. Different material properties for austenite and martensite, different limit functions in forward and reverse transformations and asymmetric behavior under tension and compression as well as thermo-mechanical coupling can be important in specific applications. Thus, these issues should be addressed in future studies.

All the proposed developments have to be followed with experimental data. Moreover, there are still more works to be carefully studied to develop robust, computationally efficient 3-D models.

Bibliography

ABAQUS/Standard, 2008. Theory Manual. SIMULIA Inc.

Abeyaratne, R., Knowles, J. K., 1990. On the driving traction acting on a surface of strain discontinuity in a continuum. *Journal of the Mechanics and Physics of Solids* 38 (3), 345 – 360.

Anand, L., 1979. On h. henckys approximate strain-energy function for moderate deformations. *ASME Journal of Applied Mechanics* 46, 78– 82.

Anand, L., 1986. Moderate deformations in extension-torsion of incompressible isotropic elastic materials. *Mechanics and Physics of Solids* 34, 293 – 304.

Arghavani, J., Auricchio, F., Naghdabadi, R., Reali, A., 2010a. An improved, fully symmetric, finite strain phenomenological constitutive model for shape memory alloys. *Finite Element in Analysis and Design*, doi:10.1016/j.finel.2010.09.001.

Arghavani, J., Auricchio, F., Naghdabadi, R., Reali, A., 2010b. On the robustness and efficiency of integration algorithms for a 3D finite strain phenomenological SMA constitutive model. *Int. Journal for Numerical Methods in Engineering*, doi: 10.1002/nme.2964.

Arghavani, J., Auricchio, F., Naghdabadi, R., Reali, A., Sohrabpour, S., 2010c. A 3-D phenomenological constitutive model for shape memory alloys under multiaxial loadings. *International Journal of Plasticity* 26, 976 – 991.

Arghavani, J., Auricchio, F., Naghdabadi, R., Reali, A., Sohrabpour, S., 2010d. A 3D finite strain phenomenological constitutive model for shape memory alloys considering martensite reorientation. *Continuum Mechanics and Thermodynamics* 22, 345 – 362.

Arghavani, J., Auricchio, F., Reali, A., Sohrabpour, S., 2010e. A class of shape memory alloy constitutive models based on a new set of internal variables. In: *Proceedings of ISME2010, 18th Annual International Conference on Mechanical Engineering*, Tehran, Iran.

- Auricchio, F., 2001. A robust integration-algorithm for a finite-strain shape-memory-alloy superelastic model. *International Journal of Plasticity* 17 (7), 971 – 990.
- Auricchio, F., Coda, A., Reali, A., Urbano, M., 2009a. SMA numerical modeling versus experimental results: Parameter identification and model prediction capabilities. *Journal of Materials Engineering and Performance* 18 (5-6), 649–654.
- Auricchio, F., Petrini, L., 2002. Improvements and algorithmical considerations on a recent three-dimensional model describing stress-induced solid phase transformations. *International Journal for Numerical Methods in Engineering* 55 (11), 1255 – 1284.
- Auricchio, F., Petrini, L., 2004a. A three-dimensional model describing stress-temperature induced solid phase transformations: solution algorithm and boundary value problems. *International Journal for Numerical Methods in Engineering* 61 (6), 807 – 836.
- Auricchio, F., Petrini, L., 2004b. A three-dimensional model describing stress-temperature induced solid phase transformations: thermomechanical coupling and hybrid composite applications. *International Journal for Numerical Methods in Engineering* 61 (5), 716 – 737.
- Auricchio, F., Reali, A., Stefanelli, U., 2007. A three-dimensional model describing stress-induced solid phase transformation with permanent inelasticity. *International Journal of Plasticity* 23 (2), 207 – 226.
- Auricchio, F., Reali, A., Stefanelli, U., 2009b. A macroscopic 1d model for shape memory alloys including asymmetric behaviors and transformation-dependent elastic properties. *Computer Methods in Applied Mechanics and Engineering* 198 (17-20), 1631 – 1637.
- Auricchio, F., Reali, A., Stefanelli, U., 2009c. A macroscopic 1D model for shape memory alloys including asymmetric behaviors and transformation-dependent elastic properties. *Computer Methods in Applied Mechanics and Engineering* 198 (17-20), 1631 – 1637.
- Auricchio, F., Taylor, R. L., 1997. Shape-memory alloys: modelling and numerical simulations of the finite-strain superelastic behavior. *Computer Methods in Applied Mechanics and Engineering* 143 (1-2), 175 – 194.
- Auricchio, F., Taylor, R. L., Lubliner, J., 1997. Shape-memory alloys: macromodelling and numerical simulations of the superelastic behavior. *Computer Methods in Applied Mechanics and Engineering* 146 (3-4), 281 – 312.

- Baêta-Neves, A. P., Savi, M. A., Pacheco, P. M., 2002. Phenomenological modeling and numerical simulation of shape memory alloys: A thermo-plastic-phase transformation coupled model. *Journal of Intelligent Material Systems and Structures* 13 (5), 261 – 273.
- Baêta-Neves, A. P., Savi, M. A., Pacheco, P. M., 2004. On the fremond's constitutive model for shape memory alloys. *Mechanics Research Communications* 31 (6), 677 – 688.
- Ball, J. M., James, R. D., 1987. Fine phase mixtures as minimizers of energy. *Archive for Rational Mechanics and Analysis* 100, 13 – 52.
- Bathe, K.-J., 1996. *Finite Element Procedures*. Prentice Hall.
- Bazant, Z., 1984. Microplane model for strain controlled inelastic behavior. In: Desai, C.S. and Gallagher, R.H. (eds), *Mechanics of Engineering Materials*, Chap. 3, John Wiley and Sons, 45 – 59.
- Bernardini, D., Pence, T., 2004. *Advances in Multifield Theories for Continua with Substructure*. Birkhauser Boston, Ch. A Multifield Theory for the Modeling of the Macroscopic Behavior of Shape Memory Materials.
- Bondaryev, E., Wayman, C. M., 1988. Some stress-strain-temperature relationships for shape memory alloys. *Metallurgical Transactions A* 19A, 2407 – 2413.
- Bonet, J., Wood, R. D., 2008. *Nonlinear Continuum Mechanics for Finite Element Analysis*. Cambridge University Press; second edition.
- Bouvet, C., Calloch, S., Lexcelent, C., 2002. Mechanical behavior of a Cu-Al-Be shape memory alloy under multiaxial proportional and nonproportional loadings. *Journal of Engineering Materials and Technology* 124, 112 – 124.
- Bouvet, C., Calloch, S., Lexcelent, C., 2004. A phenomenological model for pseudoelasticity of shape memory alloys under multiaxial proportional and nonproportional loadings. *European Journal of Mechanics - A/Solids* 23 (1), 37 – 61.
- Boyd, J. G., Lagoudas, D. C., 1994. Thermomechanical response of shape memory composites. *Journal of Intelligent Material Systems and Structures* 5 (3), 333 – 346.
- Brinson, L. C., 1993. One-dimensional constitutive behavior of shape memory alloys: Thermomechanical derivation with non-constant material functions and redefined martensite internal variable. *Journal of Intelligent Material Systems and Structures* 4 (2), 229 – 242.

- Brocca, M., Brinson, L. C., Bazant, Z. P., 2002. Three-dimensional constitutive model for shape memory alloys based on microplane model. *Journal of the Mechanics and Physics of Solids* 50 (5), 1051 – 1077.
- Bruhns, O. T., Xiao, H., Meyers, A., 1999. Self-consistent eulerian rate type elasto-plasticity models based upon the logarithmic stress rate. *International Journal of Plasticity* 15 (5), 479 – 520.
- Buehler, W. J., Gilfrich, J. V., Wiley, R. C., 1963. Effects of low-temperature phase changes on the mechanical properties of alloys near composition tni. *Journal of Applied Physics* 34, 1475.
- Cernoch, T., Landa, M., Novk, V., Sedlk, P., Sittner, P., 2004. Acoustic characterization of the elastic properties of austenite phase and martensitic transformations in cualni shape memory alloy. *Journal of Alloys and Compounds* 378 (1-2), 140 – 144.
- Christ, D., Reese, S., 2008. Finite-element modelling of shape memory alloys—a comparison between small-strain and large-strain formulations. *Materials Science and Engineering: A* 481-482, 343 – 346.
- Christ, D., Reese, S., 2009. A finite element model for shape memory alloys considering thermomechanical couplings at large strains. *International Journal of Solids and Structures* 46 (20), 3694 – 3709.
- Criscione, J. C., Humphrey, J. D., Douglas, A. S., Hunter, W. C., 2000. An invariant basis for natural strain which yields orthogonal stress response terms in isotropic hyperelasticity. *Journal of the Mechanics and Physics of Solids* 48 (12), 2445 – 2465.
- Crisfield, M. A., 1997. *Non-linear finite element analysis of solids and structures, volume 1: Essentials*. John Wiley & Sons.
- Darijani, H., Naghdabadi, R., 2010. Constitutive modeling of solids at finite deformation using a second-order stress-strain relation. *International Journal of Engineering Science* 48 (2), 223 – 236.
- de Souza Neto, E. A., 2004. On general isotropic tensor functions of one tensor. *International Journal for Numerical Methods in Engineering* 61, 880 – 895.
- Dolce, M., Cardone, D., 2001. Mechanical behaviour of shape memory alloys for seismic applications 2. austenite niti wires subjected to tension. *International Journal of Mechanical Sciences* 43 (11), 2657 – 2677.
- Duerig, T., Pelton, A., Stckel, D., 1997. Superelastic nitinol for medical devices. *Medical Plastics and Biomaterials Magazine*, 31 – 42.

- Duerig, T., Pelton, A., Stckel, D., 1999. An overview of nitinol medical applications. *Materials Science and Engineering A* 273-275, 149 – 160.
- Duerig, T. W., Melton, K. N., Stoekel, D., Wayman, C. M., 1990. *Engineering aspects of shape memory alloys*. Butterworth-Heinemann, London.
- Eterovic, A. L., Bathe, K.-J., 1990. A hyperelastic-based large strain elasto-plastic constitutive formulation with combined isotropic-kinematic hardening using the logarithmic stress and strain measures. *International Journal for Numerical Methods in Engineering* 30 (6), 1099–1114.
- Evangelista, V., Marfia, S., Sacco, E., 2009. A 3D SMA constitutive model in the framework of finite strain. *International Journal for Numerical Methods in Engineering*.
- Falk, F., 1980. Model free-energy, mechanics and thermodynamics of shape memory alloys. *Acta Metallurgica* 28, 1773 – 1780.
- Falk, F., 1983. One-dimensional model of shape memory alloys. *Archives of Mechanics* 35, 63 – 84.
- Falk, F., Konopka, P., 1990. Three-dimensional landau theory describing the martensitic transformation of shape memory alloys. *Journal de Physique* 2, 61 – 77.
- Feng, X.-Q., Sun, Q., 2007. Shakedown analysis of shape memory alloy structures. *International Journal of Plasticity* 23 (2), 183 – 206.
- Firstov, G. S., Van Humbeeck, J., Koval, Y. N., 2006. High temperature shape memory alloys: Problems and prospects. *International Journal of Plasticity* 17, 1041 – 1047.
- Fischer, F., Tanaka, K., 1992. A micromechanical model for the kinetics of martensitic transformation. *International Journal of Solids and Structures* 29 (14-15), 1723 – 1728.
- Fremond, M., 1987. Matériaux à mémoire de forme. *CR Acad Sc Paris Tome* 304 (7), 239 – 244.
- Fremond, M., 1996. *Shape Memory Alloysalloy: A thermomechanical macroscopic theory*. Springer Vienna.
- Funakubo, H., 1987. *Shape Memory Alloys*. Gordon and Breach Science Publishers, New York.
- Gall, K., Sehitoglu, H., Maier, H., 1997. Asymmetric stress–strain response in shape memory alloys. In: Khan, A. S. (Ed.), *Physics and Mechanics of Finite Plastic and*

- Viscoplastic Deformation, Proceedings of Plasticity 97: Sixth International Symposium on Plasticity and Its Current Applications. Neat Press, Fulton, Maryland. pp. 153 – 154.
- Gall, K., Sehitoglu, H., Maier, H., Jacobus, K., 1998. Stress-induced martensitic phase transformations in polycrystalline CuZnAl shape memory alloys under different stress states. *Metall. Mater. Trans. A* 29A (7), 65 – 773.
- Gandhi, M., Thompson, B. D., 1992. *Smart materials and structures*. Springer.
- Gao, X., Brinson, L., 2002. A simplified multivariant sma model based on invariant plane nature of martensitic transformation. *Journal of Intelligent Material Systems and Structures* 13, 795 – 810.
- Gao, X., Huang, M., Brinson, L. C., 2000. A multivariant micromechanical model for smas part 1. crystallographic issues for single crystal model. *International Journal of Plasticity* 16 (10-11), 1345 – 1369.
- Ghavam, K., Naghdabadi, R., 2007. Spin tensors associated with corotational rates and corotational integrals in continua. *International Journal of Solids and Structures* 44 (16), 5222 – 5235.
- Grabe, C., Bruhns, O., 2008a. On the viscous and strain rate dependent behavior of polycrystalline niti. *International Journal of Solids and Structures* 45 (7-8), 1876 – 1895.
- Grabe, C., Bruhns, O., 2008b. Tension/torsion tests of pseudoelastic, polycrystalline niti shape memory alloys under temperature control. *Materials Science and Engineering: A* 481-482, 109 – 113.
- Grabe, C., Bruhns, O., 2009. Path dependence and multiaxial behavior of a polycrystalline niti alloy within the pseudoelastic and pseudoplastic temperature regimes. *International Journal of Plasticity* 25, 513 – 545.
- Grasser, E. J., Cozzarelli, F. A., 1994. A proposed three-dimensional constitutive model for shape memory alloys. *Journal of Intelligent Material Systems and Structures* 5, 78 – 89.
- Gurtin, M. E., Anand, L., 2005. The decomposition $f=f_{fp}$, material symmetry, and plastic irrotationality for solids that are isotropic-viscoplastic or amorphous. *International Journal of Plasticity* 21 (9), 1686 – 1719.
- Haupt, P., 2002. *Continuum Mechanics and Theory of Materials*. Springer Publication House.

- Helm, D., 2001. Formgedächtnislegierungen - experimentelle untersuchung, phanomenologische modellierung und numerische simulation der thermomechanischen materialeigenschaften. Ph.D. thesis, Universität Gesamthochschule Kassel.
- Helm, D., Haupt, P., 2003. Shape memory behaviour: modelling within continuum thermomechanics. *International Journal of Solids and Structures* 40 (4), 827 – 849.
- Henann, D. L., Anand, L., 2009. A large deformation theory for rate-dependent elastic-plastic materials with combined isotropic and kinematic hardening. *International Journal of Plasticity* 25 (10), 1833 – 1878.
- Hencky, H., 1928. Über die form des elastizitätsgesetzes bei ideal elastischen stoffen. *Z. Techn. Phys.* 9, 214 – 247.
- Holzapfel, G. A., 2000. *Nonlinear Solid Mechanics: A Continuum Approach for Engineering*. Wiley.
- Hu, Y., Müller, I., 1993. Nonequilibrium thermodynamics of pseudoelasticity. *Continuum Mechanics and Thermodynamics* 5, 163 – 204.
- Huang, M., Brinson, L. C., 1998. A multivariant model for single crystal shape memory alloy behavior. *Journal of the Mechanics and Physics of Solids* 46 (8), 1379 – 1409.
- Huang, M., Gao, X., Brinson, L. C., 2000. A multivariant micromechanical model for smas part 2. polycrystal model. *International Journal of Plasticity* 16 (10-11), 1371 – 1390.
- Hughes, T., Winget, J., 1980. Finite rotation effects in numerical integration of rate constitutive equations arising in large-deformation analysis. *International Journal for Numerical Methods in Engineering* 15, 1862 – 1867.
- Huo, Y., 1989. A mathematical model for the hysteresis in shape memory alloys. *Continuum Mech. Thermodyn* 1, 283 – 303.
- Idesman, A. V., Levitas, V. I., Stein, E., 1999. Elastoplastic materials with martensitic phase transition and twinning at finite strains: Numerical solution with the finite element method. *Computer Methods in Applied Mechanics and Engineering* 173 (1-2), 71 – 98.
- Ivshin, Y., Pence, T., 1994. A constitutive model for hysteretic phase transition behavior. *Int. J. Eng. Sci.* 32, 681 – 704.
- Jacobus, K., Sehitoglu, H., Balzer, M., 1996. Effect of stress-state on the stress-induced martensitic transformation in polycrystalline ni-ti alloy. *Metall. Mater. Trans. A* 27A, 3066 – 3073.

- Kadkhodaei, M., Salimi, M., Rajapakse, R., Mahzoon, M., 2007. Modeling of shape memory alloys based on microplane theory. *Journal of Intelligent Material Systems and Structures* 19, 541 – 550.
- Kohl, M., 2004. *Shape Memory Microactuators*. Springer.
- Lagoudas, D. C., 2008. *Shape Memory Alloys: Modeling and Engineering Applications*. Springer.
- Leclercq, S., LExcellent, C., 1996. A general macroscopic description of the thermomechanical behavior of shape memory alloys. *Journal of the Mechanics and Physics of Solids* 44 (6), 953 – 957.
- Levitas, V. I., 1998. Thermomechanical theory of martensitic phase transformations in inelastic materials. *International Journal of Solids and Structures* 35 (9-10), 889 – 940.
- Levitas, V. I., Ozsoy, I. B., 2009. Micromechanical modeling of stress-induced phase transformations. Part 1. thermodynamics and kinetics of coupled interface propagation and reorientation. *International Journal of Plasticity* 25 (2), 239 – 280.
- Levitas, V. I., Stein, E., 1997. Simple micromechanical model of thermoelastic martensitic transformations. *Mechanics Research Communications* 24 (3), 309 – 318.
- LExcellent, C., Goo, B. C., Sun, Q. P., Bernardini, J., 1996. Characterization, thermomechanical behaviour and micromechanical-based constitutive model of shape-memory Cu-Zn-Al single crystals. *Acta Materialia* 44 (9), 3773 – 3780.
- LExcellent, C., Vivet, A., Bouvet, C., Calloch, S., Blanc, P., 2002. Experimental and numerical determinations of the initial surface of phase transformation under biaxial loading in some polycrystalline shape-memory alloys. *Journal of the Mechanics and Physics of Solids* 50 (12), 2717 – 2735.
- Liang, C., Rogers, C. A., 1990. One-dimensional thermomechanical constitutive relations for shape memory materials. *Journal of Intelligent Material Systems and Structures* 1 (2), 207–234.
- Liew, K. M., Kitipornchai, S., Ng, T. Y., Zou, G. P., 2002. Multi-dimensional superelastic behavior of shape memory alloys via nonlinear finite element method. *Engineering Structures* 24 (1), 51 – 57.
- Likhacev, A. A., Koval, Y. N., 1992. On the differential equation describing the hysteretic behavior of shape-memory alloys. *Scripta Metall. Mater.* 27, 223 – 227.

- Lim, T. J., McDowell, D. L., 1999. Mechanical behavior of an Ni-Ti shape memory alloy under axial-torsional proportional and nonproportional loading. *Journal of Engineering Materials and Technology* 121, 9 – 18.
- Lin, P., Tobushi, H., Tanaka, K., Hattori, T., Makita, M., 1994. Pseudoelastic behaviour of tiny shape memory alloy subjected to strain variations. *Mechanics of Materials* 5, 694 – 701.
- Lin, R. C., Schomburg, U., 2003. A novel internal dissipation inequality by isotropy and its implication for inelastic constitutive characterization. *Mechanics Research Communications* 30 (2), 125 – 133.
- Lubarda, V. A., 2001. *Elastoplasticity Theory*. CRC PRESS.
- Lubliner, J., 1984. A maximum-dissipation principle in generalized plasticity. *Acta Mechanica* 52 (3 - 4), 225 – 237.
- Lubliner, J., Auricchio, F., 1996. Generalized plasticity and shape memory alloys. *International Journal of Solids and Structures* 33 (7), 991 – 1003.
- Luig, P., Bruhns, O., 2008. On the modeling of shape memory alloys using tensorial internal variables. *Materials Science and Engineering: A* 481-482, 379 – 383.
- Machado, L., Savi, M., 2003. Medical applications of shape memory alloys. *Brazilian Journal of Medical and Biological Research* 36, 683 – 691.
- Marketz, F., Fischer, F. D., 1996. Modelling the mechanical behavior of shape memory alloys under variant coalescence. *Computational Materials Science* 5 (1-3), 210 – 226.
- Marsden, J. E., Hughes, T., 1983. *Mathematical Foundations of Elasticity*. Prentice - Hall, Englewood Cliffs, NJ.
- Masud, A., Panahandeh, M., Auricchio, F., 1997. A finite-strain finite element model for the pseudoelastic behavior of shape memory alloys. *Computer Methods in Applied Mechanics and Engineering* 148 (1-2), 23 – 37.
- Maugin, G. A., 1992. *The thermomechanics of plasticity and fracture*. Cambridge University Press.
- McNaney, J. M., Imbeni, V., Jung, Y., Papadopoulos, P., Ritchie, R. O., 2003. An experimental study of the superelastic effect in a shape-memory nitinol alloy under biaxial loading. *Mechanics of Materials* 35 (10), 969 – 986.

- Miehe, C., 1996. Exponential map algorithm for stress updates in anisotropic multiplicative elastoplasticity for single crystals. *International Journal for Numerical Methods in Engineering* 39 (19), 3367–3390.
- Miehe, C., Apel, N., Lambrecht, M., 2002. Anisotropic additive plasticity in the logarithmic strain space: modular kinematic formulation and implementation based on incremental minimization principles for standard materials. *Computer Methods in Applied Mechanics and Engineering* 191 (47-48), 5383 – 5425.
- Moumni, Z., Zaki, W., Nguyen, Q. S., 2008. Theoretical and numerical modeling of solid-solid phase change: Application to the description of the thermomechanical behavior of shape memory alloys. *International Journal of Plasticity* 24 (4), 614 – 645.
- Müller, C., Bruhns, O., 2004. An eulerian model for pseudoelastic shape memory alloys. *Mat.-wiss. u. Werkstofftech* 35 (5), 260 – 271.
- Müller, C., Bruhns, O., 2006. A thermodynamic finite-strain model for pseudoelastic shape memory alloys. *International Journal of Plasticity* 22 (9), 1658 – 1682.
- Müller, I., 1986. Pseudoelasticity in shape memory alloys - an extreme case of thermoelasticity. *Acad. Naz. Lincei. Proc. of the Meeting on Finite Thermoelasticity* 76, 123 – 150.
- Müller, I., 1989. On the size of the hysteresis in pseudoelasticity. *Continuum Mechanics and Thermodynamics* 1, 125 – 142.
- Müller, I., Wilmanski, K., 1980. A model for phase transformation in pseudoelastic bodies. II *Nuovo Cimento* 57B, 238 – 318.
- Müller, I., Xu, H., 1991. On the pseudo-elastic hysteresis. *Acta Metallurgica et Materialia* 39 (3), 263 – 271.
- Naghdabadi, R., Yeganeh, M., Saidi, A., 2005. Application of corotational rates of the logarithmic strain in constitutive modeling of hardening materials at finite deformations. *International Journal of Plasticity* 21 (8), 1546 – 1567.
- Ogden, R. W., 1984. *Non-linear Elastic Deformations*. Ellis Horwood Limited.
- Orgeas, L., Favier, D., 1998. Stress-induced martensitic transformation of a niti alloy in isothermal shear, tension and compression. *Acta Materialia* 46 (15), 5579 – 5591.
- Ortin, J., 1992. Preisach modeling of hysteresis for a pseudoelastic cu-zn-al single crystal. *J. Appl. Phys.* 71, 1454 – 1461.

- Otsuka, K., Wayman, C. M., 1998. *Shape Memory Materials*. Cambridge University Press, Cambridge.
- Ottosen, N. S., Ristinmaa, M., 2005. *The Mechanics of Constitutive Modeling*. Elsevier.
- Pai, P. F., Palazotto, A. N., Jr., J. M. G., 1998. Polar decomposition and appropriate strains and stresses for nonlinear structural analyses. *Computers and Structures* 66 (6), 823 – 840.
- Paiva, A., Savi, M. A., Braga, A. M. B., Pacheco, P. M. C. L., 2005. A constitutive model for shape memory alloys considering tensile-compressive asymmetry and plasticity. *International Journal of Solids and Structures* 42 (11-12), 3439 – 3457.
- Paiva, A., Savi, M. A., Pacheco, P. M. C. L., 2007. Phenomenological modeling of shape memory alloy thermomechanical behavior. *Mechanics of Solids in Brazil 2007*, Marcilio Alves and H.S. da Costa Mattos (Editors), 497 – 511.
- Pan, H., Thamburaja, P., Chau, F., 2007. Multi-axial behavior of shape-memory alloys undergoing martensitic reorientation and detwinning. *International Journal of Plasticity* 23 (4), 711 – 732.
- Panico, M., Brinson, L., 2007. A three-dimensional phenomenological model for martensite reorientation in shape memory alloys. *Journal of the Mechanics and Physics of Solids* 55 (11), 2491 – 2511.
- Patoor, E., Eberhardt, A., Berveiller, M., 1994. Micromechanical modelling of the shape memory behavior. In: Brinson, L.C., Moran, B. (Eds.), *Mechanics of Phase Transformation and Shape Memory Alloys*. ASME, New York, 23 – 27.
- Patoor, E., Eberhardt, A., Berveiller, M., 1996. Micromechanical modelling of superelasticity in shape memory alloys. *J. Phys. IV* 6, 277 – 292.
- Peric, D., Owen, D. R. J., Honnor, M. E., 1992. A model for finite strain elasto-plasticity based on logarithmic strains: Computational issues. *Computer Methods in Applied Mechanics and Engineering* 94 (1), 35 – 61.
- Perkins, J., 1975. *Shape Memory Effect in Alloys*. Plenum Press, New York.
- Pethö, A., 2001. Constitutive modelling of shape memory alloys at finite strain. *Z. Angew. Math. Mech.* 81 (52), 355 – 356.
- Popov, P., Lagoudas, D. C., 2007. A 3-D constitutive model for shape memory alloys incorporating pseudoelasticity and detwinning of self-accommodated martensite. *International Journal of Plasticity* 23 (10-11), 1679 – 1720.

- Qidwai, M. A., Lagoudas, D. C., 2000. On thermomechanics and transformation surfaces of polycrystalline niti shape memory alloy material. *International Journal of Plasticity* 16 (10-11), 1309 – 1343.
- Raniecki, B., Lexcellent, C., 1994. RL-models of pseudoelasticity and their specifications for some shape memory solids. *European Journal of Mechanics - A/Solids* 13, 21 – 50.
- Raniecki, B., Lexcellent, C., 1998. Thermodynamics of isotropic pseudoelasticity in shape memory alloys. *European Journal of Mechanics - A/Solids* 17 (2), 185 – 205.
- Raniecki, B., Lexcellent, C., Tanaka, K., 1992. Thermodynamic model of pseudoelastic behaviour of shape memory alloys. *Arch. Mech.* 44 (3), 261 – 284.
- Reese, S., Christ, D., 2008. Finite deformation pseudo-elasticity of shape memory alloys - constitutive modelling and finite element implementation. *International Journal of Plasticity* 24 (3), 455 – 482.
- Reinhardt, W., Dubey, R., 1996. Application of objective rates in mechanical modeling of solids. *ASME Journal of Applied Mechanics* 63 (3), 692 – 698.
- Reinhardt, W. D., Dubey, R. N., 1995. Eulerian strain-rate as a rate of logarithmic strain. *Mechanics Research Communications* 22 (2), 165 – 170.
- Rogueda, C., Lexcellent, C., Bocher, L., 1996. Experimental study of pseudoelastic behaviour of a cu zn al polycrystalline shape memory alloy under tension-torsion proportional and non-proportional loading tests. *Arch. Mech.* 48 (6), 1025 – 1045.
- Savi, M. A., Paiva, A., 2005. A constitutive model for shape memory alloys considering tensile-compressive asymmetry and plasticity. *International Journal of Solids and Structures* 42 (11-12), 3439 – 3457.
- Schwartz, M., 2002. *Encyclopedia of smart materials*. John Wiley & Sons, Inc.
- Shaw, J. A., Kyriakides, S., 1995. Thermomechanical aspects of niti. *Journal of the Mechanics and Physics of Solids* 43 (8), 1243 – 1281.
- Simo, J. C., Hughes, T. J. R., 1998. *Computational Inelasticity*. Springer-Verlag, New York.
- Sittner, P., Hara, Y., Tokuda, M., 1995. Experimental study on the thermoelastic martensitic transformation in shape memory alloy polycrystal induced by combined external forces. *Metallurgical and Materials Transactions A* 26, 2923 – 2935.
- Sittner, P., Takakura, M., Tokuda, M., 1997. Shape memory effects under combined forces. *Materials Science and Engineering A* 234-236, 216 – 219.

- Sittner, P., Takakura, P., Hara, Y., Tokuda, M., 1996. On transformation pathways of general stress controlled thermoelastic martensitic transformation in shape memory alloys. *J. Phys. IV* 6 (1), 357 – 366.
- Souza, A. C., Mamiya, E. N., Zouain, N., 1998. Three-dimensional model for solids undergoing stress-induced phase transformations. *European Journal of Mechanics - A/Solids* 17 (5), 789 – 806.
- Spillman Jr., W. B., Sirkis, J. S., Gardiner, P. T., 1996. Smart materials and structures: what are they? *Smart Materials and Structures* 5, 247 – 254.
- Stein, E., Sagar, G., 2008. Theory and finite element computation of cyclic martensitic phase transformation with finite strain. *International Journal for Numerical Methods in Engineering* 74, 1 – 31.
- Stupkiewicz, S., Petryk, H., 2006. Finite-strain micromechanical model of stress-induced martensitic transformations in shape memory alloys. *Materials Science and Engineering: A* 438-440, 126 – 130.
- Sun, Q. P., Hwang, K. C., 1993a. Micromechanics modelling for the constitutive behavior of polycrystalline shape memory alloys–I. Derivation of general relations. *Journal of the Mechanics and Physics of Solids* 41 (1), 1 – 17.
- Sun, Q. P., Hwang, K. C., 1993b. Micromechanics modelling for the constitutive behavior of polycrystalline shape memory alloys–II. Study of the individual phenomena. *Journal of the Mechanics and Physics of Solids* 41 (1), 19 – 33.
- Tanaka, K., 1986. A thermomechanical sketch of shape memory effect: One-dimensional tensile behavior. *Res Mechanica* 18 (3), 251 – 263.
- Tanaka, K., 1990. A phenomenological description on thermomechanical behavior of shape memory alloys. *ASME Journal of Pressure Vessel Technology* 112 (2), 158–163.
- Tanaka, K., Iwasaki, R., 1985. A phenomenological theory of transformation superplasticity. *Engineering Fracture Mechanics* 21 (4), 709 – 720.
- Tanaka, K., Nagaki, S., 1982. A thermomechanical description of materials with internal variables in the process of phase transitions. *Archive of Applied Mechanics* 51 (5), 287 – 299.
- Tanaka, K., Nishimura, F., Hayashi, T., Tobushi, H., Lexcelent, C., 1995. Phenomenological analysis on subloops and cyclic behavior in shape memory alloys under mechanical and/or thermal loads. *Mechanics of Materials* 19 (4), 281 – 292.

- Taylor, G. I., 1938. Plastic strain in metals. *Journal of Institute of Metals* 62, 307 – 324.
- Terriault, P., Viens, F., Brailovski, V., 2006. Non-isothermal finite element modeling of a shape memory alloy actuator using ansys. *Computational Materials Science* 36 (4), 397 – 410.
- Thamburaja, P., 2005. Constitutive equations for martensitic reorientation and detwinning in shape-memory alloys. *Journal of the Mechanics and Physics of Solids* 53 (4), 825 – 856.
- Thamburaja, P., 2010. A finite-deformation-based phenomenological theory for shape-memory alloys. *International Journal of Plasticity* In Press, –.
- Thamburaja, P., Anand, L., 2001. Polycrystalline shape-memory materials: effect of crystallographic texture. *Journal of the Mechanics and Physics of Solids* 49 (4), 709 – 737.
- Thamburaja, P., Anand, L., 2002. Superelastic behavior in tension-torsion of an initially-textured ti-ni shape-memory alloy. *International Journal of Plasticity* 18 (11), 1607 – 1617.
- Thamburaja, P., Nikabdullah, N., 2009. A macroscopic constitutive model for shape-memory alloys: Theory and finite-element simulations. *Computer Methods in Applied Mechanics and Engineering* 198 (9-12), 1074 – 1086.
- Thiebaud, F., Lexcellent, C., Collet, M., Foltete, E., 2007. Implementation of a model taking into account the asymmetry between tension and compression, the temperature effects in a finite element code for shape memory alloys structures calculations. *Computational Materials Science* 41 (2), 208 – 221.
- Tobushi, H., Shimeno, Y., Hachisuka, T., Tanaka, K., 1998. Influence of strain rate on superelastic properties of tini shape memory alloy. *Mechanics of Materials* 30 (2), 141 – 150.
- Tokuda, M., Sittner, P., Takakura, M., Haze, M., 2002. Multi-axial constitutive equations of polycrystalline shape memory alloy. *JSME International Journal Series A Solid Mechanics and Material Engineering* 45 (2), 276–281.
- Tokuda, M., Ye, M., Takakura, M., Sittner, P., 1999. Thermomechanical behavior of shape memory alloy under complex loading conditions. *International Journal of Plasticity* 15 (2), 223 – 239.
- Trochu, F., Qian, Y.-Y., 1997. Nonlinear finite element simulation of superelastic shape memory alloy parts. *Computers and Structures* 62 (5), 799 – 810.

- Van Humbeeck, J., 2010. Introduction to shape memory alloys. Proceedings of the School and Symposium on Smart Structural Systems Technologies (S3T), Porto, Portugal, 3 – 23.
- Vladimirov, I. N., Pietryga, M. P., Reese, S., 2008. On the modelling of non-linear kinematic hardening at finite strains with application to springback-comparison of time integration algorithms. *International Journal for Numerical Methods in Engineering* 75 (1), 1–28.
- Vladimirov, I. N., Pietryga, M. P., Reese, S., 2010. Anisotropic finite elastoplasticity with nonlinear kinematic and isotropic hardening and application to sheet metal forming. *International Journal of Plasticity* 26 (5), 659 – 687.
- Wayman, M., Harrison, J., 1989. The origins of the shape memory effect. *Journal of Minerals, Metals, and Materials* 41 (99), 26 – 28.
- Wriggers, P., 2008. *Nonlinear Finite Element Methods*. Springer.
- Xiao, H., Bruhns, O. T., Meyers, A., 1997. Logarithmic strain, logarithmic spin and logarithmic rate. *Acta Mechanica* 124 (1), 89 – 105.
- Xiao, H., Bruhns, O. T., Meyers, A., 1998. Strain rates and material spins. *Journal of Elasticity* 52, 1 – 42.
- Xiao, H., Bruhns, O. T., Meyers, A., 2000. A consistent finite elastoplasticity theory combining additive and multiplicative decomposition of the stretching and the deformation gradient. *International Journal of Plasticity* 16 (2), 143 – 177.
- Xiao, H., Bruhns, O. T., Meyers, A., 2001. Large strain responses of elastic-perfect plasticity and kinematic hardening plasticity with the logarithmic rate: Swift effect in torsion. *International Journal of Plasticity* 17 (2), 211 – 235.
- Xiao, H., Bruhns, O. T., Meyers, A., 2004. Explicit dual stress-strain and strain-stress relations of incompressible isotropic hyperelastic solids via deviatoric hencky strain and cauchy stress. *Acta Mechanica* 168, 21 – 33.
- Xiao, H., Bruhns, O. T., Meyers, A., 2006. Elastoplasticity beyond small deformations. *Acta Mechanica* 182 (1), 31 – 111.
- Xiao, H., Chen, L. S., 2002. Hencky's elasticity model and linear stress-strain relations in isotropic finite hyperelasticity. *Acta Mechanica* 157 (1), 51 – 60.
- Yeganeh, M., Naghdabadi, R., 2006. Axial effects investigation in fixed-end circular bars under torsion with a finite deformation model based on logarithmic strain. *International Journal of Mechanical Sciences* 48 (1), 75 – 84.

Zaki, W., Moumni, Z., 2007. A three-dimensional model of the thermomechanical behavior of shape memory alloys. *Journal of the Mechanics and Physics of Solids* 55 (11), 2455 – 2490.

Ziolkowski, A., 2007. Three-dimensional phenomenological thermodynamic model of pseudoelasticity of shape memory alloys at finite strains. *Continuum Mechanics and Thermodynamics* 19 (6), 379 – 398.

Appendices

Appendix A

Finite strain constitutive model derivation considering \mathbf{C} and T as control variables and \mathbf{C}^{in} and z_T as internal ones

In Section 5.4, we considered $\{\mathbf{C}^e, T\}$ and $\{z_\sigma, z_T\}$ as control and internal variables, respectively. Here, we assume \mathbf{C} and T as control variables as well as \mathbf{C}^{in} and z_T as internal ones, which seems more realistic.

A hyperelastic strain energy function depends only on elastic deformation through \mathbf{C}^e or according to (5.3) on $\mathbf{F}^{in-T} \mathbf{C} \mathbf{F}^{in-1}$. Now, applying the principle of objectivity, we obtain:

$$W(\mathbf{C}^e) = W\left(\mathbf{F}^{in-T} \mathbf{C} \mathbf{F}^{in-1}\right) = W\left(\mathbf{U}^{in-1} \mathbf{C} \mathbf{U}^{in-1}\right) \quad (\text{A.1})$$

An isotropic strain energy function depends on $\mathbf{U}^{in-1} \mathbf{C} \mathbf{U}^{in-1}$ only through its invariants which are equal to those of $\mathbf{C} \mathbf{C}^{in-1}$. Therefore, we assume W as a function of $\widehat{\mathbf{C}} = \mathbf{C} \mathbf{C}^{in-1}$ and define the Helmholtz free energy function in the following form:

$$\Psi(\mathbf{C}, T, \mathbf{C}^{in}, z_T) = \frac{1}{\rho_0} W(\mathbf{C} \mathbf{C}^{in-1}) + \psi(\mathbf{C}^{in}, z_T, T) \quad (\text{A.2})$$

where ψ is defined as (5.9) while z_σ substituted by $\frac{\|\mathbf{C}^{in} - \mathbf{1}\|}{2\varepsilon_L}$ (see equation (??)).

Substituting (A.2) in Clausius-Duhem inequality (5.19) we obtain:

$$\left(\mathbf{S} - 2 \frac{\partial W}{\partial \mathbf{C}}\right) : \frac{1}{2} \dot{\mathbf{C}} - \frac{\partial W}{\partial \mathbf{C}^{in}} : \dot{\mathbf{C}}^{in} - \rho_0 \frac{\partial \psi}{\partial \mathbf{C}^{in}} : \dot{\mathbf{C}}^{in} - \rho_0 \frac{\partial \psi}{\partial z_T} \dot{z}_T - \rho_0 \left(\eta + \frac{\partial \psi}{\partial T}\right) \dot{T} \geq 0 \quad (\text{A.3})$$

Using some mathematical manipulations, we also obtain following relations:

$$\begin{cases} \frac{\partial W}{\partial \mathbf{C}} = \mathbf{C}^{in-1} \left(\frac{\partial W}{\partial \widehat{\mathbf{C}}} \right)^T \\ \frac{\partial W}{\partial \mathbf{C}^{in}} = \mathbf{C}^{in} \left(\frac{\partial W}{\partial \widehat{\mathbf{C}}} \right)^T \mathbf{C} \mathbf{C}^{in-1} \end{cases} \quad (\text{A.4})$$

Substituting (A.4) into (A.3), using (5.11) and following standard arguments, we obtain:

$$\begin{cases} \mathbf{S} = 2\mathbf{C}^{in-1} \left(\frac{\partial W}{\partial \widehat{\mathbf{C}}} \right)^T \\ \eta = -\frac{\partial \psi}{\partial T} \end{cases} \quad (\text{A.5})$$

and

$$\bar{\mathbf{M}} : \mathbf{d}^{in} - \bar{\mathbf{N}} : \mathbf{d}^{tr} + X_T \dot{z}_T \geq 0 \quad (\text{A.6})$$

where

$$\begin{cases} \bar{\mathbf{M}} = 2\mathbf{F}^{in-T} \mathbf{C} \frac{\partial W}{\partial \widehat{\mathbf{C}}} \mathbf{F}^{in-1} \\ \bar{\mathbf{N}} = 2\mathbf{F}^{in} \rho_0 \frac{\partial \psi}{\partial \mathbf{C}^{in}} \mathbf{F}^{inT} \end{cases} \quad (\text{A.7})$$

and X_T has already been defined in (5.26)₃.

We may now write:

$$\frac{\partial W}{\partial \widehat{\mathbf{C}}} = \alpha_1 \mathbf{1} + \alpha_2 \widehat{\mathbf{C}}^T + \alpha_3 \left(\widehat{\mathbf{C}}^2 \right)^T \quad (\text{A.8})$$

where $\alpha_i = \alpha_i(I_{\mathbf{C}\mathbf{C}^{in-1}}, II_{\mathbf{C}\mathbf{C}^{in-1}}, III_{\mathbf{C}\mathbf{C}^{in-1}})$. Substituting (A.8) into (A.5) and (A.7) and following a similar approach used in Chapter 5, we obtain the same constitutive equations as summarized in Section 5.4.

Appendix B

Details of derivations for Hencky-based model

In this appendix, we present details of the relations we used in the previous sections. The logarithm of a tensor \mathbf{B} can be expanded as follows:

$$\log \mathbf{B} = (\mathbf{B} - \mathbf{1}) - \frac{1}{2}(\mathbf{B} - \mathbf{1})^2 + \frac{1}{3}(\mathbf{B} - \mathbf{1})^3 - \frac{1}{4}(\mathbf{B} - \mathbf{1})^4 + \dots \quad (\text{B.1})$$

which is absolutely convergent if $\|\mathbf{B} - \mathbf{1}\| \leq 1$, but $\mathbf{B} \neq \mathbf{0}$ ¹.

We substitute $\bar{\mathbf{b}}^e$ for \mathbf{B} in (B.1) to obtain:

$$\log \bar{\mathbf{b}}^e = 2\bar{\mathbf{h}}^e = (\bar{\mathbf{b}}^e - \mathbf{1}) - \frac{1}{2}(\bar{\mathbf{b}}^e - \mathbf{1})^2 + \frac{1}{3}(\bar{\mathbf{b}}^e - \mathbf{1})^3 - \frac{1}{4}(\bar{\mathbf{b}}^e - \mathbf{1})^4 + \dots \quad (\text{B.2})$$

We now show that $\bar{\mathbf{F}}^{eT} \mathbf{s}^* \bar{\mathbf{F}}^{e-T}$ is a symmetric tensor. To this end we substitute (5.134) into (5.124)₂ to obtain:

$$\mathbf{s} = \frac{\partial \psi^e}{\partial \bar{\mathbf{h}}^e} = \alpha_1 \mathbf{1} + 2\alpha_2 \bar{\mathbf{h}}^e + 4\alpha_3 \bar{\mathbf{h}}^{e2} \quad (\text{B.3})$$

We then observe that:

$$\bar{\mathbf{F}}^{eT} (\bar{\mathbf{b}}^e - \mathbf{1})^n \bar{\mathbf{F}}^{e-T} = (\bar{\mathbf{C}}^e - \mathbf{1})^n \quad (\text{B.4})$$

where n is a positive integer number. Substituting (B.4) into (B.2), we conclude:

$$\bar{\mathbf{F}}^{eT} \bar{\mathbf{h}}^e \bar{\mathbf{F}}^{e-T} = \bar{\mathbf{H}}^e \quad \text{and} \quad \bar{\mathbf{F}}^{eT} \bar{\mathbf{h}}^{e2} \bar{\mathbf{F}}^{e-T} = \bar{\mathbf{H}}^{e2} \quad (\text{B.5})$$

We now combine (B.5) and (B.3) to obtain:

$$\bar{\mathbf{F}}^{eT} \mathbf{s}^* \bar{\mathbf{F}}^{e-T} = \alpha_1 \mathbf{1} + 2\alpha_2 \bar{\mathbf{H}}^e + 4\alpha_3 \bar{\mathbf{H}}^{e2} \quad (\text{B.6})$$

¹Similar expansion can be considered if $\|\mathbf{B} - \mathbf{1}\| > 1$, for example if $\|\mathbf{B} - 2\mathbf{1}\| \leq 1$, we use:
 $\log \mathbf{B} = \log(2)\mathbf{1} + (\mathbf{B} - 2\mathbf{1}) - \frac{1}{2}(\mathbf{B} - 2\mathbf{1})^2 + \frac{1}{3}(\mathbf{B} - 2\mathbf{1})^3 - \frac{1}{4}(\mathbf{B} - 2\mathbf{1})^4 + \dots$

According to (B.6), we conclude that $\bar{\mathbf{F}}^{eT} \mathbf{s} \bar{\mathbf{F}}^{e-T}$ is a symmetric tensor.

We now show that $\bar{\mathbf{h}}^e = \frac{1}{2} \bar{\mathbf{F}}^{-T} \log(\bar{\mathbf{C}} \bar{\mathbf{C}}^{in-1}) \bar{\mathbf{F}}^T$. To this end, we observe that:

$$\bar{\mathbf{b}}^e = \bar{\mathbf{F}} \bar{\mathbf{C}}^{in-1} \bar{\mathbf{F}}^T = \bar{\mathbf{F}}^{-T} \bar{\mathbf{C}} \bar{\mathbf{C}}^{in-1} \bar{\mathbf{F}}^T \quad (\text{B.7})$$

According to (B.7), we conclude:

$$(\bar{\mathbf{b}}^e - \mathbf{1})^n = \bar{\mathbf{F}}^{-T} \left(\bar{\mathbf{C}} \bar{\mathbf{C}}^{in-1} - \mathbf{1} \right)^n \bar{\mathbf{F}}^T \quad (\text{B.8})$$

We now substitute (B.8) into (B.2) and obtain:

$$\bar{\mathbf{h}}^e = \frac{1}{2} \bar{\mathbf{F}}^{-T} \log(\bar{\mathbf{C}} \bar{\mathbf{C}}^{in-1}) \bar{\mathbf{F}}^T \quad (\text{B.9})$$

Substituting (B.9) into (B.5) we also obtain:

$$\bar{\mathbf{F}}^{inT} \bar{\mathbf{H}}^e \bar{\mathbf{F}}^{in} = \frac{1}{2} \log(\bar{\mathbf{C}} \bar{\mathbf{C}}^{in-1}) \bar{\mathbf{C}}^{in} \quad (\text{B.10})$$

We now mention the following properties:

$$\begin{aligned} \bar{\mathbf{C}} \bar{\mathbf{C}}^{in-1} - \mathbf{1} &= \bar{\mathbf{U}}^{in} \left(\bar{\mathbf{U}}^{in-1} \bar{\mathbf{C}} \bar{\mathbf{U}}^{in-1} - \mathbf{1} \right) \bar{\mathbf{U}}^{in-1} \\ \left(\bar{\mathbf{C}} \bar{\mathbf{C}}^{in-1} - \mathbf{1} \right)^n &= \bar{\mathbf{U}}^{in} \left(\bar{\mathbf{U}}^{in-1} \bar{\mathbf{C}} \bar{\mathbf{U}}^{in-1} - \mathbf{1} \right)^n \bar{\mathbf{U}}^{in-1} \end{aligned} \quad (\text{B.11})$$

Finally, substitution of (B.11) into logarithmic expansion (B.1) yields:

$$\log(\bar{\mathbf{C}} \bar{\mathbf{C}}^{in-1}) = \bar{\mathbf{U}}^{in} \log \left(\bar{\mathbf{U}}^{in-1} \bar{\mathbf{C}} \bar{\mathbf{U}}^{in-1} \right) \bar{\mathbf{U}}^{in-1} \quad (\text{B.12})$$

We assumed $G(\boldsymbol{\alpha}, q)$ to be an isotropic function of its argument, therefore, considering representation theorem, we may write:

$$\frac{\partial G(\boldsymbol{\alpha}, q)}{\partial \boldsymbol{\alpha}} = c_1 \mathbf{1} + c_2 \boldsymbol{\alpha} + c_3 \boldsymbol{\alpha}^2 \quad (\text{B.13})$$

where the coefficients c_1 , c_2 and c_3 are functions of the invariants of $\boldsymbol{\alpha}$ and q . We now multiply (B.13) from left and right by $\bar{\mathbf{F}}^{inT}$ and $\bar{\mathbf{F}}^{in}$, respectively:

$$\bar{\mathbf{F}}^{inT} \frac{\partial G(\boldsymbol{\alpha}, q)}{\partial \boldsymbol{\alpha}} \bar{\mathbf{F}}^{in} = c_1 \bar{\mathbf{F}}^{inT} \bar{\mathbf{F}}^{in} + c_2 \bar{\mathbf{F}}^{inT} \boldsymbol{\alpha} \bar{\mathbf{F}}^{in} + c_3 \bar{\mathbf{F}}^{inT} \boldsymbol{\alpha}^2 \bar{\mathbf{F}}^{in} \quad (\text{B.14})$$

We now use (5.154) in (B.14) to obtain:

$$\bar{\mathbf{F}}^{inT} \frac{\partial G(\boldsymbol{\alpha}, q)}{\partial \boldsymbol{\alpha}} \bar{\mathbf{F}}^{in} = c_1 \bar{\mathbf{U}}^{in2} + c_2 \bar{\mathbf{U}}^{in} \mathbf{Z} \bar{\mathbf{U}}^{in} + c_3 \bar{\mathbf{U}}^{in} \mathbf{Z}^2 \bar{\mathbf{U}}^{in} = \bar{\mathbf{U}}^{in} (c_1 \mathbf{1} + c_2 \mathbf{Z} + c_3 \mathbf{Z}^2) \bar{\mathbf{U}}^{in} \quad (\text{B.15})$$

In equation (5.154) we showed that the invariants of $\boldsymbol{\alpha}$ are equal to those of \mathbf{Z} . Thus, we conclude that the terms inside the parenthesis in (B.15) represent $\frac{\partial G(\mathbf{Z}, q)}{\partial \mathbf{Z}}$. Therefore, we can write:

$$\bar{\mathbf{F}}^{inT} \frac{\partial G(\boldsymbol{\alpha}, q)}{\partial \boldsymbol{\alpha}} \bar{\mathbf{F}}^{in} = \bar{\mathbf{U}}^{in} \frac{\partial G(\mathbf{Z}, q)}{\partial \mathbf{Z}} \bar{\mathbf{U}}^{in} \quad (\text{B.16})$$

Appendix C

Linearization of the asymmetric finite strain Souza model

In this appendix, we present the linearized form of equation (6.9). To this end, we define the following second order tensors¹:

$$\bar{\mathbf{U}} = \mathbf{U}^{in-1}, \quad \bar{\mathbf{C}} = \mathbf{C}^{in-1}, \quad \mathbf{Q} = \Delta\zeta\bar{\mathbf{U}}\mathbf{A}\bar{\mathbf{U}}, \quad \mathbf{G} = \exp(\mathbf{Q}), \quad \mathbf{W} = \mathbf{U}\bar{\mathbf{C}}_n\mathbf{U}, \quad \mathbf{H} = \log(\mathbf{W}) \quad (\text{C.1})$$

and the following fourth-order tensors:

$$\begin{aligned} \mathbb{U} &= \frac{\partial \mathbf{U}}{\partial \mathbf{C}^{in}}, & \bar{\mathbb{U}} &= \frac{\partial \bar{\mathbf{U}}}{\partial \mathbf{C}^{in}}, & \bar{\mathbb{C}} &= \frac{\partial \bar{\mathbf{C}}}{\partial \mathbf{C}^{in}}, & \mathbb{S} &= \frac{\partial \mathbf{S}}{\partial \mathbf{C}^{in}}, & \mathbb{X} &= \frac{\partial \mathbf{X}}{\partial \mathbf{C}^{in}} \\ \mathbb{Y} &= \frac{\partial \mathbf{Y}}{\partial \mathbf{C}^{in}}, & \mathbb{A} &= \frac{\partial \mathbf{A}}{\partial \mathbf{C}^{in}}, & \mathbb{Q} &= \frac{\partial \mathbf{Q}}{\partial \mathbf{C}^{in}}, & \mathbb{W} &= \frac{\partial \mathbf{W}}{\partial \mathbf{C}^{in}}, & \mathbb{G} &= \frac{\partial \mathbf{G}}{\partial \mathbf{Q}} \\ \mathbb{H} &= \frac{\partial \mathbf{H}}{\partial \mathbf{W}}, & \tilde{\mathbb{S}} &= \frac{\partial \mathbf{S}}{\partial \mathbf{C}}, & \tilde{\mathbb{Y}} &= \frac{\partial \mathbf{Y}}{\partial \mathbf{C}}, & \tilde{\mathbb{A}} &= \frac{\partial \mathbf{A}}{\partial \mathbf{C}} \end{aligned} \quad (\text{C.2})$$

with components:

$$\begin{aligned} \mathbb{X}_{ijkl} &= \frac{1}{2}h\mathbb{I}_{ijkl} + \frac{1}{2}(\tau_M + \gamma)\mathbb{N}_{ijkl} \\ \mathbb{S}_{ijkl} &= \frac{1}{2}\lambda\bar{\mathbb{C}}_{mnkl}C_{mn}\bar{C}_{ij} + 2\alpha_1\bar{\mathbb{C}}_{ijkl} + 2\alpha_2\bar{\mathbb{C}}_{imkl}C_{mn}\bar{C}_{nj} + 2\alpha_2\bar{C}_{im}C_{mn}\bar{\mathbb{C}}_{nijkl} \\ \mathbb{Y}_{ijkl} &= C_{im}\mathbb{S}_{mjkl} - \mathbb{I}_{imkl}X_{mj} - C^{in}_{im}\mathbb{X}_{mjkl} \\ \mathbb{A}_{ijkl} &= 2Z_{impq}\left(\mathbb{Y}_{pqkl} - \frac{1}{3}\mathbb{Y}_{nnkl}\delta_{pq}\right)C^{in}_{mj} + 2Z_{im}\mathbb{I}_{mjkl} \\ \mathbb{Q}_{ijkl} &= \Delta\zeta\bar{\mathbb{U}}_{imkl}A_{mn}\bar{U}_{nj} + \Delta\zeta\bar{U}_{im}A_{mn}\bar{\mathbb{U}}_{nijkl} + \Delta\zeta\bar{U}_{im}\mathbb{A}_{mnkl}\bar{U}_{nj} \\ \mathbb{W}_{ijkl} &= \mathbb{U}_{irkl}(\bar{C}_n)_{rs}U_{sm} + U_{ir}(\bar{C}_n)_{rs}\mathbb{U}_{sjkl} \\ \tilde{\mathbb{S}}_{ijkl} &= \frac{1}{2}\lambda\bar{C}_{ij}\bar{C}_{kl} + 2\alpha_2\bar{C}_{im}\mathbb{I}_{mnkl}\bar{C}_{nj} \\ \tilde{\mathbb{Y}}_{ijkl} &= C_{im}\tilde{\mathbb{S}}_{mjkl} + \mathbb{I}_{imkl}S_{mj} \\ \tilde{\mathbb{A}}_{ijkl} &= 2Z_{impq}\left(\tilde{\mathbb{Y}}_{pqkl} - \frac{1}{3}\tilde{\mathbb{Y}}_{nnkl}\delta_{pq}\right)C^{in}_{mj} \end{aligned} \quad (\text{C.3})$$

¹We note that, the notation in this appendix is independent from those we have used in different chapters and it should not be confused.

where,

$$\mathbb{N} = \frac{1}{\|\mathbf{E}^{in}\|} (\mathbb{I} - \mathbf{N} \otimes \mathbf{N}), \quad \mathbb{Z} = \frac{1}{\|\mathbf{Y}^D\|} (\mathbb{I} - \mathbf{Z} \otimes \mathbf{Z}^T) \quad (\text{C.4})$$

and

$$\mathbf{N} = \frac{\mathbf{E}^{in}}{\|\mathbf{E}^{in}\|}, \quad \mathbf{Z} = \frac{\mathbf{Y}^D}{\|\mathbf{Y}^D\|} \quad (\text{C.5})$$

We compute the components of tensors \mathbf{U} , $\bar{\mathbf{U}}$, $\bar{\mathbf{C}}$, \mathbf{G} , \mathbf{H} as well as \mathbb{U} , $\bar{\mathbb{U}}$, $\bar{\mathbb{C}}$, \mathbb{G} and \mathbb{H} through spectral decomposition (de Souza Neto, 2004). The components of the fourth-order identity tensor \mathbb{I} are defined as:

$$\mathbb{I}_{ijkl} = \frac{1}{2} \delta_{ik} \delta_{jl} + \frac{1}{2} \delta_{il} \delta_{jk} \quad (\text{C.6})$$

We now present the linearized form of equations (6.5) as:

$$\begin{aligned} (\mathbb{R}_{11})_{ijkl} &= \Delta\zeta \tilde{\mathbb{A}}_{ijkl} \\ (\mathbb{R}_{12})_{ijkl} &= \mathbb{U}_{imkl} H_{mn} U_{nj} + U_{im} H_{mn} \mathbb{U}_{n jkl} + U_{im} \mathbb{H}_{mnkl} U_{nj} + \Delta\zeta \mathbb{A}_{ijkl} \\ (\mathbf{R}_{13})_{ij} &= A_{ij} \\ (\mathbf{R}_{14})_{ij} &= -2\Delta\zeta \mathbb{Z}_{impq} C^{in}_{mj} (C^{in}_{pn} N_{nq} - \frac{1}{3} C^{in}_{kl} N_{kl} \delta_{pq}) \\ (\mathbf{R}_{21})_{ij} &= Z_{nm} \tilde{\mathbb{Y}}_{mnij}, \quad (\mathbf{R}_{22})_{ij} = Z_{nm} \mathbb{Y}_{mnij}, \quad R_{23} = 0, \quad R_{24} = -Z_{ij} C^{in}_{im} N_{mj} \\ (\mathbf{R}_{31})_{ij} &= 0, \quad (\mathbf{R}_{32})_{ij} = \frac{1}{2} N_{ij}, \quad R_{33} = 0, \quad R_{34} = 0 \end{aligned} \quad (\text{C.7})$$

where

$$\begin{aligned} \mathbb{R}_{11} &= \mathbf{R}_{,C}^{in}, \quad \mathbb{R}_{12} = \mathbf{R}_{,C^{in}}^{in}, \quad \mathbf{R}_{13} = \mathbf{R}_{,\Delta\zeta}^{in}, \quad \mathbf{R}_{14} = \mathbf{R}_{,\gamma}^{in} \\ \mathbf{R}_{21} &= R_{,C}^{\zeta}, \quad \mathbf{R}_{22} = R_{,C^{in}}^{\zeta}, \quad R_{23} = R_{,\Delta\zeta}^{\zeta}, \quad R_{24} = R_{,\gamma}^{\zeta} \\ \mathbf{R}_{31} &= R_{,C}^{\gamma}, \quad \mathbf{R}_{32} = R_{,C^{in}}^{\gamma}, \quad R_{33} = R_{,\Delta\zeta}^{\gamma}, \quad R_{34} = R_{,\gamma}^{\gamma} \end{aligned} \quad (\text{C.8})$$

In order to linearize the time-discrete evolution equation in the exponential form, we derive the linearized form of equation (6.5) as follows:

$$\begin{aligned} (\mathbb{R}_{11})_{ijkl} &= \Delta\zeta \bar{\mathbb{U}}_{im} \mathbb{G}_{mnpq} \tilde{\mathbb{A}}_{rskl} \bar{\mathbb{U}}_{nj} \bar{\mathbb{U}}_{pr} \bar{\mathbb{U}}_{sq} \\ (\mathbb{R}_{12})_{ijkl} &= \bar{\mathbb{U}}_{imkl} G_{mn} \bar{\mathbb{U}}_{nj} + \bar{\mathbb{U}}_{im} \mathbb{G}_{mnkl} \bar{\mathbb{U}}_{nj} + \bar{\mathbb{U}}_{im} G_{mn} \bar{\mathbb{U}}_{n jkl} \\ (\mathbf{R}_{13})_{ij} &= \bar{\mathbb{U}}_{im} \bar{\mathbb{U}}_{mn} \bar{\mathbb{U}}_{pq} \bar{\mathbb{U}}_{rj} A_{np} G_{qr} \\ (\mathbf{R}_{14})_{ij} &= -2\Delta\zeta \bar{\mathbb{U}}_{im} \bar{\mathbb{U}}_{nj} \mathbb{G}_{mnpq} \bar{\mathbb{U}}_{pr} \bar{\mathbb{U}}_{sq} \mathbb{Z}_{rmpq} C^{in}_{ms} (C^{in}_{pn} N_{nq} - \frac{1}{3} C^{in}_{kl} N_{kl} \delta_{pq}) \end{aligned} \quad (\text{C.9})$$

Appendix D

Publications

The published results of this research are as follows:

International journals:

1. **J. Arghavani**, F. Auricchio, R. Naghdabadi, A. Reali, S. Sohrabpour. A 3D phenomenological model for shape memory alloys under multiaxial loadings. *International Journal of Plasticity*, 26, 976-991, 2010,
2. **J. Arghavani**, F. Auricchio, R. Naghdabadi, A. Reali, S. Sohrabpour. A 3D finite strain phenomenological constitutive model for shape memory alloys considering martensite reorientation. *Continuum Mechanics and Thermodynamics*, 22, 345-362, 2010.
3. **J. Arghavani**, F. Auricchio, R. Naghdabadi, A. Reali. On the robustness and efficiency of integration algorithms for a 3D finite strain phenomenological SMA constitutive model, *International Journal for Numerical Methods in Engineering*, doi: 10.1002/nme.2964, 2010.
4. **J. Arghavani**, F. Auricchio, R. Naghdabadi, A. Reali. An improved, fully symmetric, finite strain phenomenological constitutive model for shape memory alloys, *Finite Elements in Analysis and Design*, doi:10.1016/j.finel.2010.09.001, 2010.
5. **J. Arghavani**, F. Auricchio, R. Naghdabadi. A finite strain kinematic hardening constitutive model based on Hencky strain: general framework, solution algorithm and application to shape memory alloys, submitted.

International conference proceedings:

6. **J. Arghavani**, F. Auricchio, R. Naghdabadi, A. Reali. *On the constitutive modeling and numerical implementation of shape memory alloys under multiaxial loadings - Part I: constitutive model development at small and finite strains*, Proceedings of the School and Symposium on Smart Structural Systems Technologies (2010).
7. **J. Arghavani**, F. Auricchio, R. Naghdabadi, A. Reali. *On the constitutive modeling and numerical implementation of shape memory alloys under multiaxial loadings - Part II: numerical implementation and simulations*, Proceedings of the School and Symposium on Smart Structural Systems Technologies (2010).
8. **J. Arghavani**, F. Auricchio, A. Reali, S. Sohrabpour. *A class of shape memory alloy constitutive models based on a new set of internal variables*, Proceedings of ISME2010, 18th Annual International Conference on Mechanical Engineering (2010).
9. **J. Arghavani**, F. Auricchio, R. Naghdabadi, A. Reali. *A finite strain SMA constitutive model: comparison of small and finite strain formulations*, Proceedings of ISME2010, 18th Annual International Conference on Mechanical Engineering (2010).
10. **J. Arghavani**, F. Auricchio, R. Naghdabadi, A. Reali, S. Sohrabpour. *An efficient, non-regularized solution algorithm for a finite strain shape memory alloy constitutive model*, Proceedings of ESDA2010, 10th Biennial Conference on Engineering Systems Design and Analysis (2010).
11. F. Auricchio, **J. Arghavani**, M. Conti, S. Morganti, A. Reali, U. Stefanelli. *Shape-memory alloys: effective 3D modeling, computational aspects and analysis of actuator and biomedical devices*, Proceedings of ACTUATOR10 - International Conference and Exhibition on New Actuators and Drive Systems (2010).
12. R. Naghdabadi, **J. Arghavani**, F. Auricchio, A. Reali, S. Sohrabpour. *Computational Issues in Finite Strain SMA Constitutive Modeling*, Proceeding of IV European Congress on Computational Mechanics (ECCM IV): Solids, Structures and Coupled Problems in Engineering, Paris, France (2010).
13. F. Auricchio, **J. Arghavani**, M. Conti, S. Morganti, A. Reali, U. Stefanelli. *Shape-memory alloys: effective 3D modeling, computational aspects and biomedical device analysis*, Proceeding of IV European Congress on Computational Mechan-

ics (ECCM IV): Solids, Structures and Coupled Problems in Engineering, Paris, France (2010).

14. E. K. Khaje-Saeed, **J. Arghavani**, S. Sohrabpour. *A model for magnetic-induced strain in NiMnGa magnetic shape memory alloy*, 17th International Conference on Mechanical Engineering, ISME2009, University of Tehran, Iran (2009).
15. R. Avazmohammadi, **J. Arghavani**, R. Naghdabadi. *Micromechanics modeling of shape memory alloy fiber composites with slightly weakened interfaces*, SPIE Smart Materials, Nano-and Micro-Smart Systems, Melbourne, Australia (2009).